DISSERTATION

SUBMITTED TO THE COMBINED FACULTIES

FOR THE NATURAL SCIENCES AND FOR MATHEMATICS

OF THE RUPERTO-CAROLA UNIVERSITY OF HEIDELBERG, GERMANY

FOR THE DEGREE OF

DOCTOR OF NATURAL SCIENCES

Put forward by
Dipl.-Phys. Joachim Hahn
born in Heidelberg, Germany

Oral examination: 8 January 2014

Supernova Remnants with H.E.S.S.:

SYSTEMATIC ANALYSIS AND POPULATION SYNTHESIS

Abstract

One of the most prominent classes of astrophysical particle accelerators are supernova remnants. These objects result from the interaction of stellar material, being ejected during supernova explosions at velocities of several thousands of kilometres per second, with the ambient medium. The H.E.S.S. experiment is able to observe such sources at very-high-energies ($>$100 GeV) with the best possible sensitivity to date. As a first part of this work, a simulation of the theoretically expected population of supernova remnants at these energies was performed, followed by an analysis of the very-high-energy gamma-ray emission from the source ensemble known at other wave lengths. Assuming currently accepted standard parameters, the simulation is able to reproduce the observed numbers of supernova remnants in the radio as well as the very-high-energy range, but only if these objects amplify their own magnetic field. It should be mentioned, however, that a large number of parameters is required in the simulation, many of which are attributed with large uncertainties. The data analysis did not result in any new detections but allowed it to determine over a hundred flux upper limits. A hint of a faint, cumulated emission from the ensemble of supernova remnants might have been observed. A comparison to the developed model gives an explanation for the gamma-ray faintness of the investigated objects and suggests a possible detection of over a hundred supernova remnants with the next generation of Cherenkov telescope experiments.

Kurzfassung

Eine der bedeutendsten Klassen von astrophysikalischen Teilchenbeschleunigern sind Supernovaüberreste. Diese sind Stoßwellen, die entstehen, wenn das in einer Supernova ausgestoßene Sternenmaterial bei Geschwindigkeiten von mehreren tausend Kilometern pro Sekunde mit dem Umgebungsmedium wechselwirkt. Das H.E.S.S. Experiment ist in der Lage, solche Quellen bei sehr hohen Energien ($>$100 GeV) mit der derzeit bestmöglichen Sensitivität zu untersuchen. Diese Arbeit befasst sich zunächst mit einer Simulation der theoretisch erwarteten Supernovaüberrestepopulation in diesem Energiebereich, um dann anschließend das aus anderen Wellenlängen bekannte Quellensemble auf die Emission bei sehr hohen Energien zu untersuchen. Die theoretische Modellierung kann, unter Annahme zur Zeit akzeptierter Standardparameter, die beobachtete Zahl an Supernovaüberresten sowohl bei Radio- als auch bei sehr hohen Energien reproduzieren - allerdings nur, wenn diese Strahlungsquellen ihr eigenes Magnetfeld verstärken. Es muss jedoch erwähnt werden, dass die Zahl an Parametern sehr groß ist und viele dieser mit hohen Unsicherheiten behaftet sind. Die Datenanalyse ergab keine neue Detektion, erlaubte allerdings die Bestimmung von über einhundert Flussobergrenzen. Es zeigte sich möglicherweise ein Hinweis auf eine schwache, akkumulierte Gammastrahlenemission vom Supernovaüberresteensemble, welche allerdings nicht statistisch signifikant ist. Der Modellvergleich liefert eine Erklärung für die geringe individuelle Gammastrahlenemission der untersuchten Objekte und legt nahe, dass die nächste Generation von Tscherenkowteleskopexperimenten womöglich über einhundert Supernovaüberreste detektieren wird.

Contents

List of Figures

List of Tables

Preface

Supernova remnants (SNRs) result from supernovae (SNe), which are among the most violent processes in nature known to date. These explosions occur at the end of the life of a star and are of such brilliance that they can outshine their entire host galaxies for a short time. Over the last 1000 years astronomers have documented bright, transitional stars on several occasions. At the time, the origin of these phenomena remained a mystery and it was not before the 20th century when supernovae could be identified as the deaths of possibly very massive stars [Baade and Zwicky, 1934b]. Hundreds of years after their observation, we can now study the remains of these historic SN explosions with modern instrumentation.

Today it is known that during the SN explosion, stellar material amounting to more than the mass of our sun is being ejected into interstellar space at velocities of several thousands of kilometres per second, see e.g. [Willingale et al., 2002]. The expanding material drives strong a shock into the surrounding medium, compressing and heating it up.

SNRs have been observed over a range of more than twenty decades in energy, from the radio up to the very high energy (VHE, E>100GeV) regime. It first became clear from radio observations that these shocks would have to be places of efficient particle acceleration. That is, the radio spectra from these objects are best interpreted as synchrotron emission from relativistic electrons. Together with theories predicting the acceleration of particles at astrophysical shocks that emerged in the 70s of the last century (see e.g. [Bell, 1978]), a convincing theoretical picture about the radio-emission from these objects could be drawn. Hundreds of SNRs, just like the historical ones, have been discovered in the radio so far [Green, 2009]. Also in X-rays these objects have been observed. In many cases, the X-ray emission can, just like at radio wave lengths, be attributed to synchrotron emission - here, however, emitted by electrons that are typically more than four orders of magnitude more energetic. In fact, synchrotron radiation at X-ray energies implies the acceleration of electrons up to $\sim$100TeV.

It is theorised that SNRs are able to accelerate hadrons to even higher energies in the PeV range, see e.g. [Ptuskin and Zirakashvili, 2005]. This idea, together with the energetics and the rate of SN explosions, renders SNR the prime source candidates for galactic CRs.

Such ultrarelativistic particles (both electrons and hadrons) are able to emit gamma-rays in the VHE regime, and the development of the imaging atmospheric Cherenkov technique (IACT) allows it today to observe the universe at

these wave lengths. One instrument leading this field is the H.E.S.S. experiment, and its observations resulted in the discovery of dozens of gamma-ray sources, including several SNRs.
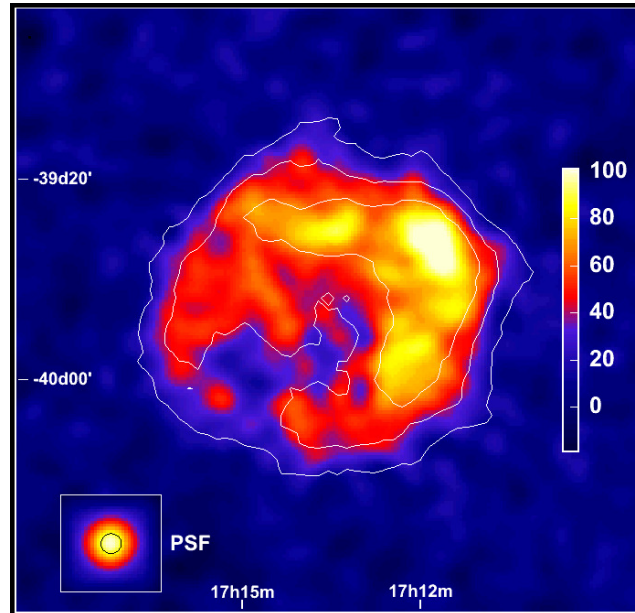
Figure 0.1.: Excess map of RXJ J1713.7-3946. The contours indicate the 5, 10 and 15σ significance levels, respectively. Figure extracted from [Aharonian et al., 2006b].

Unlike in radio astronomy, the field is at its infancy in the VHE range: While more than a dozen gamma-ray sources have been firmly associated with a SNR in this energy regime, only for eight of them a clear shell-like structure could be determined. As an example, the SNR RXJ J1713.7-3946 is shown in Fig.0.1. In the other cases, the VHE emission originates not only from the shell itself but rather from energetic processes close to an associated pulsar or the interaction of the SNR shock with interstellar gas clouds.

The interpretation of the VHE emission from SNRs is challenging: Not only electrons but also hadrons are able to emit photons at these energies. There are many unanswered questions regarding SNRs in the TeV regime, for instance:

- What is the nature of the VHE gamma-ray emission - is it caused by hadrons or electrons?

- What is the shape of the underlying particle distribution?

- How efficient are SNRs in accelerating particles?

- How bright is the SNR population at VHE energies and what can we expect to see with future instruments?

The presented work will try to address some of these questions. This is attempted not by studying individual sources but rather by investigating the population of known SNRs as a whole.

Consequently, over a hundred radio and X-ray SNR positions have been analysed for their VHE emission in a uniform method. In parallel, a simulation was created that aimed at synthesising the expected SNR population in the VHE range and was then used in a comparison to the analysis results.

This work is organised in five chapters: In Chapter 1 the H.E.S.S. instrument and the analysis methods that have been used will be shortly presented. How a good data quality is achieved for analysis will be described in the second chapter. Also, a new atmospheric monitoring quantity will be presented there. This chapter is followed by a generic introduction to the physics of SNRs in chapter 3. There, several models will be presented that are used in chapter 4, where the population synthesis model for SNRs in the VHE range will be described and the results of this study will be discussed. Lastly, in chapter 5 the analysis of the VHE emission from the SNR population known from other wave lengths will be present. The analysis results will then be discussed and a comparison to the model from chapter 4 will be performed.

1. The Imaging Atmospheric Cherenkov Technique

In order to observe photons above energies of E$\sim$50MeV, one has to reconstruct the characteristic properties of these particles from the electron-positron pairs that are created when such energetic gamma-rays interact with matter. This process is the theoretical basis of all techniques used to observe photons above this energy. Modern gamma-ray satellites apply solid state detectors where the creation of electron-positron pairs is triggered and their tracks are reconstructed. This allows a reconstruction of direction and energy of the primary particle.

Since gamma-rays from non-thermally distributed particles often follow steep power-law spectra, relatively small collecting areas ($\sim$1m^2) suffice for observations at photon energies smaller than several GeV. Detectors of that size fit into space craft which is why this energy range is the domain of satellite experiments. However, at higher energies, due to its spectral shape the gamma-ray flux quickly decreases and much larger detector areas are required. Within the current technological possibilities, this is only possible on the Earth's surface. Here, one can replace the solid state detector by a combination of atmosphere and optical telescopes: The atmosphere acts as the calorimeter and the telescopes can reconstruct the primary particle from the track of secondaries in form of extended air showers (EAS), because they emit short pulses of Cherenkov light.

In 1960, Chudakov et al. first attempted to observe gamma-rays from astrophysical objects and were able to give a flux upper limit on the VHE gamma-ray emission from the Crab nebula. This experiment was followed by the Whipple telescope eight years later, but also this instrument was not able to detect the Crab. The field developed slowly until two breakthroughs were made. In 1989, a 37 pixel camera of photo-multipliers (PMTs) was installed in the Whipple telescope, allowing the image analysis of EAS. This *imaging* technique almost immediately resulted in the detection of the Crab at a high significance. About five years later, the stereoscopic approach was introduced in the HEGRA experiment, which further improved the sensitivity and accuracy of the IACT method by each air shower at different observation angles. These important milestones allowed for interesting discoveries in the non-thermal universe and opened the new discipline of VHE astronomy, accessible with the current generation of *Imaging Atmospheric Cherenkov Technique* (IACT) instruments MAGIC, VERITAS and H.E.S.S.

A comprehensive review on the IACT technique can be found in [Völk and Bernlöhr, 2009], and the following short introduction is in parts along the lines of this work.

1.1. Air Showers

Upon entering the Earth atmosphere, cosmic rays (CR) and VHE photons trigger the creation of particle cascades by interacting with atmospheric nuclei. The resulting EAS are referred to as either *hadronic* or *electromagnetic*, depending on the nature of the primary particle.

1.1.1. Electromagnetic Air Showers

The dominant interactions of gamma-rays and electrons with the atmospheric material are Bremsstrahlung and pair production in the Coulomb field of the gas nuclei. The interplay between these two processes results in a particle cascade: Gamma rays produce $e^{\pm}$ pairs, and those electrons and positrons in turn emit Bremsstrahlung quanta. Fig.1.1 illustrates this process. This chain reaction ends as soon as the photon energies drop below $\sim$80MeV (typically after $\sim 10^{-4}$s), where the cross-section for the ionisation of gas molecules becomes dominant.

Development of gamma–ray air showers
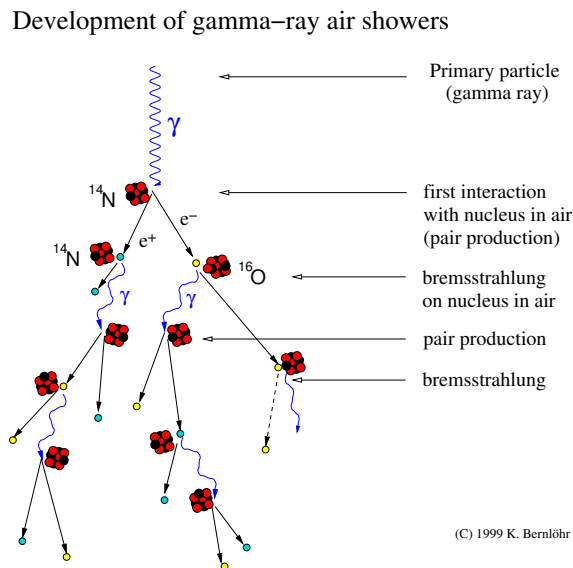
Figure 1.1.: Scheme showing the development of an electromagnetic air shower. Courtesy of Konrad Bernlöhr.

The characteristic length-scale of these processes is given by the radiation

length X_0 of the Bremsstrahlung process, which is 36.6g/cm^2 in air. This quantity corresponds to the travel distance of photons undergoing Bremsstrahlung to the point where their energy is reduced to $1/e$ of the initial value. The mean free path of pair production is similar, $\bar{\lambda} = 9/7 X_0$. The number of shower particles reaches a maximum at $\sim$250-450g/cm^2 (assuming gamma energies between 20GeV-20TeV) which corresponds to a height of $\sim$7-12km in the atmosphere [Völk and Bernlöhr, 2009]. The total particle number in the EAS is roughly proportional to the primary particle's energy.

1.1.2. Hadronic Air Showers

If the incident particle is a proton or nucleus, hadronic interactions are important in the development of EAS. That is, such particles produce mostly neutral and charged pions which in turn decay into gamma rays and muons (plus two neutrinos), respectively. As a result, gamma rays from π^0-decay initiate electromagnetic sub-showers while muons and neutrinos carry away a large part of the primary's energy. These processes are shown in Fig.1.3.
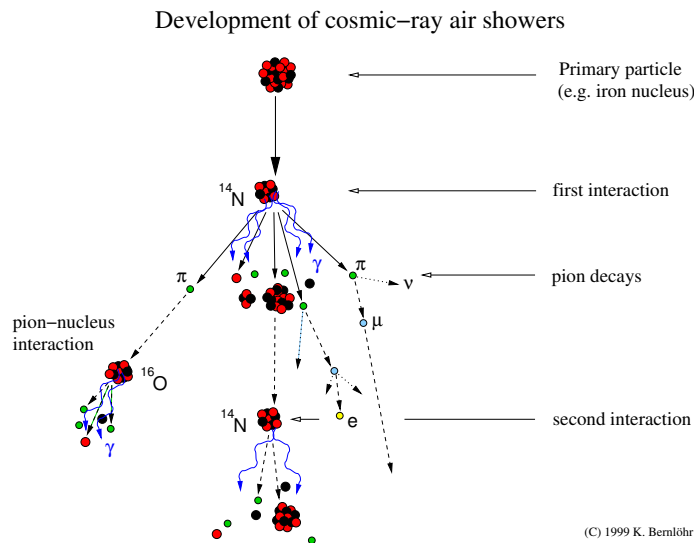
Figure 1.2.: Scheme showing the development of a hadronic air shower. Courtesy of Konrad Bernlöhr.

Because of the these additional hadronic processes, the resulting showers appear irregular and, because of the high transverse momentum transfer in the mentioned hadronic interactions, show a broader shower profile than their electromagnetic counterparts. Also, at the same energy, hadronic showers contain less charged particles compared to electromagnetic EAS.

1.1.3. Cherenkov Emission

The charged particles from the EAS polarise the local medium faster than it can relax because they exceed the speed of light in the atmosphere. This results in a constructive interference of electromagnetic waves in the optical along a cone of $\cos\theta = 1/(\beta n)$ opening angle, where n is the local refractive index and β is the particle's Lorentz factor. This so-called Cherenkov emission is observed at the ground as flashes of several nanosecond duration with a spectral maximum at blue wavelengths.

1.2. The H.E.S.S. Telescopes

Figure 1.3.: The five telescopes of the H.E.S.S. instrument. The smaller CT1-CT4 are arranged along a square of 120m sidelength with CT5 in the centre.

The H.E.S.S. instrument is an array of five IACTs designed to probe the VHE-energy regime. In this domain, H.E.S.S. is currently one of the most sensitive experiment. Its name is an acronym for **H**igh **E**nergy **S**tereopscopic **S**ystem and a tribute to the discoverer of Cosmic Rays and Nobel Prize laureate Victor Hess.

1.2.1. Position and Layout

Situated in the Khomas highland in Namibia (23°16'18" S, 16°30'00" E) at 1800 m above sea level, the instrument can boast excellent atmospheric conditions, low values of the geomagnetic field and a good view on the Galactic Centre. The four initial telescopes CT1-CT4 are arranged on a square of 120m side-length while the new, large telescope CT5 is positioned in the centre. This spacing is a good compromise between stereoscopic properties and overlap between the individual telescope's effective areas as this distance corresponds to the typical extension of gamma-ray induced Cherenkov light pools on the ground.

1.2.2. Mirrors and Mount

While already the 4 smaller H.E.S.S. telescopes have large mirror areas of $108m^2$ each, CT5 features an impressive $\sim 600m^2$. Each mirror on the telescopes is attached to actuators which allow for a precise adjustment of the reflector which follows a parabolic geometry (with a focal length F=36m) in the case of CT5 and a Davies-Cotton design (F=15m) for the other telescopes (DaviesCotton). The drive systems allow a fast positioning of any point in the sky within 2 minutes in the case of CT1-CT4, while CT5 will get there first with a peak positioning speed of 200°/min and the possibility of a fast tracking by moving the telescope over the zenith in extreme situations (such as GRBs). For more information on tracking, see [Bolz, 2004], [Hofverberg et al., 2013].

1.2.3. Cameras and Trigger

The H.E.S.S. telescopes are equipped with fast-electronics (ns time-scale) cameras that consist of 2048 PMTs (CT5) and 960 PMTs (CT1-4), respectively. For more information, see [Aharonian et al., 2004], [Bolmont et al., 2013]. Light funnels (Winston cones) are attached to the front of the PMT and collect the light that would otherwise be lost in the gaps between the pixels. The physical side-length of these pixels is 42mm. For CT5, this corresponds to 0.067° sky coverage and 0.16° for the other telescopes. While such a small pixel size guarantees high-resolution shower images, the large FoV of the cameras (3.2° for CT5, 5° for CT1-4) allows the observation of extended sources and is ideal for surveys, making the huge success of the H.E.S.S. Galactic Plane Survey (HGPS) possible which resulted in the discovery of dozens of galactic VHE gamma-ray sources, see [Carrigan et al., 2013].

The pixels in each camera are organised in overlapping *sectors*. If at least three PMTs in a sector detect a signal of 4 photo-electrons (p.e.) or more within a time interval of 1.5ns, the camera image is read out and a trigger signal is sent to the central trigger system. CT5 has the ability to optionally apply an additional topological trigger which allows to discard irregular (i.e. hadronic) events already on the trigger level.

The whole array triggers in stereoscopy if at least two cameras send a trigger signal within an coincidence window of 80ns. By doing so, most of the night sky background (NSB) noise induced triggers is eliminated, resulting in a large reduction of the system dead time. Since CT5 has a lower energy threshold and therefore higher trigger rate compared to the other telescopes, the central trigger system allows also CT5 mono-telescope triggers. A detailed description of the central trigger system can be found in [Funk et al., 2005].

1.2.4. Data Taking

VHE gamma-ray source observations must be performed in astronomical darkness, i.e. in the absence of moon and sunlight. Instead of pointing directly at the target, the telescopes do so at an offset between 0.5-1°. This method allows it to find a background estimation region (*OFF-region*) not only in the same field of view as the source but at a position that, with respect to the camera centre, is mirrored to the trial region (*ON-region*). The advantages of this method are discussed in section 1.3.4. Individual observations (*observation runs*) have a duration of 28 minutes after which the telescopes assume a new offset pointing position relative to the target. This style of observations is called *wobble mode* and the offset is referred to as *wobble offset*, accordingly.

1.3. The H.E.S.S. Analysis

In the following, a basic overview of the analysis of the VHE-gamma ray raw data will be given. The discussion is along the lines of the detailed publications [Aharonian et al., 2006a] and [Aharonian et al., 2004] to which the interested reader is referred to for more information. Throughout this work, the Heidelberg branch of the *H.E.S.S. Analysis Program*, hap-HD, will be used.

1.3.1. Data Calibration

The data analyis is done on camera images of air showers in intensity units of photo electrons. Before the Cherenkov light is detected in the camera pixels, it is reflected by the telescope mirrors, funneled by light collectors (H.E.S.S. uses Winston cones) and converged into p.e. by the first PMT dynodes. Each step depends on hardware properties, described by parameters such as the reflectivities of the optical components and quantum efficiencies of the PMTs. These numbers benchmark the optical efficiency of the instrument and have to be accounted for in the data processing.

All those parameters can be quantified by a single observable, the muon efficiency μ. This analysis exploits the fact that muons are able to penetrate the atmosphere and to emit Cherenkov light at low altitudes above the telescopes. Typical Cherenkov light cone opening angles from muons and the field of view of the H.E.S.S. telescopes lead to distances of only a few hundred meters between light emission and telescope. Thus, individual light cones from muons are seen by the single H.E.S.S. telescopes as ring-shaped images (so-called muon rings). There are reliable theoretical models on the expected image photon intensity as a function of the geometrical muon ring properties. By comparing the actual measured ring intensity (in p.e., n_e) to the theoretically expected one (in photons, n_γ, available from Monte-Carlo (MC) simulations), one has found a parameter that includes all of the optically relevant hardware parameters. The

muon efficiency is then defined as

$$\mu = n_e/n_\gamma, \tag{1.1}$$

which can be compared to values that are typical for the instrument, obtained in MC simulations (μ_{MC}). The quotient μ/μ_{MC} is then used as a correction factor in the energy reconstruction of the primary particle.

After the electronic conversion, the signal is amplified and digitalised. The result of this procedure is an analogue-to-digital converted (ADC) count in each pixel. Through special calibration procedures one can measure the pixel signal baseline (the pixel pedestals) and gain g_i for every pixel i, which determines the ratio of ADC counts to primary p.e. This allows it to derive shower images in units of p.e., which are then used in the data analysis.

1.3.2. Data Selection

An important step in data analysis is to guarantee a satisfactory data quality (DQ), as hardware and atmospheric conditions may have a large impact on the analysis results. This task is achieved in an automated way by the *hap-HD* software framework, with which all the data analysis in this work has been performed. Chapter 2 provides a relatively detailed discussion of the DQ selection.

1.3.3. Image Processing

Image Cleaning

In order to allow an efficient analysis of the shower images, they have to be isolated from background noise in the camera pictures, which arises mainly from the night-sky background (NSB). This is achieved via the so-called *tail-cut cleaning*, an algorithm that applies a two-level filter to the pixel amplitudes. The low level cut retains pixels if they show least an intensity of 5 p.e. but only in the presence of least one neighbour with more than 10 p.e. Vice versa, the high level cut requires pixels to have more than 10 p.e. and a minimum of one neighbouring PMT with at least 5 p.e.

After this procedure, contingent regions of triggered pixels, i.e. the shower images, are cleaned from the uniform background. The shape and intensity of these regions contains information about the primary particle's energy, direction and species. In order to extract these informations, the standard H.E.S.S. analysis uses a technique introduced by Hillas [Hillas, 1985], which is based on the idea of parameterising the shower image by a two-dimensional ellipse. The corresponding ellipse parameters can be obtained by calculating the second moments of the shower image and are called *Hillas parameters*.

Direction Reconstruction

The shower direction lies at some point along the line that is defined by the extension of the ellipse major axis and can be fixed if one includes additional parameters. However, as the ellipse function is mirror-symmetric, solutions are found to either side of the shower image and the direction reconstruction is often ambiguous.

All modern IACT experiments make use of the stereoscopic approach, which - among other advantages - solves this problem naturally. That is, if the same shower is imaged at different angles, the shower direction is fixed by the intersection of the major axes of the Hillas ellipses, see Fig.1.4.
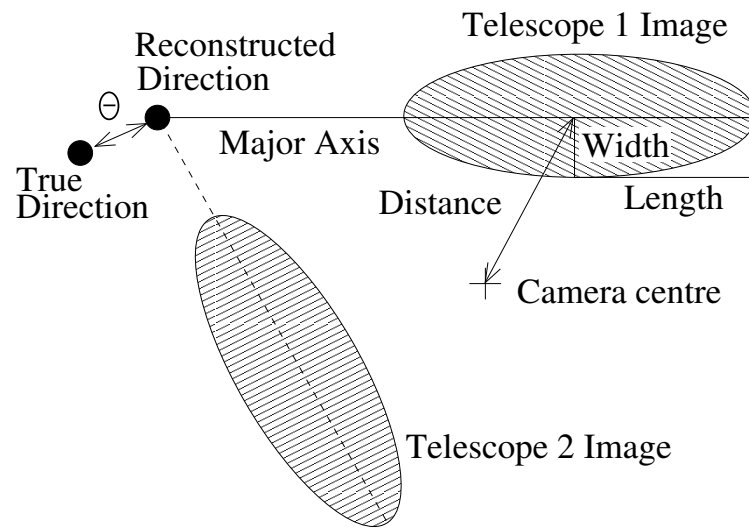
Figure 1.4.: Schematic illustration of the Hillas parametrisation of air showers and the stereoscopic direction reconstruction. Image extracted from [Aharonian et al., 2006a].

In order to guarantee a proper parameterisation to the shower images, selection cuts are performed on the distance of shower image to camera centre in order to dismiss images that are truncated at the camera edge as well as on the image intensity as the analysis of very small showers is often unreliable.

The accuracy of the directional reconstruction of the primary particles is reflected in the *point spread function (PSF)* of the instrument. It can be approximately described by the sum of 2 or 3 Gaussians with at 68% containment radius of $\sim 0.1°$.

Energy Reconstruction

For the energy reconstruction, the so-called impact distance d is required, which describes the distance from the extrapolated particle's point of impact on the

ground to the telescope. This quantity is, just like the shower direction, obtained by intersecting the major image axes, however in this case in the coordinate system of the telescope array. Together with the image amplitude, d allows it to derive the particle energy from lookup tables that have been filled in Monte-Carlo simulations. These tables are generated for different observational zenith angles θ and the actual telescope-wise energy estimate is derived by a linear interpolation in $\cos(\theta)$. Here, also the muon correction is applied. The described procedure results in one energy value per telescope, and as the final result the mean energy for an event is used,

$$E_{reco} = \frac{\sum_{i=1}^{N} E_i w_i}{\sum_{i=1}^{N} w_i},$$ (1.2)

where i indicates the telescope, w_i are weighting factors based on the uncertainty on the energy determination and N is the number of telescopes that recorded the event. The rms-error of the reconstructed energy is about 15%. Close to the energy threshold of the instrument a selection effect, where showers with a large amount of Cherenkov light are favoured, introduces a positive bias. The energy at which this bias amounts to 10% percent is called the *save energy* threshold. For a reliable spectral analysis only events above this energy should be used.

Gamma-Hadron seperation

The IACT technique operates in a deeply background-dominated regime: The number of proton-induced showers exceeds that of gamma-ray origin by typically four orders of magnitude. An efficient gamma-hadron separation is therefore of critical importance to the sensitivity of the analysis. Fortunately, the difference in shower shapes between electromagnetic and hadronic EAS provides leverage to discriminate between those events.

Compared to their electromagnetic cousins, hadronic showers evolve in a much more complex way which includes the formation of sub-showers. As a result, the shower images that are produced by these species show a much broader and irregular shape than those initiated by gamma-rays.

This morphological difference is parameterised by the widths and lengths of the fit ellipses. Therefore, a event selection based on these Hillas parameters results in a highly efficient gamma hadron seperation.

The situation is improved if one combines the fit values from multiple images into the *mean reduced scaled* parameters. From each telescope image, the reduced scaled width and length is derived. For instance, the reduced scaled length is given by

$$l_{sc} = (l - \langle l \rangle)/\sigma_l,$$ (1.3)

where the expected mean and standard deviation values of l, $\langle l \rangle$ and σ_l, are retrieved from lookup tables that are filled in gamma-ray MC-simulations.

These quantities are then telescope-averaged to give the mean reduced scaled width (MRSW) and length (MRSL). In the case of the ellipse length, it holds:

$$MRSL = \frac{\sum_{i=1}^{N} l_{sc,i} s_i}{\sum_{i=1}^{N} s_i},$$

(1.4)

with the same notation as in Eq.1.2 and the squared relative error $s_i = (\sigma_l / \langle l \rangle)^2$.

In the standard H.E.S.S. analysis, the gamma-hadron separation involves cuts on MRSW, MRSL, the image amplitude and the distance of reconstructed shower to source position (the latter of which is referred to as the θ^2-cut). This typically reduces the hadronic background by a factor of $\sim$100.

TMVA

The hadronic background can be suppressed further by including more parameters in the event selection. This is done in the *TMVA* analysis [Ohm et al., 2009], where boosted decision trees are applied to derive a single discriminating parameter ζ that combines the separation power of MRSW, MRSL, analogously defined mean reduced scaled parameters for simulated background events (MRSWO and MRSLO), X_{max} as well as the averaged spread in energy reconstruction of the different telescopes $\Delta E / E$. As a result, the sensitivity is increased and the required time for a source detection on the 5σ-level is reduced by 20-40%.

Selection Cuts

Depending on the expected spectral properties of the observed gamma-ray source, a specific set of cut values yields an optimal sensitivity. The H.E.S.S. analysis provides predefined sets of cut values, such as *hard cuts* that are optimised for the detection of hard (α=2), pointlike and faint (1%Crab) sources or *loose cuts*, which excel at the analysis of soft (α=3) and strong ($\sim$1CU) sources. Unless *a priori* very soft or very hard spectra are expected, the set of *standard cuts* is recommended in the search of sources [Aharonian et al., 2006a]. The cut values of this set lie between the *hard* and *soft* cuts: It is optimised for the detection of sources whose gamma-ray spectra feature spectral indices of (α=2.6) and integrated fluxes of 10%Crab.

1.3.4. Background Determination

The gamma-hadron separation described in the previous section leaves only gamma-like events. However, even after selection, this sample is still dominated by hadronic showers.

In that situation, the estimation of the source detection probability depends critically on a reliable knowledge of the number of background events in the analysis region. If this knowledge is available a number of excess events can

be derived, the significance of which may then be estimated with the likelihood ratio test proposed by Li and Ma [Li and Ma, 1983].

A number of background determination methods are available in the H.E.S.S. analysis software, see [Berge et al., 2007]. The two most commonly used ones will be presented in the following. Fig.1.5 schematically describes the working principles of these methods. Both methods define regions where no gamma-ray
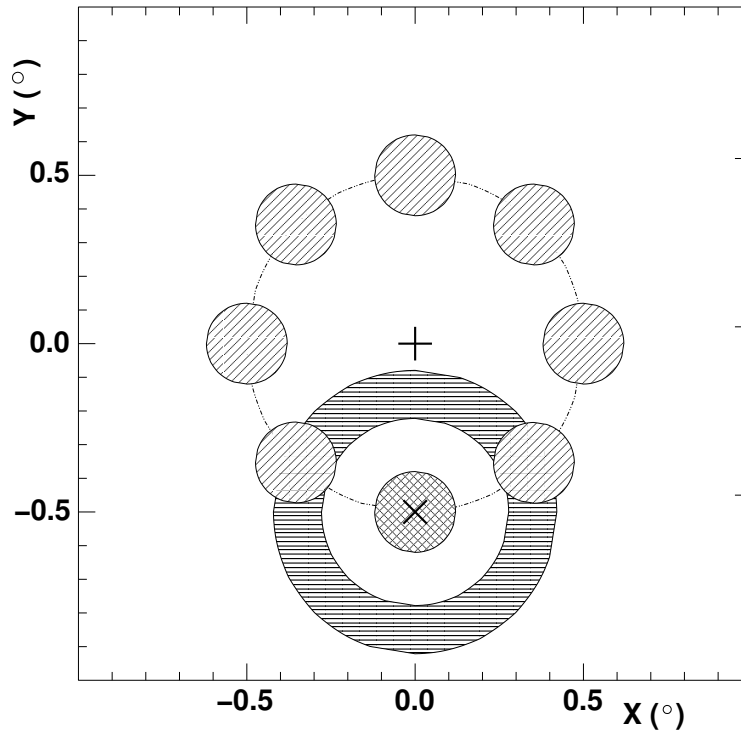
Figure 1.5.: Background estimation regions as defined in the *ring* method (horizontally striped) and the *reflected* method (diagonally striped). The test region is indicated by the hatched circle and coincides with the source position (X). The cross in the centre of the image represents the observational direction. Image extracted from [Aharonian et al., 2006a].

signal is expected (also called 'OFF'-regions). Accordingly, such regions have to be at a save distance from gamma ray sources and emission hot-spots. To that end, *exclusion regions* are defined where the creation of OFF-regions is forbidden.

Both methods are performed on the raw counts map i.e. a map where all gamma-ray candidates are filled in.

Reflected Background Method

In this method, the ON-region and the OFF-regions are equal sized areas, arranged at equal offset around the camera centre. Since the gamma-ray acceptance is approximately radial symmetric in the camera, this geometry guarantees the same acceptance in all regions. The signal from the OFF-regions (diagonally striped in Fig.1.5) is averaged (i.e. summed and multiplied with a factor $\alpha=1/m$, where m is the number of OFF-regions) and can be used as an estimate for the background in the ON-region (hatched). Because the acceptance is the same in all regions at any energy, the Reflected background method is the preferred method in the reconstruction of source spectra.

Ring Background Method

Another technique is the Ring background method, where a ring-shaped region around the trial region is defined which is used to count the background events. This is schematically shown in Fig.1.5. As a matter of fact, this procedure can be done for each pixel in the raw counts (ON-counts) map, and the result is a ring-correlated background (OFF-counts) map. In this method the changing radial camera acceptance has to be accounted for by applying a correction factor to each pixel. Because with this method the background for each pixel is estimated, it is perfectly suited for the creation of sky maps. Also, the ratio of ON to OFF region area is usually smaller in the Ring than in the Reflected background method and so the background estimation is based on a larger statistics.

However, contrary to the reflected method the ring-shaped OFF-regions do not feature a homogeneous acceptance. This is problematic in the reconstruction of source spectra since the acceptance might be energy-dependent which may introduce undesired systematic effects. For that reason, the Ring background method is not used in this case.

Recently, this method was improved to dynamically find an optimal ring radius in regions where fixed geometries might run into problems, e.g. in proximity to large exclusion regions. This technique is referred to as the *adaptive* Ring method.

1.3.5. Spectrum Reconstruction

With the knowledge of the background in the analysis region, the number of excess counts N_γ after an observation time T_{obs} can be derived. Because the energy for each event is reconstructed, strongly simplifying one can write

$$\frac{\Delta N_\gamma}{\Delta E_{reco}} = A_{eff} \cdot T_{obs} \cdot F(E_{reco}), \tag{1.5}$$

where F is the differential flux spectrum of the source in units of $(\mathrm{cm}^{-2}\mathrm{s}^{-1}\mathrm{TeV}^{-1})$, ΔE_{reco} is an arbitrary energy bin width and A_{eff} is the *effective area* of the instrument. This quantity can be roughly understood as the area on the ground

into which gamma rays fall that are in principle detectable, multiplied by the detection probability of the latter. [1] The effective area is a function of energy as well as a large number observational parameters (zenith and azimuth angles, offset, telescope pattern, optical efficiencies etc.) $A_{eff} = A_{eff}(E_{reco}, \phi, \theta, \psi...)$.

If the functional dependencies of the effective area are known, it is possible to isolate the differential flux spectrum $F(E)$ in Eq.1.5. To that end, one has to sum over the individual ON and OFF counts, each divided by the appropriate effective area value for the event. The reconstructed flux in each energy bin Δ_i can then be derived as

$$F(E_{reco})_i = \frac{1}{(T_{obs} \cdot \Delta E_{reco,i})} \left\{ \sum_{j=0}^{N_{ON}} A_{eff,j}^{-1} - \alpha \sum_{k=0}^{N_{OFF}} A_{eff,k}^{-1} \right\}. \qquad (1.6)$$

The flux is sensitive to a large number of error sources, see [Aharonian et al., 2006a]. As a result, the total systematic error on the flux normalisation is $\sim 20\%$.

---

[1]The effective areas are derived from gamma-ray MC-simulations. There are different realisations available: By using only MC events that are reconstructed within a certain radius of the simulated source position, one obtains the so-called *point-like* effective areas. This radius depends on the analysis cuts used, see [Aharonian et al., 2006a]. Omitting this restriction results in the *extended* effective areas which are suitable for the analysis of extended sources.

2. Atmospheric Data Quality Monitoring

In order to guarantee well-understood and reproducible results from observations of the VHE sky, the H.E.S.S. experiment applies a uniform data quality (DQ) selection in order to control systematic effects in the data analysis. An uniform DQ selection is also very important for the analysis of large data sets and especially for population studies such as the work presented in chapter 5, where a large number of test positions coincident with radio SNRs was analysed. In the following, I will shortly present how this is accomplished within the *hap-HD* software framework.

Recently, due to hardware maintenance, some of the DQ checks have been revisited. Here, a new atmospheric DQ quantity, the *Cherenkov Transparency Coefficient T*, will be presented. This quantity provides a nearly hardware-independent measure of atmospheric transparency and is calculated exclusively from Cherenkov data, independently of standard atmospheric monitoring devices.

2.1. Heidelberg Data Quality Selection

The DQ selection in the hap-HD framework uses a mechanism[1] that is able to apply selection cuts to arbitrarily large data sets. Those cuts are divided into two categories: *Detection* and *Spectral* cuts. This chapter mainly discusses the latter and the detection cuts will be discussed only very briefly. For more information see [Hahn et al., 2013b] where a summary and documentation of the H.E.S.S. DQ over an eight year period between 2004 and 2012 can be found. Some of the plots and tables shown in the following are borrowed from this document. Also, some passages of this chapter in the introduction and discussion of the Cherenkov Transparency Coefficient are taken from [Hahn et al., 2013a].

2.1.1. Detection Cuts

This set of cuts represents a basic check to exclude data that has been recorded in the presence of hardware problems which might result in undesired systematic effects; for instance from a misunderstood camera acceptance or wrong

---

[1]via the *findruns.pl* script, which collects the relevant data from DB tables for arbitrarily large data sets and performs the DQ cuts.

shower direction reconstruction. It encompasses checks on the truncation of observation runs, the data integrity, the performance of the cameras as well as the tracking system. Tab.2.1 lists the cut range of the different hardware cuts as well as their selective power. In the following, these cuts will be briefly presented. Note that criteria for the same hardware components are highly correlated.

Criterion	cut range (unit)	affected runs	failed tels
run duration	600:7200 (sec)	1574 (8.57%)	system
DST check	DST has to exist	164 (0.89%)	system
participation fraction	0:0.4 (rel. fraction)	961 (5.23%)	1182
pixels with 'hardware' flag	0:120 (number)	1258 (6.85%)	1562
pixels with 'HV-off' flag	0:50 (number)	822 (4.48%)	990
RMS of Az dev. distr.	0:10 (arcsec)	12 (0.07%)	13
RMS of Alt dev. distr.	0:10 (arcsec)	21 (0.11%)	21
mean deviation in RA	0:1 (arcmin)	42 (0.23%)	43
mean deviation in Dec	0:1 (arcmin)	73 (0.39%)	73

Table 2.1.: Hardware data quality criteria. Shown are cut values and the number of runs that are affected (total and percentage of all observation runs). In case of a system-wide selection criterion (e.g. run duration), 'affected' is defined as a whole run failing. For telescope-wise criteria (i.e. the number of problematic pixels), it is defined as at least one telescope not passing the cut. Also the total number of telescopes that failed the respective telescope-wise cut is shown.

General Criteria

There are two basic cuts that are not telescope-specific but rather affect the collected data system-wise. Contrary to the other detection cuts that discard data from single telescopes, runs that fail at least one of the general criteria are discarded for data analysis completely.

As one of the general criteria, a minimum run duration is required for the determination of the pixel pedestal values, as a certain statistics has to be accumulated. Runs that do not pass a corresponding cut are referred to as *truncated runs* and are not used for data analysis. Also, the data integrity is checked. If the *DST creation* fails for a given run it is regarded as not usable for data analysis.

Camera Criteria

In the DQ selection scheme, three camera monitoring quantities are in place. One of them is the *telescope participation fraction*. A cut on this quantity deselects data from telescopes that show a decreased participation in the stereoscopic central trigger events. This happens when the data stream from a cam-

era is decreased and is usually related to camera problems, for instance an increased amount of nonfunctional pixels or problems with the camera trigger system.

The remaining two camera monitoring quantities check the *number of broken pixels* in the cameras. In view of the large number of camera pixels it always happens that a fraction of them shows hardware problems. However, too high a number of nonfunctional pixels will have an undesired impact on the camera acceptance and might very well lead to adverse systematic effects. Two different pixel diagnostics are in place, checking the number of pixels where the high voltage is switched off ("switched-off") and those that behave erratic ("hardware"). For more information see [Hahn et al., 2013b].

These quality checks are performed telescope-wise: If one telescope does not meet the DQ camera requirements, its data is not used in the analysis.

Tracking Criteria

To guarantee the proper tracking of the telescopes on the observed object, cuts are implemented on the *fluctuations in azimuthal and altitudinal tracking*. This is done by measuring the RMS values of the distributions filled with coordinates of the telescopes' tracking position (in Alt-Az) that are transmitted by the tracking system in regular time intervals. A similar method compares the *deviation between scheduled and actual observation position* (as transmitted by the tracking system) in RADec.

Data from telescopes that fail at least one of the camera or tracking cuts is not used in the analysis.

This set of cuts represents the minimal DQ requirement for the analysis of data. Data that fulfils these criteria shows both satisfactory directional shower reconstruction as well as camera acceptances. The systematics of this data in the ON-signal and background reconstruction are well-understood and it may be used for the creation of skymaps and to statistically detect sources. Therefore, this set of cuts is called *detection* cuts.

2.1.2. Spectral Cuts

The spectral analysis of VHE sources critically depends on the proper energy reconstruction of the air showers. This requires not only a well-understood camera acceptance and accurate directional reconstruction but also an adequate atmospheric monitoring as non-ideal atmospheric conditions may result in biased reconstructed source spectra. Therefore, additional to the detection cuts, a set of atmospheric cuts is applied to the data. This extended set of DQ checks is referred to as *spectral* cuts.

In order to reconstruct the energy of primary particles, shower images are compared to Monte Carlo shower simulations where nominal hardware param-

eters[2] and average atmospheric conditions at the H.E.S.S. site are assumed [Bernlöhr, 2000].
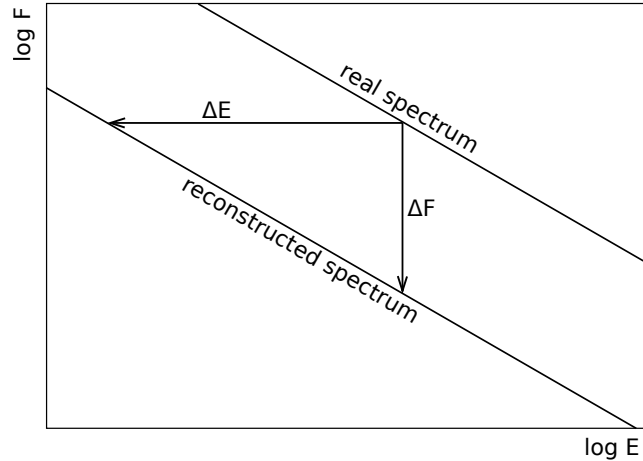
Figure 2.1.: A mis-reconstruction of the gamma-ray energy leads to a bias in the reconstructed flux normalisation.

Some atmospheric phenomena will act as atmospheric light absorbers that attenuate Cherenkov light from EAS particles and therefore reduce the amount of Cherenkov photons that reach the detector. Thus, it is expected that a reduction of the actual atmospheric Cherenkov light transparency compared to the Monte Carlo model assumptions results in underestimated energies, which in turn leads to a biased reconstruction in spectral parameters. This effect has the greatest impact on the flux normalisation, as an underestimated gamma-ray energy shifts the spectrum to lower energies. In the case of a spectral power-law shape, this is equivalent to a reduction in flux normalisation, see Fig.2.1.

In the following the most important atmospheric absorbers and their detection within the DQ scheme will be discussed briefly.

Clouds

The maximum of the Cherenkov emission from air showers, developed by primary particles of energies within the H.E.S.S. energy domain (E$\geq$ 300 GeV), takes place at altitudes between $\sim$6-11 km [Bernlöhr, 2000]. Thus, one can assume that cloud layers below those altitudes act as atmospheric light absorbers that may attenuate Cherenkov light from the whole shower or parts of it, resulting in fewer photons reaching the camera and a lower trigger probability. As a

---

[2]In order to account for the degradation of the optical components of the instrument, these simulations are recalculated on regular intervals corresponding to epochs of different optical efficiency.

result, single telescope trigger rates and consequently the central trigger rate[3] (see [Funk et al., 2005]) are reduced. The reductions in the trigger rates can therefore be used to detect data that has been taken in the presence of clouds.

For instance, if absorbing structures (local clouds) pass through the field of view, a fluctuating behaviour in the central trigger rate on time scales smaller than the duration of an observation run can be observed. On the other hand, if a thin, very extended cloud layer is moving into the field of view (FoV), this may result in a continuous drop of the central trigger rate. Examples of these effects are shown in Fig.2.2.
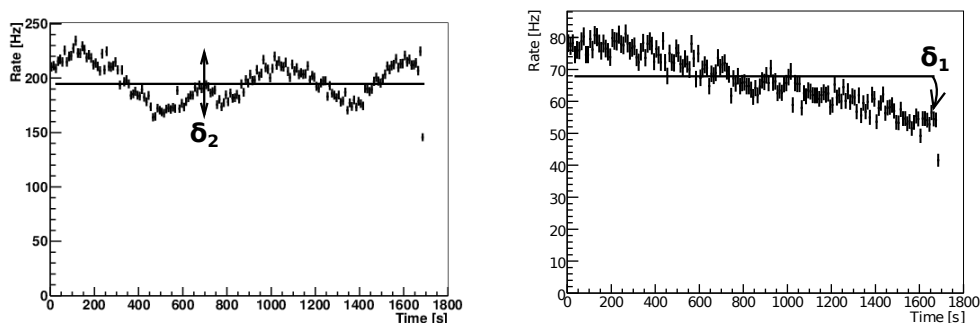
Figure 2.2.: Small clouds cause fluctuations in the central trigger rate (left). Large cloud layers lead to a continuous decline as they move into the field of view (right). Additionally, the definitions of the δ_1 and δ_2 parameters are illustrated.

To quantify those phenomena, two separate cuts are used, both being based on a linear fit to the time evolution of the trigger rate (see Fig.2.2). The discussed small to medium-scale clouds cause modulations to the trigger rates on time-scales small or comparable to the duration of single observation runs (typically 28 minutes). Therefore it is possible to detect such structures by analysing the trigger rates of single runs.

Monitoring the rms value of the time binned (10s bins) trigger rate data points to the fit function allows it to detect short time-scale clouds. The according cut-quantity (in the following called δ_2-cut, see left panel of Fig.2.2) is defined as

$$\delta_2 \equiv \frac{100}{\langle R \rangle} \cdot \sqrt{\sum_{i=1}^{N} \frac{(R_i - L(t_i))^2}{N}}, \tag{2.1}$$

---

[3]In the following, all trigger rates are assumed to be corrected for a diminishing effect that comes with increasing observational zenith angles. That is, the trigger rate decreases with the zenith angle even in absence of atmospheric light absorbers due to the increase of the distance of the shower maximum. This zenith angle (θ) dependence in the trigger rate is corrected by a second order polynomial, $\zeta(\theta) = p_0 + p_1 * \cos(\theta) + p_2 * \cos^2(\theta)$.

where R_i is the time-binned central trigger rate and L is the fitted line.

The slope of the fitted line is used to detect data taken in the presence of large cloud layers moving into the FoV. An appropriate DQ quantity is given by

$$\delta_1 \equiv 100 \cdot |L(t_{max})/\langle R \rangle|, \qquad (2.2)$$

see also the right panel in Fig.2.2.

The cut criteria are $\delta_2 <10\%$ and $\delta_1 <30\%$.

Aerosols and Large-Scale Clouds

Unfortunately, large-scale clouds and aerosol layers cannot be detected in this way. This class of absorbers may impact the trigger rates on time scales from weeks to a couple of months, far exceeding the typical run duration. In particular, aerosol layers can be very extended. These structures can be transported over large distances to the H.E.S.S. site resulting in elevated aerosol concentrations over several kilometres in altitude as they are typically mixed up horizontally in the boundary layer.

If one wants to detect such structures in a similar way as it is done with δ_1 and δ_2 (i.e. by fitting the trigger rates), then this requires the inclusion of data from time intervals on the scale of weeks to months, in order to get a handle on the trigger rate variations caused by these atmospheric absorbers.

Up until the beginning of 2010, such an approach was viable to detect data that has been collected in a hazy / foggy atmosphere (see Fig.2.3). To that end, the long-term evolution of the zenith-corrected central trigger rate was (manually) fitted by an exponential function, reflecting the optical and electronic performance degradation of the telescopes (dashed lines in Fig.2.3).

This degradation is connected to factors like the ageing of the instrument, especially the mirrors and the light collectors, but also to decreasing values of the gain in the camera PMTs. Regular maintenance, such as the cleaning of the Winston-cones and the adjustment of the PMT voltage for a gain re-adjustment is thus required. This maintenance improves the instrument's performance but also leads to jumps in the trigger rate, see Fig.2.3. Thus, the fit to the long-term evolution of the central trigger rate had to be performed anew every time modifications to these components were made.

The corresponding DQ quantity was defined as

$$\delta_3 \equiv R(t)/E(t), \qquad (2.3)$$

where R is the zenith-corrected central trigger rate and E represents the fit function. The cut was at $\delta_3 > 0.8$, corresponding to an allowed decrease of the trigger rate of 20%.

The usage of this DQ quantity became problematic during the years 2010-2011, where the frequency of hardware adjustments dramatically increased.
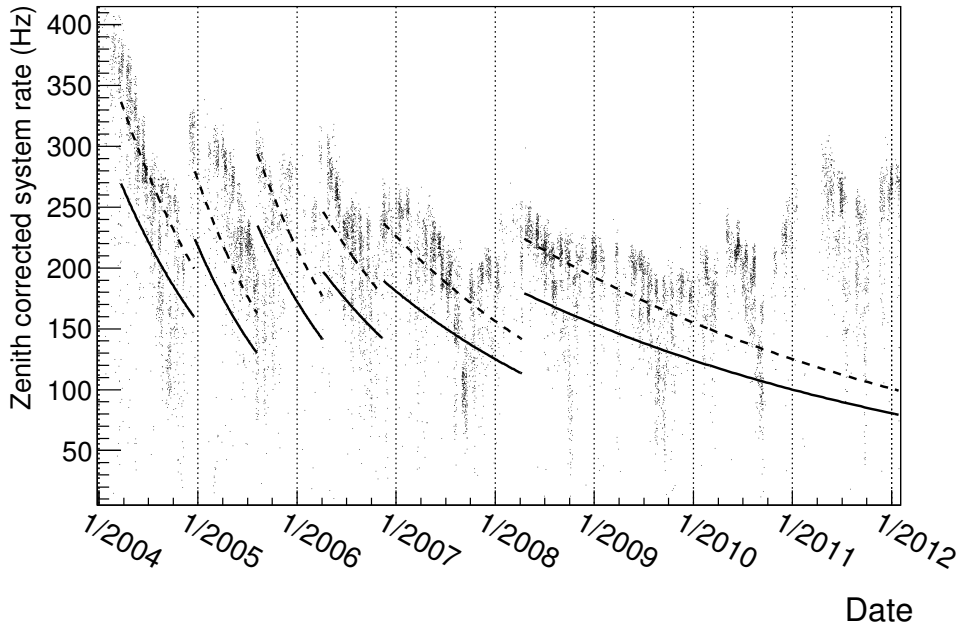
Figure 2.3.: Zenith-corrected central trigger rate as a function of time. Dashed lines: Fit to the long-term evolution of the trigger rate, solid lines: Cut values (defined as $0.8 \cdot \delta_3$).

Most notably, in February 2011 the mirror exchange campaign[4] started. One can see that after mid-2010 the trigger rate varied on time scales smaller than ~ 6 months and a viable long-term fit to the data became quite impossible.

2.2. The Cherenkov Transparency Coefficient

Due to the maintenance work on the H.E.S.S. telescope hardware, a quantity is desired that disentangles the effect of hardware ageing and maintenance on the trigger rate from that of atmospheric attenuation as far as possible. To accomplish this, the most important hardware parameters that describe the optical and electronic instrument performance are suitably included in its definition. This approach is contrary to the previous method where the hardware effects were accounted for by finding a fit function to the trigger rate evolution and using that as a reference. This new quantity is referred to as the *Cherenkov Transparency Coefficient T* and will be described in the following [Hahn et al., 2013a].

The derivation of T is straight-forward if one assumes that the factors which adapt the Cherenkov light between its emission and recording can be approxi-

---

[4]In this campaign, the mirrors of the telescopes CT1-CT4 were re-coated for each telescope consecutively in 6-month intervals.

mately described by the three parameters: Muon efficiency μ, telescope-averaged pixel gain $g = \sum_{i=0}^{N} g_i / N$ (for the pixel gain g_i see section 1.3.1) and a model parameter η that is assumed to be proportional to the atmospheric transparency. This quantity η is the sought-after component and has to be disentangled from the other parameters.

In first approximation, the faintest detectable air-shower (as determined by the camera trigger thresholds, see [Aharonian et al., 2004]) in terms of the Cherenkov photon number is inversely proportional to μ, g and η, see Fig.2.4. Since the light intensity of the shower goes roughly linearly with the energy of the primary particle, it follows that

$$E_0 \propto n_{\mathrm{min}} \propto (\eta \cdot \mu \cdot g)^{-1}. \tag{2.4}$$
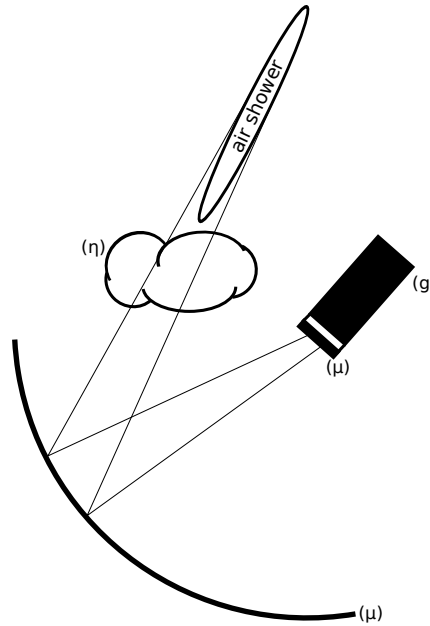
Figure 2.4.: Sketch describing the possible fate of n Cherenkov photons emitted above the H.E.S.S. site. The light is attenuated by the atmosphere, leaving $n \cdot \eta$ photons, only to be reflected by mirrors, funnelled by light collectors and absorbed by the PMT dynodes. The efficiency of these processes is measured by μ, and as a result $n_e = n \cdot \eta \mu$ photo-electrons constitute the unamplified PMT signal. This signal is then amplified by the gain g to a number of $n'_e = n \cdot \eta \mu g$ p.e. which is the recorded intensity of the shower image. Thus, in first approximation, it holds for the image size $n \propto n'_e \cdot (\eta \mu g)^{-1}$.

Another simplifying assumption is that the zenith-corrected single telescope trigger rates are dominated by the CR proton flux. The local CR proton spectrum in the relevant energy range is approximately

$f(E) = 0.096 \cdot (E/\text{TeV})^{-2.70} \text{m}^{-2} \text{s}^{-1} \text{TeV}^{-1} \text{sr}^{-1}$ [Sanuki et al., 2000]. Hence, the trigger rates can be estimated as

$$R \quad \sim \quad \int_{E_0}^{\infty} \mathrm{d}E A_{\text{eff}}(E) f(E) \tag{2.5}$$

$$\simeq \quad k \cdot E_0^{-1.7+\Delta}, \tag{2.6}$$

where E_0 is the energy threshold of the telescopes. The term Δ allows higher order corrections to be taken into account, such as energy-dependent shower profiles.

Combining the expressions of E_0 in Eqs.2.4 and 2.6 allows it to give an estimate of the atmospheric transparency seen by each telescope i:

$$\eta \propto \frac{R_i^{\frac{1}{1.7-\Delta}}}{\mu_i \cdot g_i} \equiv t_i. \tag{2.7}$$

The array-averaged quantity

$$T \equiv \frac{1}{N \cdot k_N} \sum_i t_i \tag{2.8}$$

defines the Cherenkov Transparency Coefficient T.

To make this cut as stable as possible against electronic artefacts and other single telescope effects, the single telescope *read-out* rates instead of the raw telescope trigger rates are used. Telescopes are read out when at least two telescopes are triggered in coincidence [Funk et al., 2005]. The coincidence requirement suppresses the mentioned undesired single telescope effects and improves the stability of the quantity. However, it also introduces a correlation between the telescope rates. Furthermore, due to the coincidence requirement, the single telescope read-out rates depend on the number of active telescopes. Observations with three active telescopes[5] show, on average, decreased read-out rates and T is multiplied with a correction factor of $C = 1.12$ in these cases (for the derivation of C see [Hahn et al., 2013b]).

After this correction, the transparency coefficient distribution over the whole run range is peaked at a value of 3.42 for 4-telescope runs and 3.37 for 3-telescope runs. These peak values are used as the normalisation factors k_3 and k_4 in Eq.2.8. After rescaling, the T-distribution peaks at unity, independent of the telescope multiplicity. Additionally, the other CR species that have been omitted in Eq.2.5 (and which are implicitly included in k_N) are approximately cancelled out.

Also, a value of $\Delta=0$ is assumed. In section 2.3 it will be seen that this is a valid first-order approximation.

In Fig.2.6 one can see the time evolution of T over a time period of eight years. The distribution peaks at $T=1$ over a time period of eight years in a very

---

[5] Only 3- and 4-telescope runs are treated as 2-telescope runs are not used for spectral analysis.

stable manner with a FWHM of $\sim$9%, which illustrates that T is indeed mostly independent from hardware effects. There are periodic downward-fluctuations, which will be discussed at a later point in this chapter.

In the right panel of Fig.2.5 the distribution of transparency coefficients is shown for both 3 and 4-telescope data recorded during the months of May (from the same time period as shown in Fig.2.6). As one can see, the two distributions are similar in shape and peak narrowly around unity.
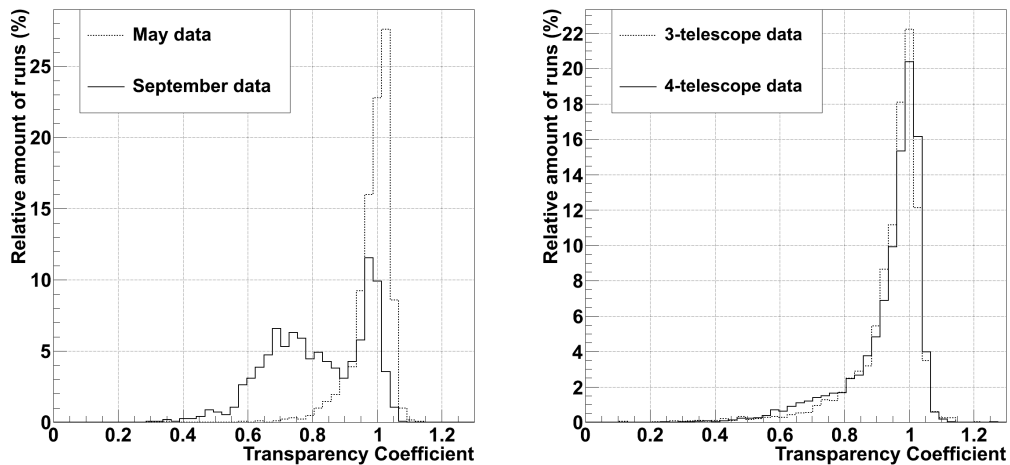
Figure 2.5.: Left panel: T-distributions for the May and September months, respectively. Right panel: Cherenkov Transparency Coefficient distributions for 3 and 4-telescope runs, respectively. Both plots correspond to the complete data set between the years 2004 and 2012. Plot extracted from [Hahn et al., 2013a].

The left panel of Fig.2.5 shows the complete (3 and 4-telescope data) distribution of transparency coefficients for both May and September data (again in the same period as in Fig.2.6). The peak, which is close to a value of one, is present in both distributions indicating the presence of good atmospheric conditions in May and to some degree also in September. However, a second, much broader peak in the distribution of transparency coefficients during September can be observed. This additional feature corresponds to the periodic downward fluctuations that can be seen in Fig. 2.6 and will be discussed in section 2.5. First, the influence of aerosols and large-scale clouds, as measured by T, on the spectral reconstruction of VHE gamma-ray sources will be discussed.
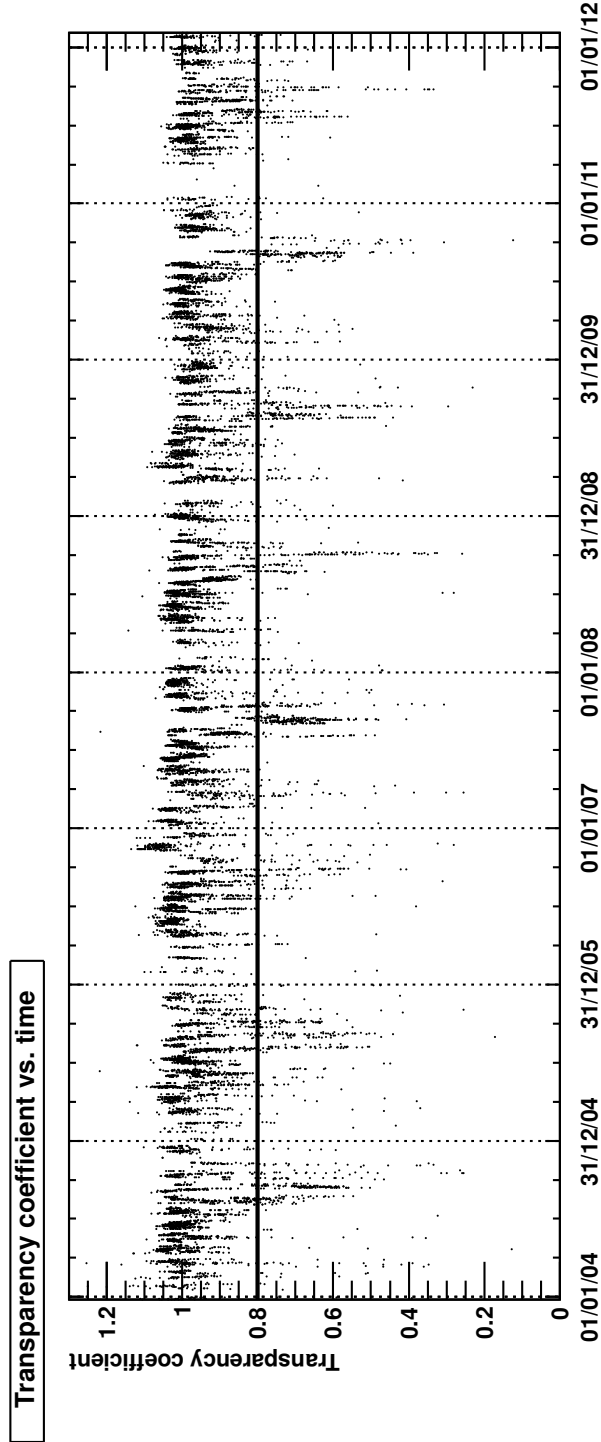
Figure 2.6.: Evolution of transparency coefficients over the 8 years between 2004 and 2012. The solid line indicates the cut value at 0.8. The distribution is sharply peaked at 1 with a FWHM ~9%. Plot extracted from [Hahn et al., 2013a].

2.3. Effect on Spectral Reconstruction

As will be shown in section 2.5, the comparison to independent satellite, radiometer and LIDAR measurements has confirmed the sensitivity of T to aerosols in the atmosphere. It can thus be used to estimate the effect of elevated atmospheric aerosol concentrations on the spectrum reconstruction of VHE sources.

This was done on the example of the Crab Nebula, a standard candle at TeV energies that to date has not shown any detectable variability in this domain. The investigated data set has been recorded over 8 consecutive years from 2004 to 2011. In order to isolate the effect of aerosols, all hardware DQ cuts as well as the δ_1 and δ_2 cuts have been applied to the data. The full data set was subdivided into subsets of data corresponding to different intervals in T. The resulting individual data sets were then analysed and spectrally reconstructed with the H.E.S.S. standard analysis (see section 1.3).

The gamma ray spectrum of the Crab Nebula has been measured by H.E.S.S. (see [Aharonian et al., 2006a]) and was found to have an approximate power-law shape with some softening at the high end of the spectrum. A pure power-law fit in the energy range (0.41-40)TeV yields a flux normalisation at 1 TeV of $\phi_{0,Crab} = (3.45 \pm 0.05_{stat} \pm 0.69_{sys}) \times 10^{-11} \mathrm{cm}^{-2}\mathrm{s}^{-1}\mathrm{TeV}^{-1}$ and a spectral index of $\Gamma_{Crab} = 2.63 \pm 0.01_{stat} \pm 0.10_{sys}$.

As already mentioned, in first approximation an underestimation of the reconstructed energy by a constant attenuation factor should lead to a reduced flux normalisation, compare to Fig.2.1.

Quantitatively, assuming the reconstructed gamma ray energy E_{reco} and the true energy E_{true} to be related via $E_{reco} \propto T \times E_{true}$, one finds

$$\frac{\mathrm{d}F}{\mathrm{d}E_{true}} \propto E_{true}^{-\Gamma} \quad \Leftrightarrow \quad \frac{\mathrm{d}F}{\mathrm{d}E_{reco}} \propto E_{reco}^{-\Gamma} \cdot T^{\Gamma-1} \tag{2.9}$$

In the left panel of Fig.2.7 one can see the reconstructed flux normalization ϕ_0 as a function of T. The result confirms the expected strong dependency of ϕ_0 with the Cherenkov Transparency Coefficient. A fit to the data with a power law function $\propto T^{\Gamma-1}$ (as predicted from Eq.2.9) results in a value of $\Gamma_{fit} = 2.69 \pm 0.13$, which perfectly agrees with the published value of Γ_{Crab}.

The analogue diagram for the spectral index can be found in the right panel of Fig.2.7. There might be some indication for a spectral hardening with increasing T-values in the range $0.7 \leq T \leq 1$, but it is not significant. This feature may be attributed to the interplay between the deviating shape of the Crab spectrum from a power law and the increasing energy threshold due to decreasing values of T. As the presence of aerosols results in a spectral shift towards lower energies, a spectral softening would be observed in the test energy range. Another factor might be a possible energy-dependent effect of atmospheric absorption on the shower shapes. However, since the T-dependence with the spectral index is found to be non-significant it can be concluded that the simple model defined
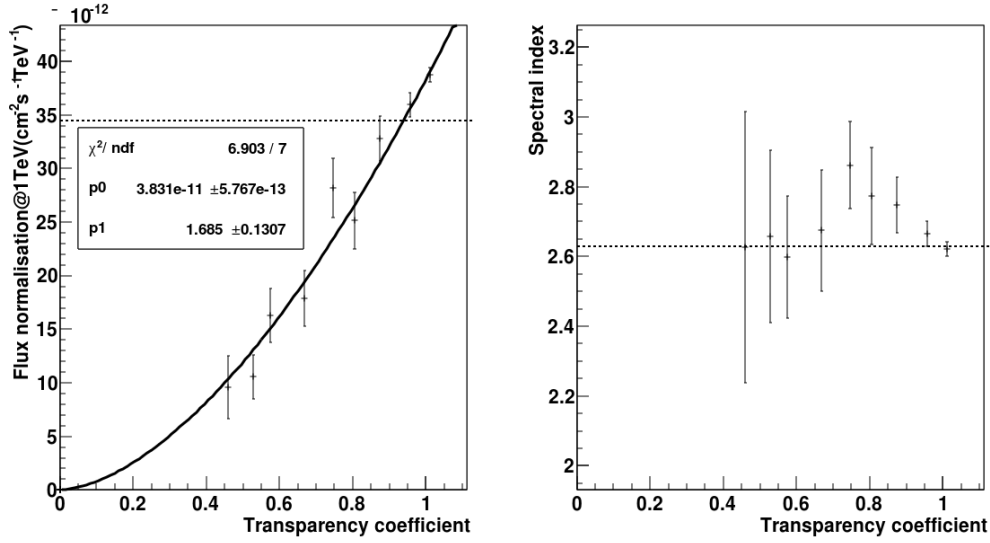
Figure 2.7.: Flux normalization at 1 TeV (left) and spectral index (right) for Crab Nebula data taken during 8 years of H.E.S.S. operation. Abscissa values are given by the mean value of the transparency coefficient in the respective subset. In the left panel, best fit values for a power-law fit are shown for the flux normalization at T=1 (p0) and the exponent (p1). The full data set investigated has an exposure of 84 hours, using only observations within one degree offset from the source. Also, to minimize a possible zenith-dependent energy bias, only data taken at zenith angles smaller than 47 degrees have been selected. The analysis performed uses the Hillas method where standard cuts [Aharonian et al., 2006a] have been applied. Dashed lines represent the published results [Aharonian et al., 2006a]. Plot extracted from [Hahn et al., 2013a]

in Eq.2.9 is a viable first order approximation to the effect of aerosol absorption on the shower energy reconstruction.

The left panel of Fig.2.7 shows that in the data range T>0.8 relative flux variations (to the mean flux in that range) are limited to about 20%. This value is therefore chosen as the cut value on T in the DQ selection in order to limit systematic effects accordingly.

2.4. T in Data Quality

The Transparency Coefficient has replaced the δ_3-quantity. A comparison between the selective powers of δ_3 and T can be seen in Fig.2.8, which shows the amount of runs that pass the hardware DQ cuts but fail the weather DQ cuts.

The solid line shows the selection result of the currently implemented set of cuts (δ_1, δ_2 and T), while the dashed line shows the same for the previous set of criteria (δ_1, δ_2 and δ_3).
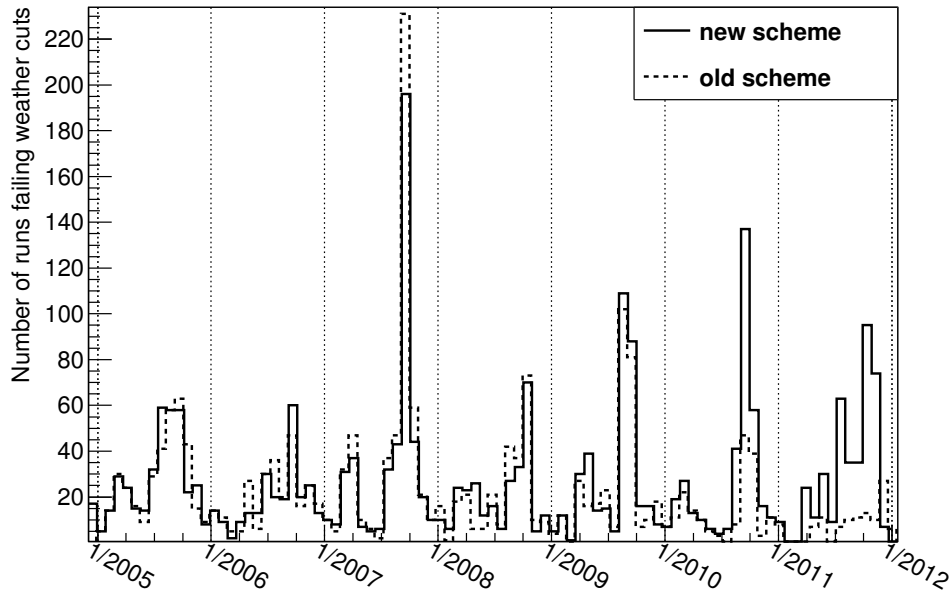
Figure 2.8.: Selective power of the weather cuts in the data quality selection. Shown is the number of observation runs that pass hardware cuts but fail the weather cuts, both before (dashed) and after (solid) the Cherenkov Transparency Coefficient replaced the δ_3 quantity.

As one can see, T and δ_3 have a very similar selective effect on the data sample up until 2010, after which the δ_3 cut loses its viability (compare to Fig.2.3). The Cherenkov Transparency Coefficient continues to select runs efficiently after this point. Its main impact on the run selection is around the September months, as can already be assumed from Fig.2.5. The seasonal change in the selective power (in terms of total number of rejected runs) of T is shown in Fig.2.10 on a monthly basis.

Of all three weather cuts, T is the most important (as was δ_3 before it) in that it affects the largest amount of observational data. Of course, there is a large overlap between the cut quantities (see Fig.2.9) as they are all sensitive to variations in the atmospheric transparency.

It should again be noted that this cut is only applied in the spectral DQ selection. Even if data does not pass the cut on T (or δ_1 and δ_2), it can still be used in source detection and the creation of maps.

Also, the cut on T is only necessary because the MC simulations were per-

Figure 2.9.: Relative importance of and overlap between the three atmospheric monitoring quantities.

formed assuming a single, year-averaged atmospheric aerosol model. This atmospheric model is valid for Namibia within a 10% accuracy over the whole year [Bernlöhr, 2000], without taking data around September into account. Additional simulations including different aerosol profiles might render this cut obsolete in the future. The same holds if it is possible to correct the aerosol induced bias in reconstructed energy (see Fig.2.1) using atmospheric parameters such as T.

2.5. Correlation with Independent Atmospheric Measurements

In order to confirm the sensitivity of the new parameter T to elevated aerosols concentrations in the atmosphere, a correlation study with different, independent atmospheric measurements was performed. Since thin, large-scale cloud layers might also affect T, satellite data is used to select periods of increased atmospheric aerosol levels at the H.E.S.S. site.

2.5.1. Correlation with Satellite Data

Biomass Burning as Seen by Satellites

The atmospheric effects of biomass burning in Southern Africa are well known in satellite observations. In a first instance, the analysis of MODIS data [Arola et al., 2007] showed that in regions where biomass burning takes place, aerosols from these processes absorb up to 50% of the UV solar radiation before reaching the surface [Kalashnikova et al., 2007]. The MISR instrument on-board the Terra satellite ([Diner et al., 2002]) later confirmed this observation. This
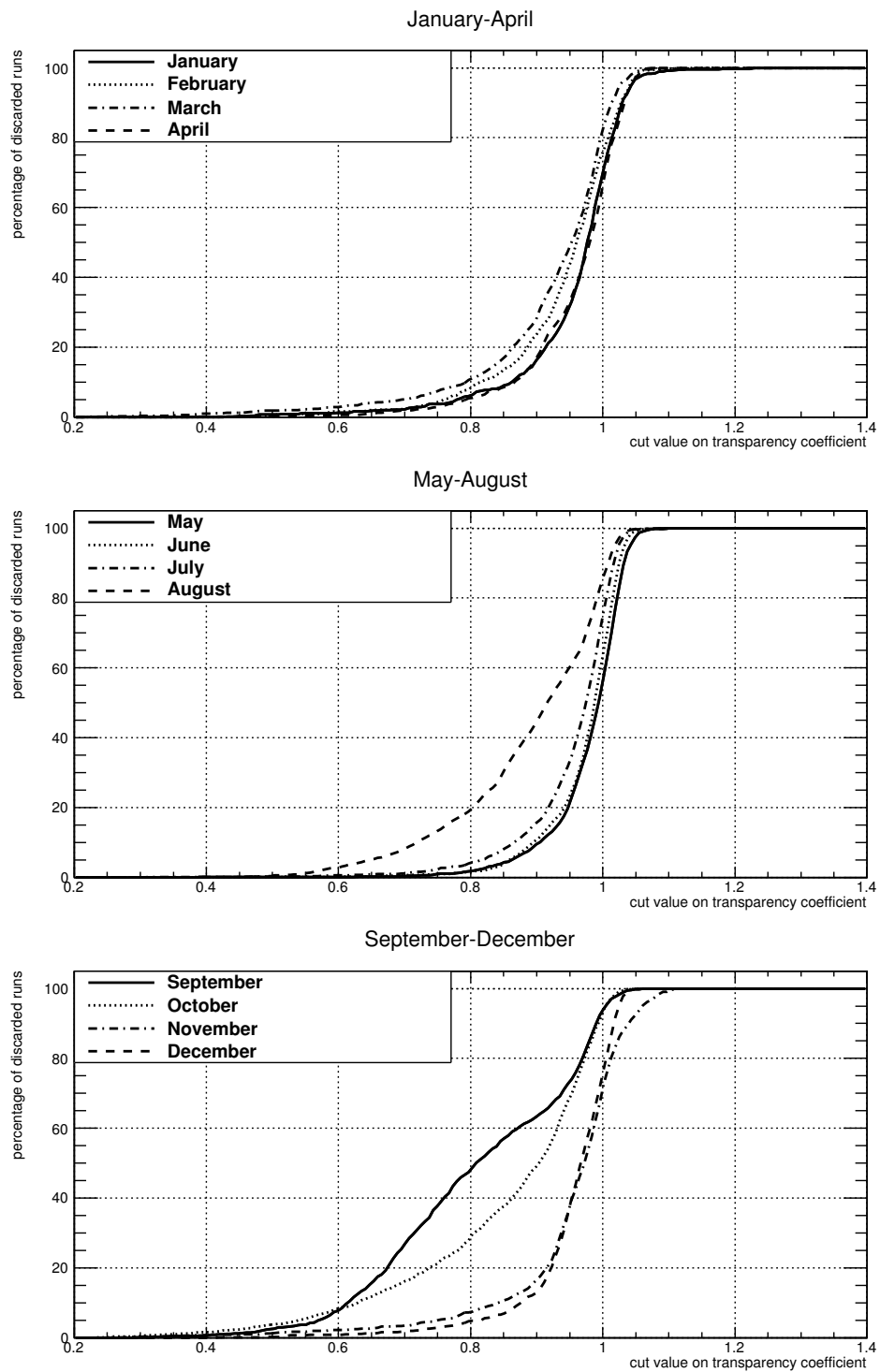
Figure 2.10.: Selective power of T in DQ selection during the different months of the year.

experiment has a higher spatial resolution ($\sim$1×1km) and is able to view the atmosphere at different observation angles that allows it to differentiate between different types of land surfaces, clouds and aerosols.

A MISR study by [Tesfaye et al., 2011] on the atmosphere over South Africa revealed elevated aerosol concentrations in the North. Here, the corresponding values are 34% higher than in South Africa's southern regions. Furthermore, the authors saw also a seasonal change in the aerosols composition. Accumulation and coarse-mode particles (aerosols with 1-20μm radius) typically result from air mass transport from arid/semi-arid regions and make up for the largest part of the aerosol mix during summer and early winter (December-June months). During the months between August and October, it is dominated by sub-micron particles that cause an increase in the optical depth at UV wavelengths that are typical for Mie scattering. The main sources of such aerosols are industrial and rural burning activities.

Similarly, drops in T can be found in the H.E.S.S. data at the same periods of the year (see Fig 2.6 and 2.5). The comparison with satellite observations (see Fig. 2.11) therefore supports the presumption of the annual reduction in T-values around September being caused by aerosols from agricultural biomass burning in the surroundings of the H.E.S.S. site.

Correlation With MISR Data

The satellite measurements performed with MISR [6] provide measurements on the aerosol optical depth (AOD) which is defined as the integrated extinction coefficient over a vertical column of unit cross section. Since by construction T measures a decrease in light intensity, for a linear correlation the quantity $\exp(\text{-AOD})$ instead of AOD itself was used. The AOD values are measured at the three different wavelengths 443nm, 555nm and 670nm.

Even though both MISR and H.E.S.S. took data in the years 2004 to 2012, the temporal overlap between measurements from the two instruments is sparse. That is, MISR records its data during daytime while H.E.S.S. observes at night. More importantly, MISR samples the same location on the ground only every 2-9 days. For this study a maximum time difference between MISR and H.E.S.S. observations of 24h is imposed. Furthermore, the detection set of DQ cuts as well as the δ_1 and δ_2 cuts (with conservative values of 5%) where applied to the H.E.S.S. data set in order to minimize the contamination of clouds that are completely excluded in the satellite data. As a result, only 2% off the whole H.E.S.S. data set has a contemporaneous MISR data point in the mentioned time interval.

The time evolution of contemporaneous T and MISR AOD data is shown in Fig.2.11. Although the data set is limited, one can clearly see a correlation

---

[6]In this work, the Level 3 data product was used. This level corresponds to a data reduction by decreasing the spatial (to 0.5×0.5 degrees) and temporal (1 day) resolution.
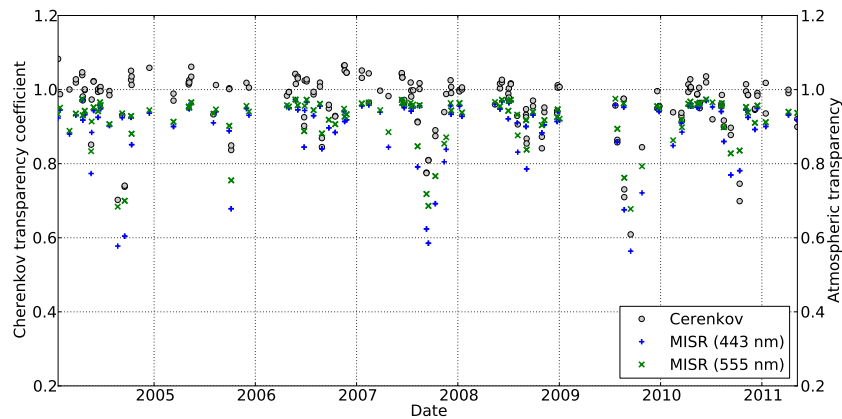
Figure 2.11.: Time evolution of T and MISR AOD data. The points correspond to the subset of data where both H.E.S.S. and MISR observed the atmosphere over the H.E.S.S. site within a time interval of 24 hours. Figure extracted from [Hahn et al., 2013a].
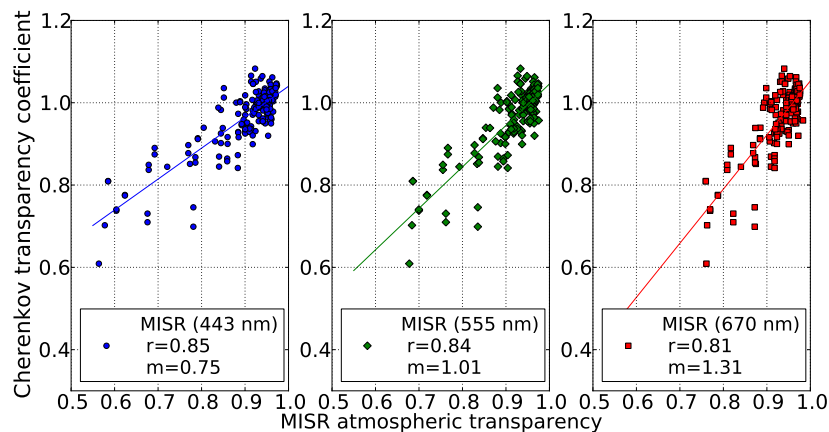
Figure 2.12.: Correlation between MISR measurements and T at the three different wavelengts that are observed by the satellite. Figure extracted from [Hahn et al., 2013a].

between H.E.S.S. and MISR data. Quantitatively, the Pearson's correlation coefficients are r=0.85,0.84 and 0.81 at the blue, green and red wavelength, respectively. This strong and positive correlation is shown in Fig.2.12.

From a theoretical point of view one should expect an increasingly better correlations towards shorter wavelengths as the Cherenkov light intensity per path length is maximal in the UV-blue part of the electromagnetic spectrum,

which is where H.E.S.S. is most sensitive. The increasing values of r might be in accordance with this expectation although within the errors this trend is not significant.

2.5.2. Correlation with Data from the H.E.S.S. Radiometers

Each telescope on the H.E.S.S. site possesses a paraxially mounted radiometer plus one all-sky monitor. These devices measure the air temperature and operate between 8 and 14μm. While they are optimised for the detection of clouds and are primarily used as cloud monitors, it was recently found that they are sensitive to the presence of aerosols as well [Daniel et al., 2012].

A set of 28 4-telescope runs, recorded between July 2011 and March 2012 with the all-sky radiometer, has been investigated for a correlation with the Cherenkov Transparency Coefficient. These runs were selected for a good quality of the radiometer data. The H.E.S.S. Cherenkov data was selected in an analogue way as in the MISR correlation study. Furthermore, the data has been corrected for the air temperature and zenith angle, as these factors correlate with the measured radiometer temperature.
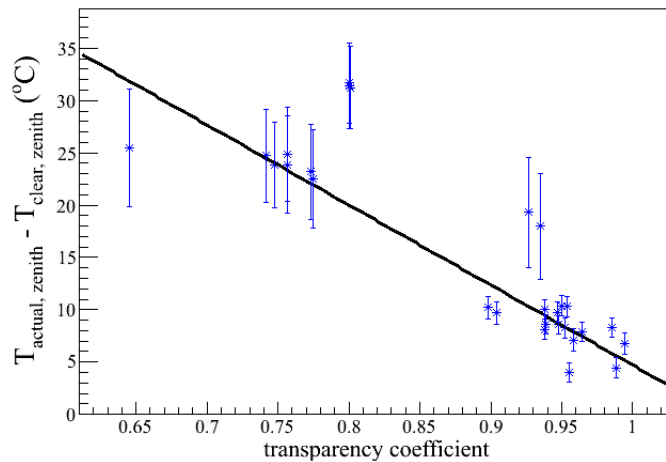
Figure 2.13.: Correlation between T and the difference of zenith corrected measured- to ideal-condition sky temperature. Figure extracted from [Hahn et al., 2013a].

In Fig.2.13 one can see the correlation between T and the difference of zenith corrected sky temperature to what would be expected for a clear sky.

The data set is limited, but also here a strong correlation can be observed with a Pearson's factor of $\sim$-0.86. This further confirms the sensitivity of Cherenkov Transparency coefficient to elevated atmospheric aerosol levels.

2.5.3. Correlation with Data from the H.E.S.S. LIDAR

Since 4 years a new LIDAR instrument is available at the H.E.S.S. experiment. This elastic LIDAR possesses a 60cm mirror and operates at green (532nm) and UV (355nm) wavelengths. Located in a separate hut at a distance of 850m to the H.E.S.S. telescopes, it is capable of performing fully automated measurements between observation runs at a fixed around zenith.

This device is able to directly measure the aerosol content in the atmosphere by comparing the measured atmospheric profiles to such obtained from a clear-sky. Aerosols from biomass burning populate the troposphere up to altitudes of ~3km, see Fig.2.14. By deriving the area between measured and reference (clear-sky) backscatter profiles in an altitude range of ~1-3km, one can quantify the aerosol content in the atmosphere (so called LIDAR ratio).
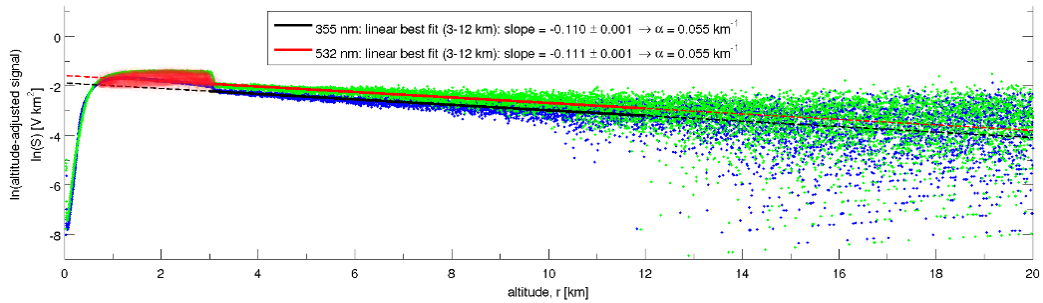
Figure 2.14.: Atmospheric back-scatter profile as measured by the H.E.S.S. LIDAR. Shown are both profiles for a clear (blue) and an aerosol-rich atmosphere (green). As one can see, aerosols populate the atmosphere up to altitudes of a few kilometres. The red-shaded area between good and bad atmosphere curves can be used to quantify the aerosol content and defines the so called LIDAR ratio. Courtesy of G. Vasileiadis.

In Fig.2.15 the correlation between this quantity and the transparency coefficient for the two measured LIDAR wave lengths is shown. As one can see, also in this case a strong correlation is found with Pearson's coefficient of R=0.9 and R=0.89 in the UV and green, respectively. This result further demonstrates the sensitivity of T to aerosols in the atmosphere.
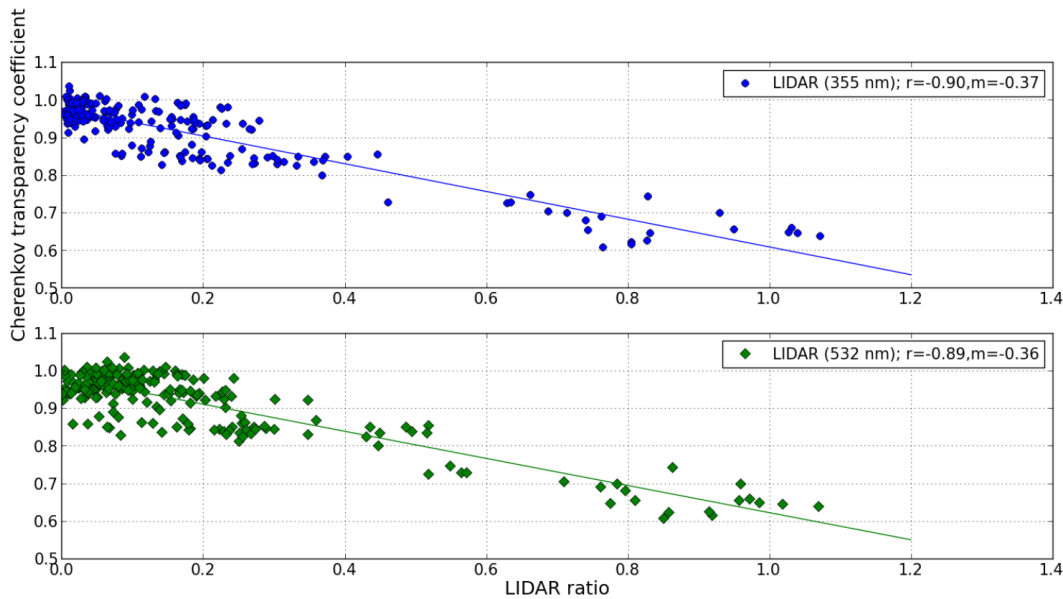
Figure 2.15.: Correlation between T and the aerosol content measured with the H.E.S.S. LIDAR. Courtesy of G. Vasileiadis.

2.6. Conclusions and Outlook

The *hap-HD* analysis framework uses an automated data selection scheme that allows it to guarantee a uniform data quality for the entire H.E.S.S. data set. This is especially important for the analysis of large amounts of data such as in population studies. In this process, hardware as well as atmospheric properties are monitored. The former category encompasses checks on the data integrity, camera status and source tracking and selects data that is suitable for the creation of maps and the detection of sources. The spectral analysis of sources requires additional checks on the atmospheric conditions at the H.E.S.S. site since an increased atmospheric opacity interferes with the energy reconstruction of primary particles. In the DQ scheme, quantities are in place that are sensitive to small and large clouds as well as to haze and aerosol layers (long-term absorbers). Recently, connected to the extensive hardware upgrades to the H.E.S.S. instrument, the DQ quantity which was used to monitor long-term absorbers lost its validity.

A new quantity, the Cherenkov Transparency coefficient T, was developed with the goal to isolate hardware-related effects from that of sub-optimal atmospheric conditions. As both these effects impact the trigger rates in a similar magnitude, they are often hard to disentangle. It was shown in this chapter that T is indeed quite hardware-independent.

Furthermore, a correlation study with satellite-, radiometer- and LIDAR data

confirmed the sensitivity of T to aerosols in the atmosphere through positive and large correlation factors (r∼0.85-0.9) with each of the independent data sets. The comparison to the MISR satellite data was especially helpful as it allowed to attribute the cause of the annual drops in the trigger rates around September to aerosols from biomass burning in the surroundings of the H.E.S.S. site.

A systematic study investigating the impact of aerosols, as measured with T, on the spectral reconstruction of the Crab Nebula showed a strong correlation between the values of the reconstructed flux norm and T. A simple model assuming a reduction in reconstructed energy by a constant factor proportional to T is able to reproduce the observed correlation. In the future it might be therefore possible to correct the reconstructed energy with the Cherenkov Transparency Coefficient. Previous methods, using other atmosphere-sensitive parameters, have already applied this idea (see [Pühlhofer et al., 2003], [Lebohec and Holder, 2003], [Dorner et al., 2009] and [Nolan et al., 2010]). Work in this direction is currently ongoing.

Also, since for the derivation of T only standard IACT calibration quantities and observables are used, this quantity provides an aerosol measure that does not require any additional instrumentation. For the same reason it is generic to the IACT technique and will thus be available to the future CTA.

3. Supernova Remnants

This chapter gives a short overview over Supernova remnants (SNRs), ranging from the different types of supernova (SN) events over the formation of the SNR shock front to the acceleration and spectral evolution of cosmic rays (CRs) at the shock. Finally, the most important emission mechanisms of these CRs are introduced. Chapter 4 will present a population synthesis simulation for non-thermally emitting SNRs which requires many of the aspects that will be discussed in the following. Therefore, these components will be elaborated upon in somewhat more detail.

SNRs are the remains of massive stars that end their lives in extremely luminous Supernova explosions. The first SNRs were observed at optical wavelengths as diffuse structures situated at positions of historically recorded SN explosions. It was therefore assumed that these nebulae are the remnants of these events.

These objects were later also detected in the radio, and it became clear that SNRs have to be places where particle acceleration occurs. That is, the spectral radio shape of these objects indicated that the radio emission stems from synchrotron scattering of highly energetic ($\sim$1GeV), non-thermally distributed electrons. This effect was shown by Shklovsky, who was the first to interpret the broadband emission from the Crab Nebula as synchrotron radiation of electrons, see [Shklovsky, 1957].

This theory was later supported by X-ray observations of SNRs where a non-thermal spectral component was observed. With the detection of SNRs at higher energies by satellite instruments and ground-based IACT experiments, it is today established that these objects are highly efficient particle accelerators. As a matter of fact, SNRs are suspected to be the prime sources of galactic CRs as the energetics and frequency of SN events in the Milky Way allows to describe the estimated total energy in galactic CRs [Baade and Zwicky, 1934a]. Of course, this would require the efficient acceleration not only of electrons but also of hadronic particles, especially protons. Determining the nature of high energy (HE) and VHE gamma-ray emission with respect to the radiating particle species is therefore one of the main motivations for the observations of SNRs at these energies. Recently, the Fermi-LAT instrument was able to resolve the signature of π^0-decay in the HE gamma spectrum of IC 443 and W44 [Ackermann et al., 2013], which strongly supports the notion of SNRs being the sources of galactic CRs.

Because SNRs are the result of stellar material being propelled into the surrounding medium, both the SNR progenitor as well as the circum-stellar

medium (CSM) at the time of the SN determine its physical properties. As a result, SNe and their remnants come in various shapes. The different types of SNe and their progenitors will be discussed in the next section.

3.1. Supernova Types and their Progenitor Stars

SNe are categorised into groups depending on the absorption features and temporal evolution of their optical spectra. If hydrogen lines are apparent, SNe are called type II, otherwise they are referred to as type I. These two groups constitute the main *observational* classes of SNe are and are further sub-divided according to the presence of further elemental absorption lines and the shape of their light-curves. The current classification of SNe is sketched in Fig.3.1.
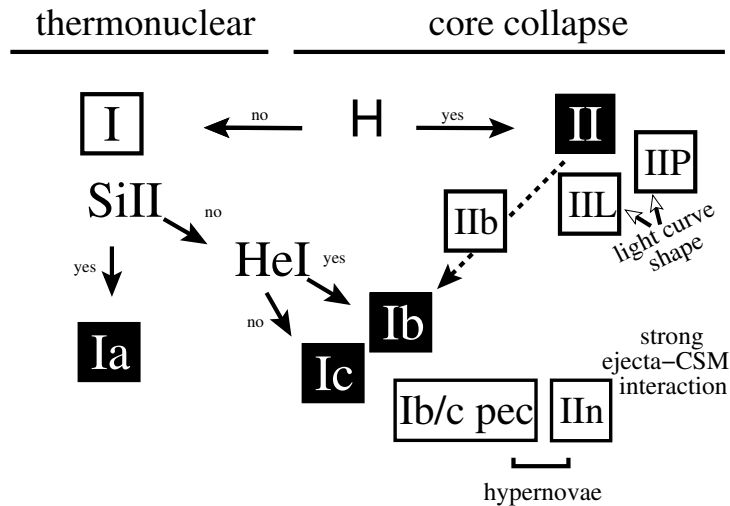
Figure 3.1.: Current classification scheme of SNe. This plot has been extracted from [Turatto, 2003].

This variety in observed SN emission behaviour is believed to be connected to the progenitor object. In the current picture, one distinguishes two fundamentally different SN mechanisms, namely thermonuclear and core-collapse SNe (cc-SNe).

3.1.1. Thermonuclear Supernovae

A peculiar subgroup of SNe is that of type Ia. These events show a striking homogeneity in their spectral and temporal properties. They appear in all known galaxy types and unlike all other SN types, they are not associated to star-forming regions. Furthermore, no compact objects can be associated [Turatto, 2003]. These circumstances, together with a spectral absence of hydrogen lines leads to the current belief that the progenitors of SNIa are White Dwarfs (WDs)

that accrete matter from a companion star. By doing so, the WD exceeds the Chandrasekhar limit of $M_{Ch} \sim 1.4 M_{\odot}$ upon which the density in the center jumps up and the fusion of carbon is started. Now, a stage of carbon burning follows that may persists for several hundred years. This period ends when one or several highly localised regions enter a state of thermonuclear runaway and lead to the explosion and consequently the complete destruction of the White Dwarf. A detailed description of these processes can be found in [Roepke, 2008]. This explosion releases an enormous amount of energy: A SNIa releases $\sim 10^{51}$erg of nuclear binding energy in a short amount of time, outshining its entire host galaxy and rendering it one of the brightest events in the universe. About 25% of all observed SNe are of this type. Because of their uniform properties and their brightness, SNIa can be today detected to red-shift values of z>1.5 (see e.g. [Riess et al., 2001]) and are therefore used as standard candles in the measurement of cosmological distances [Perlmutter et al., 1997].

3.1.2. Core-Collapse Supernovae

All other SN types behave quite differently: They are under-represented in early-type galaxies and show a strong correlation with star forming regions. Also, in many cases an association with pulsars is possible. Unlike thermonuclear SNe, they come in great observational variety. It is believed that these events are connected to the final evolutionary stage of massive stars (M>8M$_{\odot}$), the gravitational collapse of their iron nuclei. Thus, these explosions are powered by the release of gravitational energy, unlike thermonuclear SNe that take their energy from nuclear binding energies.

In the final stages of a massive star, an iron core develops at the center of the star. Fusion halts at this point, disturbing the equilibrium between radiation pressure and gravitation in the core. Furthermore, the extreme densities in this region ($>7 \cdot 10^9$g/cm^{-3}) lead to electron capture which reduces the electrons' degeneracy pressure. To make matters worse, energy is consumed by photodisintegration of iron nuclei. As a result, the core is no longer able to maintain its own weight and collapses at a speed of 0.25c. This core-collapse is ended after less than a second when a neutron rich degenerate nucleus is formed on which the still in-falling material bounces back. The consequent shock wave moves outward and suffers extreme photodisintegration and especially neutrino losses which stop it after a few milliseconds. Now the central structure is accreting at a rate of several $\sim$0.1M$_{\odot}$/s. This causes the emission of $>1 \cdot 10^{53}$erg worth of neutrinos in a few seconds time. A part of this energy is deposited in form of a hot bubble consisting of radiation and e$^{\pm}$ pairs which is rapidly expanding is visible as the SN explosion. Depending on the initial mass of the star, a neutron star or a black hole is created in the process. The most massive stars might not explode in SNe as they probably collapse directly to black holes. A review of cc-SNe is given in [Woosley and Janka, 2005].

The large variety in observational properties can be attributed to the evo-

lution of the massive progenitor stars, which in a very complex manner critically depends, among other attributes, on its stellar mass. More precisely, the strength of the progenitor's stellar winds determine the extent of its envelope material prior to the SN. The most massive stars (M>35 M$_\odot$)feature strong stellar winds in their post-main sequence phases with mass luminosities exceeding 10^{-5} M$_\odot$/yr, shedding the star of most or even all of its H-envelope. As a result, no H-lines are apparent in their SN spectra. These objects constitute the sub-class of type Ib, Ic and to some extent IIb (in this case, only initially weak H-absorption is observed). Lower mass stars feature at least partially intact hydrogen envelopes which is why H-lines are observed in the SN spectra. The state of the H-envelope also determines the time evolution of SN light curves: Roughly speaking, it is believed that the more massive the outer layer, the slower the decline of the lightcurve, attributing SNIIP ('P' for a *plateau* in the lightcurve) to less massive stars with more intact H-envelopes than those of the more massive SNIIL ('L' for a *linear* lightcurve decline) progenitors. In the current picture, it is believed that stars with initial masses of ∼8-25 M$_\odot$ end their lives in SNII-P explosions, those of initial masses ∼25-35 M$_\odot$ give rise to SNe of types II-L/b and the most massive stars (M>35 M$_\odot$) explode in SNIb/c SNe, see e.g. [Heger et al., 2003]. While the mentioned numbers are under debate (see e.g. [Smartt et al., 2009] for a different scheme), they will be accepted in the following.

This picture attributes each SN type to a certain range in the progenitors' initial mass M, and if the number distribution of stars in M is known, the relative ratio between the different SN types is fixed. Such mass distributions are called *initial mass functions* (IMF). A classical expression was derived by [Salpeter, 1955]. From optical observations of near-by stellar populations, the author found that the stars are mass-distributed in a power-law

$$\mathrm{d}N/\mathrm{d}M' \approx 0.03(M')^{-2.53}, \tag{3.1}$$

where $M' = M/M_\odot$ is the initial mass of the progenitor star in units of solar masses.

Using this IMF, results in relative frequencies of the different cc-SN types as SN-IIP to SN-Ib/c: 10 and SNIIP to SNIIL/b: 7.6.

These numbers are close to the result of [Heger et al., 2003] who estimate the relative rates of cc-SNe[1] from sophisticated theoretical considerations as SN-IIP to SN-Ib/c: ∼10 and SNIIP to SNIIL/b: ∼5.

From a recent study of ∼1000 SNe with the Lick Observatory, [Li et al., 2011] estimate an average rate of SNe in the Milky way of 2.84±0.6 per century.

---

[1]It should be noted that these numbers change if a significant fraction of cc-SN progenitors is part of a binary systems. Also, the authors assume a slightly higher minimal progenitor mass for cc-SNe of 9 M$_\odot$.

3.2. Circum-Stellar Environment of Supernova Remnants

Core-collapse SNe are associated with massive OB stars which are able to re-shape the medium around the star. As the structure of the so-modified circum-stellar medium (CSM) has a critical impact on the properties of SNRs, a basic picture of the involved processes and resulting structures will be outlined in the following.

3.2.1. The Stellar Bubble

Massive stars feature strong and fast winds during their evolution along the main sequence. In the most extreme cases, stellar material is expelled with terminal velocities that can reach values of $V_w \sim 1500 \text{kms}^{-1}$ at mass loss rates close to $\dot{M}_w \sim 10^{-5} \text{M}_\odot \text{ yr}^{-1}$. [Castor et al., 1975] developed a comprehensive theory on the evolution and structure of the resulting wind-blown bubbles, which will now be shortly presented.

At the time of the SN event, the bubble is typically older than 10^6yrs. The wind bubble structure around the star at this point can be sketched as follows: The star is nested in a compact hypersonic stellar wind, which itself is embedded in a hot and dilute region (a) that is made up mainly of shocked wind material but also some swept-up ISM matter and makes up for by far the largest part of the bubble volume. The outermost structure is a thin, but dense shell at a radius R_b which constitutes the border to the ISM.

The authors find the following expressions for bubble radius R_b and particle density n_b in zone (a):

$$R_b = 28 \left(\frac{\dot{M}_{w,6} V_{w,2k}^2}{n_0} \right)^{1/5} t_6^{3/5} \text{pc} \tag{3.2}$$

$$n_b = 10^{-2} n_0^{19/35} (\dot{M}_{w,6} V_{w,2k}^2)^{6/35} t_6^{-22/35} \text{cm}^{-3} \tag{3.3}$$

Here, $t_6 = t/10^6$yrs is the time of the progenitor star on the main sequence, n_0 is the ambient gas particle density around the bubble, $\dot{M}_{w,6} = \dot{M}_w/10^{-6} \text{M}_\odot \text{yr}^{-1}$ and $V_{w,2k} = V_w/2000 \text{kms}^{-1}$.

It should be noted that this model of stellar bubbles does not take combined winds from multiple OB-stars into account which is not unlikely to happen considering typical birthrates in molecular clouds. Also, the motion of the star is neglected, which may result in deviation from the spherical bubble shape.

3.2.2. The Red Giant Wind

OB-stars in the initial mass range $8 < M_i/M_\odot \leq 35$ go through a final red supergiant phase (see, e.g., [Kippenhahn and Weigert, 1990]) during which a Red Giant Wind (RGW) , often connected with massive loss of matter, is launched.

This wind expands into the previously created stellar bubble and, depending on the mass loss rate, creates a medium around the star that can be orders of magnitudes more dense than the bubble interior.

The radial density profile in this wind is determined by the mass loss rate of the RGW, $\dot{M}_{RGW}$, and its speed V_{RGW}:

$$\rho_{RGW}(R) = \frac{\dot{M}_{RGW}}{4\pi V_{RGW} R^2} \tag{3.4}$$

The values of $\dot{M}_{RGW}$ and V_{RGW} are not very well known. However, typical values have been inferred by observations as well as theoretical considerations (see e.g. [Pooley et al., 2002], [Schaller et al., 1992]). Characteristic values of $\dot{M}_{RGW}$, V_{RGW} and the extension of the RGW zone (RGZ) R_{RGW} as well as of the SN ejecta mass M_{ej} are listed in Tab.3.1.

	SNIIP	SNIIL/b	SNIb/c
$\dot{M}_{RGW}$ (10^{-5}M$_\odot$/yr)	$\sim$0.1-0.2	$\geq$2	1
V_{RGW} (10km/s)	1	1.5	100
R_{RGW} (pc)	1	5	-
M_{Ej} (M$_\odot$)	6-8	1	$\sim$2-4

Table 3.1.: Typical parameters for the RGW of cc-SN progenitors. Values taken or inferred from [Chevalier, 2005], [Smartt et al., 2009], [Ptuskin et al., 2010], [Woosley et al., 1993].

Progenitor stars of SNIb/c behave very differently than SNII in that they go through an additional phase after their existence as red supergiants. Such stars can enter a so-called Wolf-Rayet (WR) stage after losing their H envelope which are characterised by massive mass loss, with loss rates similar to that of SNIIL/b. However, WR eject a very hot wind with characteristic speeds that surpass those of SNIIL/b by two orders of magnitude. It is believed that the WR wind sweeps up and disrupts the RGW zone into which it expands. [Dwarkadas, 2005] performed 2D hydrodynamical simulations of the interaction between WR and RGW ejecta. Six snapshots from the density evolution of the bubble, as found by the author, are shown in Fig.3.2. They describe a messy situation in which both ejecta mix turbulently and approximately fill out the main sequence stellar bubble.

3.3. The Supernova Remnant Blast Wave

SNRs are the results of the interaction of stellar matter, expelled at high velocities in the SN explosion, with the circum-stellar environment (which is typically pre-modified as discussed in the previous section).
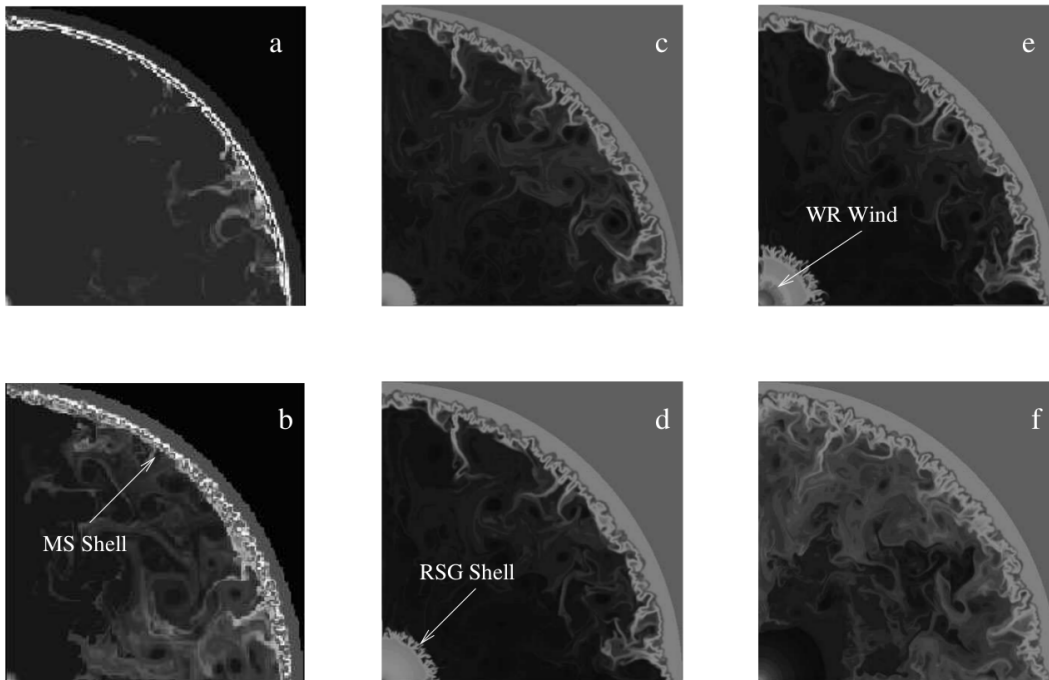
Figure 3.2.: Evolution of the CSM density around a $35M_\odot$ star. Panels a,b show snapshots from the main sequence phase, c,d from the red super-giant phase and e,f from the Wolf-Rayet phase. These simulations were performed in [Dwarkadas, 2005], where also this figure is extracted from.

SN ejecta velocities exceed the local speed of sound, and consequently a shock front is formed ahead of the expelled material, the *blast wave*. The hydrodynamical evolution of a classical[2] SNR shock front can be divided into two stages (see e.g. [Woltjer, 1972]):

- A so-called *non-radiative* stage, where the high temperatures ($\sim10^7$K) of the shocked material allow it to cool only moderately via free-free radiation with H and He. In this domain, the shock dynamics are determined by pressure forces. Since the energy losses are small, it can be regarded as approximately adiabatic. This is the phase where efficient particle acceleration occurs in SNRs, see e.g. [Reynolds, 2008].

- As the SNR shock front slows down, the temperature of the shocked material decreases below $5\cdot10^6$K where line emission from heavier nuclei grow more important and the SNR enters its *radiative* stage, where it quickly slows down below the ambient speed of sound and dissolves into the ISM.

Because the radiative phase is not critical for the VHE luminosity of SNRs, it will not be discussed in the following. That is, particle acceleration in SNRs

---

[2]i.e. neglecting the effect of relativistic particles on the SNR dynamics

is believed to occur when the blast waves are highly super-sonic, i.e. when the remnants are in the non-radiative phase. This phase can be divided into two extreme limits:

- An early-time phase where only a small amount of CSM material has been swept up and the dynamics is that of a freely expanding piston. Since the ejecta determine the properties of shock propagation in this case, it is referred to as the *ejecta-dominated* (ED) phase. The shock wave accelerates and heats the ambient medium which in turn exerts a pressure back onto the expanding shell, triggering the onset of a reverse shock which travels inwards, shocking and slowing down the previously freely expanding SN ejecta. The reverse shock mediates information about the ISM into the SNR interior. The SN ejecta (shocked and unshocked) are separated from the blast wave by a contact discontinuity; the blast wave therefore 'sees' only the CSM material.

- A late-time phase at which the majority of the SN blast energy has being transferred to the ambient material by sweeping up a mass $M_{SW} \approx M_{ej}$ to a fraction of the blast wave speed. Because it was first described independently by [Sedov, 1946], [Taylor, 1950] and [von Neumann, 1947], it is referred to as the *Sedov-Taylor* (ST) phase.

In the following, only the forward shock dynamics will be discussed. A detailed treatment of the reverse shock can be found in [Truelove and McKee, 1999].

The evolution of the blast wave (expanding at a radius R_s with a speed of v_s) in both phases can be described with so-called *self-similar* solutions. Self-similar solutions have the remarkable property that they show radial profiles of hydrodynamical quantities, like velocity or density, that stay form-invariant in time and simply scale with a function of the so-called similarity variable $\zeta = r/R(t) = r/t^\eta$. A famous example is the solution of Sedov for ST-phase shocks in homogeneous ambient media

$$R_s(t) = (\xi E_{\mathrm{SN}}/\rho_0)^{1/5} t^{2/5}, \tag{3.5}$$

where $\xi = 2.026$ is a constant, ρ_0 is the ambient density and E_{SN} is the SN blast energy. In this case, $\eta = 2/5$. Further theoretical considerations show that, for example, the downstream density may be written as $\rho = (\gamma + 1)/(\gamma - 1)\rho_0 f(\zeta)$. The function $f(\zeta)$ (as well as analogous functions for other quantities) can be derived analytically.

For the ED phases of SNRs, self-similar solutions were found e.g. by [Chevalier, 1982a] and [Nadezhin, 1985]. In this case, the swept-up mass is small and the evolution of the blast wave is determined by its ram pressure and the density at the shock. The authors find $\eta = 1$, corresponding to a blast with constant velocity so that $R \propto t$.

3.3.1. Unified Shock Solution

Truelove and McKee developed a theoretical framework that is able to describe the intermediate range between the two phases by what the authors call *unified* solution of the hydrodynamical problem [Truelove and McKee, 1999]. Unified solutions of any flow variable F can be written as dimensionless expressions of shock radius and age, $F = F(R^*, t^*)$ where the rescaled quantities $R^* = R/R_{ch}, t^* = t/t_{ch}$ are defined through characteristic length- and time-scales,

$$R_{ch} = M_{ej}^{1/3}\rho_0^{-1/3} \text{ and } t_{ch} = E^{-1/2}M_{ej}^{5/6}\rho_0^{-1/3}, \tag{3.6}$$

that are unique to the problem. They are the only instance where the initial dimensional parameters enter the solution, so that once the unified solution to a problem is found, they can be applied to similar cases simply by recalculating the characteristic time and radius.

The solution of the blast wave motion in the Sedov-Taylor phase is based on the classical result given by Eq.3.5. Introducing a to-be-determined set of radius and time that characterises the onset of the Sedov-Taylor phase (R_{ST},t_{ST}) as well as rescaling it with R_{ch} and t_{ch} yields:

$$R_s^*(t^*) = [R_{ST}^{*5/2} + \xi^{1/2}(t^* - t_{ST}^*)]^{2/5} \tag{3.7}$$

$$v_s^*(t^*) = \frac{2}{5}\xi^{1/2}[R_{ST}^{*5/2} + \xi^{1/2}(t^* - t_{ST}^*)]^{-3/5} \tag{3.8}$$

Function Eq.3.7 reverts to Eq.3.5 in the extreme ST limit $t \to \infty$. At earlier times, the parameter η smoothly transitions from unity to 2/5.

A very important parameter is the density index n, which is the exponent in the power-law that describes radial shape of the SN ejecta. SNIa/b/c are believed to feature a value of $n = 7$ [Colgate and McKee, 1969], [Chevalier, 1981] while SNe where the H-envelope is at least partially intact show steeper indices of $n = 10 - 12$ [Ptuskin and Zirakashvili, 2005]. In these cases, the solution for the forward shock dynamics in the ED phase is found by the authors as

$$R_s^*(t^*) = \left\{\frac{27}{4\pi}\frac{1}{n(n-3)}\frac{l_{ED}^{n-2}}{\phi_{ED}}\left[\frac{10}{3}\left(\frac{n-5}{n-3}\right)\right]^{(n-3)/2}\right\}^{1/n}t^{*(n-3)/n} \tag{3.9}$$

$$v_s^*(t^*) = \frac{(n-3)}{n}\frac{R_s^*(t^*)}{t^*}. \tag{3.10}$$

Note that here $R_s \propto t^{(n-3)/n}$ and not $R_s \propto t$ as in the early free-expansion limit. This can be understood by the fact that Eqs.3.9 and 3.10 are only valid outside a core region which is required in the mathematical treatment of SNRs featuring the mentioned ejecta profiles. Thus, this solution is only valid at times $t > 0$ and not strictly comparable to the self-similar ED solution, which holds for $t \to 0$. The dimensionless parameters l_{ED} and ϕ_{ED} describe the relation between forward and reverse shock and are functions of the dimensional

initial parameters. Together with R_{ST} and T_{ST} they are used to seamlessly connect the ED solution (Eqs.3.9-3.10) to the ST solution (Eqs.3.7-3.8). Tab.3.2 list these parameters for $n = 7, 10$ and 12.

n	l_{ED}	ϕ_{ED}	R_{ST}	T_{ST}
7	1.26	0.47	0.881	0.732
10	1.17	0.57	0.687	0.481
12	1.15	0.60	0.636	0.424

Table 3.2.: Trajectory parameters in Eqs.3.7-3.10 for the cases of n that are relevant for this work. Values extracted from [Truelove and McKee, 1999].

The set of solutions Eqs.3.7-3.10 to the hydrodynamics of SNR forward shocks is only valid under certain assumptions for the ambient medium density. That is, the solutions were obtained assuming a constant density of the surrounding gas.

3.3.2. The Thin-Shell Approximation

[Ostriker and McKee, 1988] describe an approximate solution for an spherically symmetric adiabatic shock wave that allows for more complex radial density profiles of the ambient gas. It is called the *thin-shell* approximation because by construction all of the gas shell mass (the swept-up ambient material with the radial density profile $\rho(R)$ plus M_{ej}) is assumed to be distributed in a infinitely thin shell just behind the shock front, moving at the post-shock velocity v_p. The second main simplification is that the pressure profile within the SNR follows a specified profile that has only one parametric dependence with time, $P_{in}(t)$.

From these assumptions, [Ptuskin and Zirakashvili, 2005] derive the differential equation

$$\frac{d(Mv_s)^2}{dR_s} = \frac{12(\gamma - 1)}{(\gamma + 1)R_s}\left(EM - \frac{1}{2}(Mv_s)^2\right) \tag{3.11}$$

which leads to

$$v_s(R_s) = \frac{\gamma + 1}{2}\left[\frac{2wE}{M^2(R_s)R_s^w}\int_0^{R_s} dr\, r^{w-1}M(r)\right]^{1/2}, \tag{3.12}$$

$$t(R_s) = \int_0^{R_s} dr \frac{dr}{v_s(r)}, \tag{3.13}$$

where $w = \frac{6(\gamma - 1)}{y + 1}$ and $\gamma = 4/3$, as it is assumed that the downstream pressure is mainly generated by relativistic particles.

While it is not in the convenient self-similar form, this solution has the important property that it does not put any conditions on the radial density profile

of the ambient medium. Hence, this approach may be applied to treat complex features in the ambient medium where it can be used to replace the solution given by Eqs.3.7-3.10.

3.4. Supernova Remnants as Particle Accelerators

It is an observational fact that SNRs are places of efficient particle acceleration. In the second half of the 1970's, a theory was developed independently by [Krymskii, 1977], [Blandford and Ostriker, 1978], [Axford et al., 1977] and [Bell, 1978] that is able to describe the apparent population of non-thermal particles in SNRs. This theory is referred to as $First Order Fermi Acceleration$ or $Diffusive Shock Acceleration$ (DSA).

3.4.1. First Order Fermi Acceleration

The supersonic motion of one fluid at a velocity v_s in another causes a shock and in its rest frame, density as well as streaming velocities on both sides are given by the conservation of mass:

$$\rho_U v_U = \rho_U v_s = \rho_D v_D. \tag{3.14}$$

Here, v are velocities, ρ stand for densities and the indices U, D represent upstream and downstream, respectively. From classical hydrodynamics it is known that the material downstream is compressed by a *compression ratio* $\sigma_0 = 4$ [Rankine, 1870], [Hugoniot, 1889]. From Eq.3.14 it follows that $v_D = v_s/4$, see also Fig3.3.
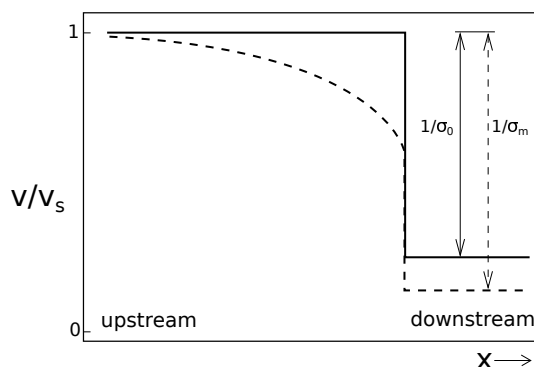
Figure 3.3.: Sketch displaying velocity profiles in the restframe of a classical (solid) and a modified shock (dashed).

In the context of SNRs, particles are scattered off magneto-hydrodynamical waves in the magnetic fields (so-called *collision-less scattering*). In the rest frame of the scattering centres, energy and momentum are conserved. If the

scattered particle crosses the shock, its energy and momentum have to be Lorentz-transformed into the new scattering rest frame. For instance, the particle momentum p changes after crossing upstream→downstream $\Delta p_1 = p\frac{\Delta v}{c}\cos\theta$, where $\Delta v = 3/4 v_s$ and θ is the (random) relative angle of the particle to the shock normal [Bell, 2011]. Averaging over the angle yields a mean momentum gain per crossing of $\langle\Delta p_1\rangle = p\cdot v_s/2c$. If particles are scattered downstream→upstream, the transformation is identical because again $\Delta v = 3/4 v_s$ and therefore particles gain on average $\langle\Delta p_2\rangle = \langle\Delta p_1\rangle$. Per round-trip, particles on average gain a fractional energy of

$$\frac{\Delta E}{E} = \frac{\langle\Delta p_2\rangle + \langle\Delta p_1\rangle}{p} = \frac{v_s}{c} \tag{3.15}$$

While particles gain energy in each crossing, a certain amount of them leave the shock. That is, particles stream away downstream at a rate $\rho_{CR}v_s/4$, where ρ_{CR} is the cosmic ray density. At the same time particles cross the shock upstream→downstream at a rate $\rho_{CR}v_s/4$ because the average particle velocity in perpendicular to the shock is $\langle v_x\rangle = c/2$ and half of the particles move towards it. These two processes result in a fractional net loss of particles per crossing of

$$\frac{\Delta N}{N} = -\frac{v_s}{c}. \tag{3.16}$$

Combining Eqs.3.15 and 3.16 yields the differential equation $dN/dE \approx \Delta N/\Delta E = -N/E$ which corresponds to an integrated power-law spectrum $N \propto E^{-1}$. The interplay between fractional energy gain and energy-independent particle loss results thus in the famous result for the differential particle spectrum of

$$\frac{dN}{dE} \propto E^{-2}. \tag{3.17}$$

The exponent of α=-2 in Eq.3.17 derives from the compression factor of σ_0=4. This is the solution for the so-called test-particle limit where the CRs do not back-react onto the shock.

More realistically, a certain amount of accelerated and ultrarelativistic particles will propagate upstream. As a result, the pressure ahead of the shock is increased and the in-streaming CSM material is decelerated. Furthermore, those particles take away energy from the shock, and the downstream streaming velocity is reduced. This picture of a modified shock is indicated by the dashed line in Fig.3.3. An interesting consequence of this shock structure is that the compression factor a given particle experiences depends on its energy: The highest energetic particles have large gyroradii and travel far ahead of the original shock (which is now called *subshock*) per round-trip. It follows that they 'see' an increased compression ratio $\sigma_m > \sigma_0$ (see Fig.3.3). Lower energy particles stay in the vicinity of the subshock and may even see compression factors that are smaller than in the test-particle scenario. Thus, the slope of the generated particle spectrum depends on the energy and is expected to show a convex shape.

3.4.2. The Particle Distribution at the Shock Front

With a mechanism that allows for particle acceleration at SNR shocks (see previous section) and the hydrodynamical models for shock speed and radius (section 3.3) as well as the CSM density profile (section 3.2), it is possible to calculate particle energy distribution at the shock front.

The temporal evolution of particles in energy space, $N(E, t)$, can be expressed as a partial differential equation [Ginzburg and Syrovatskii, 1964]

$$\frac{\partial N}{\partial t} = \frac{\partial}{\partial E}(PN) - \frac{N}{T} + Q, \tag{3.18}$$

where $P = -(\partial E/\partial t)$ is the energy loss power, T is the particle escape time and Q is the source term, i.e. the function that describes the rate and energy distribution of the accelerated particle population that enters the system.

In this approach, the distribution of particles in space is not accounted for so the spatial coordinate is not present. However, Eq.3.18 implies a scale for the spatial extension of the described system. It has to be large enough to encompass the acceleration zone in order to account for the source term Q. Here, this zone is represented by the SNR extension. On the other hand, it has to be of limited size since otherwise the assumption of particle escape is pointless. Particles leave the system by diffusion, so the upper value on the size is the SNR radius plus a certain critical particle diffusion length. This length is typically a fraction of ~ 0.1 of the shock radius (see e.g. [Zirakashvili and Ptuskin, 2008a]). Thus, the volume of the described system is basically identical to that of the SNR.

Eq.3.18 can be solved analytically if P is constant in time. An intuitive derivation of the solution can be found in [Atoyan and Aharonian, 1999].

The Green's function to problem Eq.3.18 is

$$G(E, t, t_0) = N_0(\varepsilon_{t_0})\frac{P(\varepsilon_{t_0})}{P(E)} \exp\left[-\int_{t_0}^{t} \frac{dx}{T(\varepsilon_x(E, t), x)}\right] \tag{3.19}$$

and describes the energy distribution of particles that results from the propagation in energy space and particle loss from an initial distribution N, burst-like injected at $t = t_0$. Here, the function $\varepsilon(E, t)$ has been introduced, which is defined via

$$t - x = \int_{E}^{\varepsilon_x(E,t)} \frac{dE}{P(E)}, \tag{3.20}$$

and describes the motion of particles in energy space. A particle with the energy E at time t had a (higher) energy $\varepsilon_x(E, t)$ at time x.

The quotient $P(\varepsilon_{t_0})/P(E)$ in Eq.3.19 describes the effect of cooling on the particle distribution. Particle escape is represented by the exponential function in the same equation.

In the case of a continuous injection, obtainable through Eq.3.19 by replacing $N_0(\varepsilon_{t_0}) \rightarrow Q(\varepsilon_{t_0}, t_0)dt_0$ and integrating over t_0,

$$N(E,t) = \frac{1}{P(E)} \int_0^t dt_0 P(\varepsilon_{t_0}) Q(\varepsilon_{t_0}, t_0) \exp\left[-\int_{t_0}^t \frac{dx}{T(\varepsilon_x(E,t), x)}\right] \qquad (3.21)$$

cooling manifests itself in a morphing of the spectral shape of the particle distribution while a time and energy dependent particle escape typically results in a high-energy cut-off.

This cut-off describes the maximum energy up to which the SNR is able to contain and thus to accelerate particles. Efficient particle acceleration takes place if

$$D(E) \leq \kappa v_s R_s, \qquad (3.22)$$

where $D(E)$ is the diffusion coefficient and $\kappa \sim 0.1$ is a constant (see e.g. [Drury et al., 2001]).

3.5. Non-thermal Photon Emission from Supernova Remnants

At the SNR shock-front, hadrons (mostly protons) as well as leptons (mostly electrons) are accelerated to relativistic velocities. These energetic particles interact with their surroundings and emit electromagnetic radiation. The following considerations are from [Blumenthal and Gould, 1970] and [Kelner et al., 2006], where a comprehensive picture of the involved radiation processes is presented.

3.5.1. Leptonic Emission

CR electrons are able to emit photons over an astonishingly large energy interval from radio to VHE energies. They do so by interacting with photons. Depending on the target photon field, one can differentiate:

- *Inverse Compton Scattering:* the electron scatters with a photon from the ambient radiation field

- *Bremsstrahlung:* the electron scatters with virtual photons of the Coulomb field of the ambient medium nuclei (this is the Weizsäker-Williams approach)

- *Synchrotron Radiation:* the electron scatters with virtual photons of the local magnetic field

Inverse Compton Scattering

Inverse Compton scattering occurs when a high energy electron traverses a photon gas. Energy is transferred from the electron to the photon. An electron of energy $\gamma m_e c^2$ in a blackbody photon distribution $\rho_i(\epsilon)$ emits a gamma-ray spectrum of

$$\frac{dN_{\text{IC,i}}}{dEdt} = \frac{2\pi r_0^2 c}{\gamma^2} \frac{\rho_i(\epsilon)d\epsilon}{\epsilon} \left[2q \ln q + (1+2q)(1-q) + \frac{1}{2} \frac{(\Gamma q)^2}{1+\Gamma q}(1-q) \right], \qquad (3.23)$$

with the quantities r_0 as the classical electron radius, $\Gamma = 4\epsilon\gamma/m_e c^2$ and $q = E/(\Gamma \cdot (E_e - E))$. Γ is a parameter that determines the *domain* of the radiation process: For $\Gamma \ll 1$ the scattering occurs in the Thomson-limit where electrons lose only small fractions of their initial energies, while the case $\Gamma \gg 1$ indicates that the inverse Compton process takes place in the extreme-Klein-Nishina regime. Here, the electron loses a substantial fraction of its initial energy in each scattering event.

Integrating $E(dN_{\text{IC,i}}/dEdt)$ over E, one finds that an electron loses its energy at a rate of

$$\frac{dE_e}{dt} = -\frac{4}{3}\sigma_T c w_{ph} \gamma^2 \qquad (3.24)$$

in the Thomson regime. In the Klein-Nishina limit the loss rate is

$$\frac{dE_e}{dt} = -\frac{\sigma_T (m_e ckT)^2}{16\hbar} \left(\ln \frac{4\gamma kT}{m_e c^2} - \frac{5}{6} - C_E - C_l \right), \qquad (3.25)$$

with the constants $C_E = 0.5772$ and $C_l = 0.57$. Hence, even though electrons loose more energy in individual scatterings, overall the IC process becomes less efficient at high energies as the radiative power increases only logarithmically with the electron energy.

Bremsstrahlung

Relativistic electrons passing through the Coulomb fields of the ambient gas nuclei are accelerated and emit photons in the process. This radiation mechanism is called relativistic Bremsstrahlung. The photon spectrum emitted by an electron with energy E_i in this way can be written as

$$\frac{dN_{Brems,i}}{dEdt} = c \sum_s n_s (d\sigma_s/dE), \qquad (3.26)$$

where s indicates the gas species, n_s the corresponding gas number density and $(d\sigma_s/dk)$ is the corresponding differential cross-section which depends on various parameters, such as the charge of the nucleus and the amount of shielding

it receives from valence electrons. The total energy loss rate can be written as [Aharonian, 2004]

$$\frac{dE_e}{dt} = -\left(\frac{m_p m_e c^3 n}{X_0}\right)\gamma,$$

(3.27)

where X_0 is the radiation length (e.g. for hydrogen gas $X_0 \approx 60\text{g/cm}^2$ [Aharonian, 2004]).

Synchrotron radiation

Magnetic fields accelerate moving electrons, which in turn radiate away photons. If the electrons move at relativistic speeds, this radiation is called synchrotron radiation.

Relativistic particle with arbitrary pitch angle relative to the magnetic field lines emit a photon spectrum that can be approximated as [Ghisellini et al., 1988]

$$\frac{dN_{Sy}}{dEdt} \simeq \frac{4\pi\sqrt{3}e^2\nu_B}{hcE}x^2\left[K_{4/3}(x)K_{1/3}(x) - \frac{3}{5}x\left(K_{4/3}^2(x) - K_{1/3}^2(x)\right)\right].$$

(3.28)

The electron's total energy loss rate due to synchrotron scattering is

$$\frac{dE_e}{dt} = -\frac{4}{3}\sigma_T c U_B \gamma^2,$$

(3.29)

which is identical to the loss rate for inverse Compton scattering in the Thomson limit (Eq.3.24) except that the photon field energy density $w_p h$ is replaced by the magnetic field energy density U_B.

3.5.2. Hadronic Emission

Additionally to the leptonic emission channels another primary mechanism for the creation of gamma-rays in SNRs is inelastic p-p scattering. In this process, approximately 17% of the initial proton energy is released in form of gamma-rays resulting from the decay of secondary η and π^0 mesons [Kelner et al., 2006]. Here, π^0 decay dominates with a relative amount of about 75% of produced gamma-rays.

The creation of π^0 and η-mesons is possible for protons above threshold energies of 1.22GeV and 2.35GeV, respectively, which is easily accessible in first-order Fermi acceleration at SNR shock fronts. A spectra proton density distribution J_p then leads to a differential gamma ray production rate[3] of [Kelner et al., 2006]

$$F(E)_{\pi^0+\eta} = cn_H \int_E^\infty \sigma_{inel}(E_p)J_p(E_p)F_\gamma(E,E_p)\frac{dE_p}{E_p},$$

(3.30)

---

[3]i.e. the number of photons per volume, time and energy

where σ_{inel} is the cross-section for inelastic p-p interactions and F_γ is the emitted gamma-ray spectrum per proton, which is shown in Fig.3.4 for the most relevant decay channels.
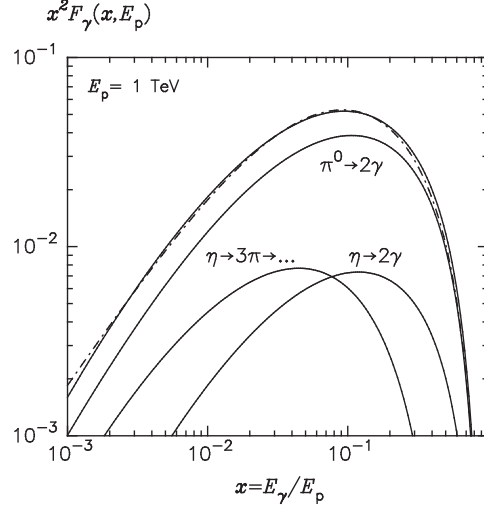
Figure 3.4.: Gamma-ray spectra from single π^0 and η mesons produced in the inelastic p-p interaction of 1TeV protons. The dashed line shows the analytical solution by Kelner et al. Plot extracted from [Kelner et al., 2006].

This calculation does not take the presence of heavier nuclei in neither the target nor the non-thermal particle distribution into account. A multiplication factor of 1.8 may be applied to Eq.3.30 to compensate for this shortcoming [Mori, 2009].

4. SNR population synthesis

In this chapter, modeling work towards a SNR population synthesis model will be presented. This work can help in the understanding of the VHE emission from SNRs and allows it to get an idea of what to expect from observations with the future Cherenkov Telescope Array (CTA) [Actis et al., 2011] regarding the galactic SNR population.

While such a model is of general astrophysical interest, it represents the theoretical counterpart to the analysis of the galactic SNRs which is described in chapter 5. The predictions of this simulation may then be used for a comparison with the analysis results and to provide observation recommendations.

4.1. The General Approach

In order to simulate an entire population of VHE-bright SNRs, one has to model several ingredients, namely the spatial distribution of SNRs in the galaxy, the environment around the SNR, the dynamical evolution of the shock-wave, the distribution of accelerated particles in SNRs and lastly the subsequent emission of non-thermal photon emission. Each of these building blocks is implemented with a simple model, most of which have been presented in chapter 3.

Here, a MC-approach is chosen to simulate the galactic distribution of SNRs in the VHE band: First, a set of parameters is sampled from the mentioned model distribution, namely the

- SNR type and relevant parameters of the progenitor star (initial mass, main-sequence and red giant wind speeds and luminosities, time on main sequence, SN blast energy, ejecta mass)

- position of the SNR in the galaxy

- age of the SNR

- values of the ISM gas density and magnetic field strength.

Once all these parameters are determined, it is possible to calculate forward shock speed and radius. This gives the particle distribution at the shock, which in turn allows it to derive the VHE gamma-ray and also the radio emission.

4.2. Spatial and Temporal Distribution in the Milky Way

4.2.1. Planar Structure

It is well established that our galaxy shows a spiral structure in the galactic plane. An exhaustive meta-study of data from radio, infra-red, optical and X-rays observations tracing the Milky Way material has been performed by [Vallée, 2005], and his best guess of the arm shape and their parameters is used in this work. From these observations Vallée finds a number of $n = 4$ arms, all of which feature the same pitch angle of $\psi = 12°$. In his paper, the spiral arms are modelled by logarithmic spirals,

$$\theta = \frac{1}{\tan(\psi)} \ln\left(\frac{r}{r_i}\right) + \theta_i \tag{4.1}$$

where the model parameters r_i and θ_i are obtained by a fit to the observational data. As a result, the author finds a value of $r_i = 2.3$kpc for all arms. The starting angles are $\theta_1 = 0°$(Norma), $\theta_2 = -90°$(Scutum), $\theta_3 = -180°$(Sagittarius) and $\theta_4 = -270°$(Perseus).

The spiral arm structure reflects regions of increased matter density in the galaxy, associated to places of star formation. Since cc-SNe result from massive, short-lived stars, they are expected to be correlated with the galaxy arms.
For each cc-SNe, the position is sampled from the galactic arm shape described by Eq.4.1. Additionally, it is shifted randomly by a Gaussian variate (with a width of σ_{shift}=300pc) in order to obtain a realistic arm width. This value represents an educated guess, comparable values have been used by [Taylor and Cordes, 1993], [Vallée, 2005]).

It is believed that the interstellar matter in the Milky Way features a barred-spiral (i.e. SBc) structure. The bar implementation in this simulation follows the work of [Freudenreich, 1998] , who modelled the bar to fit DIRBE data. Here, just the relative orientation of $\sim 14°$ with respect to the sun-GC line as well as the maximum bar radius of $\sim$3kpc are used. The sampled positions are then randomised in the same manner as in the case of the spiral arms, although with an arbitrary smaller scattering width of σ_{shift}=150pc.

In contrast, due of the stellar motion and age of WDs, remnants of type Ia SNe do not necessarily trace regions of increased matter density (i.e. the spiral arms). Thus, these objects are assumed to be uniformly distributed in the polar angle θ.

4.2.2. Distribution Perpendicular to the Galactic Plane

In the direction perpendicular to the galactic plane, the SNRs are MC sampled from two exponential profiles. The scale-height of the exponential functions is assumed to be smaller for cc-SNRs than for thermonuclear SNe. This is attributed to the fact that WD stars are possibly old and may therefore disperse
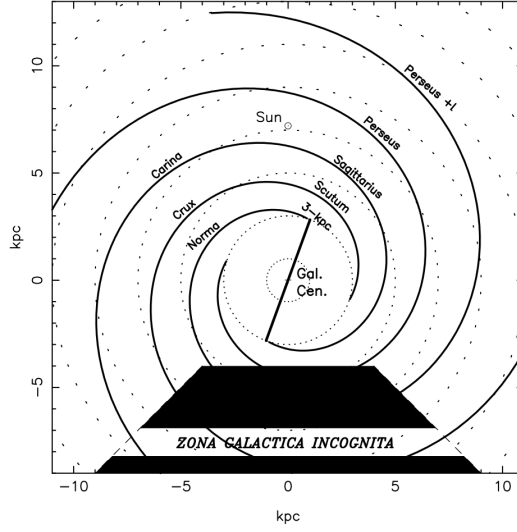
Figure 4.1.: The spiral arm and central bar model of the Milky Way inferred from the meta-study performed by Vallée (taken from [Vallée, 2005]).

away from their birth places which results in a broader distribution perpendicular to the galactic plane.

Here the scale height for SNRs from cc-SNe is taken as 50pc, following the studies of [Faucher-Giguère and Kaspi, 2006].

Barring a better estimate on the distribution of SNIa remnants, their corresponding distribution in the z-direction is modelled after the population of milli-second pulsars. That is, milli-second pulsars are, much like WDs, possibly very old objects that have diffused away from the galactic plane. Recently, [Lorimer, 2013] published new results for the milli-second pulsar distribution and finds that these objects are distributed like an exponential with a large scale-height of 500pc perpendicular to the galactic plane.

Fig.4.2 shows the probability density that is used in the MC-sampling.

4.2.3. Radial Distribution

Due to the sparse sample of observational SNR distance samples, the radial distribution of SNRs in the galaxy is not well known. In a phenomenological approach, [Case and Bhattacharya, 1998] used the proportionality of surface brightness to diameter (also called $\Sigma - D$ relationship, see e.g. [Clark and Caswell, 1976]

$$\Sigma_\nu = AD^\beta \simeq d^\beta \theta^\beta \qquad (4.2)$$

where A is a proportionality constant, Σ_ν is the surface brightness of the SNR at the frequency ν, in a fit to 37 SNRs for which a fairly precise distance estimate is available. This allowed the authors to constrain the parameters A and β and
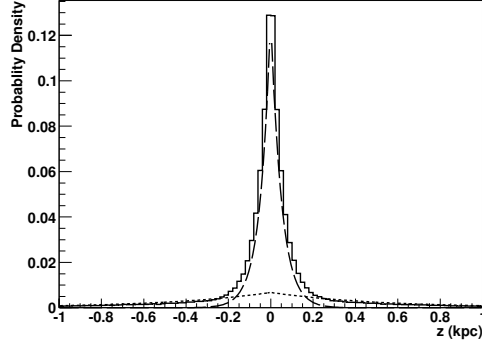
Figure 4.2.: Distribution of SNRs in the z-direction. Overplotted are the distribution functions for SNR of core-collapse(coarse-dashed) and thermonuclear (fine-dashed) origin.

they found

$$\Sigma_{1GHz} = 2.07^{+3.10}_{-1.24} \cdot 10^{-17} \left(\frac{D}{1\text{pc}} \right)^{(-2.38\pm0.26)} \text{Wm}^{-2}\text{Hz}^{-1}\text{sr}^{-1} \qquad (4.3)$$

Using this method, Case and Bhattacharya calculated the distances of the known radio SNRs and fitted the resulting radial distribution with the function

$$f(r) = \left(\frac{r}{r_\odot} \right)^\alpha \exp \left(-\beta \frac{r - r_\odot}{r_\odot} \right), \qquad (4.4)$$

where $r_\odot$ is the distance Sun-Galactic Centre and α and β are fit parameters.

In a recent study, Green investigated the effect of selection effects in the radio observations of SNRs and obtained updated values of α and β [Green, 2012]. To that end, Green selected only bright SNRs ($\Sigma_{1GHz} > 10^{-20}\text{Wm}^{-2}\text{Hz}^{-1}\text{sr}^{-1}$) and compared their distribution in galactic longitude with expected projections of different models describing the radial SNRs distribution. This approach does not require the uncertain $\Sigma - D$ relation. Due to the brightness of the selected SNRs, selection effects in the ensemble of these SNRs should be small.

Fig.4.3 shows the resulting SNR surface density models (solid lines) as well as the original result found by Case and Bhattacharya (dashed).

In the presented work, model (c) will be used. The corresponding fit parameters are $\alpha = 2$ and $\beta = 5.1$.

4.2.4. Source Age

In this simulation an average value of three SN events per galaxy is assumed (see section 3.1.2). Correspondingly, the time between SNe Δt is sampled from a Poisson distribution with a mean value of 33 years. The simulation starts at a time $t = 0$ (the present), and the age t of the $k-$th SNR is therefore given by the sum of the time intervals Δt_i between the preceding SNRs, $t(k) = \sum_i \Delta t_i$.

Figure 4.3.: Surface density models of Case and Bhattacharya (blue-dashed line) and Greens (solid lines) normalised to the peak values. The dashed-red line indicates the position of the sun. Plot is extracted from Greens2012.

4.3. The Interstellar Environment Around Supernova Remnants

This section outlines the environment into which the SNR is embedded . The most important quantities for the purposes of this simulation are the large-scale ISM gas density and magnetic field strength around the SNR as well as the possibly modified local CSM structure. At this point it is mentioned that the CMB is the only radiation field accounted for in the IC-scattering. However, since SNRs are bright and hot, also IR, UV and optical fields are expected to play a role. Future work including the study of IR-,UV- and optical maps might improve this situation.

4.3.1. Ambient Magnetic Field

The model for the galactic magnetic field used here is following the approach of [Jaffe et al., 2010], which is a 2-dimensional model in the galactic plane. In this picture, the magnetic field at a given position consists of three components:

- a large scale coherent field $\mathbf{B}_{coh}$, which follows the galactic spiral structure, along which the field lines are unidirectional.

- a large scale ordered component $\mathbf{B}_{ord}$, which in direction but not in orientation follows the spiral arms. In this case, the field lines are randomly flipped either in or opposite to the arm direction.

- a random component $\mathbf{B}_{iso}$, which does not follow the spiral arm structure at all.

It is not clear whether the magnetic spiral arms exactly follow the matter arms, although the spiral parameters obtained from rotation measurements seem to agree with results from starlight polarisation measurements

([Han and Qiao, 1994], [Heiles, 1996]). Here, the magnetic and matter spiral arm structures are simply assumed to be identical.
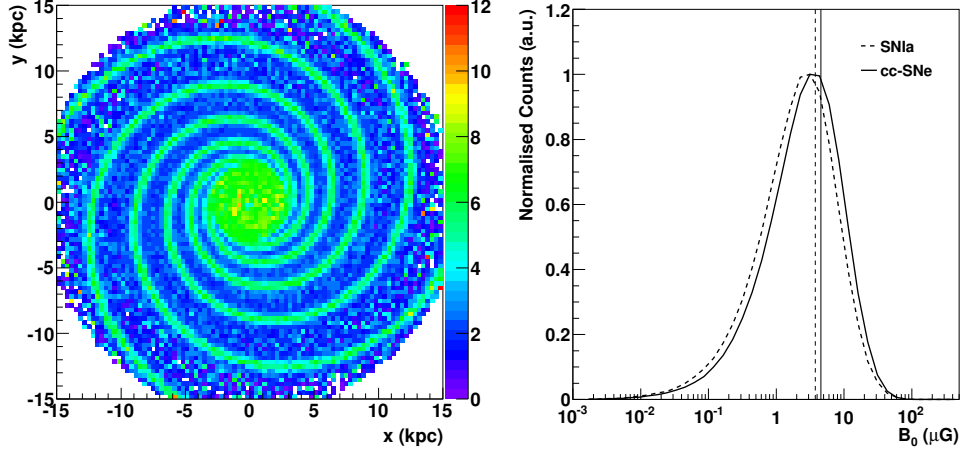
Figure 4.4.: Model for the galactic magnetic field. Left panel: the magnetic field is strongly enhanced in the spiral arms. As a result, SNIa SNRs see on average lower values than their core-collapse colleagues (left panel). The mean mean values are 3.8μG and 4.5μG, respectively.

For the purposes of this simulation, merely the amplitude of the total magnetic field at a given position is required. The corresponding ambient B-Field value is obtained by sampling from an exponential function with scale-height $B_{tot} = abs(\mathbf{B}_{coh} + \mathbf{B}_{iso} + \mathbf{B}_{ord})$. This results in average B-Field strengths of $\sim 3.8\mu$G and $\sim 4.5\mu$G around SNIa and cc-SNe, respectively, see Fig.4.4.

4.3.2. Ambient Gas Density

As a first step in determining the ambient matter profile around a SNR, the large scale ISM gas density at its position has to be modelled.

Here, a crude 3D-model of the galactic molecular and atomic gas density distribution is used that is following the work of [Ferrière, 2001] and which is based on azimuth-averaged radio measurements. This model is described in detail in Apendix A. The resulting density distribution is shown in Fig.4.5. In the left panel, a top-down view on the galaxy of the average ambient density is shown. The right panel shows the total distribution of ambient density values for SNIa (dashed line) and cc-SNRs (solid line).

The latter are distributed around ~ 1cm^{-3} with a sizeable fraction of objects in a quite dense medium of ≥ 10cm^{-3}. SNIa are situated in lower-density environments of on average ~ 0.3cm^{-3}. This is on the one hand due to the broader distribution perpendicular to the galactic plane and on the other because these
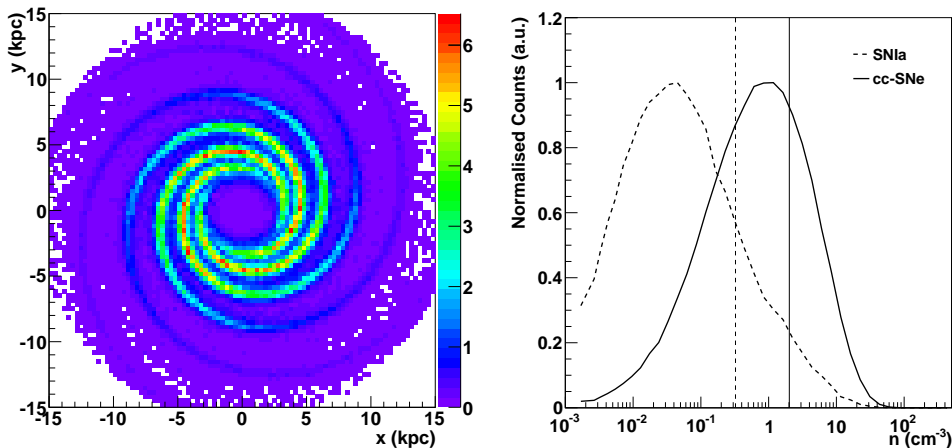
Figure 4.5.: The ISM densities in the galaxy. Left: Top-down view on the galaxy showing average density values. Right: Total distribution of ambient density values as seen by SNIa (dashed line) and cc-SNe (solid line). The corresponding total average values are indicated by the vertical lines.

object are distributed homogeneously in the galactic plane and are thus not following the spiral arms, where the density is higher.

In this simulation, SNIa remnants are assumed to expand into a homogeneous medium of this density.

This is not the case for cc-SN remnants, which are assumed to evolve in a main-sequence stellar bubble and, in all other cases than SNIb/c remnants, also to encounter a red giant wind zone. The corresponding models for both components used in this simulation have been described in section 3.2. The properties of the main-sequence wind are determined by the wind speed and mass luminosity, as well as the progenitor's time of evolution on the main sequence, compare to Eqs.3.2 and 3.3. These quantities are sampled from empirical functions that follow the respective correlations with the progenitor's initial mass. Here, the correlations compiled by [Chen et al., 2013] are taken, see Fig.4.6. The initial mass is sampled from the Salpeter IMF (Eq.3.1) between $8 < M/M_\odot < 100$.

Fig.4.7 shows the resulting distribution of MS bubble extensions. Progenitors of relatively low initial mass are typically surrounded by a stellar bubble of around $\leq$30pc radius. The most massive stars can boast stellar bubbles of more than 100pc radius.

For the red giant wind zone, the typical parameters listed in Tab.3.1 are used, attributed with an ad-hoc Gaussian scatter of 30%.

As a simplification, a uniform medium, comprised of the WR and RGW ejecta, is assumed to fill out the main sequence bubble in the case of SNIb/c rem-
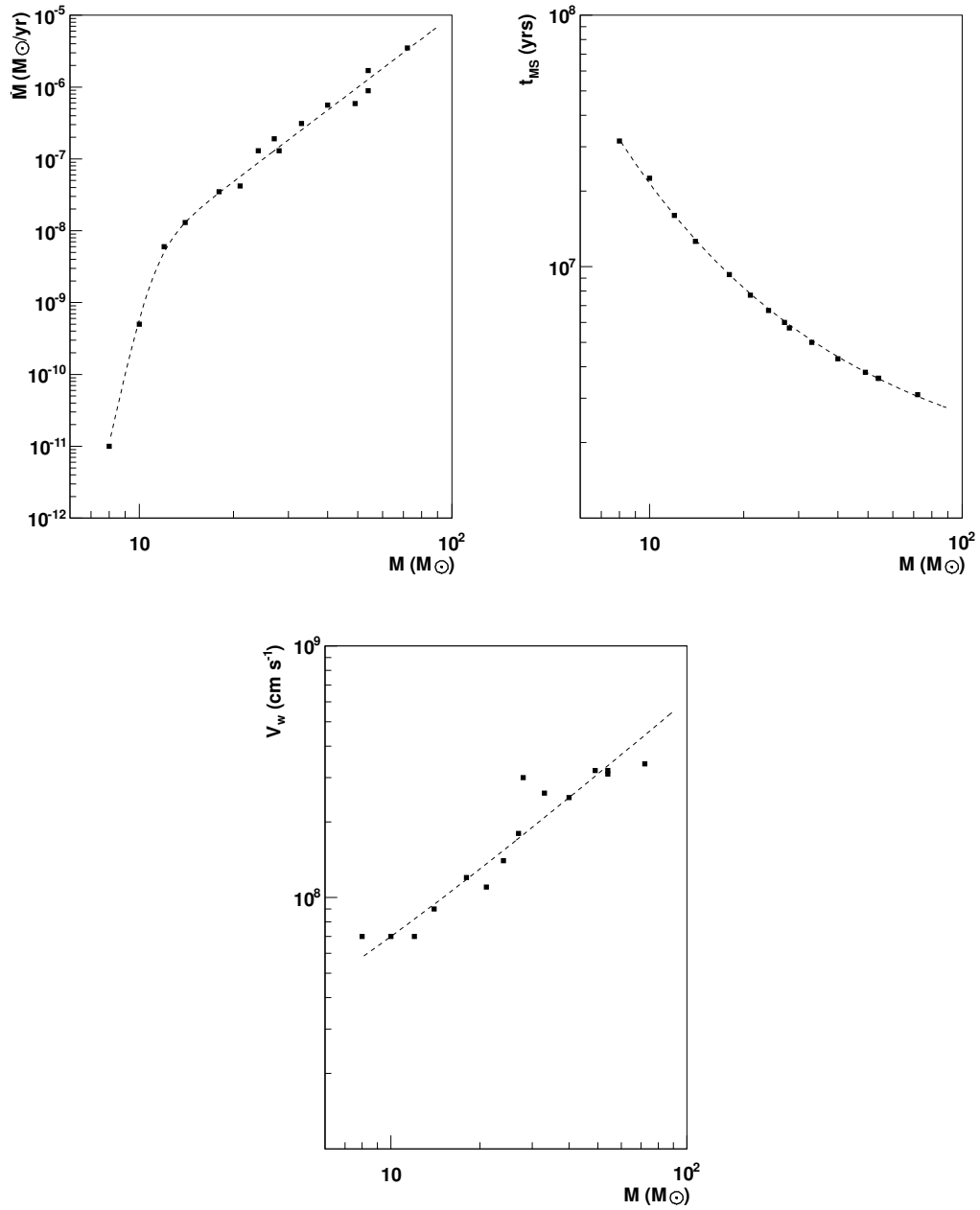
Figure 4.6.: Correlations of the progenitor star initial mass with parameters relevant for the evolution of stellar bubbles. Top left: Mass loss rate, top right: time on the main sequence, bottom: wind speed. The dashed lines represent the functions from which the corresponding values are sampled. The values are taken from [Chen et al., 2013].
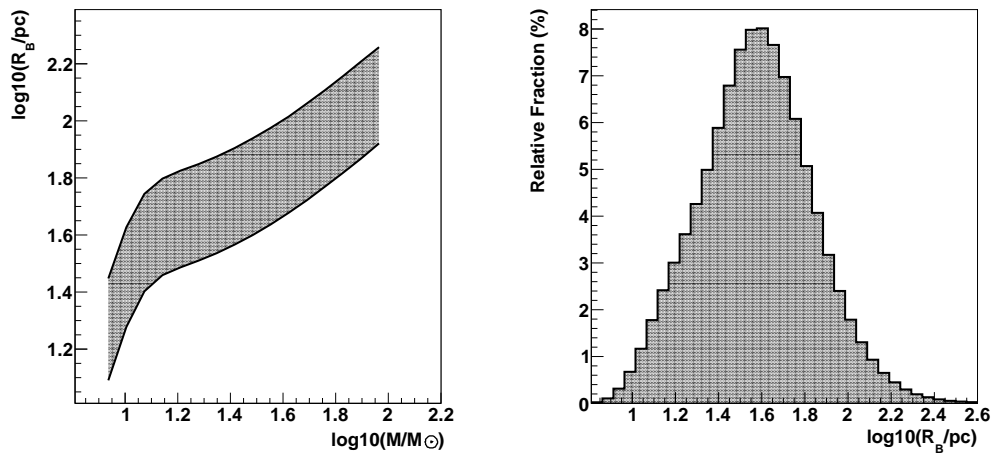
Figure 4.7.: The extension of stellar bubbles. Left panel: Extension as a function of the progenitor star initial mass. The error bands indicate one standard deviation. Right panel: Total size distribution of the stellar bubbles as implemented in this simulation. The mean is at ~38pc.

nants. This approximates the turbulent mixing of stellar wind material in the bubble, see Fig.3.2. Wolf-Rayet stars end their lives with masses of M_{Ej} ~4-6$M_\odot$ [Woosley et al., 1993], and the mass difference M_I - M_w - M_{Ej} is used to estimate the homogeneous density in the WR/MS bubble.
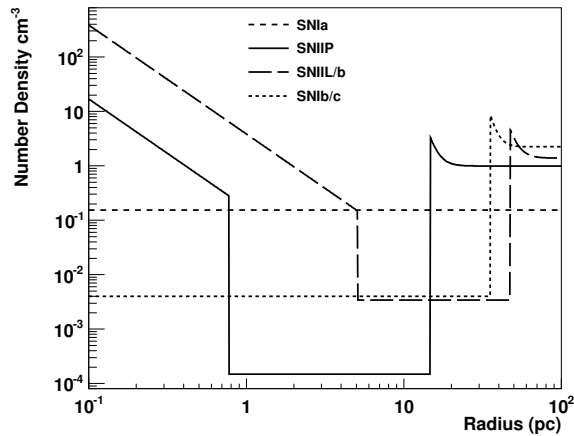
Figure 4.8.: Example density profiles around the four different SNR types that are assumed in this model.

Fig.4.8 shows typical model density profiles for the four different SNR subtypes. Thus number shows the gas number densities. In order to account for

heavier nuclei in the ISM, the mean mass per gas nucleus is assumed to be $1.4m_p$ which is a common assumption, see e.g. [Ptuskin and Zirakashvili, 2005].

4.4. Modeling the Shock Dynamics

In this work, non-uniform density profiles of the ambient medium are assumed (see Fig.4.8) for cc-SNe. While Truelove and McKee's solutions (see section 3.3.1) are applicable in all stages of remnants of SNIa (where a homogeneous ambient medium is assumed), it might hold only in the ED phase in all other scenarios. That is, at later times the shock experiences the step in ambient density when hitting the stellar bubble edge.

In these cases, following the approach of [Ptuskin and Zirakashvili, 2005], the ED phase solutions found by Truelove & McKee are coupled to the ST solutions from the Thin-Shell approximation (see section 3.3.2).

4.4.1. The Dynamics of SNIa

The dynamics of SNIa, as implemented in this model, represents the simplest case of all the considered SN-types in this work, because the ambient gas is assumed to be homogeneous. This means that the solution of Truelove and McKee can be applied during the whole non-radiative phase and the shock dynamics are modelled using Eqs.3.7 - Eqs.3.10. The SN ejecta density index is set to $n = 7$, see 3.3.1.

Fig.4.9 shows the dynamical evolution for typical specimen of the four SNR types as a function of its radius.

In the early time of the ED-phase at times $\leq$100yrs, the shock moves at high velocities v_s >100kms^{-1}. The radius and velocity evolve as $R_s \sim t^{4/7}$ and $v_s \sim t^{-3/7}$, compare to Eqs.3.9-3.10.

The time of the transition to the ST phase is given by Eq.3.6 and t_{st} from Tab.3.2. For the set of parameters ($E =10^{51}$erg,$\rho =0.12$cm^{-3}, $M_{ej} = 1.4M_\odot$), this happens after ~950yrs. Thereafter the SNR blast waves continues its evolution as $R_s \sim t^{2/5}$ and $v_s \sim t^{-3/5}$ following Eqs.3.7-3.8.

4.4.2. The Dynamics of SNIIP

SNe of type IIP expand into a hot, rarified stellar bubble that has been created during the main-sequence evolution of the progenitor star. Also, a RGW zone is present but is omitted for a technical reason in the treatment of the source dynamics.

Of all SN types treated in this work, SNIIP have the largest ejecta mass since due to the relatively moderate mass-loss rate of the progenitor RSG the H-envelope is still mainly intact. A typical value of the ejecta mass is 8M$_\odot$ (see also Tab.3.1). As a result, in this case a larger amount of CSM than for all other
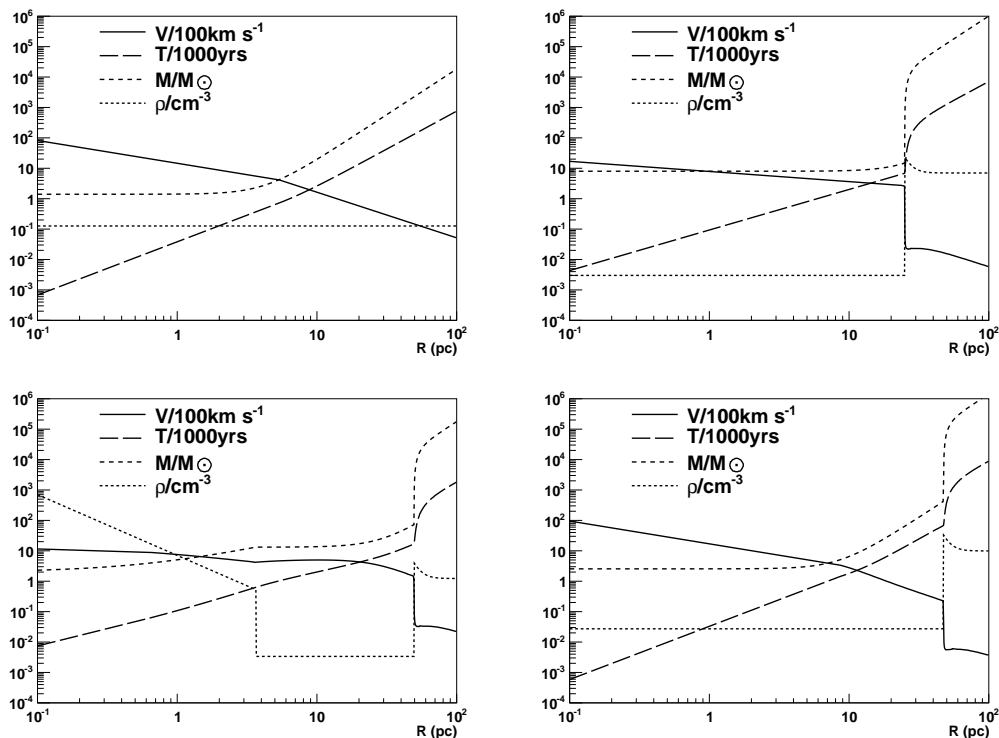
Figure 4.9.: Dynamical evolution of a typical examples of the four different remnant types.

SN types has to be swept up in order to trigger the onset of the Sedov-Taylor phase. In practical terms this means that the SNR blast wave is still in the ED-phase when the transition from the RGW zone to the stellar bubble occurs. However, such transitions are not covered by Truelove and McKee's solution and thus, the RGW zone is neglected in the treatment of the SNR dynamical evolution[1] in this work.

This simplification has only a minor impact on the expected gamma ray brightness since the typical RGW extension is ≤ 1pc and the density is moderate. Such RGW zones are traversed by the blast at times < 100yrs, which means that on average 1.8 SNRs per simulated galaxy feature a SNIIP SNR still inside the RGZ.

However, neglecting the RGZ has a non-negligible effect on the dynamics of the blast wave. That is,the presence of a RGW zone (blue lines in Fig.4.10) leads to a faster deceleration of the blast wave than it would be the case if the shock expands into a uniform, thin medium (black lines in Fig.4.10). The velocities in both cases converge within 1kyr and already after ~ 300 yrs the values are within $\sim 15\%$. This means that by omitting the presence of a compact RGZ, the

---

[1]A similar approach was chosen by [Ptuskin et al., 2010] who omitted the RGW zone for SNIIP.

bulk of all SNIIP SNRs show an extension and speed that would be expected from a $\sim 300\text{yrs}$ older source. Note that in a strict sense, this comparison is not valid. Truelove and McKee cannot handle the transition from RGZ to rarified bubble and thus the blue lines have to be taken with a grain of salt. That is, they are overestimating the effect since they assume a RGZ at times when the shock has already left it ($\geq$100yrs).
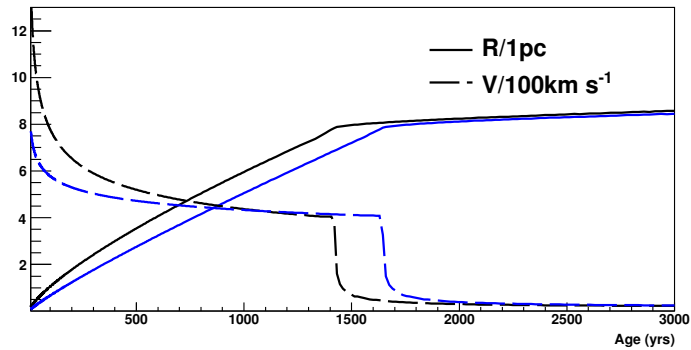
Figure 4.10.: Effect of neglecting the RGW zone in SNIIP on the blast wave dynamics. Black: without RGW zone, blue: with RGW zone.

These sources are assumed to have SN ejecta structure indices of $n = 12$ and the ED phase during the expansion into the main-sequence bubble is modelled using Eqs.3.10 and 3.9. In this phase, the shock radius and speed go as $R_s \sim t^{3/4}$ and $v_s \sim t^{-1/4}$. Here, it encounters a low-density environment and the blast waves only very slowly sweeps up mass (medium-dashed line in top-right panel of Fig.4.9). As a result, the blast wave is typically still in the ED-phase when it hits the inner edge of the stellar bubble, which poses a problem since, as already pointed out, Truelove&McKees solution does not cover steps in the ambient density profile. Instead, the Thin-Shell approximation is applied just before the shock collides with the bubble shell, using Eqs.3.13 and 3.13. Upon exiting the cavity, the blast wave sweeps up a large mass almost instantly. The latter exceeds the SN ejecta mass very quickly and so this treatment of the transition out of the stellar bubble is an acceptable approximation [2].

The collision with the ISM slows the blast wave down by one to two orders of magnitude and the shock practically stagnates.

4.4.3. The Dynamics of SNIIL/b

Blast waves from SNIIL/b events expand into the most complex environments of this simulation. The progenitors of these SNe possess RG dense winds that extend out to several pc from the star. It has shed most of its H-envelope by these winds and is thus reduced to masses of only 4-5M$_\odot$ [Smartt et al., 2009]

---

[2]Note that this solution is strictly valid only in the ST phase.

at the time of the SN explosion. As a result, the ejecta mass is typically on the order of 1-2$M_\odot$ [Ptuskin et al., 2010].

In contrast to SNIIP, both the larger radius and higher density of the RGW as well as the lower SN ejecta mass trigger the onset of the ST-phase while the blast wave is still in the RGZ. Prior to that point, the shock evolution follows the ED-solution with an density index of $n = 10$ [Ptuskin and Zirakashvili, 2005]. The evolution in this initial phase is following the self-similar solution found by [Chevalier, 1982b] and [Nadezhin, 1985] (this treatment follows the approach in [Ptuskin and Zirakashvili, 2005]). It then transitions into the Sedov-Taylor phase and is modelled by the thin shell approximation because of the non-uniform transition from the RGZ to the rarified bubble.

After this transition, the velocity increases slightly, connected to the density contrast between RGZ and stellar bubble.

Much like in the case of SNIIP, the shock brakes down when it hits the stellar bubble edge. However, since on average the main sequence bubble size increases with the initial mass of the progenitor (see Fig.4.7, an increased amount of material has been piled up in front of the bubble. Therefore, the deceleration at the bubble edge is typically more pronounced than in the case of SNIIP SNRs.

4.4.4. The Dynamics of SNIb/c

Blast waves from SNIb/c are treated similarly to those of SNIIPs in that the shock first expands into a uniform and dilute CSM and then hits the stellar bubble. The major difference to SNIIP in this model are the typically larger extensions of the stellar bubbles, so SNIb/c remnants can become more extended and spend a longer time in this rarified environment.

4.5. Spectral Modeling

With the knowledge of forward shock velocity and radius as well as the ambient gas density and magnetic field, it is possible to model the particle- and subsequently gamma-ray spectra of SNRs.

The former is based on the solution Eq.3.21. However, in order to allow for a more realistic treatment of particle acceleration by including effects arising in modified shocks, in this work an approach is chosen that follows the spectral modelling presented by [Ptuskin and Zirakashvili, 2005], and the exponential escape term in Eq.3.21 is replaced by a theta function

$$N(E,t) = \frac{\theta(E - E_{max}(t))}{P(E)} \int_0^t dt_0 P(\varepsilon_{t_0}) Q(\varepsilon_{t_0}, t_0) \theta(E - E_{max,t_0}), \qquad (4.5)$$

where E_{max} is the maximum particle energy following from Eq.3.22. This implies a simplified picture where particles which the SNR cannot contain leave the system immediately.

The source term in Eq.3.21 is assumed to be power-law shaped, $Q(E,t) = Q_0 E^{-\Gamma}$, and the normalisation is determined from the assumption that a certain fraction Θ of the momentum flux entering the shock is transferred to CR pressure. Thus, the normalisation of the source term is given by the equation

$$Q_0 \int_{E_0}^{E_{max}} dEEE^{-\Gamma} = \Theta L_{mech} = 2\pi \Theta \rho R^2 v^3, \tag{4.6}$$

where E_0 is the rest mass of the respective particles, $L_{mech} = \dot{M}v^2$ is the mechanical luminosity of the blast wave and ρ is the ambient density. A small fraction of L_{mech} goes into the acceleration of electrons. This fraction is referred to as the electron-to-proton fraction K_{ep}. Assuming that electrons are accelerated in the same manner as protons, the shape and normalisation of the corresponding source term is determined analogously. As the only difference, ΘL_{mech} is replaced by $K_{ep}\Theta L_{mech}$ in Eq.4.6.

4.5.1. Energy Losses

Four different types of energy loss mechanisms are implemented in the model: The radiative losses due to the Bremstrahlung (P_{Brems}), inverse-Compton (P_{IC}) and synchrotron (P_{Synch}) processes (see section 3.5) as well as adiabatic losses (P_{Ad}). The latter result from the fact that during the shock expansion, the relativistic gas exerts a pressure on the ambient material and therefore loses energy adiabatically. This results in an energy loss rate that is determined by the shock dynamics and goes as [Atoyan and Aharonian, 1999]

$$P_{Ad} = \left(\frac{v_s}{R}\right) E. \tag{4.7}$$

Because of their high rest mass, protons suffer only mildly from radiative processes in typical SNR environments. Also the amount of cooling by inelastic p-p scattering is negligible. Therefore, protons are assumed to lose energy only by adiabatic cooling.

The situation is different for electrons. Here, all cooling mechanisms[3] are considered. Since $P_{Ad}, P_{Brems} \sim E$ and $P_{IC}, P_{Synch} \sim E^2$, as well as in SNRs typically $P_{Ad} > P_{Brems}$ and $P_{Synch} > P_{IC}$, adiabatic cooling is practically always the dominant energy loss mechanism for low-energy electrons. At high energies, synchrotron losses are most severe.

Eq.4.5 is strictly valid only for time-independent losses. However, the potentially complex ambient density profile, a possible magnetic field amplification (see the next section) and the time dependency of the adiabatic loss coefficient lead to a time-dependent energy loss rate. In order to cope with this situation, the solution Eq.4.5 is approximated by assuming quasi-stationarity, i.e. by dividing it in time intervals that are much smaller than the characteristic time scale on which the loss rate changes, $\Delta t \ll \dot{E}(t)/\ddot{E}(t)$.

---

[3]Here, losses due to the inverse-Compton process are assumed to be always in the Thomson limit, see section 3.5.

4.5.2. The Maximum Particle Energy and Magnetic Field Amplification

It is theorised that the accelerated particles themselves amplify their own acceleration. That is, the CR precursor causes a streaming instability ahead of the shock, which results in turbulence. This turbulence in turn generates strong random magnetic fields δB. Magnetic field amplification has important consequences for the VHE emission from SNRs.

Firstly, the diffusion at the acceleration site slows down since the diffusion coefficient in the case of Bohm diffusion goes as $D \sim B^{-1}$. As already mentioned, the ability to keep the particles in the shock determines the maximum energy to which they can be accelerated and is connected to the diffusion speed (see Eq.3.22). Thus, magnetic field amplification allows for a particle acceleration to higher energies compared to a classical shock.

Secondly, Synchrotron losses are increased and cool away high-energy electrons more efficiently. This effect can strongly suppress the leptonic VHE emission from SNRs in the presence of magnetic field amplification.

Here, the theoretical approach of [Ptuskin and Zirakashvili, 2005] on the B-Field amplification is adapted. The resulting diffusion coefficient is approximated by the authors as

$$D = \frac{(1 + A^2)^{1/2}}{3A^2} v_p r_g, \tag{4.8}$$

assuming that particles exceeding the maximum energy leave the SNR rapidly. In Eq.4.8, B_0 is the unamplified magnetic field strength and $v_p = c$ is the particle velocity. The amplification factor A is defined through the amplitude of the random magnetic field $\delta B = AB_0 = \int dk W(k)$, where $W(k)$ is the energy density of turbulences with wave number k. Thus, compared to the classical Bohm limit ($D = v_p r_g / 3$), the diffusion coefficient is decreased by a factor of $(1 + A^2)^{1/2}/A^2$ which goes as $\sim 1/A$ if $A \gg 1$.

Together with Eq.3.22, this results in a maximum energy of

$$E_{max} = \frac{\kappa A^2 v R m c^2}{(1 + A^2)^{1/2} v_p r_g}. \tag{4.9}$$

The derivation of A is complex and will not be presented here. For a detailed description see [Ptuskin and Zirakashvili, 2003]. It is merely stated that the random magnetic field amplitude and therefore the turbulence energy density $W(k)$ is determined by three mechanisms:

- The streaming instability caused by the CRs that creates the turbulences in the first place.

- The damping of the turbulences due to ion-neutral collisions in a partially ionised gas.

- The damping of the turbulences due to the interaction of Alfvén waves with thermal particles.
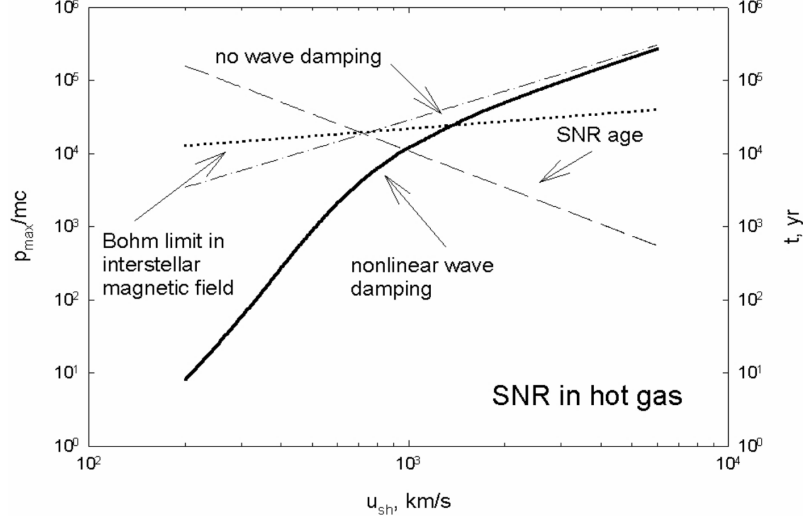
Figure 4.11.: Maximum particle momentum as a function of shock speed. Plot extracted from [Ptuskin and Zirakashvili, 2003].

Fig.4.11 shows the relation of maximum particle energy with shock speed. At high shock velocities (i.e. at young SNR ages), the maximum energy significantly exceeds the value that would be expected for Bohm diffusion in the interstellar magnetic field. Protons may be accelerated to PeV energies and higher at shock speeds $v > 10^4$km/s. The shock decelerates with time and the wave damping of the turbulences leads to a decrease in maximum energy. In fact, the value drops below that resulting from classical Bohm diffusion. Hence, this theory indicates that the diffusion away from the shock is overestimated by a pure Bohm diffusion at early SNR ages and underestimated for older SNRs. It is able to naturally explain several observational facts, namely the high magnetic field strengths observed in X-ray filaments of young SNRs such as Cassiopeia A [Patnaude and Fesen, 2009] and the fact that VHE emission from SNRs has been observed so far only in young to middle-aged sources. Furthermore, it supports the paradigm of SNRs being the main sources of galactic CRs up to PeV energies.

The treatment of the maximal particle energy requires additional considerations in the case of electrons. That is, electrons suffer strongly from radiative (i.e. mainly synchrotron) losses and the maximum energy for this CR species is therefore the result of a competition between acceleration and loss rates. [Zirakashvili and Aharonian, 2007] find the expression

$$E_{max,e} = (1 + k^{1/2})^{-1} \frac{m_e^2 c^3 v_s (\sigma - 1)}{3\sigma \sqrt{2\eta q^3 B/27}}, \tag{4.10}$$

where $k = (B_0 + \delta B)/B_0$, B is the total magnetic field strength, q is the elemental charge, $\eta = 1$ is a model parameter and σ is the compression ratio of the shock[4].

In the case $E_{max,e} < E_{max}$, the electron injection spectrum follows a power-law with a super-exponential cut-off, $Q(E)_e = Q_{0.e}E^{-\alpha}\exp(-E^2/E_{max,e}^2)$.

Both modified (CRs modify the shock) and unmodified (corresponding to the classical test-particle approximation) shocks are included in this simulation. As already discussed in section 3.4.1, the unmodified shock features a compression ratio of $\sigma = 4$ and thus the magnetic field strength is σB_0 downstream. In this scenario, the maximal energy of the accelerated particles is given by Eqs.3.22 and 4.10. The modified shock is assumed to have a larger compression ratio of $\sigma = 6$, resulting in downstream values magnetic field values of $B = \sigma A B_0$. Here the maximal energy is given by Eqs.4.9 and 4.10.

4.5.3. Resulting Particle Spectra

Figs.4.12-4.15 show the spectral evolution of protons (top panel) and electrons (middle panel) in typical SNIa and SNIIP remnants.

The underlying calculations are discussed in Appendix A.

In the bottom panels the time evolutions of $\dot{E} \equiv \Theta L_{mech}$, E_{max}, B as well as the ambient particle density ρ are displayed. The spectra are shown for five points in time during the SNR evolution, indicated by the colored vertical lines in the bottom panel.

The modified shock solution with B-field amplification are shown in Figs.4.12 and 4.14, while Figs.4.13 and 4.15 display the solutions for the same objects but without B-field amplification (unmodified shock).

SNIa

Figs.4.12 and 4.13 show the spectral particle evolution for a SNIa remnant.

- *Protons*

The proton distributions are straight power-laws in the modified shock scenario, with a sharp cut-off at E_{max}. Some bending at the high ends of the distributions due to adiabatic cooling can be observed. Initially, the normalisation increases rapidly due to the almost constant behaviour of $\dot{E}$ (going as $\sim t^{-1/7}$ in the ED phase for a density index of n=7) but stagnates at later times when the SNR transitions into the adiabatic stage and $\dot{E}$ declines as t^{-1}. While reaching PeV energies at an age of 100yrs, E_{max} quickly decreases at later stages and drops below the corresponding values in the unmodified shock scenario.

In contrast, proton energies do not exceed several tens of TeV in the unmodified shock scenario. The spectra are not as sharply cut-off as in the previous case but rather rounded because E_{max} initially actually increases as $\sim$

---

[4]It should be noted that together with the gas, also the magnetic field is compressed downstream where it is enhanced by this factor.

$t^{1/7}$ which 'stretches' the particle spectrum somewhat towards higher energies. E_{max} reaches its maximum value at the transition to the adiabatic phase after which it decreases slowly as $\sim t^{-1/5}$.

- *Electrons*

The magnetic field amplification has a strong impact on the electron spectra in young SNR, as can be seen in the middle panel of Fig.4.12. At an age of 100yrs, the electron population above 100GeV is strongly depleted by the enhanced synchrotron radiation in an amplified magnetic field and the spectral shape is steepened. As the remnant gets older, the B-field assumes the (compressed) ISM value and the steepening is shifted to higher energies[5]. However, this break is washed out by the additional adiabatic cooling as well as a non-constant particle injection.

As the synchrotron cooling is initially much weaker in unmodified shocks, electrons reach higher energies at young SNR ages in this scenario ($\sim$100TeV) and their spectra do not show the pronounced spectral steepening that is observed in the modified shock solution.

SNIIP

Figs.4.14 and 4.15 show the analogous plot for a SNIIP remnant. There are some additional features in the particle spectra:

Firstly, both protons and electrons show bumps shortly after the shock exits the RGW zone. This bump is constituted by accelerated RGW material which has been cooled down to lower energies. Because electrons cool much faster in the modified shock scenario, this feature is more pronounced in this case.

Secondly, connected to the deceleration of the shock, the maximum energy decreases very rapidly once the shock hits the shell of the main-sequence bubble. In the classical shock scenario E_{max} reaches its maximum value of 200TeV just before hitting the bubble shell. Upon colliding with this structure, E_{max} quickly decreases. However, here it stabilises at a relatively high value of $\sim$10TeV. This means that in this scenario the SNR is able to emit VHE radiation even after exiting the main-sequence bubble. At the same time, the amplitude of the accelerated particle spectra jumps upwards as the ambient particle density is $\sim$10cm^{-3} just outside the bubble. In the modified shock scenario, the situation is quite different. The maximum particle energy has already dropped to about 100TeV prior to the collision of the SNR shock with the main sequence bubble shell. After the collision, E_{max} is drastically reduced by many orders of magnitude which is why only four lines are visible in the top and middle panels of Fig.4.14.

---

[5]The energy of the spectral transition is $E_{break} \propto (B^2 \cdot t)^{-1}$.
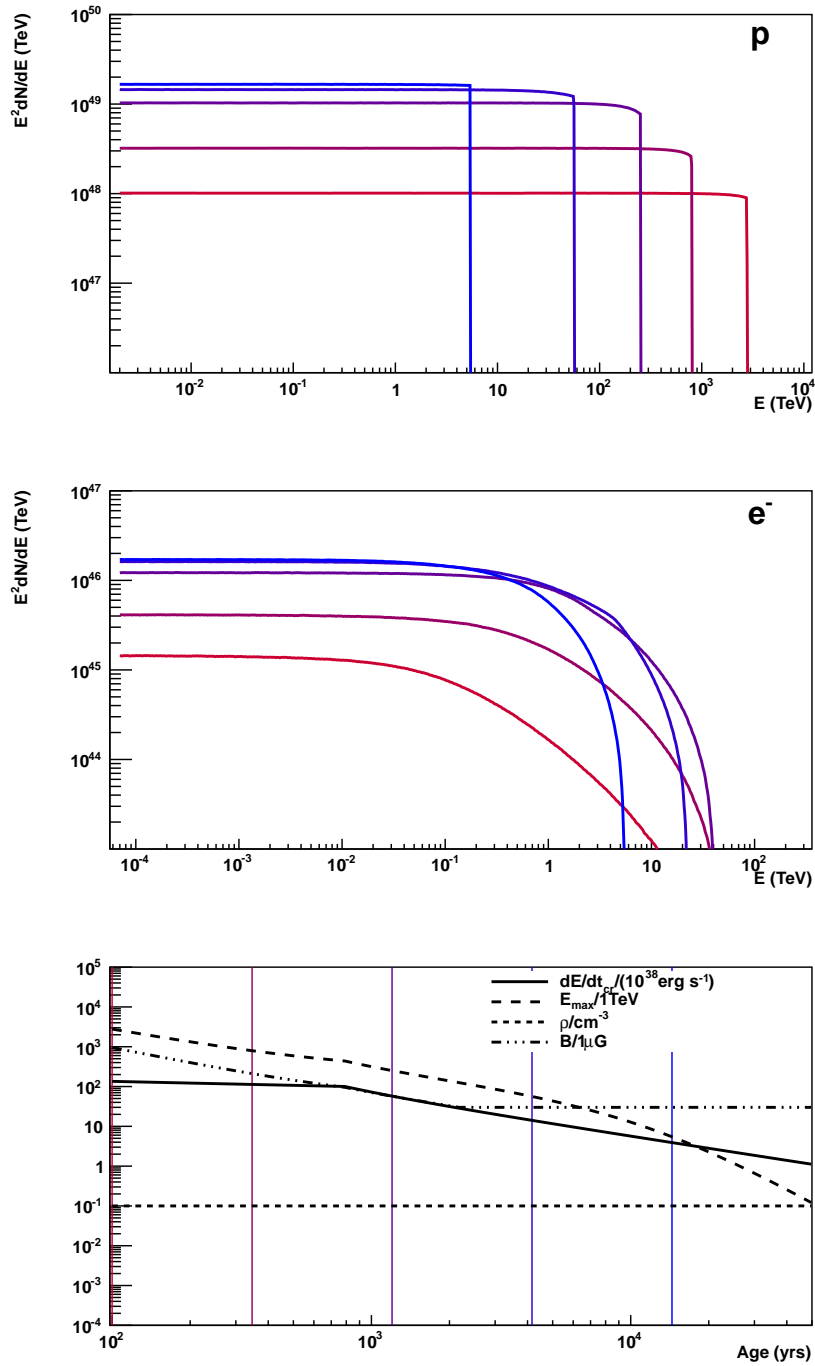
Figure 4.12.: Evolution of proton (top) and electron (middle) spectra of a typical SNIa remnant in the presence of B-field amplification. The spectra are shown for five points in the SNR's life, indicated by the vertical lines in the bottom panel, where also the temporal evolution of important parameters is shown.
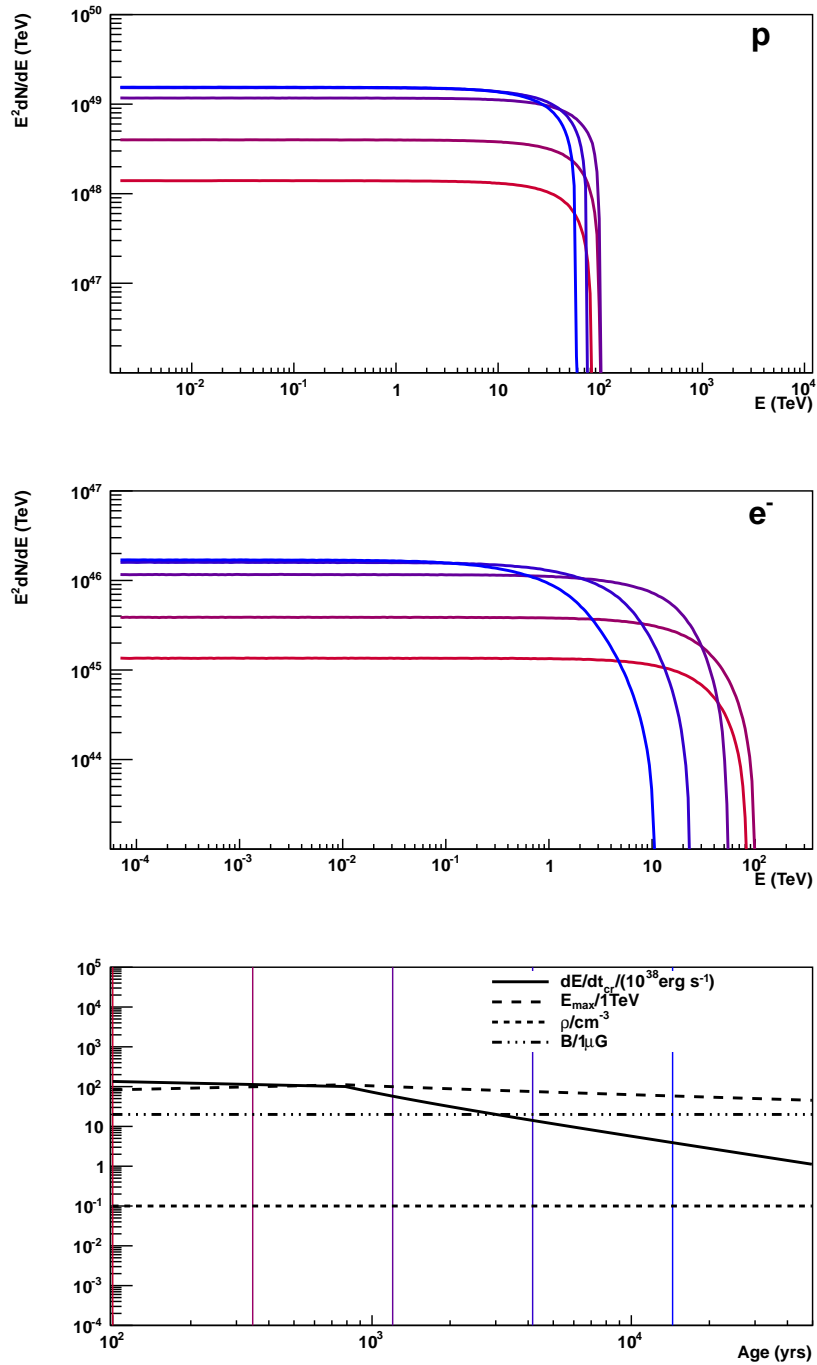
Figure 4.13.: Same plot as in Fig.4.12, but here without B-field amplification.
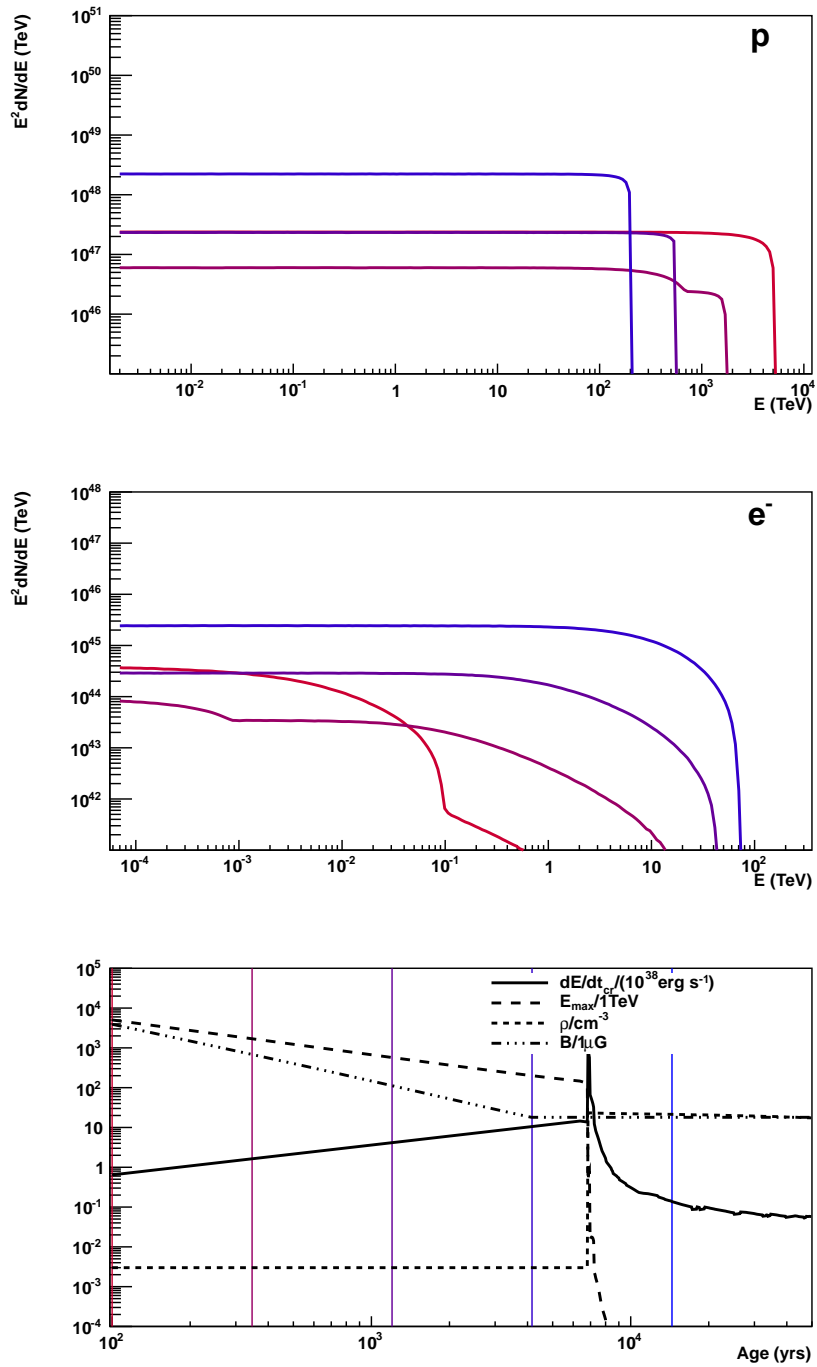
Figure 4.14.: Same as in Fig.4.12, but in this case for a typical SNIIP remnant.
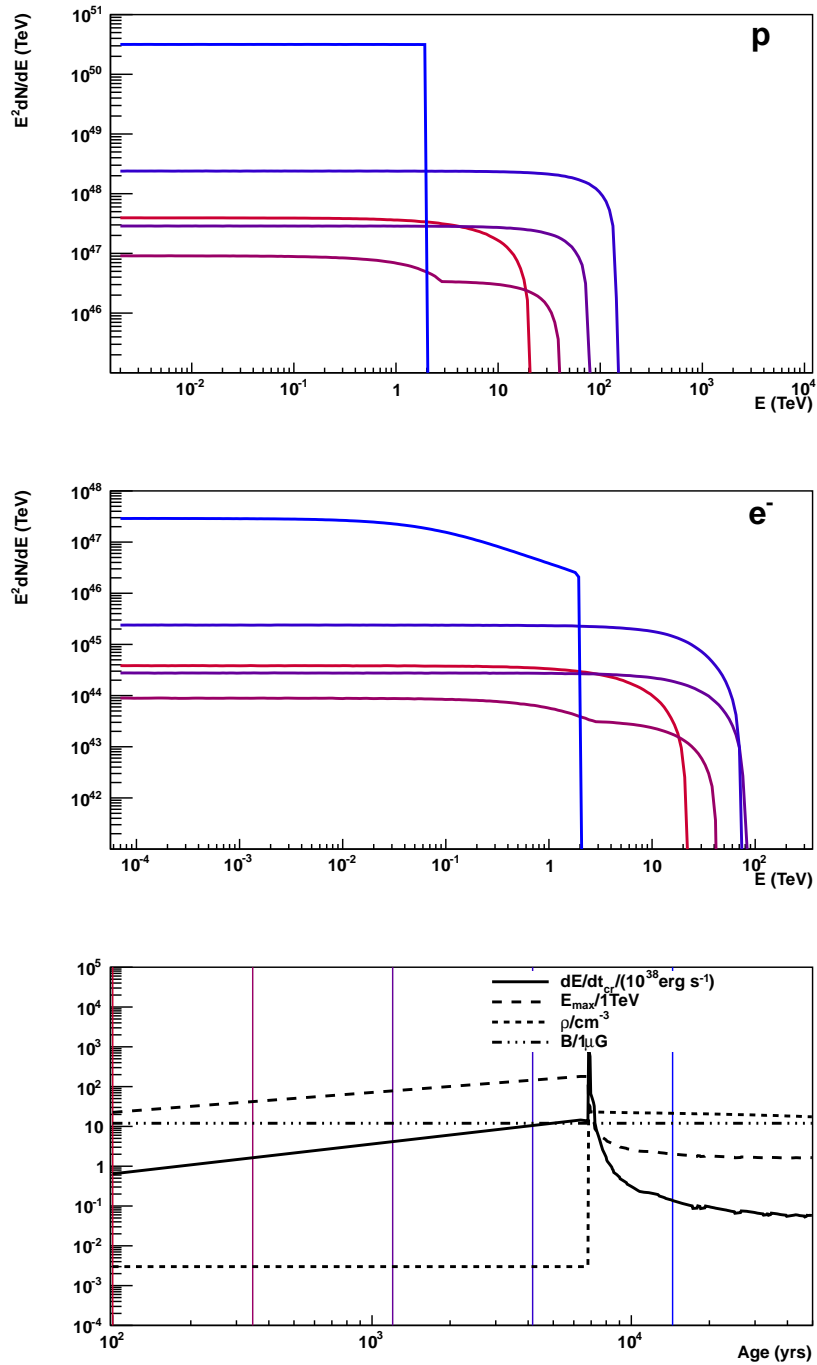
Figure 4.15.: Same as in Fig.4.14, but here without B-field amplification.

4.5.4. Resulting Photon Spectra

Once the particle distributions are calculated, the spectra for π^0-decay, IC, Bremsstrahlung and Synchrotron radiation can be derived (see chapter 3.5). The SED time evolution of the two exemplary SNRs presented in the previous section are shown in Figs.4.16 and 4.17.

Again, the underlying calculations are discussed in Appendix A.

The effect of the magnetic field amplification on the SED is drastic, as can be seen in both cases, and the following observations can be made:

- *With B-field amplification*
  The IC-emission is suppressed completely in young SNRs and thus, the VHE emission is predicted to be strongly hadronic-dominated. At the same time, the Radio and X-ray emission is enhanced. As the SNR gets older, the value of E_{max} decreases together with the B-Field amplification and, if the surrounding medium is not too dense, IC-emission can become dominant. In the early SNR phases, the spectral cut-off in the gamma-ray spectra is at energies $E >$100TeV. The gamma-ray emission from SNIIP is quenched upon hitting the stellar bubble, corresponding to the rapid drop in the maximum energy of the accelerated particles (see previous section).

- *Without B-field amplification*
  Here, the VHE emission is dominated by IC-radiation. Hadronic-dominated emission in this scenario requires high values of the circumstellar magnetic field (here, 5μG are assumed) and a very low electron-to-proton fraction (the value here is $K_{ep} =$10^{-3}). The spectral cut-off in the gamma-ray spectra even at young SNR ages does not exceed several tens of TeV. After colliding with the main-sequence bubble shell the gamma-ray brightness is strongly enhanced (see the deviating line in Fig.4.17). If this acceleration model were correct, the VHE sky would be full of bright, soft-spectrum SNRs

In view of the observed low magnetic field strengths in the ISM and the high values directly at the shock, as well as the fact that only a couple of shell-type SNRs have been observed at VHE so far, the modified shock scenario seems to yield more realistic results. It will be therefore regarded as the default model in the following discussions.

The spectral shape around 1TeV evolves quite differently for the two exemplary remnants:

- For the SNIa remnant, leptonic emission plays no role during the first several hundred to thousand years and as the π^0-decay energy cut-off shifts towards lower energies over time, the gamma-ray spectrum softens at $E=$1TeV.
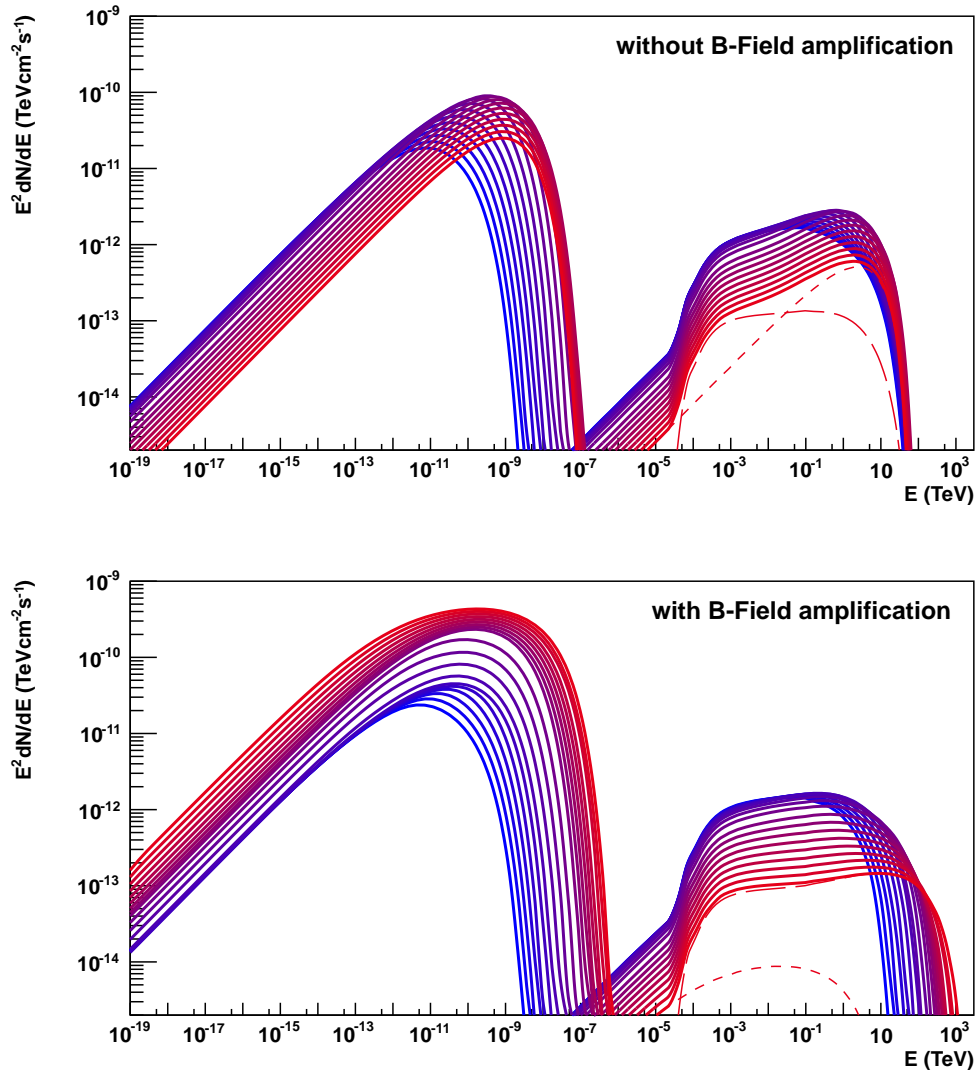
Figure 4.16.: SED time evolution of the SNR described in Fig.4.12 with (bottom) and without magnetic field amplification (top). The displayed evolution spans the time from 100yrs (red) to 10kyrs (blue). The dashed line show the IC-radiation (fine) and π^0-decay contributions for the earliest SED.
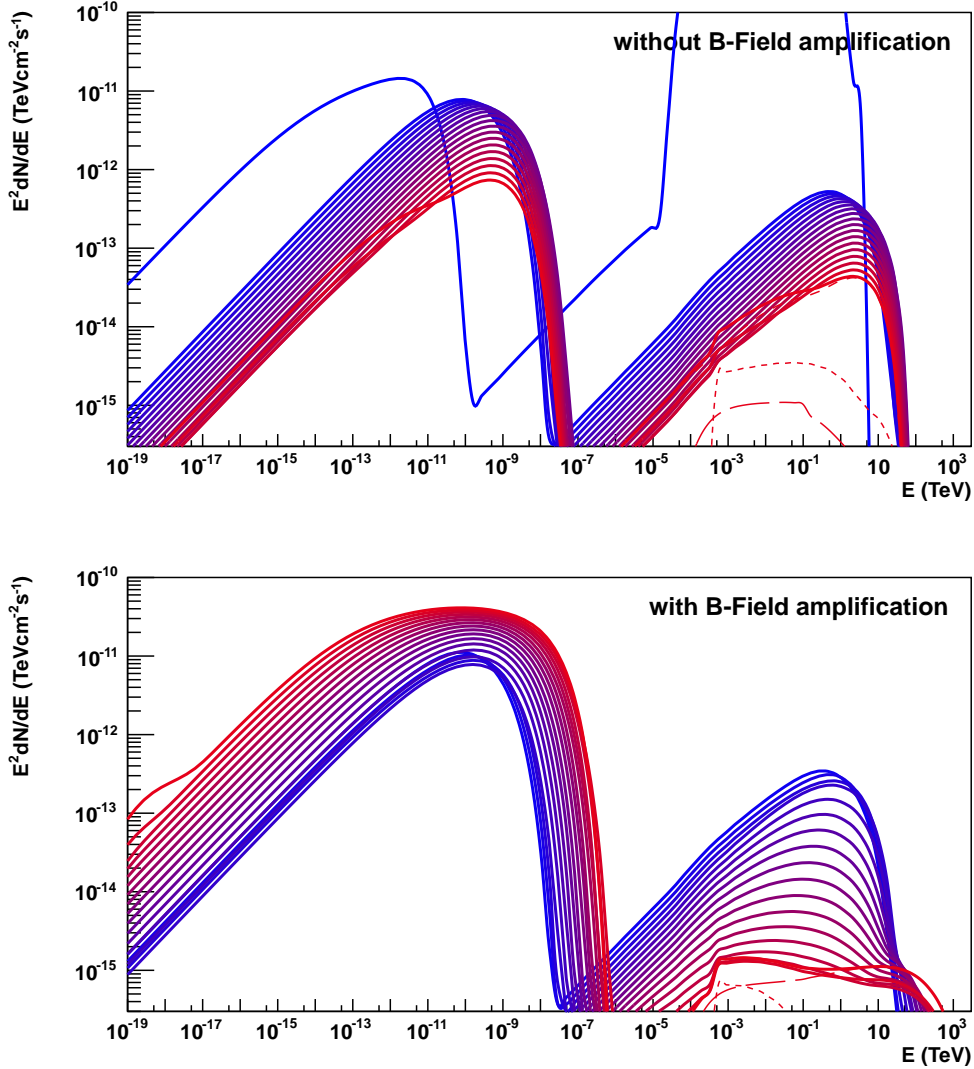
Figure 4.17.: SED time evolution of the SNR described in Fig.4.14 with (bottom) and without magnetic field amplification (top). The displayed evolution spans the time from 100yrs (red) to 10kyrs (blue). The dashed line show the Bremsstrahlung (very fine), IC-radiation (fine) and π^0-decay (coarse) contributions for the earliest SED. Note that Bremsstrahlung is only modelled to a lower boundary of $700 m_e$. The deviating line in the top panel is the result of the shock's collision with the main sequence bubble shell leading to an unrealistic scenario in the classical shock scenario, see text.

- In contrast, the presented SNIIP remnant shows a spectral hardening with time at the same energy. That is, since the medium in the main-sequence bubble is rarified, the IC component overtakes the π^0 emission after a few hundred years. Thus, at later times the remnant shows a hard, leptonic-dominated VHE emission at E=1TeV.

The spectral SNR model that has been presented in this section is indeed able to describe multi-wavelength measurements from radio to VHE energies while reproducing realistic values of observed parameters such as SNR radius, shock speed and local magnetic field strength. In Appendix A, one can find the modeling of the spectral energy distributions (SED) of four historic SNRs.

4.5.5. Electron-to-Proton Fraction and Acceleration Efficiency

Two critical parameters have been only poorly constrained so far, namely the acceleration efficiency θ and the electron-to-proton fraction K_{ep}. Both quantities are not well known; estimates on θ extend from modest values of 10% (e.g. [Caprioli, 2011]) to numbers as high as 50% (e.g. [Ptuskin and Zirakashvili, 2005]) in strongly modified shocks. The situation is similar for the electron-to-proton fraction in SNR shocks, where in the literature one can find values of K_{ep} in the range[6] of 10^{-5} to $\geq 10^{-2}$ (e.g. [Acciari et al., 2011]).

In the following, results from radio observations will be used in the attempt to constrain these two parameters, because they determine the radio brightness of SNRs. In radio, a complete coverage of the galaxy is reached at a surface brightness of $\Sigma(1\text{GHz}) > 10^{-21}\text{Wm}^{-2}\text{sr}^{-1}\text{Hz}^{-1}$ [Green, 2009] which is well above the sensitivity of current radio telescopes. The corresponding distribution of observed radio brightnesses can thus be used to fix a meaningful range of the two parameters K_{ep} and θ.

The remaining parameter space is considerable due to the rather large amount of model assumptions made in this simulation. Here, whenever possible, these parameters will be fixed to the typical values that have been found by the authors of the respective model component and which were already presented in the corresponding subsections of this chapter or chapter 3.

There is some degeneracy between K_{ep} and θ with respect to the radio surface brightness, and the following three models are defined, all of which are able to describe the corresponding distribution for shell-type SNRs that is given by the Greens-catalogue [Green, 2009] (see Fig.4.18):

- Model I: $K_{ep} = 4\cdot10^{-4}$,θ =0.5

- Model II: $K_{ep} = 1\cdot10^{-3}$, θ =0.3

- Model III: $K_{ep} = 4\cdot10^{-3}$, θ =0.1

---

[6]The latter value roughly reflects the corresponding value in the local CR-composition, see e.g. [Torii et al., 2008].
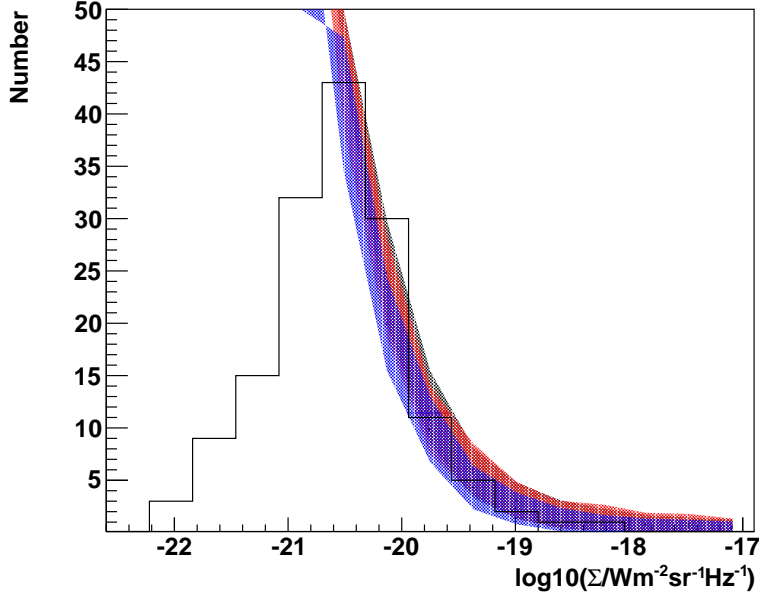
Figure 4.18.: The observed radio surface brightness distribution for shell-type SNRs as provided by Green's catalogue. Above $\Sigma(1\text{GHz}) > 10^{-20} \text{Wm}^{-2}\text{sr}^{-1}\text{Hz}^{-1}$ the coverage of the galaxy in radio is complete. The coloured bands represent the three models I (red), II (black) and III (red) (see text) that define the range in the parameter space spanned by K_{ep} and θ which allows for a fit to the data.

Models I and III mark the boundaries of the allowed parameter space in K_{ep} and θ, and Model II represents an intermediate set of these parameters. As a spectral index of the injected particles a value of 2.1 is chosen which seems to be typical for SNRs (the spectral index in radio flux density is distributed around values ≥ 0.5 which implies (uncooled) electron spectra with indices close to this value. Furthermore, this spectral index allows to model three out of four of the SEDs in sectionA.3.).

It is important to mention at this point that the distribution in Fig.4.18 can not be modelled without magnetic field amplification. Any such attempt results in an unreasonably huge number of VHE-bright objects.

4.6. Results

Fig. 4.19 shows the number of sources above a given integrated flux level above 1TeV (usually called the *LogN-LogS* plot) for the three models. These values result from averaging over many simulated galaxies[7].
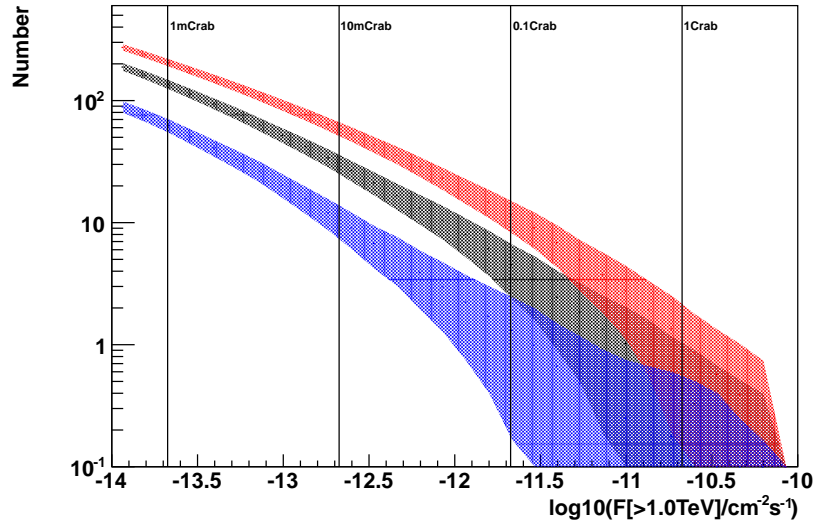
Figure 4.19.: LogN-LogS plot for models I (red), II (black) and III (blue). The bands represent the Poissonian errors for an averaged galaxy.

As one can see, Model I yields the brightest galactic SNR sample at gamma-ray energies above 1TeV, Model III the faintest. This fact implies that at these energies the emission is hadronic-dominated; the increased number of electrons in model III is not sufficient to compensate the higher acceleration efficiency in model I which (in first approximation) determines the number of both non-thermal electrons and protons in equal measure.

The numbers of SNRs above 1mCrab, 10mCrab, 0.1Crab and 1Crab for Models I-III are listed in Tab.4.1.

Current IACT instruments typically achieve sensitivities on the order of 1% Crab flux and better in deep pointed observations. Above these flux levels, there are 8 clear detections of SNR shells at VHE with counterparts at other wavelenghs: Vela Jr (with an integrated flux above 1TeV of ~1Crab), RX J1713.7-3946 (~64%Crab), HESS J1731-347 (~33%Crab), RCW86 (~11%Crab), Cassiopeia A (~4%Crab), CTB 37B (~3%Crab),SN1006(~2%Crab) and Tycho's SNR (~1%Crab).

---

[7]A number of 200 galaxies in the case of models I and III and 1373 galaxies in the case of model II have been simulated. The latter will be regarded as the reference model in the following sections and was thus simulated to a larger extent.

Model	> 1mCrab	> 10mCrab	> 0.1Crab	> 1Crab
I	191±14	54.1±7.4	10.9±3.3	1.3±1.1
II	124±11	26.7±5.2	4.2±2.0	0.5±0.7
III	56.9±7.5	9.2±3.0	1.2±1.1	0.1±0.3

Table 4.1.: Number of SNRs at different integral flux levels above 1TeV as predicted by Models I-III.

When comparing it to the numbers from the simulations, this set of sources should be regarded as a conservative subsample of the $\sim$50 H.E.S.S. sources that are coincident with galactic SNRs known from Radio or X-ray . Many of the remaining sources are situated in complex regions and a firm SNR association has not been possible so far. Furthermore, in a number of cases a SNR-MC interaction is suspected (e.g. W28 or CTB 37A) or an association with a pulsar wind nebula. These sources feature additional VHE-emission components that are not covered by this simulation. So, especially at lower flux levels, the number of detected, but confused shell-type SNRs is probably higher than what is quoted here.

On the other hand, the interaction of CR streaming from the shock front into the material of the main sequence bubble shell is not accounted for in this simulation. Therefore, cc-SNe might be brighter in gamma-rays than what this simulation predicts. This mechanism might be observed for example in RX J1713.7-3946 [Fukui, 2013], where it leads to a very bright and inhomogeneous gamma-ray emission. In contrast, the SNR VHE emission in this simulation rapidly decreases when the blast wave interacts with the bubble shell and therefore the number of gamma-ray bright cc-SN remnants is probably underestimated.

For a better comparison to the H.E.S.S. observations, especially in the case of rather faint sources, the instrument's degrading sensitivity with increasing source extension is approximated by multiplying the flux thresholds with a factor $\kappa = \sqrt{PSF^2 + R^2}/PSF$ [Renaud, 2009], where R is the source radius and PSF is the instrument point spread function (see section 1.3.3). Here, the conservatively approximation of $PSF = 0.1$ is assumed. Furthermore, only sources in the HGPS region are considered. The result can be understood as an expected number of detections in this region and is shown in Tab.4.2.

These numbers should be taken with a grain of salt, as the factor κ is a rather simple assumption and might not be applicable to very bright sources that are easy to detect.

As one can see, Model III predicts too little detections. From the presented simulations, it seems that an acceleration efficiency of $\theta = 0.1$ is not sufficient to reproduce the observed number of SNRs.

The figures obtained by Model I seem high but not entirely unreasonable in

F (CU)	Model I	Model II	Model III	Observed
> 0.001	$104(118)\pm10(11)$	$57.0(68.0)\pm7.6(8.3)$	$25.1(32.5)\pm5.0(5.7)$	$\{5(8)\}$
> 0.01	$30.8(33.3)\pm5.6(5.8)$	$13.2(14.4)\pm3.6(3.8)$	$2.7(3.4)\pm1.6(1.9)$	$5(8)$
> 0.1	$5.5(5.9)\pm2.3(2.4)$	$1.8(2.0)\pm1.3(1.4)$	$0.4(0.5)\pm0.6(0.7)$	$4(4)$
> 1	$0.5(0.5)\pm0.7(0.7)$	$0.1(0.2)\pm0.3(0.4)$	$0(0)$	$1(1)$

Table 4.2.: Estimated and observed number of detections in the HGPS region and whole sky (in brackets).

view of the large number of the 50 observed sources that are coincident with radio- or X-ray bright SNRs.

Model II predicts values that lie between those of I and III and which are in agreement with observations at the 1%Crab level. However, it underestimates the number of very bright detections somewhat.

The obtained numbers are comparable to the results of a recent study by [Cristofari et al., 2013] in which the galactic SNR population in simulated in a similar approach.

In the following discussions, Model II will be used unless noted otherwise.

4.6.1. Impact of the Spectral Index of Injected Particles

The spectral index of the particle injection spectra, Γ, plays an important role as it determines what portion of the SN blast energy will eventually be visible in VHE energies. From the classical shock solution, a value of $\Gamma=2$ is expected, while the modification of the shock by the CR pressure is believed to lead to somewhat harder spectra, see section 3.4.1. [Zirakashvili and Ptuskin, 2008b] showed that the injection spectra might be considerably softer in modified shocks if the CR advection velocity significantly differs from that of the downstream gas. In the following, the impact of different values of Γ on the gamma-brightness of the SNR population above 1TeV will be investigated.

Fig.4.20 shows the effect when changing the spectral index of injected particles in Model II (all other parameters are unchanged, simulations with changed spectral index account for 200 galaxies each).

Clearly, the assumption on the spectral index of the injection spectrum is critical for the gamma-ray brightness of the simulated galaxies. As expected, a harder particle spectrum results in brighter SNRs: The number of predicted detections in the HGPS range increases from 13.2 ± 3.6 to 22.8 ± 4.8 above 1% Crab if the spectral index Γ is changed from the default value of 2.1 to 1.9. It should be mentioned, that in this case the radio surface brightness distribution at 1GHz is shifted downwards by $\sim60\%$ and does not fit the observational data.

On the other hand, a softer spectrum of injected particles results in a decrease of detections in the HGPS region. Going from the default value of $\Gamma=2.1$
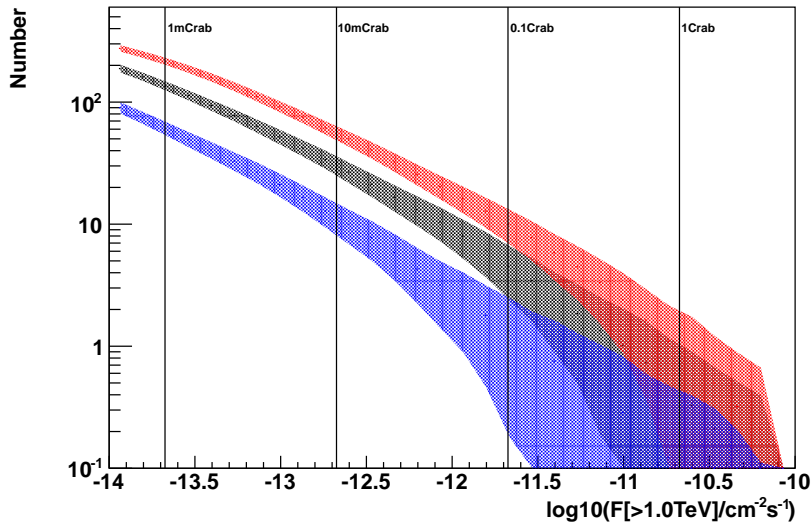
Figure 4.20.: LogN-LogS plot for Model II if changing the spectral index of injected particles to 1.9 (red) and 2.3 (blue). The original value is 2.1 (corresponding to the black line). The bands represent the Poissonian errors for an averaged galaxy.

to Γ=2.3, the number of predicted detections above 1% Crab decreases from 13.2$\pm$3.6 to 5.0$\pm$2.2 detections which is a value that seems too low compared to the (already conservatively estimated) observed number of 8 detected shell-type SNRs above that level.

Concluding it can be stated that in this simulation it is easier to describe the number of observed shell-type SNRs with relatively hard injection spectra of $\Gamma \leq 2.1$.

4.6.2. Impact of the Spatial Distribution

In the following, the impact of different models for the spatial distribution of SNRs in the galaxy on the gamma-ray brightness (above 1TeV) of the SNR population will be investigated.

Fig.4.21 shows the LogN-LogS plots for Model II (black) in addition to two similar scenarios where as the only difference to Model II a different spiral arm shape (red) or radial distribution function (blue) was chosen (for each of these two scenarios, 200 galaxies were simulated).

The alternative spiral arm model is taken from [Taylor and Cordes, 1993] where the authors abandon an axisymmetrical spiral arm structure and base their model on distance measurements of giant HII regions. As an alternative radial distribution function the work of [Yusifov and Küçük, 2004] is used, which based on the surface density distribution of pulsars.
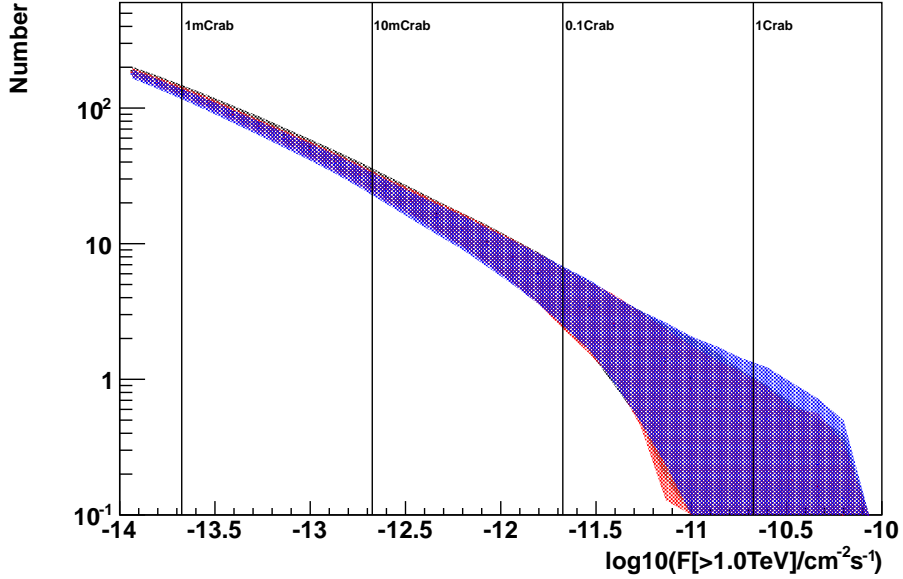
Figure 4.21.: LogN-LogS plot for Model II if applying the spiral arm shape proposed by Taylor&Cordes (1993) or assuming the radial distribution function found by [Yusifov and Küçük, 2004]. The original model is again given by the black line. The bands represent the Poissonian errors for an averaged galaxy.

It seems that the spatial distribution of the SNRs is of secondary importance to the number of detectable objects at VHE, as in the presented flux range the numbers agree within errors. From the presented simulations it appears that the spatial distribution does not have a major impact on the VHE-brightness of the galactic SNR population.

An important property of the LogN-LogS plots has not been discussed so far, namely their curved shape. That is, the curvature of these distributions contains information on the spatial distribution of SNRs. It is expected that in the case of an uniform distribution on a thin disk the number-intensity relation would follow $N \propto F_{>E}^{-1}$ [Casanova and Dingus, 2008]. Any deviation from this shape indicates a non-uniform distribution and the curvature in the LogN-LogS distributions is in agreement with this expectation.

4.6.3. Assuming The Parameters from the SED Fit

In this section, values for the parameter set θ, K_{ep} and Γ are used that are taken from the SED fit of the historic SNRs performed in Appendix A. There, the broadband spectra of four famous objects Cassiopeia A, Tycho's SNR, Kepler's SNR and SN1006 are modelled.

While the sample of modelled SNRs consists of only four sources, a number which undoubtedly is too low to allow any conclusions on the complete population of SNRs, it is interesting to look at the predictions from a model that is able to describe the spectra of real sources. Because the SED model for CasA is not very good, in the following the average values of the remaining three sources are assumed. These averaged values are as follows:

- $\langle K_{ep} \rangle_{Fit} = 2 \cdot 10^{-3}$

- $\langle \theta \rangle_{Fit} = 0.22$

- $\langle \gamma \rangle_{Fit} = 2.1$

Assuming this set of parameters results in the following numbers:

	All	detections	detections (HGPS range)
$> 1\text{mCrab}$	109 ± 10	59.9 ± 7.7	48.4 ± 6.9
$> 10\text{mCrab}$	20.3 ± 4.5	8.7 ± 3.0	7.6 ± 2.8
$> 0.1\text{Crab}$	2.7 ± 1.6	1 ± 1	0.9 ± 0.9
$> 1\text{Crab}$	0.3 ± 0.5	0.1 ± 0.3	0.1 ± 0.3

Table 4.3.: Predicted SNR numbers assuming a set of parameters that reflects the fit results from three historic SNRs.

The predicted values are low but compatible with the observed SNR detections. If the fit parameters as obtained in Appendix A are representative for all SNRs, we have already detected a large fraction of the detectable shell-type SNRs with the current generation of IACT instruments.

4.6.4. The Type composition

In Fig.4.22 one can find the LogN-LogS plots for the different subtypes of SNRs. Again, Model II was used.

The simulated population of VHE-bright SNRs is dominated by such sources that originate from SNIa events. Above a flux level of 1%Crab, 69.3% of all sources are of that type, 19.1% result from SNIIPe, 10.5% from SNIIL/b and 1.1% from SNIbc. The low number of SNIIP SNRs is surprising at first glance, since SNIIPe make up for the largest fraction of all SNe ($\sim$61%). However, this behaviour can be understood keeping in mind that in these sources the blast wave expands into the thin circum-stellar cavity created by the progenitor star. Consequently, due to a lack of accelerating as well as target material (in the case of π^0-decay), SNIIP SNRs are rather faint in gamma-rays.

With over 10%, SNRs resulting from SNIIL/b events are over-represented at VHE compared to their relative share in SN rate ($\sim$6.5%). Similar to SNIIP
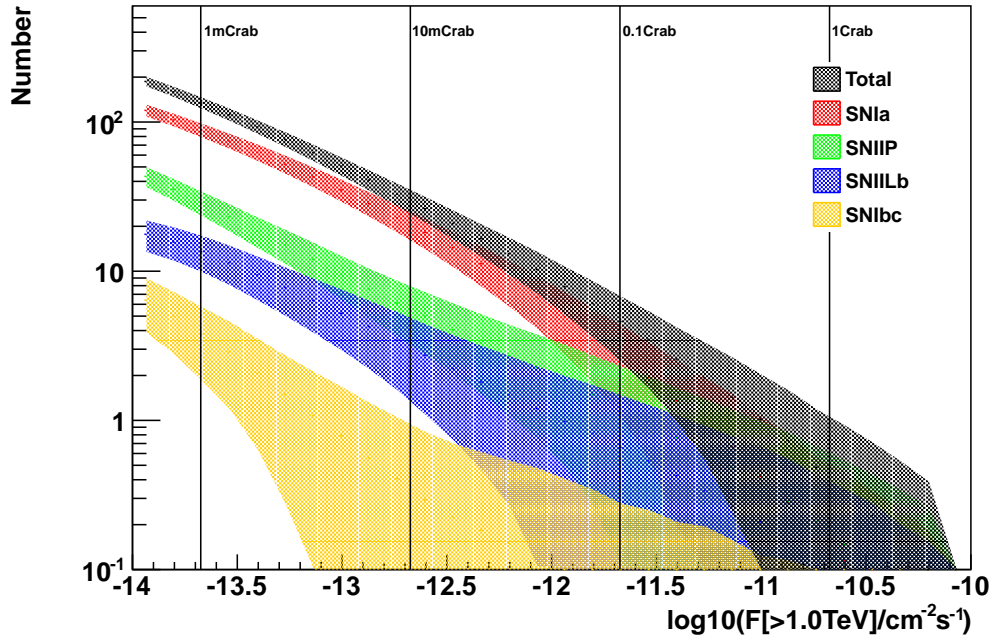
Figure 4.22.: LogN-LogS plot for the different SNR types in Model II. The bands represent the Poissonian errors for the SNR sub-types in an averaged galaxy.

SNRs, they too expand into a wind-blown bubble. However, these sources are modelled to possess extended RGZs, dense regions where the blast wave spends roughly the first few hundreds to a thousand years. Thus, at young ages, SNRs of this type are gamma-bright. As a matter of fact, they amount to the largest fraction of SNRs above 1%Crab at source ages smaller than few hundred years, see Fig.4.23.

SNRs from SNIb/c make up for only 1.1% of gamma-bright SNRs above 1%Crab. They are surrounded by a circum-stellar medium that, in a strong simplification, is modelled to be homogeneous and thin. With a relative fraction of all SN events of merely ∼8%, this results in the low simulated numbers.

These results are not in disagreement with the limited information on the type of observed SNRs at VHE in that most of them have been identified as resulting from SNIa (Kepler's SNR [Patnaude et al., 2012], Tycho's SNR [Krause et al., 2008b], SN1006 [González Hernández et al., 2012], RCW86 [Williams et al., 2011]). Cassiopeia A has been identified as the remnant of a SNIILb [Krause et al., 2008a], while RX1713-394 is compatible to a SNII/Ib scenario [Berezhko and Völk, 2010]. W49B most probably results from the SN of a supermassive star expanding into a pre-modified CSM [Keohane et al., 2007].
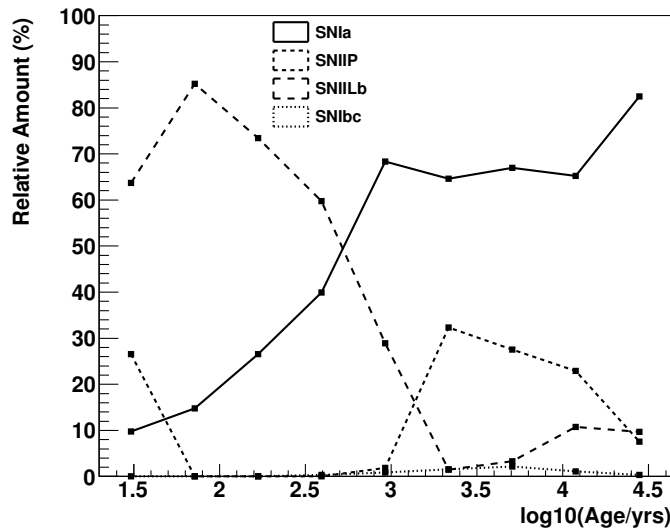
Figure 4.23.: SNR type composition at different source ages.

Looking at Fig.4.23, one can see that at young ages, as already stated, SNRs from SNIIL/b with their dense and extended RGZ make up for the largest fraction of gamma-bright SNRs. For ages larger than ∼600yrs, SNIa SNRs take over. The initially faint SNRs resulting from SNIIP build up in brightness over the first few thousand years (compare also to the energy injection rate evolution in the bottom panel of Fig.4.14) and account for roughly a third of all SNRs at ages around ∼3kyrs.

4.6.5. The Nature of the VHE Gamma-Ray Emission

As already deduced from Fig.4.19, the simulated VHE emission from SNRs is hadronic dominated. Fig.4.24 shows the ratio of the leptonic to the hadronic integrated flux component above 1TeV.

There is, however, a sizeable fraction of sources where the gamma-ray emission is mainly of leptonic origin. Looking at the different SNR types, SNIIP SNRs show a larger leptonic flux fraction than SNIa. This was already seen in Fig.4.17 and is due to the fact that hadronic VHE luminosity in first approximation goes with the square of the ambient density (ambient hadrons serve both as accelerating material and collision targets) while the IC component does so only linearly. Note, that this arguments also holds for SNIa remnants in very low-density ISM, thus the amount of SNRs with leptonic-dominated gamma-ray emission.

Furthermore, in the case of most of the young SNIa SNRs, the denser ISM (compared to the bubble interior) results in a stronger magnetic field amplification, (see section 4.5.2) which efficiently suppresses IC-radiation.
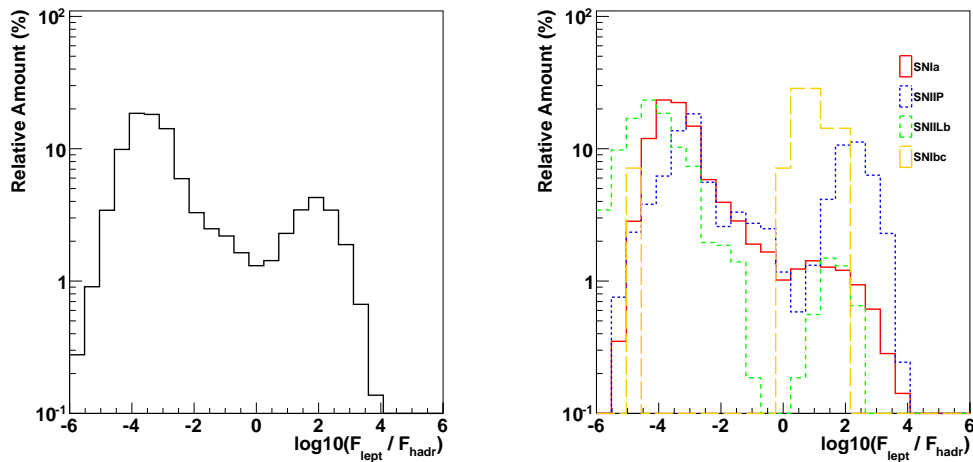
Figure 4.24.: Distribution of the ratio of the leptonic component of the integrated flux above 1TeV to the hadronic one. Only those sources with a total flux larger than 1%Crab have been selected for these plots. Left: All SNRs, Right: separated into types. The areas of all distributions are normalized to 100%.)

Summarising, it seems that the thinner the ambient medium and the older the source, the larger the leptonic contribution to the VHE emission. From an observational point of view, this has the unfortunate side effect that such SNRs are typically quite extended and thus difficult to detect. This selection effect, as approximated by applying the already introduced sensitivity factor κ, can be seen in Fig.4.25. A larger number of detections with a leptonic-dominated VHE emission is expected with CTA, see the dashed line in Fig.4.25.

Fig.4.26 shows the time evolution of the spectral index of gamma-rays α at 1TeV for the different source types. Here, only those sources with integrated fluxes ($>$1TeV) above 1%Crab have been chosen. Additionally, those rare SNRs from cc-SNe that have already encountered the bubble edge but are still visible at VHE were removed from the shown sample, because their particle spectra are strongly deformed, resulting in very chaotic and steep gamma-ray spectra.

The underlying proton spectrum has a spectral index of 2.1 and as gamma-rays from hadronic interactions are distributed somewhat harder in energy than their parent particles, a value of $\alpha \sim$2.0 is the minimum achievable index in this case. As one can see in Fig.4.26, the gamma-ray spectra show the expected shape in young SNIa and SNIIL/b remnants, where the proton spectrum extends to high energies and the emission is hadronic-dominated (because electrons are cooled efficiently by strongly amplified B-Fields).

The spectra of SNIa steepen with increasing age as the maximum proton energy decreases and the gamma spectrum at 1TeV is placed more and more in the cut-off regime of the π^0-decay emission.
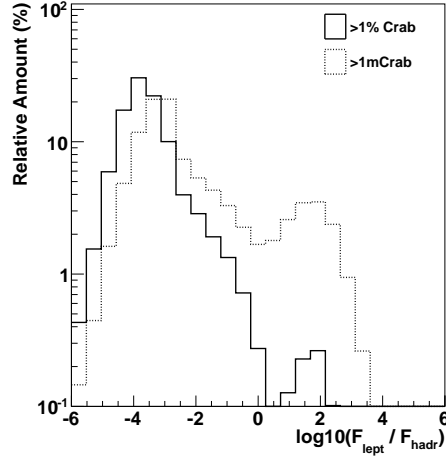
Figure 4.25.: Same plot as in the left panel of Fig.4.24. Additionally, the decreasing sensitivity with increasing source extension has been taken into account which provides an estimate on the detection probability. Additionally, the same distribution at a lower flux level of 1mCrab is shown (dashed).

In contrast, SNIIL/b remnants exit the dense RGZ after about 1000yrs and the majority of protons gets gradually cooled away by adiabatic expansion. The ambient density is now thin and leptonic emission plays a larger role. From this point on, the spectral index evolves similarly to those in SNIIP and SNIb/c scenarios: They are initially rather soft but then harden with time, as the IC-component gradually takes over. This has already been discussed in section 4.5.4.

4.6.6. Distribution in Age

Each of the four types of SNRs modelled here evolve quite differently in time. SNIa remnants which expand into an uniform medium are faint in the beginning, but by accumulating accelerated particles they quickly become the brightest SNR type after a few hundred to a thousand years. With increasing age, the shock slows down and is not able to hold the most energetic particles, which leads to a decline in the VHE-brightness of these sources.

SNIIP are bright in roughly the first hundred years, where the blast wave is still located in the RGZ. This is followed by a dark period where the SNR is travelling through the very thin stellar bubble. Slowly, a non-thermal population builds up in the SNR shell and after a few thousand years these objects become visible at very high energies. After roughly ten thousand years the shock hits the outer edge of the stellar bubble and the SNR becomes gamma-dark almost instantly, see section 4.5.4. The relatively faint nature of these sources dur-

95
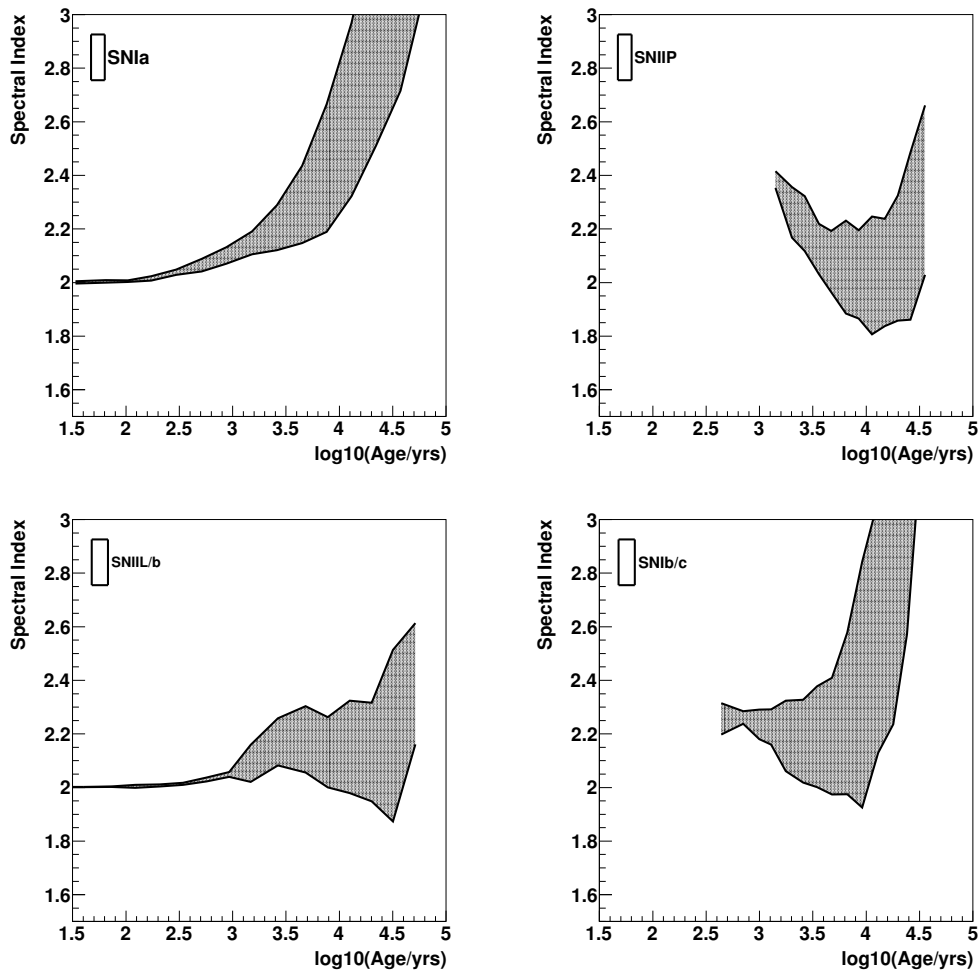
Figure 4.26.: Evolution of the spectral index at 1TeV for the different source types. Only objects with integrated fluxes (>1TeV) above 1%Crab have been selected. Furthermore, only such cc-SNR were chosen that have not yet hit the stellar bubble edge. The areas are given by the 1-σ confidence intervals (in logarithmic flux) for each x-bin.

ing the first few thousand years lessens the effect of neglecting the RGZ in the treatment of the shock dynamics (see section 4.4.2) to a second-order effect.

The evolution is identical for SNIb/c SNRs, except that they are modelled not to posses a RGZ at all.

Also very similar is the evolution for SNRs from SNIIL/b, but here the RGZ is extended and dense, and at early ages, this class holds the VHE-brightest SNRs.

Fig.4.27 shows the correlation between source Age and integrated gamma-

flux above 1TeV.

Because this plot is binned logarithmically in time and SNs go off every ∼30 years, the structure of the early-age bins is not visible. Thus, for comparison, also the evolutionary tracks of the four SNR types in this space are shown. They are given by the 1-σ confidence intervals (in logarithmic flux) for each x-bin.

As one can see, the bulk of sources is located at flux levels ≤1mCrab and an age of 6-20kyrs. Beyond this age, sources rapidly become gamma-ray dark. The SNIa line is overall at a higher level than that of SNIIP, which agrees with the dominance of this source type at flux levels >1% Crab. However, more sensitive observations should result in a higher relative fraction of SNIIP detections.

The resulting cumulated number distributions for possible detections at different flux-levels is shown in Fig.4.28. Here, also a number of expected radio detections is shown. This number is derived by a sharp cut in radio surface brightness at Σ_{1GHz} >10^{-21}Wm^{-2}sr^{-1}Hz^{-1}. While this cut is only a very crude description of the real radio surface brightness distribution (compare to Fig. 4.18), it results in a quite reasonable number of 174 predicted radio shells (the observed number of radio shells is 164). Note that only a fraction of 72 shell-type SNRs comes with an age estimate, so the corresponding line in Fig.4.28 represents an incomplete sample.

It can be seen that at integrated fluxes of 1%Crab and above most the SNRs are middle aged and younger than 10kyrs. At lower flux levels, also the detection of rather old SNRs is expected. The median values are 2.2kyrs at >10%Crab, 5kyrs >1%Crab and 10kyrs >1mCrab.

These numbers seem compatible with the age estimations of observed gamma-ray SNRs. While at ages ≤1kyr four of them are quite young (SN1006, Kepler, Tycho,CasA), current estimates place RX1713-3946 at an age between 1 and 10 kyrs and Vela Jr. between 700 and 9000 yrs. RCW86 is believed to be older than 2000 years, as may be CTB37B (0.35 - 3.15 kyrs). With a suspected age of ∼27kyrs, HESS J1731 seems to be an example of an evolved SNR. All quoted numbers are taken from the SNRcat [Ferrand and Safi-Harb, 2012] and the references therein.

4.6.7. The Expected Extension of Gamma-Bright Supernova Remnants

Fig.4.29 shows the SNR distribution in the source radius - integrated flux (>1TeV) plane. Again, the tracks of the different types, as given by their 1-σ intervals in each abscissa-bin, are shown.

As can be seen, the majority of the SNR population shows source extensions between ∼3.8 and 34 arc minutes, which means that in many cases, IACT experiments should be able to resolve the shell-structure.

At very small source radii, SNIIL/b remnants constitute the brightest source class. This is not surprising, as they are very gamma-luminous at young ages (compare to Fig.4.28). Going to larger extensions, SNIa remnants govern the
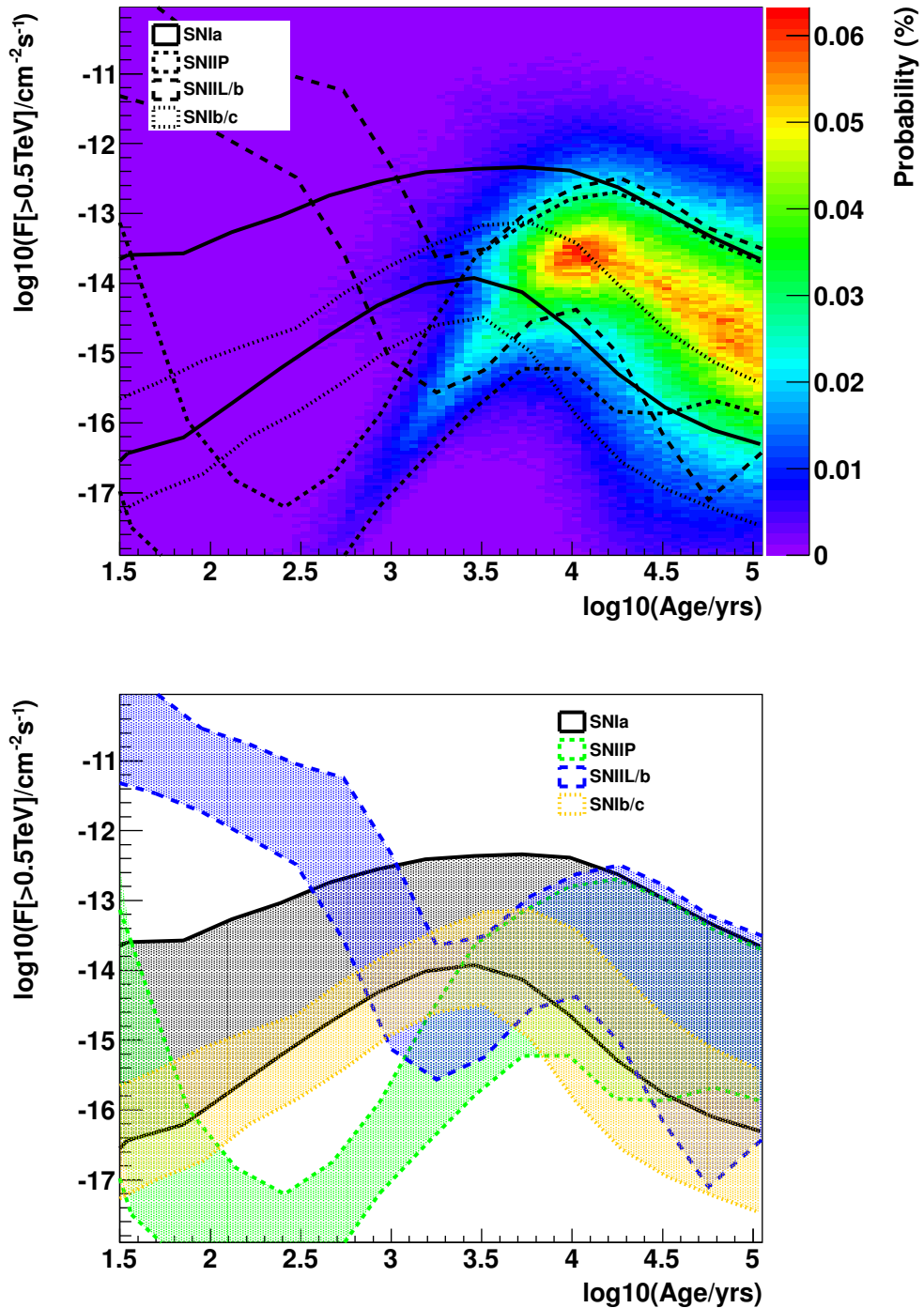
Figure 4.27.: Source probability density distribution in the age-flux (integrated above 1TeV) plane. Each decade along the abscissa and ordinate is binned in 20 logarithmic bins. The lines indicate the evolutionary tracks of the four SNR types. They are given by the 1-σ confidence intervals (in logarithmic flux) for each x-bin and are also presented separately in the bottom panel.
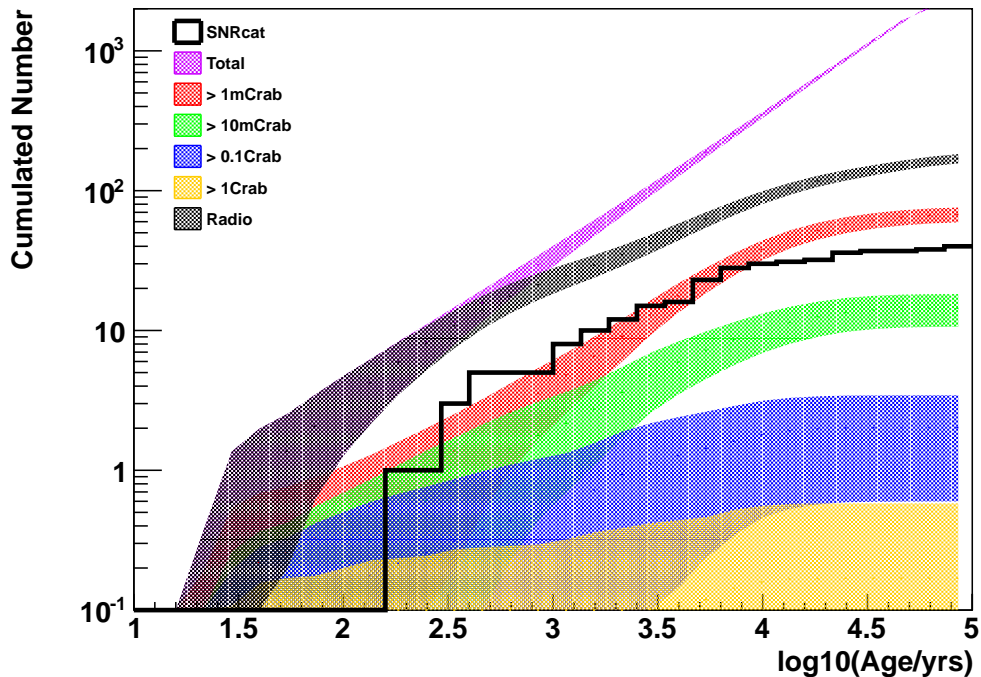
Figure 4.28.: Cumulated number of expected SNR detections as a function of age and at different flux levels. Additionally, the distribution of known shell-type SNR ages from radio is shown, as well as the simulated distribution in radio. The bands represent the Poissonian errors for an averaged galaxy.

SNR population until at at radii of $\sim 0.2°$ SNIIP SNRs take over as the dominant source type.

The rare species of SNIb/c SNRs is expected to be distributed at around $0.1°$.

Fig.4.30 shows the total distribution of the extensions of expected VHE detections at different flux levels.

The size distributions are very similar to those found in radio data. Compared to the values from the SNRcat, the distribution for the simulated Radio-SNRs seems to be tilted towards lower radii. This is probably connected to the sharp cut at a surface brightness of $\Sigma_{1GHz} > 10^{-21} \text{Wm}^{-2}\text{sr}^{-1}\text{Hz}^{-1}$ that is crudely used to estimate the radio sensitivity of the SNRcat. One can see in Fig.4.18 that this cut rejects some sources at low surface densities, which often are bright but very extended. Such sources would add to the higher end of the distribution.

Another point worth mentioning is that there is is a non-zero probability for the detection of very large sources of up to $10°$ radius, especially at low flux levels.
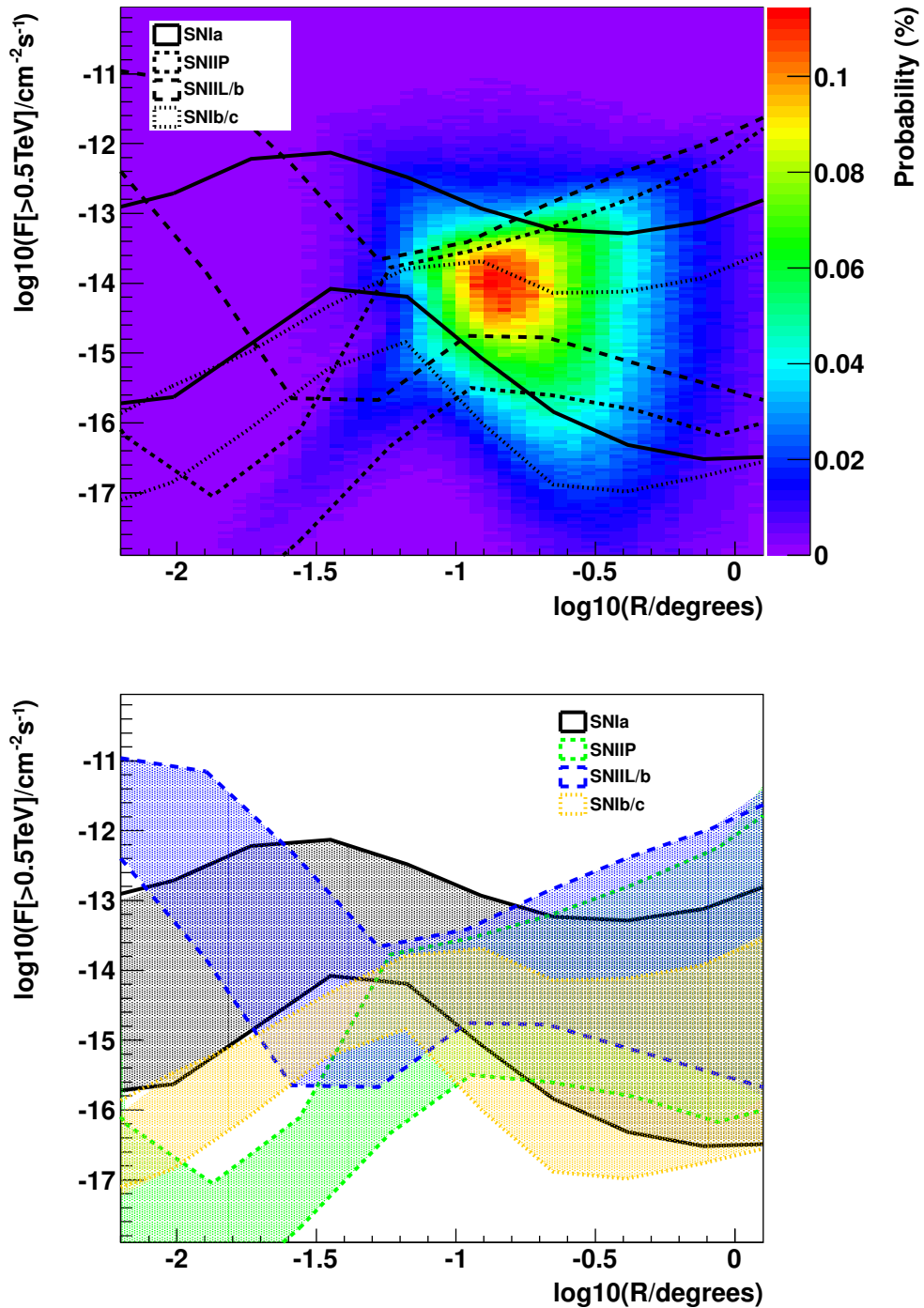
Figure 4.29.: Source probability distribution in the source radius - integrated flux (>1TeV) plane. Each decade along the abscissa and ordinate is binned in 20 logarithmic bins. The lines indicate the evolutionary tracks of the four SNR types. They are given by the 1-σ confidence intervals (in logarithmic flux) for each x-bin and are also presented separately in the bottom panel.
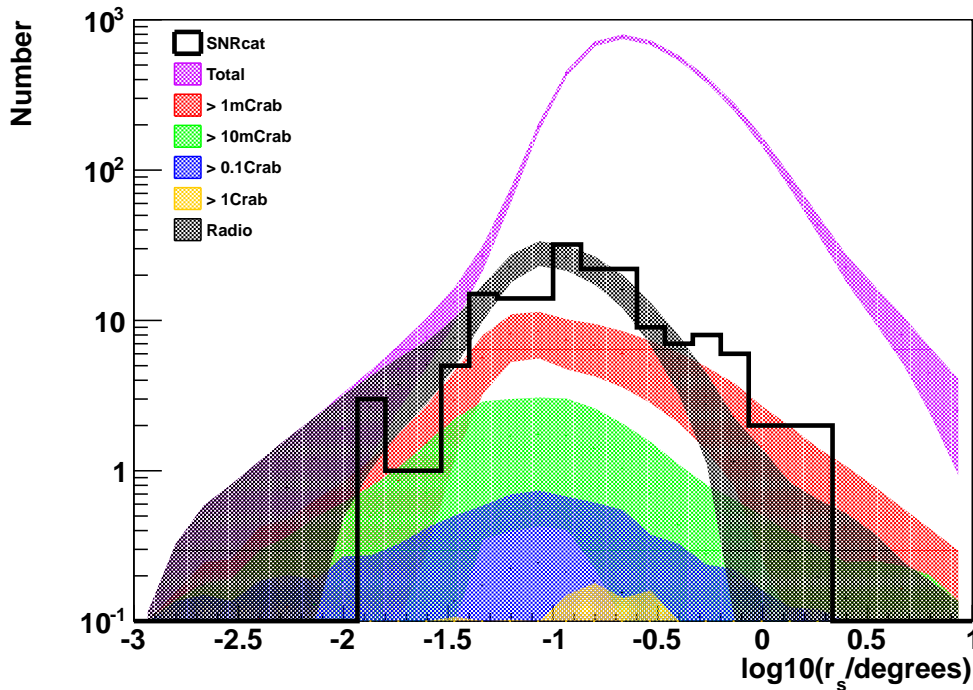
Figure 4.30.: Size distribution of gamma-bright as well as radio-bright sources. The bands represent the Poissonian errors for an averaged galaxy.

4.6.8. Galactic Horizon of Gamma-Bright Supernova Remnants and their Distribution in the Galaxy

Fig.4.31 shows the SNR-horizon of expected detections in VHE at three different flux-levels. Over-plotted are the position of the sun as well as the eight detected VHE shell-type SNRs.

As expected, at the higher flux levels one expects to see mainly nearby SNRs. However, there is also a finite chance to detect SNRs at large distances, as it is the case for H.E.S.S. J1731-347 (positioned at x=-2.5 pc, y=-4.5 pc).

Fig.4.32 shows the fraction of all remnants younger than a given age (here, 100yrs, 1kyr, 10kyrs and 100kyrs are shown) that is expected to be detected at sensitivity levels of 1%Crab (left panel) and 1mCrab (right panel) as a function of the distance to the source. This corresponds to an estimate of the completeness of SNR observations. With the current IACT instruments (corresponding roughly to the left panel), except for the immediate galactic neighbourhood where it is more probable to detect SNRs, the completeness is between 5% and 10% for young and middle-aged SNRs out to distances of ∼15kpc, beyond which the detection probability gradually drops to zero. The majority of evolved SNRs
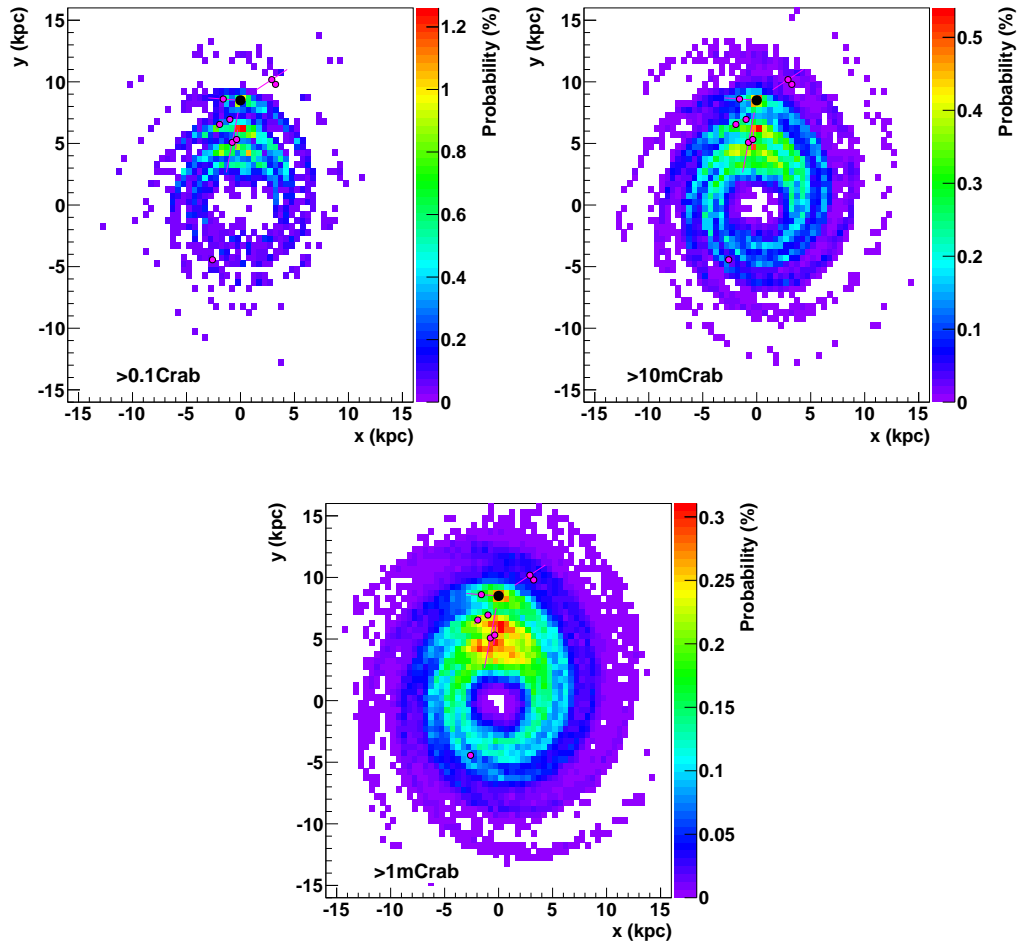
Figure 4.31.: Top left, top right, bottom: Probability density distribution for the detection of sources with F>10%Crab, 1%Crab and 1mCrab, respectively. Each bin is 0.5kpc×0.5kpc in size. Overplotted are the position of the sun (large circle) as well as the eight detected shell-type SNRs (small circles, lines are error-bars).

(age band <100kyrs) is only weakly emitting gamma-rays and less than ∼1-2% of these objects are expected to be detectable throughout the galaxy. With CTA (roughly corresponding to the right panel in Fig.4.32) the completeness is expected to increase to ∼10-15% out to distances of 15kpc, and values between ∼15% to ∼40% between earth and the galactic center. Compared to the current generation of instruments, the increase in detection efficiency for middle-aged and evolved SNRs is most pronounced. Note, however, that here again κ was applied, which probably will be considerably smaller with CTA, and so the presented numbers are rather on the conservative side.

Already at a flux levels of 1%Crab, a ring-like structure stands out around
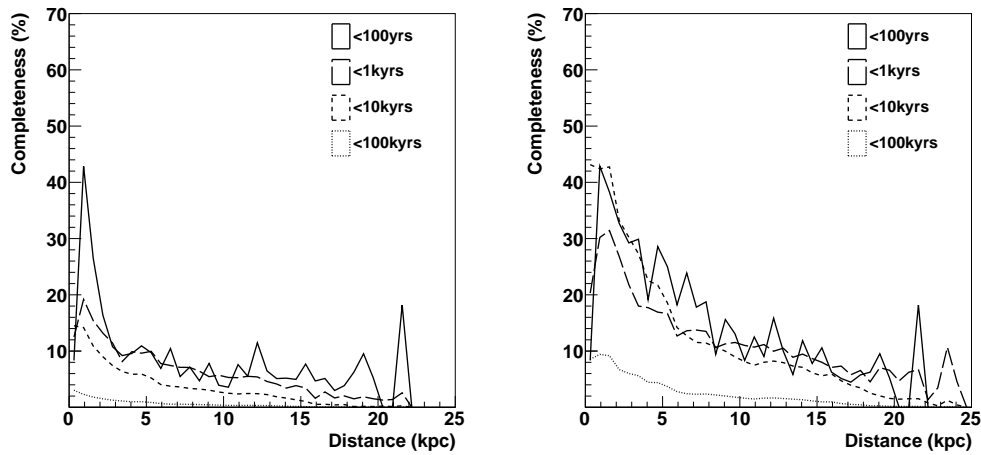
Figure 4.32.: Predicted completeness of SNR observations as a function of distance for different source ages. Left: Assuming a sensitivity of 1%Crab, right: assuming a sensitivity of 1mCrab (both for integrated fluxes above 1TeV)

the galactic centre that results from both the radial distribution function of SNRs as well as the increased gas densities there. Projected onto galactic longitudinal coordinate l, this structure is visible as a double-peak, see top panel in Fig.4.33. This feature is not seen in radio, both simulated and observed, as Synchrotron emission does not depend as critically on the ambient medium as π^0-decay. Apart from that, all distributions reproduce the radio SNR distributions[8].

---

[8]The distribution in l and b (galactic latitude) is independent of source age and CSM properties, so radio- and gamma-bright SNRs should, to first approximation, follow the same spatial distribution.
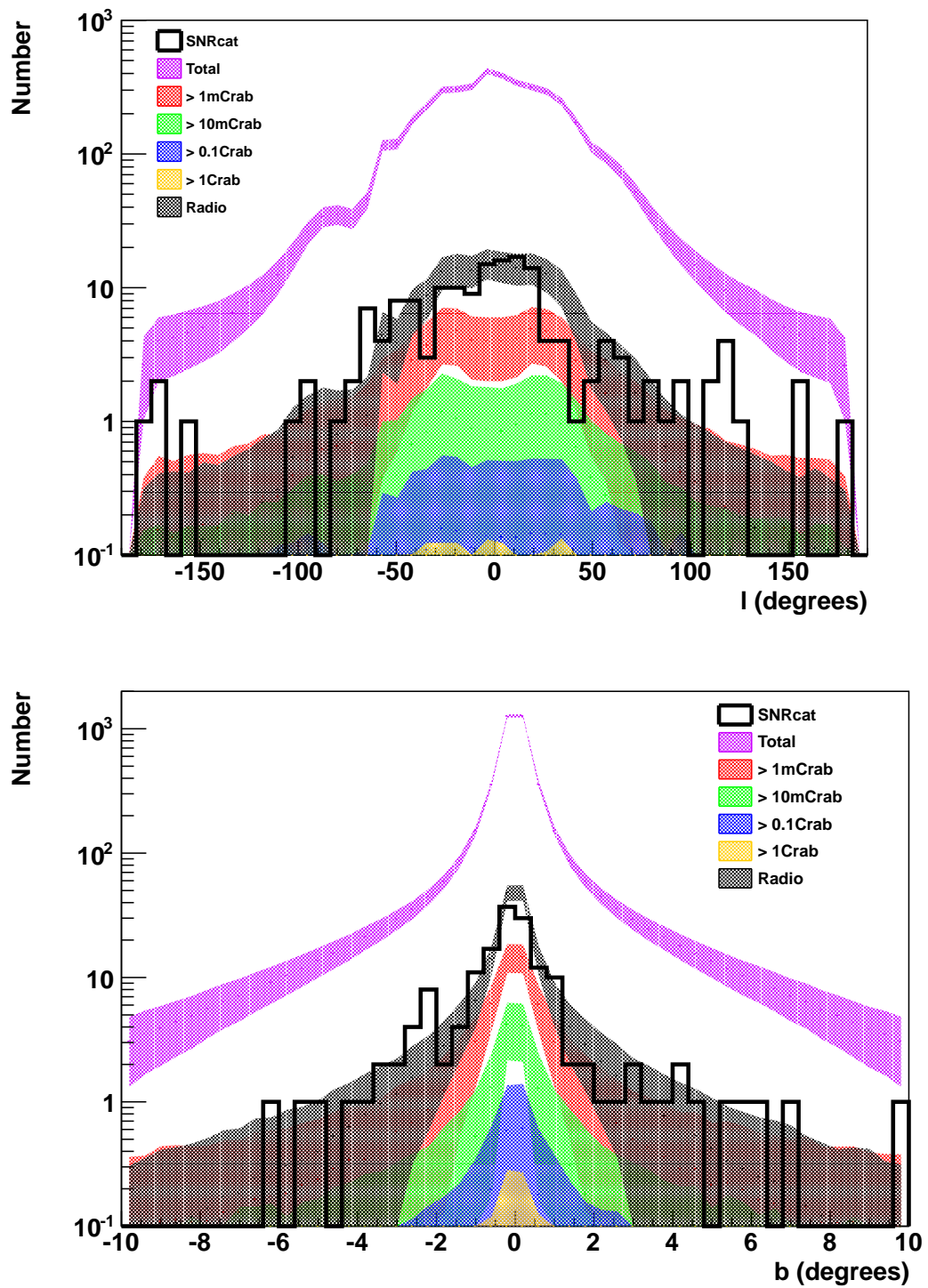
Figure 4.33.: Distribution of gamma-bright as well as radio-bright sources in galactic longitude and lattitude. The bands represent the Poissonian errors for an averaged galaxy.

4.6.9. The Galactic Plane in Gamma-Bright Supernova Remnants

While the diffusion of particles from the shock is not covered in this simulation, one can approximate their spatial distribution by a thin, spherical shell. By looking at the sky, we observe a 2D-projection of this spherically symmetric shell, whose radial profile is shown in Fig.4.34.
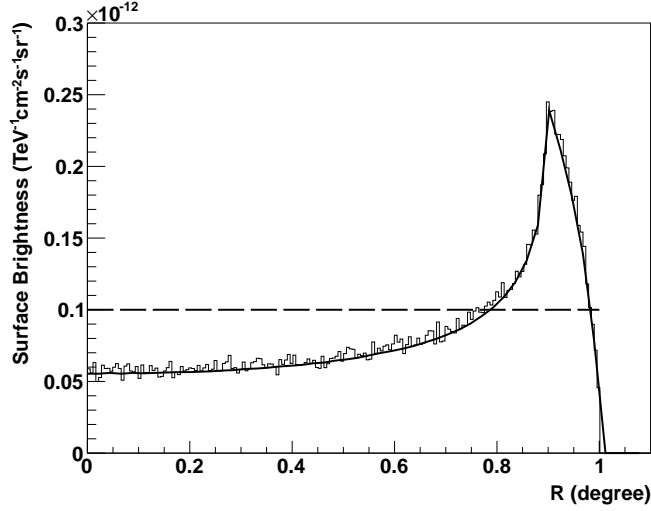
Figure 4.34.: Radial profile resulting from the projection of a sperical shell into two dimensions. The dotted line represents a homogeneous surface brightness that leads to the same total flux after angular integration. The histogram showcases the flux distribution along the shell, see text.

Here, the flux of a given SNR is distributed along this functional shape in a MC approach. To that end, the total integrated flux from a SNR is divided in a large number of 'sub-portions'[9]. To each of these portions, an angle is diced (uniformly) as well as a radial distance to the source centre (using the projected shell as PDF, see Fig.4.34). Each flux portion is then filled into its corresponding 2D-histogram bin.

The so obtained raw image is then smoothed in l and b with a Gaussian kernel where the width reflects the assumed PSF. This map can now be used to produce correlated flux maps.

Two simulated flux maps (from Model II, integrated above 1TeV) of the HGPS region are shown in Figs.4.35 and 4.36. In both cases, a flux correlation radius of $0.1°$ is chosen. The same value is assumed for the PSF. In Fig.4.35, the minimum value of the flux is 1%Crab, which roughly approximates the H.E.S.S. sensitivity in the inner galactic plane. For this galaxy specimen and integration radius, a number of 10 shell-type SNRs would be visible with H.E.S.S.

---

[9] the number of which is determined by the SNR size
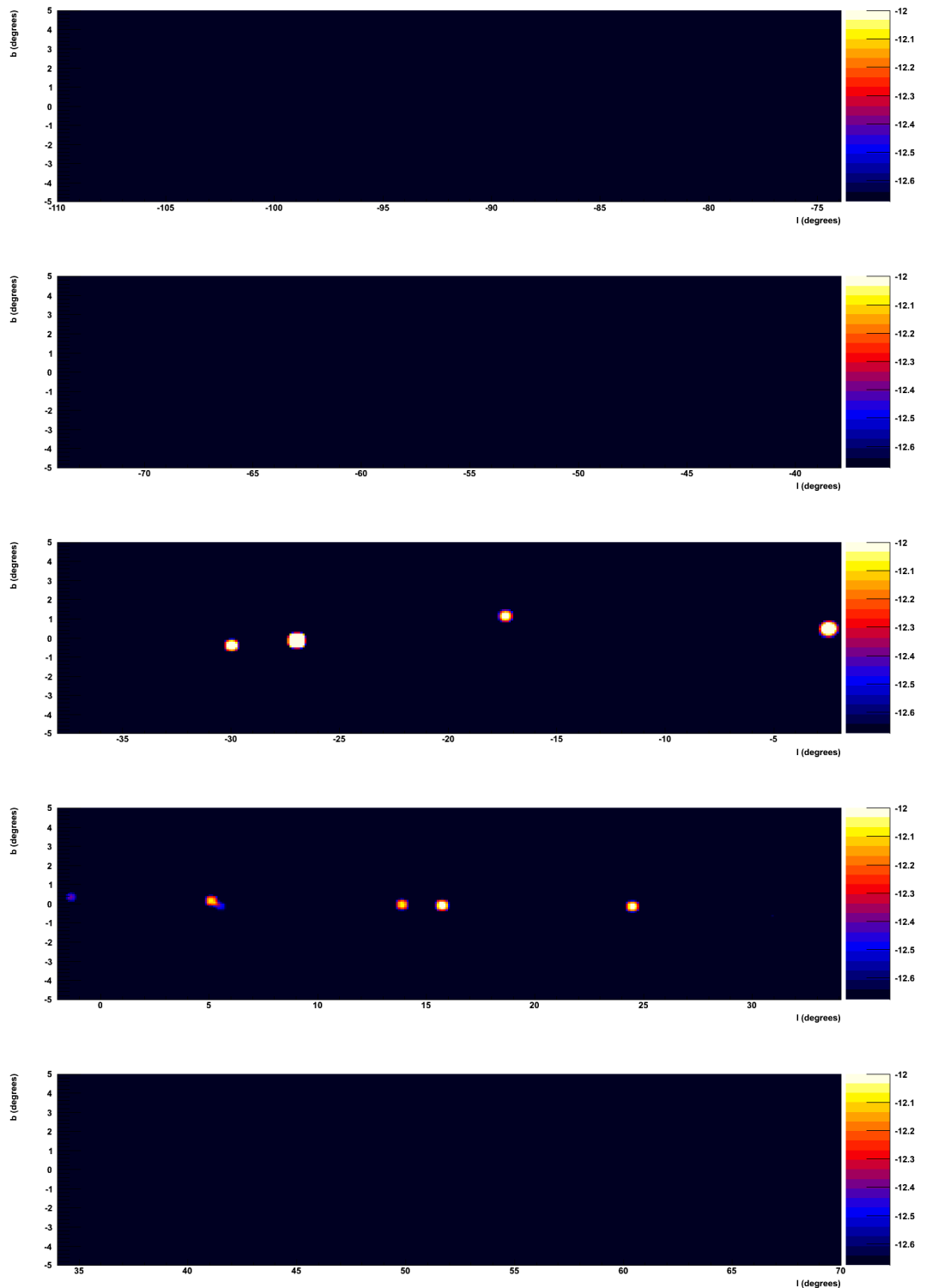
Figure 4.35.: Flux map of simulated VHE-bright SNRs in the HGPS region. Here, Model II was assumed. The lower boundary on the flux (1% Crab) is chosen to approximate the sensitivity of H.E.S.S..
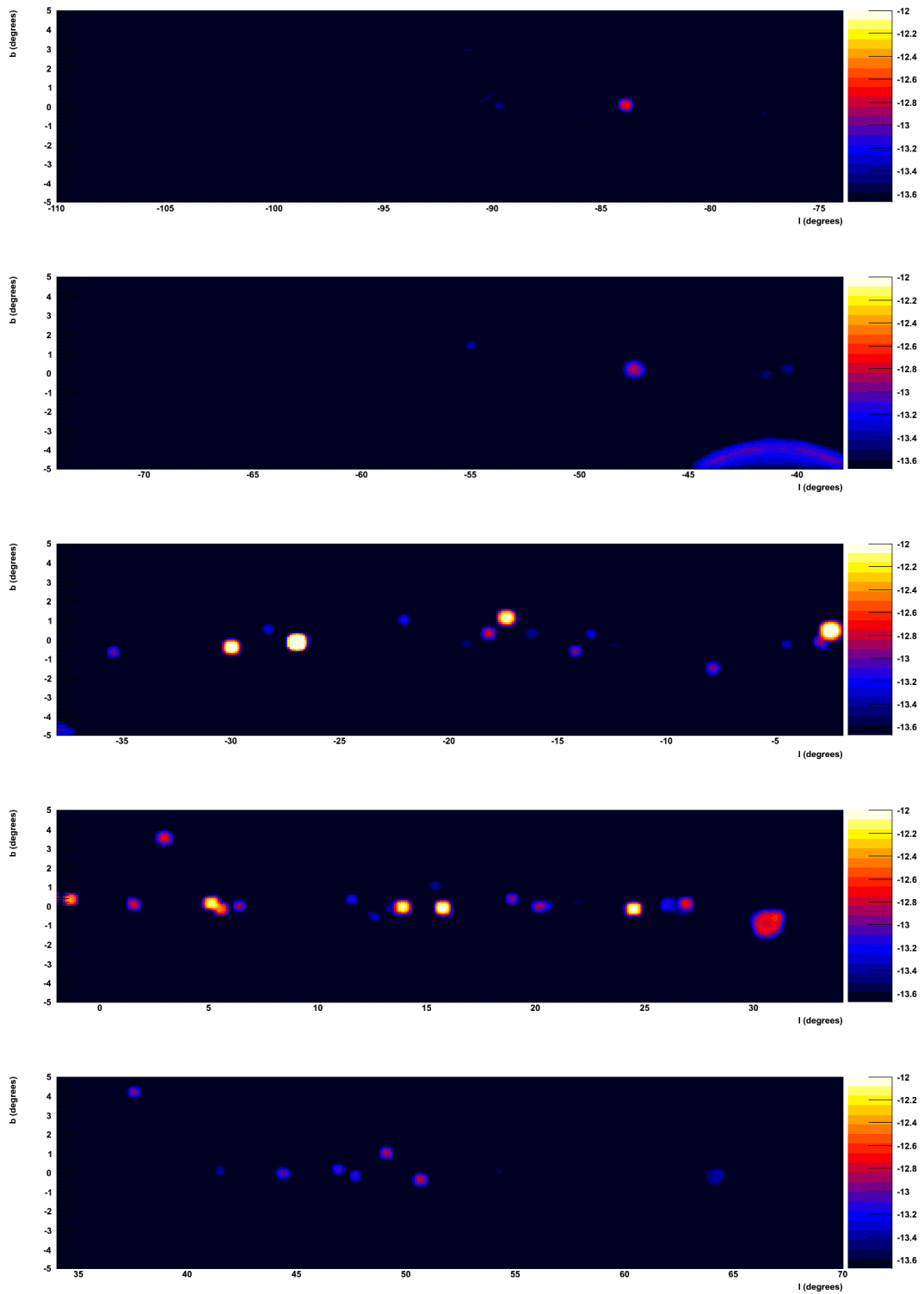
Figure 4.36.: Same as Fig4.35 but with a lower flux boundary of 1mCrab which roughly reflects the estimated CTA sensitivity.

in this range. Allowing minimum flux levels of 1mCrab results in Fig.4.36. This approximates the expected CTA sensitivity. As one can see, the VHE SNR sky seen with CTA will be pretty crowded. While these maps provide a somewhat realistic prediction of the SNR VHE sky as seen with H.E.S.S. and CTA, work is ongoing to further improve them by combining them with estimated instrument response functions. This will allow actual analysis from these maps, which might be helpful in various studies like e.g. performance optimisations and the investigation of the diffuse galactic gamma-ray background.

4.6.10. Conclusions and Outlook

In this chapter, a population synthesis model for VHE-bright SNRs has been presented. It applies models for the spatial distribution of SNRs in the galaxy, the B-fields and gas densities in the ambient interstellar medium around these objects as well as on the possibly pre-modified circum-stellar density profiles. For each SNR, the shock dynamics during the non-radiative phase of the SNR, the accelerated CR distribution at the shock and subsequently the gamma-ray emission from the non-thermal particles is computed.

All involved models are strongly simplifying the real picture, which is acceptable in so far as the aim of this work is not provide a very detailed description of individual sources, but rather an averaged picture of the SNR population at VHE as a whole[10].

However, many of the model components are presently not very well understood and observational information is limited. To name just a few examples: The gas distribution and magnetic field strength in the galaxy are known only on relatively large scales compared to typical SNR extensions. Also, the properties of red giant wind zones, which potentially have a large impact on cc-SN remnants, are not well understood. Even the most fundamental quantity used in this study - the SN rate in the galaxy - is attributed with a large uncertainty.

In addition, this model provides only the emission from CR contained inside the SNR. The interaction of CR that stream away from the shock and interact with galactic matter, such as molecular clouds or, in the case of cc-SNe, the material in the stellar bubble shells, is not accounted for.

With these caveats in mind, the observed sample of radio-SNRs was used to constrain some model parameters that were used in the population synthesis. As is turned out, a set of standard model parameters allowed it to reasonably reproduce the observed SNR distributions in radio-surface brightness, galactic coordinates, source extension and a reasonable number of expected VHE detections. It was found that this is only possible in the presence of magnetic

---

[10] This does not mean that the modeling applied here is not able to describe the gamma-ray emission of individual objects, as has been displayed in sectionA.3, where the SEDs of three out of four of the most prominent SNRs were successfully modelled, together with the values of the B-field, the source size and the shock speed.

field amplification as SNRs with shocks in the test-particle limit resulted in a unrealistically bright population at VHE.

On the other hand, assuming magnetic field amplification resulted in numbers of predicted detections in the VHE range that are compatible with observations if the mean acceleration efficiency is high, $\theta > 0.2$, the spectra of injected particles are hard, $\Gamma < 2.3$, and the electron-to-proton fraction does not exceed a few per mille, $K_{ep} < 4 \times 10^{-3}$.

Assuming such parameters, it followed that remnants of thermonuclear SNe constitute the brightest class of SNRs at VHE. They make up for almost 70% of all SNRs at integrated (>1TeV) flux levels above 1%Crab. The remaining 30% are remnants of cc-SNe. This SN class accounts for 75% of all supernova events and their remnants are thus under-represented at VHE energies. However, the rare SNIIL/b remnants are expected to be dominant among the very young SNRs.

It was also found the absolute number of bright sources is quite unaffected by assuming different galactic structures.

Overall, the VHE emission from detected SNRs is predicted to be hadronic-dominated. This is in part due to an observational bias, as it are typically old sources in dilute media that are predicted to show leptonic-dominated gamma-ray emission. However, those sources are generally very extended and therefore difficult to detect.

The simulations suggest that the current generation of IACT instruments like H.E.S.S. allows it to detect an estimated amount of less than 20% of all gamma-ray emitting SNRs within 1kpc and less than 5% within 12kpc to the Earth.

That is, the bulk of the VHE gamma-ray emission from SNR is at at integrated flux levels (> 1TeV) of $F \leq 1$mCrab. This is the regime that CTA will be able to probe. If this simulation is correct, more than ~ 120 shell-SNRs are in this flux range, heralding a golden age in SNR astrophysics at TeV energies.

5. VHE Data Analysis Of Radio SNRs

In this chapter the SNR population as known from other wavelengths will be investigated. This is done by analysing the corresponding source positions in the extensive data set of the H.E.S.S. Galactic Plane Survey (HGPS).

Since there are several hundred known galactic SNRs in the HGPS range, this analysis focusses on a uniform and automated treatment of the source population as a whole rather than a detailed investigation of individual sources. Thus, SNR-associations that have already been detected with H.E.S.S. will not be re-analysed but treated separately in some of the discussions.

The total source sample, its selection and analysis as well as an interpretation of the results will be presented in the following.

5.1. SNRcat

SNRs have been observed in a wide energy range, extending from radio to VHE. The university of Manitoba is maintaining a catalogue of SNRs that combines the data from many of the instruments that cover this large energy interval spanning 20 decades.

This catalogue is called SNRcat[1] [Ferrand and Safi-Harb, 2012] and contains information about galactic coordinates, radio flux, extension and, if known, distance and age of the object. In many cases, a positive association with a pulsar is possible. If this is the case, the according information on pulsar distance and characteristic age is also provided in SNRcat.

Sources are divided into four types with respect to their radio morphology:

- shell-like (S) where a shell-shaped remnant is observed

- filled-centre (F) where the emission is concentrated in the source centre,

- composite (C) where a combination of (S) and (F) is observed and

- uncertain (?) where no clear determination can be done.

Table 5.1 summarises the composition of SNRcat.

The SNRcat is based on Green's catalogue of radio and infra-red SNRs which also accounts for the largest part of the dataset in the SNRcat. Amongst others,

---

[1]Here, the version from 15.7.2013 is used.

	Type				
	S	C	F	?	total
All	164	46	25	80	315
SNR distance known	62	41	5	39	147
PSR distance known	3	15	17	15	50
SNR age known	41	37	2	23	103
PSR char. age known	8	17	16	16	57

Table 5.1.: Composition of the SNRcat.

the data compiled in this catalogue is the result of galactic plane surveys of major radio observatories like the Effelsberg 100m telescope, the Parkes 64m telescope, the Molonglo telescope and the VLA but also of infra-red instruments like IRAS and Spitzer. Additionally, SNRcat complements these low-energy measurements with X-ray observations from ASCA, ROSAT, XMM-Newton, Chandra and Suzaku as well as gamma-ray satellite data collected by Agile and Fermi. At the high-energy end, data from the ground-based Water-Cherenkov instrument Milagro and from the state-of-the art IACTs experiments Veritas, MAGIC and H.E.S.S. is provided (see [Ferrand and Safi-Harb, 2012] and references therein).

The sample of SNRs suffers from selection effects. In radio, faint as well as small sources may be under-represented. Firstly, the angular resolution of the instruments limits the ability to identify the structure of small ($<$few arcmin) SNRs. Secondly, the galactic radio background decreases the sensitivity for the detection of faint SNRs. As a result, the latter are found to a relatively larger amount at high and low galactic longitudes than in the region around galactic centre [Green, 2009].

5.1.1. The Distribution in Galactic Coordinates

The source distribution in galactic coordinates can be seen in Fig.5.1.

In galactic longitude, 87% of the SNRs are populating the corresponding HGPS range (the HGPS covers a range in galactic longitude (GL) of $\{75°, 247°\}$ and in galactic lattitude (GB) of $\{-5°, 5°\}$, indicated by the dashed lines in Fig.5.1). A maximum can be seen at $l \simeq 10°$.

The distribution in galactic latitude is found to be sharply peaked around $b = 0$. Of all sources, 94% are distributed within the galactic latitude interval $|b| < 5°$.

In total, the HGPS region encompasses 251 sources which amount to 80% of the whole sample.
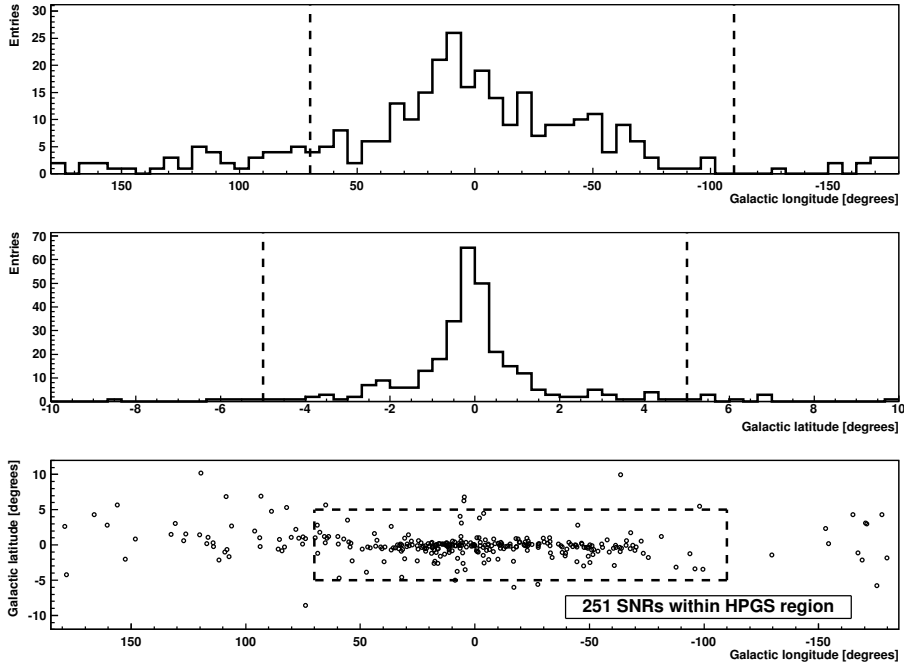
Figure 5.1.: Distribution of SNRs in galactic longitude (top), galactic lattitude (middle) and in the GL-GB plane(bottom). Dashed lines indicate the HGPS region.

5.1.2. Distance Estimates

The available distance estimates are mostly obtained from the analysis of SNR radio line spectra (see e.g. [Tian and Leahy, 2008]). If in the SNR's line of sight absorption from HI (i.e. the 21 cm absorption line) is observed, a distance estimate can be made by comparing the relative velocity of the hydrogen gas to the observer, as given by the spectral Doppler-shift, with a galactic rotation curve that can be modelled from observational data of galactic spiral structure tracers (see e.g. [Brand and Blitz, 1993]).

This method has its pitfalls since in many cases the measured velocity corresponds to two sets of coordinates. This can be understood by imagining concentric rings around the galactic centre. Assuming a galactic rotation curve, each galacto-centric distance (and thus each of the rings) corresponds to a specific velocity value. If a SNR is observed, it is located somewhere along the observational direction. In measuring the velocity of the object, the position is fixed by the intersection of the line of sight with the galactocentric ring that corresponds to that velocity. Except for the case where the observational direction is the tangent to this ring, two solutions for the distance to the galactic centre result from this procedure - the 'near' and the 'far' solution. Especially in the inner galaxy the situation can be difficult, and the inclusion of additional
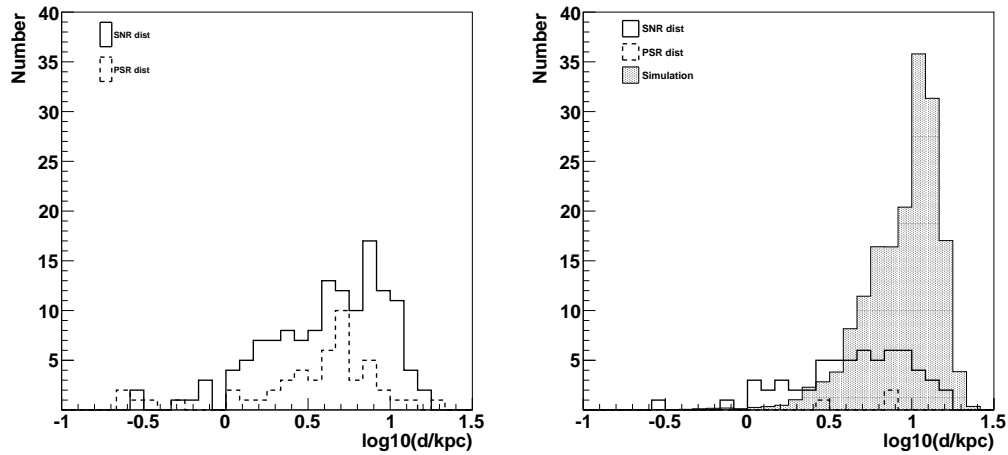
Figure 5.2.: Distribution of source distances. Left: All sources in the SNRcat with a distance estimation for SNRs as well as associated pulsars. Right: Same as in left panel but for the sub-set of shell-type SNRs. Additionally, the model prediction (ModelII, see section 4.5.5) is shown. If a range of distance values is given, the arithmetic mean is assumed.

data is often required. For example, the analysis of absorption lines in HII Bremsstrahlung spectra, if such material is in the field of view, is often used to resolve this distance ambiguity [Kolpak et al., 2003].

It is also possible to obtain a distance estimate if a pulsar can be associated to the SNR. In this case, one can measure the radio pulse broadening that is connected to the electron column density towards the object. This effect is quantified with the Dispersion Measure (DM). In conjunction to models of the galactic distribution of free electrons (such as the frequently used NE2001 model [Cordes and Lazio, 2002]), the dispersion measure allows a distance estimation. A detailed description of this method can be found in [Taylor and Cordes, 1993].

The top left panel in Fig.5.2 shows the distribution of distances estimates, both for direct SNR measurements (solid line) and DMs, if a pulsar can be associated. The distribution of direct SNR measurements rises to a maximal value at about 10 kpc and then rapidly falls off, while the PSR distances peak at a lower value of about 5kpc and features a somewhat smoother decline. In the right panel, the same distribution for the subset of shell-type SNRs is displayed.

Additionally, the predicted distribution from ModelII (see section 4.5.5) is shown with the shaded curve. A comparison is difficult as the observations are not complete. However, it is found that the model under-predicts close-by SNR radio detections. This is probably due to the crude cut on the radio surface brightness ($\Sigma_{1GHz} > 10^{-21}\text{Wm}^{-2}\text{Hz}^{-1}\text{sr}^{-1}$) in Model II (see section 4.5.5):
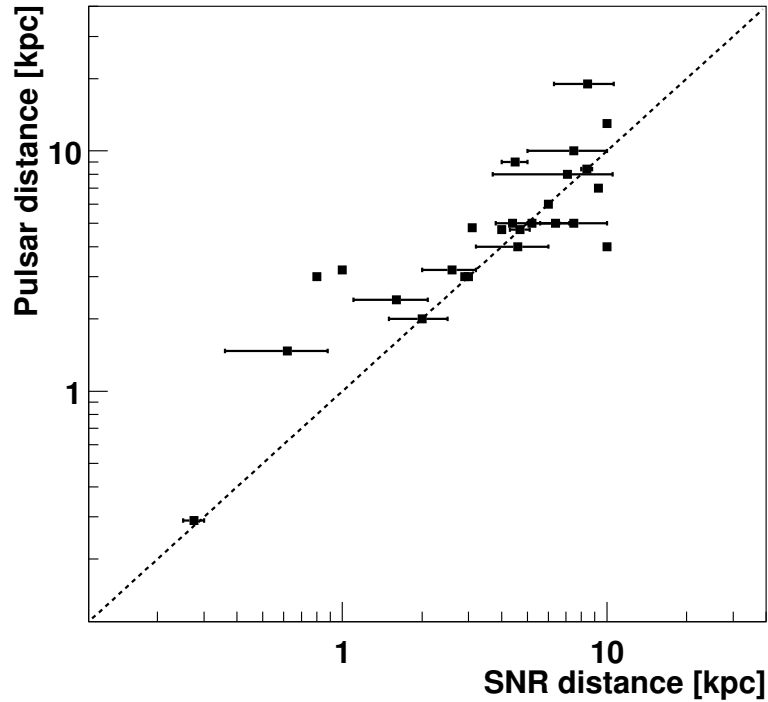
Figure 5.3.: Correlation between distance estimates of SNRs and that of their associated pulsars.

By definition, Σ_{1GHz} is distant independent. Therefore, a cut on this quantity does not introduce any selectional bias with respect to the source distance. As a result, the predicted distribution in the right panel of 5.2 reflects the overall radial structure of the simulated galactic SNR distribution (with the Earth's position as a reference point) which is peaked at $\sim$10kpc. In contrast, radio observations favour close sources with a high level of total radio flux but a comparably low surface brightness.

In 28 cases, both direct SNR and associated Pulsar distance estimates are provided. Fig. 5.3 shows that these two independent measurements are correlated. As one can see, they are correlated. In the following, I will thus accept DM-derived distance estimates if no direct SNR measurement is available.

5.1.3. Age Estimates

If an estimate on the distance to a SNR is possible, its extension and knowledge about the ambient medium as well as certain SN parameters allows it to deduct a source age. That is, many authors apply the classical ED or ST solutions (see

section 3.3) to the object and provide a corresponding age estimate.
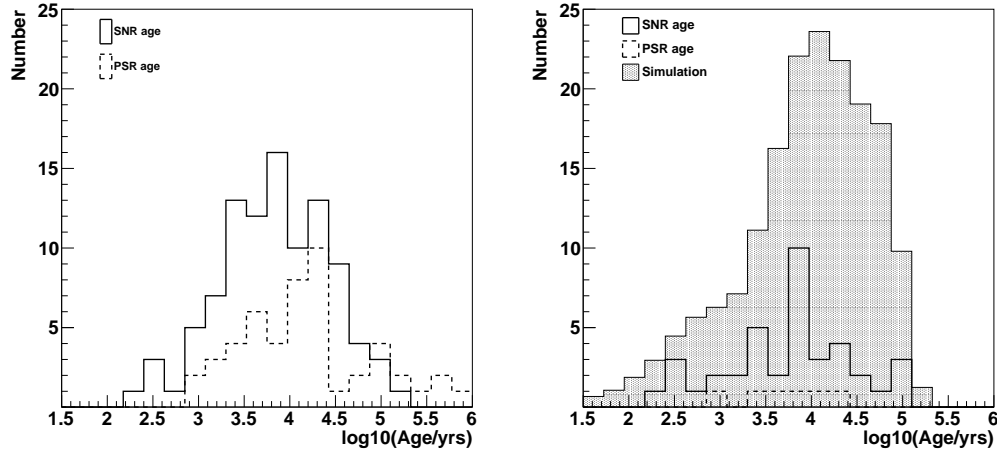
Figure 5.4.: Distribution of source ages. Left: All sources in the SNRcat with an age estimate. Right: Shell-type SNRs and the model prediction (ModelII, see section 4.5.5). If a range of age values is given, the arithmetic mean is assumed.

As it has been shown in the previous chapters, these solutions may not be able to cover more complex scenarios than the expansion of the blast wave into a homogeneous medium and should be taken with care. This is especially true as in most cases the required model parameters, such as ambient density or SN ejecta mass, are only poorly known and also the distance measurement is usually attributed with considerable uncertainties.

In four cases (SN1006, Kepler's SNR, Tycho's SNR, Crab Nebula), astronomers of ancient times have recorded SN events whose remnants we can observe today so that we are in the lucky position of knowing the precise age of those sources. This makes them invaluable for SNR astrophysics.

Again, if a pulsar can be associated an independent estimate can be given. The guess on the pulsar age is usually given by its characteristic age, which derives from the theoretical expectation of the decrease in pulsar spin-down period (see e.g. [Taylor and Manchester, 1977]). However, the reliability of this quantity as an age estimator is doubtful (see [Kaspi et al., 2001]) and tends to overestimate the pulsar age.

In the left panel of Fig.5.4, the age distributions for the whole SNRcat are shown. As one can see in Fig.5.2, the estimated age distribution of the SNRs themselves peaks at ~10kyrs after which it quickly declines. Characteristic PSR ages extend to far larger values and exceed 1Myr.

One can find the analogous plot for the subset of shell-type SNRs together with the predicted distribution from ModelII in the right panel of Fig.5.4. The distributions are in agreement, but a quantitative statement is difficult to make
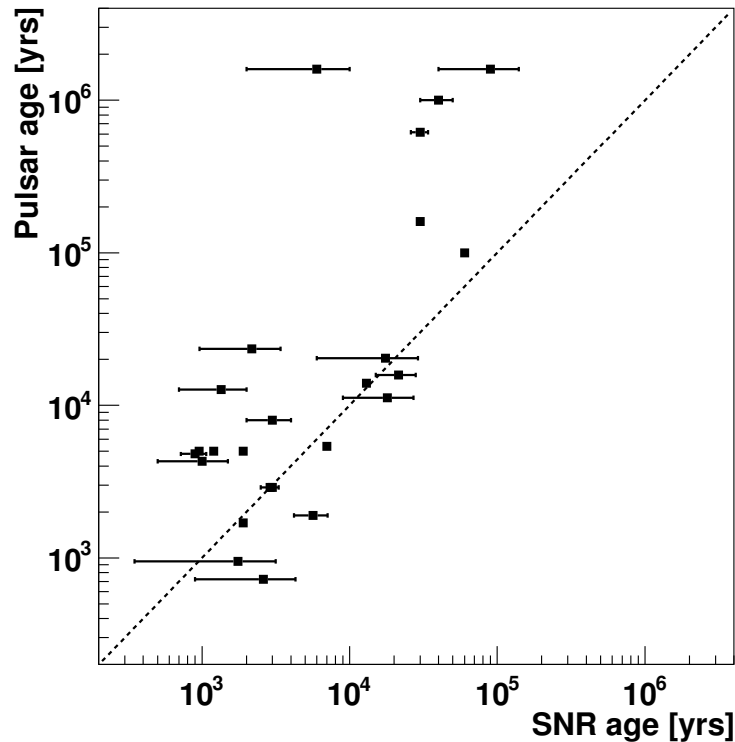
Figure 5.5.: Correlation between age estimates of SNRs and that of their associated pulsars.

since the set of literature age-estimates is very incomplete. However, the maximum values of observed and simulated distributions agree within 40%. The selectional bias of the cut in radio surface brightness has a smaller impact in this case compared to the situation for the distance estimation. That is, this bias mirrors a geometric effect which, in first approximation, is independent of the source age.

In 25 cases, both estimated pulsar and SNR ages are given and Fig.5.5 shows the corresponding correlation plot. The two different age estimations are poorly correlated, especially for older remnants the pulsar age is systematically higher than the estimate for the SNR itself. Therefore, I rely only on the direct SNR age values that are provided by SNRcat.

5.1.4. Source Extension

Fig. 5.6 shows the distribution of source radii from radio observations. Note that here the distribution of effective radii, as defined in section 5.6, is shown.

There is no clear trend or difference between the extension distributions of
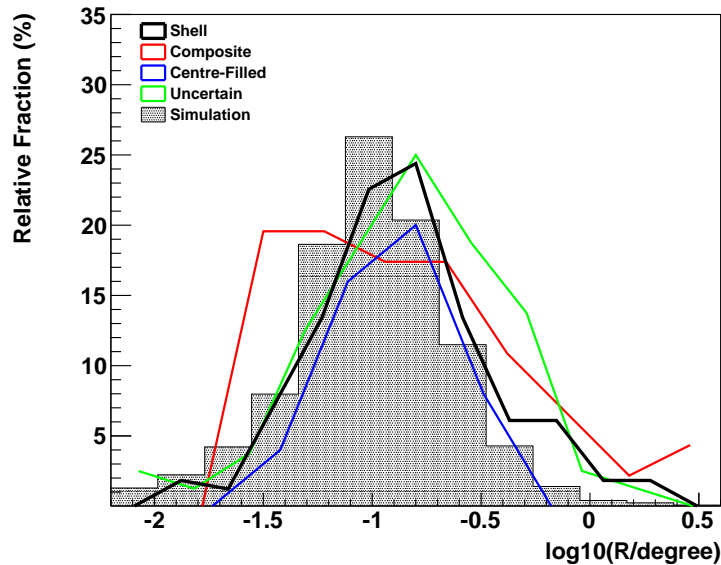
Figure 5.6.: Source radius distribution for the four different morphological SNR sub-groups. Also, the simulated prediction is plotted (ModelII).

the four morphological SNR sub-groups. One might state that the distribution of composite SNRs seems a bit broader and the one of the 'Uncertain' category extends to somewhat larger extensions. Also, the model prediction ('Simulation', ModellII) is shown in this plot. Compared to the measured distribution of shell-SNR extensions it is somewhat shifted to lower values. This again is a result of the hard cut on the surface brightness which, compared to real observations, discards too many bright but extended sources.

5.1.5. Radio Flux

For most sources a flux density point at 1GHz is provided. In many cases, this value results from the extrapolation of spectra measured below or above this frequency.

In Fig.5.7, radio flux density distributions for the different SNR morphology types are shown. The distribution for shell-type SNRs peaks at about 5Jy, the other kinds show distributions that are shifted to higher flux densities. Especially the composite-SNRs show elevated flux densities which might be caused by the additional radio emitter, the PWN, in the centre of the source. Again, the simulated distribution (Modell II) is displayed in this plot. As one can see, the simulation is able to approximate the measured shell-SNR distribution (although it represents a somewhat pessimistic scenario).
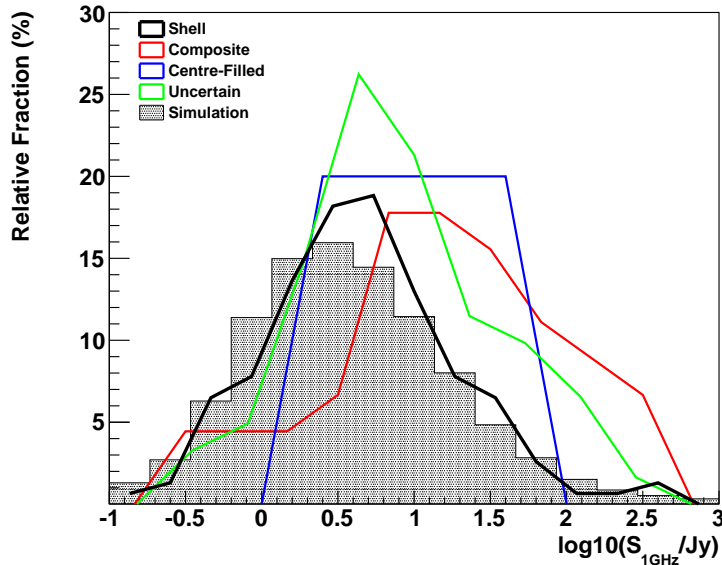
Figure 5.7.: Radio flux density distribution for the different SNR morphology types. Additionally, the simulated prediction is shown (ModelII).

5.2. Source Selection

In this study, only sources within the H.E.S.S. galactic plane survey (HGPS) region are considered. This survey region is populated by ≈ 70 known H.E.S.S. sources. Hence, there is potential for positional overlap of SNRcat sources with H.E.S.S. objects, see Fig.5.8, either physically related or not.

In order to obtain a clean sub-sample of SNRs in a sense that there is no signal contamination from nearby or overlapping unrelated H.E.S.S. sources, an adequate selection method has to be applied to the SNRcat source sample.

Of course, some of these H.E.S.S detections in the galactic plane have been associated with galactic SNRs, but for the most part the situation is unclear in that regard. Known H.E.S.S. (but also MAGIC and VERITAS) SNR-shells are excluded from the analysis sample and instead their published properties are used in the discussion.

Previous work ([Bochow, 2011a]) applied a source selection scheme where a fixed minimum distance between candidate SNR and H.E.S.S. source was required, see Fig.5.9. If the outer boundary of the Green's catalogue source would fall within $0.5°$ of the outer boundary of the H.E.S.S. source, the object was removed from the source sample.

From the Green's catalogue [Green, 2009] (which is a subset of the SNRcat consisting of 273 Radio-SNRs), a source sample of 60 SNRs was obtained.

While this method is a viable and straight-forward approach, it has the caveat that it does not take the source intensity into account. The signal leakage,
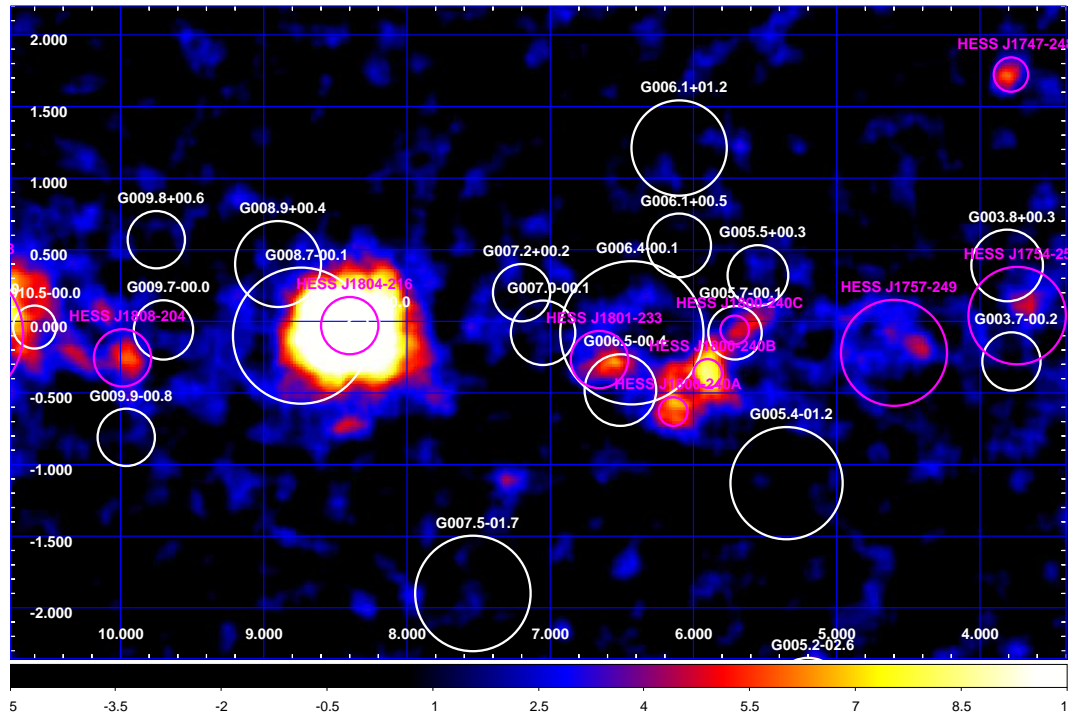
Figure 5.8.: Significance map of a complex region in the inner galactic plane as seen with H.E.S.S. Magenta: H.E.S.S. detections and emission hot spots. White: SNRs from SNRcat.
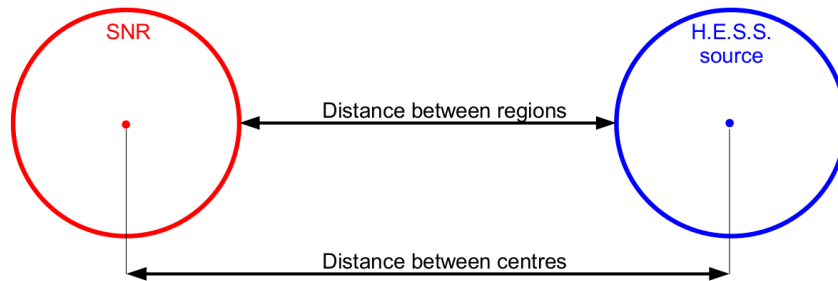
Figure 5.9.: Previous selection scheme based on a fixed cut on the minimal angular distance of 0.5° between source regions. Extracted from [Bochow, 2011a].

mediated by the H.E.S.S. PSF, depends strongly on the source excess, as it is schematically shown in Fig.5.10: If a source is a strong VHE gamma-ray emitter, the PSF is scaled up and the tail of the signal distribution causes an excess at larger angular distances from the source than in the case of a weak emitter.

Hence, this selection scheme with a fixed angular distance of 0.5° might be too conservative with respect to faint H.E.S.S. sources and too loose for very bright objects. This can be seen in Fig.5.11 which shows the significance map (*std zeta*
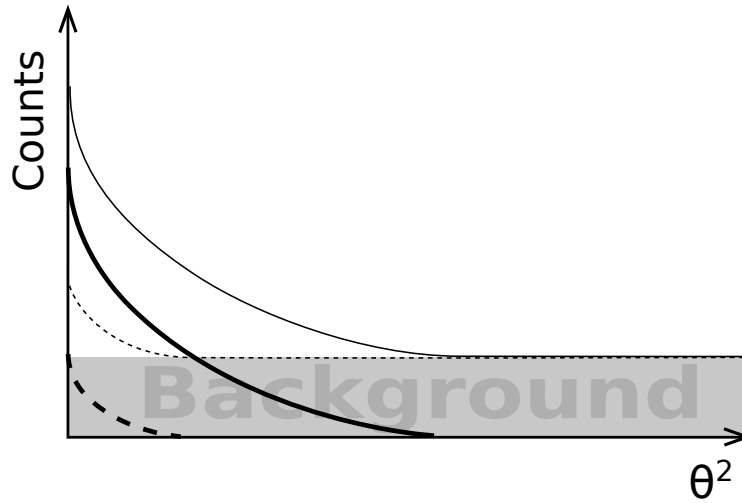
Figure 5.10.: The angular distance where signal leakage can occur depends on the source brightness. Dashed: faint source, solid: bright source. Thin: Count Distributions, thick: Excess distributions. The bright source signal is a scaled up version of the faint signal.

cuts, $0.2°$ correlation radius) of a region close to HESS J1825-137 (large source to the left): Due to its proximity to HESS J1818-155, the SNR G015.9+0.2 (red) is removed from the sample while G016.0-0.5 (yellow) is retained even though a larger signal contamination might be expected for this source.

This problem can be avoided if the source selection takes real signal information into account. In this study, a selection scheme is applied that makes use of 'deselection' regions which are derived from the HGPS significance maps. These regions are given by significance contours, which are only calculated around known[2] H.E.S.S. sources (see Fig.5.12). The algorithm to obtain the deselection regions works as follows:

1. define a threshold significance σ_T

2. go to the position of a known H.E.S.S. source position on the significance map

3. obtain the significance σ_i of the neighbouring pixels.
   If $\sigma_i \begin{cases} > \sigma_T & \text{add pixel to deselection region. Repeat (3) with adjacent pixels.} \\ \leq \sigma_T & \text{stop iteration around this pixel.} \end{cases}$

4. Fill up holes and artefacts[3].

---

[2]The list of known H.E.S.S. sources used in this method can be found in Appendix B.

[3]Technically, this is obtained by applying the so-called *dilate* and *erode* operations, that are commonly used in image processing(see e.g. [Gonzales and Woods, 2008]).
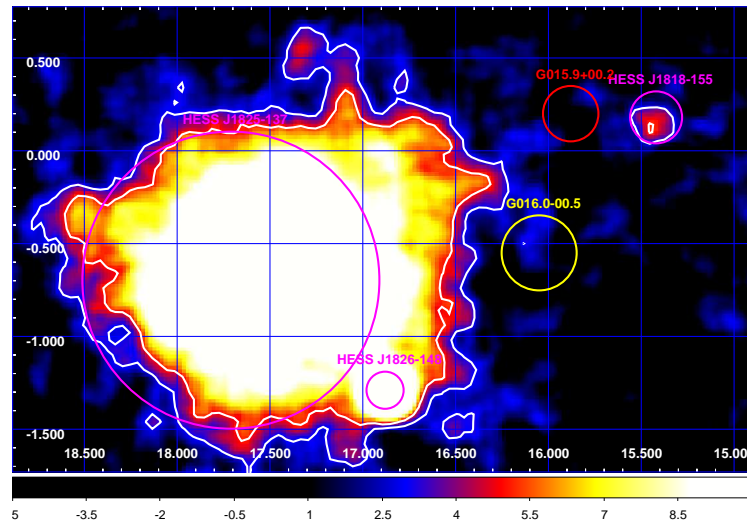
Figure 5.11.: Significance map of a region close to HESS J1825-137. The contours represent the 3 and 5σ levels. By applying a fixed minimum angular distance cut of $0.5°$ as the source selection, the SNR G15.9+0.2 is removed while G16.0-0.5 is retained, even though it is not obvious that the ON-region of G15.9+0.2 (red) suffers of greater signal contamination from HESS J1818-155 than G16.0-0.5 (yellow) from HESS J1826-148 and HESS J1825-137.

This algorithm produces contingent regions around known H.E.S.S. sources that extend out to the predefined significance level σ_T.

If the ON-region (see section 5.4) of a given SNRcat source encompasses one or more pixel from a deselection region, this source will be excluded from the source sample. This procedure is illustrated in Fig.5.12. In this example, G015.9+00.2 is in the *loose* but not in the *conservative* sample. G16.0-0.5 is excluded from both samples. Note that the deselection regions are larger than one would expect from Fig.5.11. The reason for this is that Fig.5.11 shows the $0.1°$ correlated significance map while the deselection regions are derived from those with a correlation radius of $0.2°$, resulting in large and thus rather conservatively selecting masks.

The size of a resulting region is determined by the σ_T value as well as the correlation radius that is used in the map creation. Lower values of σ_T and higher values of the correlation radius yield larger regions and thus a more conservative source selection.

Here, this is done on significance regions using a $0.2°$ correlation radius which results in rather conservative deselection regions.

One of the key-points of this method is that significances exceeding σ_T are only added to the deselection region if they are connected to a known H.E.S.S. source. Hence, it is possible for analysis regions to feature significances larger
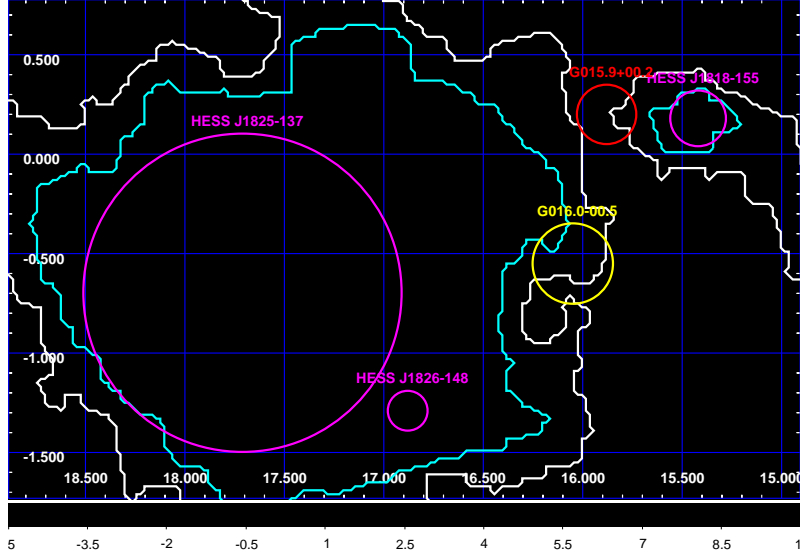
Figure 5.12.: Source selection: The deselection regions, as given by black-listed pixels, are shown with white (*conservative*) and cyan (*loose*) contours. On-regions are represented by circles, for illustration the same sources as in Fig.5.11 are shown.

than σ_T.

In the following, two sets of sources will be considered, corresponding to two different values of σ_T:

- $\sigma_T = 2$, deselection regions will be large and the resulting selection therefore *conservative*

- $\sigma_T = 4$ smaller deselection regions than in the previous case which results in a more *loose* selection.

Fig.5.13 shows the significance distributions over all pixels in the HGPS significance map[4](red) and those outside the deselection regions (black) for the *loose* (left) and *conservative* (right) selection. One can see that above the value of σ_T the majority of pixels is excluded. However, there is still a steep tail towards higher significances because the deselection regions are only defined around known H.E.S.S. sources. Because the deselection regions are smoothed, there is no sharp transition at $\sigma = \sigma_T$.

Exemplary deselection regions for both the *loose* and *conservative* selection are shown in Fig. 5.14.

The two sets are used to estimate the possible systematic influence of the source selection method on the results. They encompass 104 and 138 sources for the *conservative* and the *loose* sample, respectively. The lists of sources can

---

[4]Assuming TMVA analysis with *std* cuts and a 0.2° correlation radius.
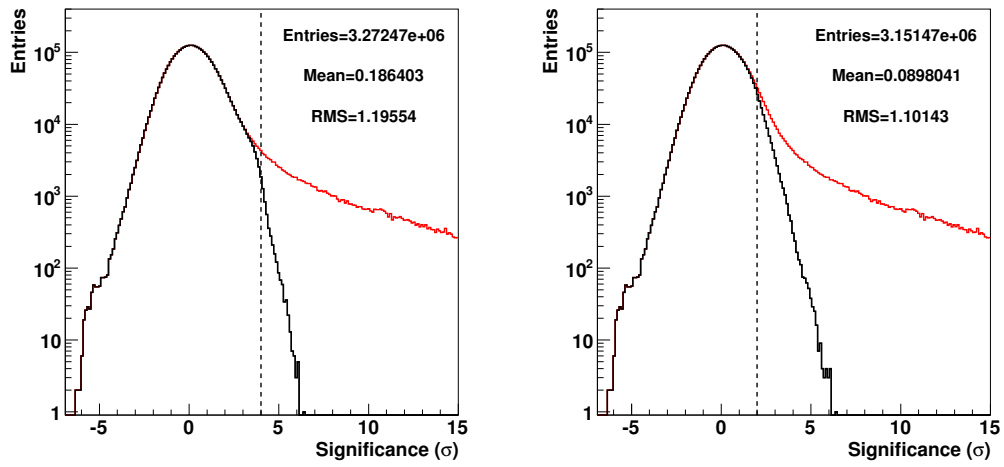
Figure 5.13.: Pixel significance distributions from the HGPS significance maps off all pixels (red) those outside the deselection regions (black). Left: With *loose* deselection regions, Right: with *conservative* ones. The vertical lines indicate the values of σ_T.

be found in Appendix B, Tab.B.1. Tab.5.2 lists the type composition of the two samples.

	Type				
	S	C	F	?	total
loose	88	17	4	29	138
conservative	66	14	4	20	104

Table 5.2.: Composition of the analysis samples.

Figure 5.14.: Significance map (assuming TMVA analysis with *standard* cuts and a 0.2° correlation radius) overlaid with the deselection maps that are used to pick the *conservative* sample ($\sigma_T = 2$, green contours) and the *loose* sample ($\sigma_T = 4$, white contours), respectively. Known H.E.S.S. sources are given in red. One can see that, in contrast to significance contours, distant regions of elevated significance values are still allowed as possible test positions.

5.3. Flux Upper Limit Calculation

The sample of sources that is obtained by the source selection method described does not contain H.E.S.S. detections. Therefore, the investigation of the spectral properties of those SNRs is limited to a derivation of flux UL values.

Two ingredients are needed for the calculation Flux ULs, namely a number of expected counts from the source assuming a specific spectral shape of the emission as well as an upper limit on the signal counts from the ON-region.

The former requires the definition of a reference flux,$\Phi_{ref}(E)$. If this is given, it is possible to estimate the amount of expected excess counts n_{exp} that would be recorded from a hypothetical source after an observational time T and a set of observational parameters q, including the observational zenith angle, the optical efficiency of the telescope, atmospheric conditions, the offset of the source to the observation position, the telescope multiplicity and so on. Formally, the number of expected signal counts is given as

$$n_{exp} = \int_{E_0}^{\infty} dE \; \Phi_{ref}(E)A(E,q)T, \tag{5.1}$$

where A is the energy-dependent effective area of the instrument which implicitly contains the information about the whole parameter set q.

Since H.E.S.S. records its data on a run-by-run basis, equation (5.1) can be written as

$$n_{exp} = \sum_r n_{exp,r} = \sum_r \int_{E_0}^{\infty} dE \; \Phi_{ref}(E)A_r(E,a)T_r \tag{5.2}$$

where the index r symbolises the individual observation runs. The shape of the reference flux function $\Phi_{ref}(E)$ should reflect the expected nature of VHE emission from SNRs. In the following, a simple power-law with a spectral index of $\alpha =$2.1 is chosen which is probably typical for young and medium aged SNRs while older SNRs might show considerable spectral steepening. However, in order to keep the analysis as simple and uniform as possible, this spectral shape is assumed for the whole sample.

The second component, the upper limit on the excess counts n_{UL}, is obtained using the approach developed by [Rolke et al., 2005]. This method obtains confidence intervals based on the logarithmic profiles of the likelihood function

$$L(S,B|ON,OFF) = \frac{(S+\alpha B)^{ON}}{ON!}e^{-(S+\alpha B)} \cdot \frac{B^{OFF}}{OFF!}e^{-B} \tag{5.3}$$

which describes the likelihood that the number of ON and OFF counts (which are assumed to be Poisson-distributed) are a realisation of S signal and B background events.

A detailed description of this method can be found in [Rolke et al., 2005].

The knowledge of n_{UL} and n_{exp} allows the calculation of the UL on the flux, because the quotient n_{UL}/n_{exp} represents a rescaling factor for the spectral assumption $\Phi(E)$. For instance, if the UL on the expected signal counts is only half of what would be expected from a reference spectrum $\Phi(E) = \Phi_0 f(E)$, then the normalisation has to be reduced by a factor 0.5 accordingly in order to obtain the upper limit on the differential flux as

$$\Phi(E) = \frac{n_{UL}}{n_{exp}} \cdot \Phi_{ref}(E) \tag{5.4}$$

Note that the normalisation Φ_0 is also used in the derivation of n_{exp} (Eq.5.1) and therefore cancels out, so that only the spectral shape $f(E)$ plays any role.

It is also important to mention that n_{UL} and n_{exp} have to be obtained from identical energy intervals. Here, all events above the safe energy threshold are taken into account and the corresponding energy range is used to calculate n_{exp}.

A similar energy range is used for the calculation of the UL on the integral flux. In the following, integrated flux ULs between 0.5 and 100TeV

$$\Phi_{Int} = \frac{n_{UL}}{n_{exp}} \int_{0.5\text{TeV}}^{100\text{TeV}} dE \Phi_{ref}(E) \tag{5.5}$$

at the 99% confidence level will be investigated.

5.4. Analysis Method

Software and Selection Cuts

All analysis results that will be shown in this document are obtained with the *hap-13-06* analysis software, applying the TMVA technique with *standard cuts* (see section 1.3.3). This cut configuration is chosen because it is expected that the spectral index of the gamma-ray emission may vary considerably from source to source, warranting neither a configuration optimised for either hard sources (*hard cuts* nor soft sources (*loose cuts*).

ON-Region Definition

The size of the ON-region has to be chosen in a way that the signal-to-background ratio is optimal. In the following, ON-regions are determined by the radio extensions of the according sources. An effective radius R for each source is defined throughout this work as

$$R = \begin{cases} R^{\text{SNRcat}} & \text{if circular} \\ \sqrt{R_{\text{maj}}^{\text{SNRcat}} \cdot R_{\text{min}}^{\text{SNRcat}}} & \text{if elliptic} \end{cases} \tag{5.6}$$

where R^{SNRcat} are given by the diameters provided in SNRcat.

The ON-regions R_{ON} are then calculated by the adding a conservative estimate of the instrument PSF (see section1.3.3) to the effective source extension R:

$$R_{ON} = R + 0.1°$$

This is done to collect the majority of the source signal that is smeared out by the limited directional resolution. The ON-region should not be too large, however, since then the signal-to-backround ratio becomes suboptimal. Thus, I decide for this ON-region definition as a compromise. In order to prevent undesired systematic effects, a minimum ON-region size, given by the θ^2-cut in the event selection, is imposed.

This definition results in circular ON-regions which seems to be an acceptable simplification as the source ellipticity has no major effect on the results (see Appendix B).

Effective Areas

Full-enclosure effective areas (see section1.3.5) are assumed for the whole sample in order to guarantee an uniform analysis. However, this uniformity comes at the price of a somewhat decreased sensitivity for point-like sources.

Event Offset

In order to select only well-reconstructed events, a cut on the angular distance from observational direction to reconstructed shower distance is applied. This cut is usually called the Ψ-cut. In this study, the cut is at

$$\Psi = 2.7°.$$

Data Quality Selection

The data quality selection applies the standardised and automated method described in chapter 2, using the *spectral* set of selection cuts.

Background Estimation and Basic Analysis Quantitites

Two analysis pipelines were applied to analyse the SNR sample:

Method I uses the Ring-Background method, and makes use of the standard HGPS maps, for which the *Adaptive Ring* method has been applied with a constant thickness of $0.44°$, a minimum inner ring radius of $0.7°$ and a maximum outer ring radius of $1.7°$.

Here, the data is in an already binned form: for each pixel ON as well as OFF counts are calculated. The same holds for the α-value because the ring geometry is adaptable and might change from one pixel to the other.The base quantities thus have to be calculated pixel-wise and are given by:

- $N_{ON} = \sum_i N_{ON,i} \in A_{ON}$

- $N_{OFF} = \sum_i N_{OFF,i} \in A_{ON}$

- $\alpha = \sum_i Exposure_{(ON,i)} / \sum_i Exposure_{(OFF,i)} \in A_{ON}$

Here, i represents the map pixels. This method is very fast as the analysis is performed from the already pre-produced HGPS maps.

Method II uses the Reflected-Background method (see section 1.3.4) and is a standard analysis dedicated to each source and the base parameters are given by:

- $N_{ON} = \sum_i N \in A_{ON,i}$

- $N_{OFF} = \sum_i N \in A_{OFF,i}$

- $\alpha = \sum_i 1/m_i$

where i is the number of observation runs, m_i is the number of OFF-regions per run and A_x symbolises the angular surface of the ON as well as the OFF regions.

As already mentioned, both analyses only use events above the safe energy threshold (see section 1.2).

5.5. Analysis Results

The detailed analysis results for each source are listed in Appendix B, Tab.B.1. Some cross-check diagrams for the two analysis methods are also shown there. Unless noted otherwise, analysis results from Method I (see previous section) will presented in the following.

5.5.1. Significance Distribution

Fig.5.15 shows the significance distributions for both the *conservative* and the *loose* sample (see section 5.2) while Fig.5.16 shows the cumulated significance distributions for the four different morphology types of SNRs.

The following observations can be made:

- As expected, no significant sources are found.

- The shell and composite type distributions are shifted to higher significance values compared to those of uncertain or centre-filled shape in radio. The emission from ON-regions coincident with composite-type SNRs does not show higher significance values than the other species, as might optimistically expect (compare the elevated radio flux from this source type shown Fig.5.7).

- Most interestingly, the distributions are not centred around zero, which would be expected if there was no signal in the analysis ON-regions. Gaussian fits yield mean values of 0.72σ and 1.03σ for the *conservative* and *loose* source sample, respectively.
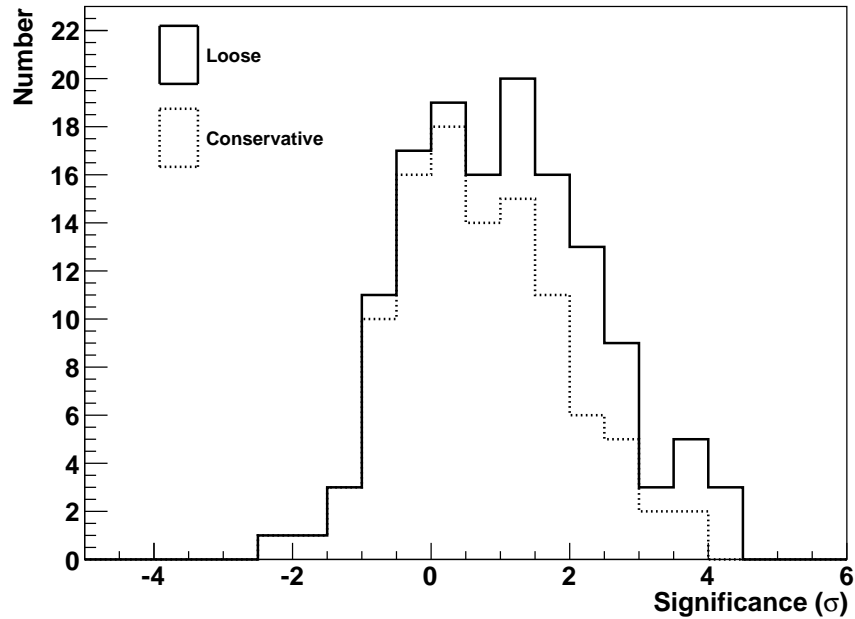
Figure 5.15.: Significance distribution of the SNRcat sample after selection. Solid line: *loose* sample, dashed line: *conservative* sample.

Interpretation of the Significance Offset

The positive offset in the significance distributions may be caused by several effects:

- (i) systematic effects from the source selection method

- (ii) systematic effects from the analysis

- (iii) physical effects not connected or associated with the SNRcat sources

- (iv) physical effects connected or associated with the SNRcat sources

In order to address these possibilities, a study using randomly generated test positions has been performed. These random positions are obtained by shifting the values given in the SNRcat (before selection) with Gaussian variates. The so-obtained randomised analysis regions are then subjected to the previously
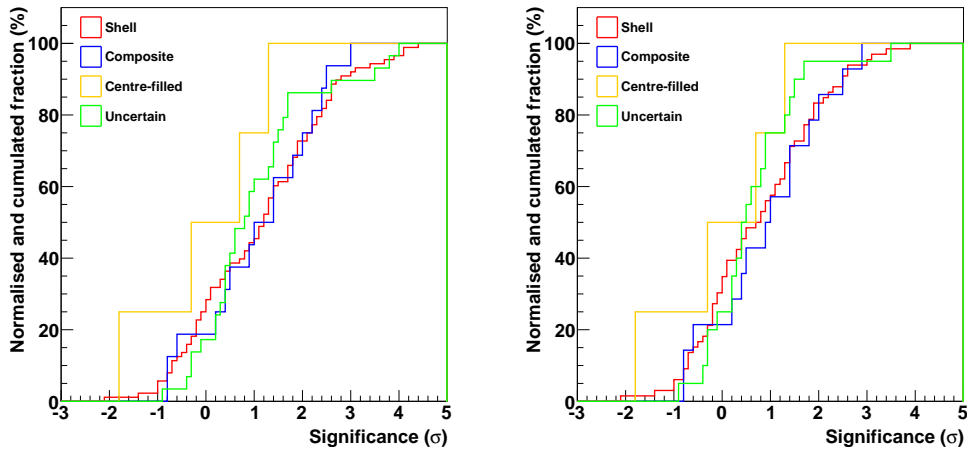
Figure 5.16.: Significance distribution of the SNRcat sample after selection for the different morphology types. Left: *loose* sample, right: *conservative* sample.

described selection mechanism and analysis. One random realisation of this procedure is shown in Fig.5.17
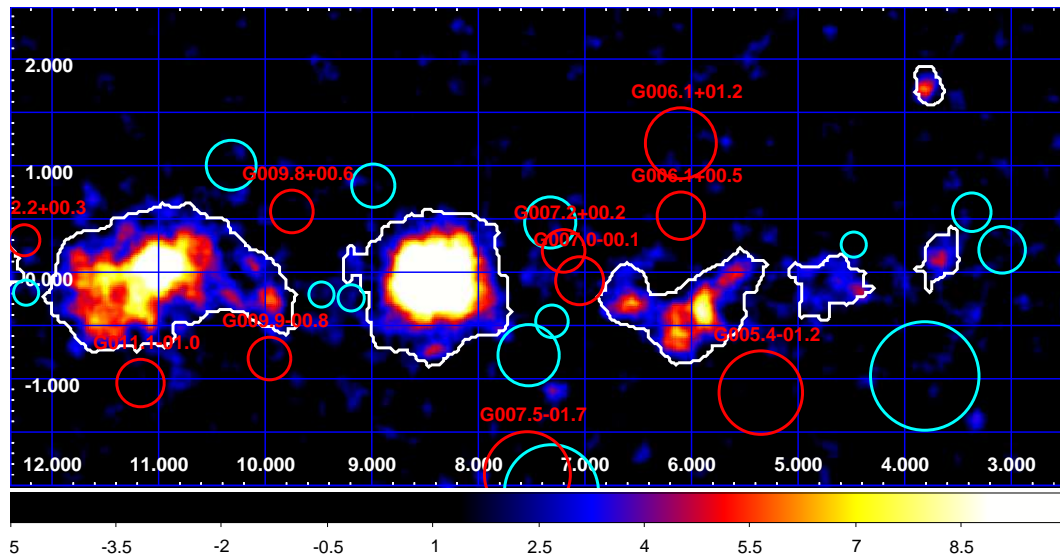
Figure 5.17.: Significance map of the latitude range $\{3°, 12°\}$. White contours represent the *loose* deselection regions, red circles are the ON-regions of the real SNRs after selection, cyan circles indicate their randomly generated counterparts.

Care has to be taken in the choice of the the width of the scattering Gaussians, referred to as σ_l, σ_b and σ_s, respectively. These quantities should not

be too small (because in this case the original distribution would be reproduced) nor too large (since then characteristic features in the l,b and size distributions would be washed out). In the following, the values for $\{\sigma_l, \sigma_b, \sigma_s\} = \{10°, 0.3°, 0.04°\}$ are chosen.

In this study, a total of over 100000 random source positions has been investigated with the ring method and a total of over 1000 with the reflected BG method. Latitude, longitude and size distributions of 1000 random positions are shown together with the real sample in Fig.5.18. As one can see, the randomised test positions reproduce the corresponding source distributions.

In principle, contributions (i), (ii) and (iii) should also be present in the significance distributions derived from the randomised source samples. They can thus be used to estimate if and to what amount the shift in significance is caused by effect (iv).
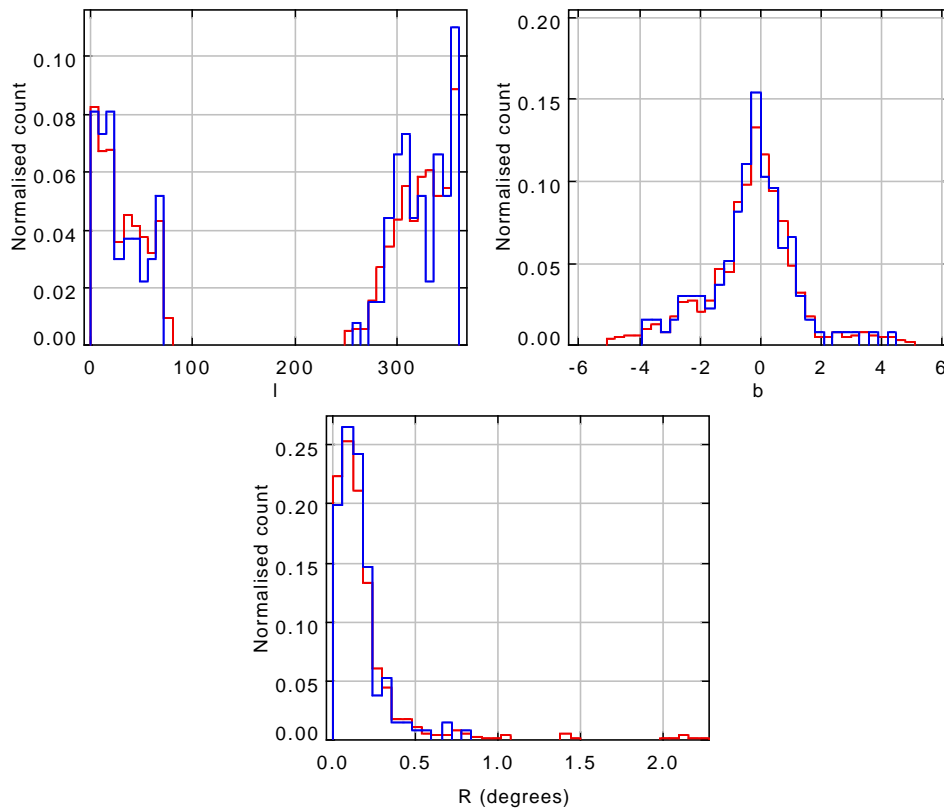
Figure 5.18.: Longitude (left), latitude (right) and size distributions of 1000 random positions (red) as well as the real sample (blue) after the *loose* selection.

The resulting cumulated significance distributions are displayed in Fig.5.19. It can be seen that the median values of the random significance distributions are not at zero, which would correspond to a sample of test positions where only

background fluctuations were present. Just like the significance distributions of the real SNRcat sources, the median values of the random sample are, although to a considerably smaller extent, shifted towards positive values with $p(0.5) \sim 0.4$ for the *loose* and $p(0.5) \sim 0.2$ for the *conservative* sample.

One can estimate the probability that the significance distribution from the real source positions and that of the random sample originate from the same probability distribution (which in this case is the null-hypothesis) with a Kolmogorov-Smirnoff test (Kolmogorov). The null-hypothesis can be dismissed on the 3.8σ and 2.8σ levels for the *loose* and the *conservative* samples, respectively. Method II yields very similar significance values of 3.9σ (*loose* sample) and 2.8σ (*conservative* sample).
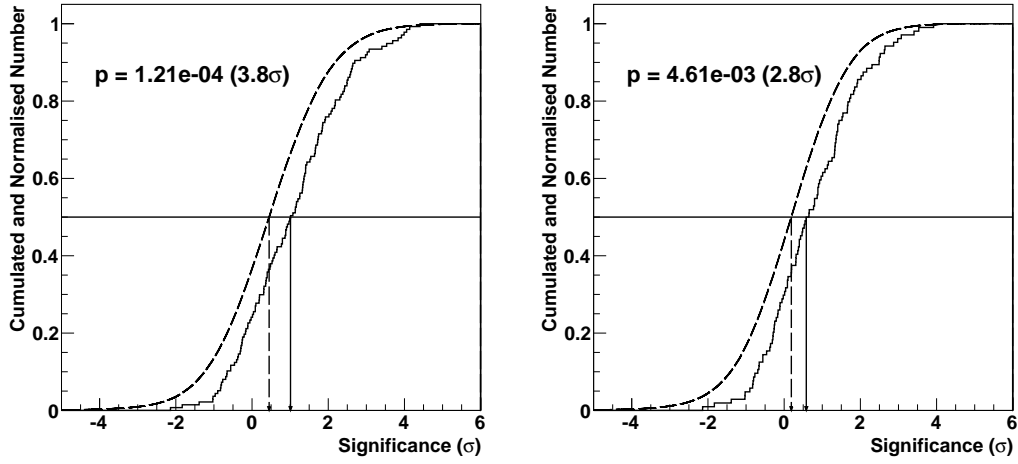
Figure 5.19.: Cumultative significance distributions. Solid: real source sample, dashed: randomly generated analysis regions. Left panel: *loose* sample selection, right panel: *conservative* selection. Arrows indicate median values.

Another possibility to estimate the significance of the shift is to perform a stacking analysis. In this method, counts and exposures of all ON and OFF regions in a sample of i sources are given by

$$N_{\mathrm{on}} = \sum_i N_{\mathrm{on},i} \tag{5.7}$$

$$N_{\mathrm{off}} = \sum_i N_{\mathrm{off},i} \tag{5.8}$$

$$\mathrm{Exposure}_{\mathrm{on}} = \sum_i \mathrm{Exposure}_{\mathrm{on},i} \tag{5.9}$$

$$\mathrm{Exposure}_{\mathrm{off}} = \sum_i \mathrm{Exposure}_{\mathrm{off},i} \tag{5.10}$$

$$\alpha = \mathrm{Exposure}_{\mathrm{on}}/\mathrm{Exposure}_{\mathrm{off}} \tag{5.11}$$

This results in a stacked significance and flux UL value for the whole sample. By performing this method for a number of randomly generated source samples, a distribution of stacked significances is obtained which follows a Gaussian shape (see distributions in Fig.5.20).

As can be seen, the stacked significance distribution that follows from a *loose* selection of the random test positions is fitted by a Gaussian function with a mean value of σ_S=4.1, which indicates that this selection might be too loose and the so-selected ON-regions might be contaminated with signal spilled over from known H.E.S.S. sources. In contrast, the fitted mean of the *conservative* selection sample is at 0.6, so this sample seems to be rather save in this regard.
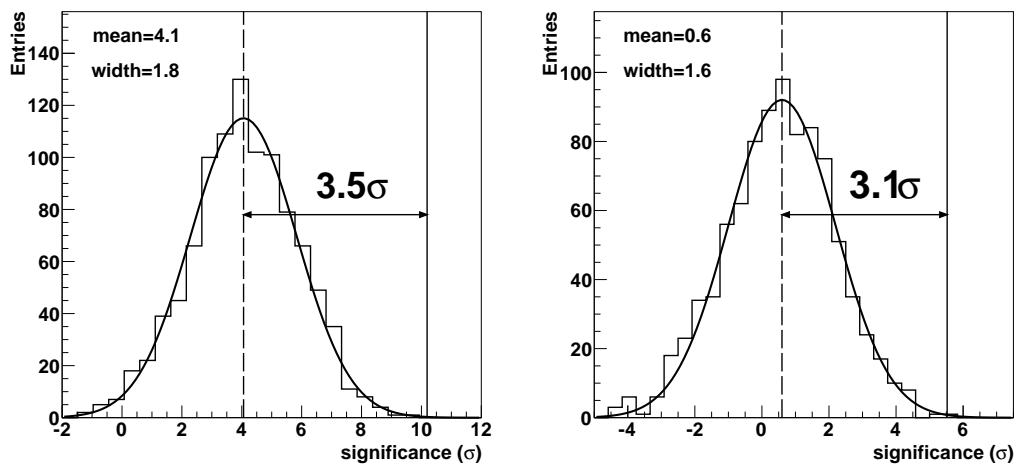
Figure 5.20.: Stacked significance distributions for randomised source catalogues in the case of *loose* (left panel) and *conservative* (right panel) source selection criteria. Gaussian fit function are shown together with the according best-fit parameters. Stacked significance values for the real source sample are indicated by the vertical lines.

The stacked significance distribution of the random sampled source catalogues allows it to estimate the probability of the corresponding real value (vertical lines in Fig.5.20) being just a statistical up-scatter. The distances between the mean randomised and the real stacked significance values are 3.1σ and 3.5σ for the *conservative* and *loose* selection, respectively. These numbers lie between the results from the Kolmogorov-Smirnoff test for the two samples. Interestingly, the results for the *conservative* and *loose* selection are very close, independently of a possible ON-region contamination in the case of the *loose* selection.

A possible latitude dependency of the significance shift was investigated. To that end, the real as well as random samples after the *loose* selection were divided into two latitude subsets each. Fig.5.21 shows the cumulated significance

distributions for the real sample (solid) and the randomised sample (dashed) for test position at galactic latitudes $b < 1°$ (black) and $b > 1°$ (red).
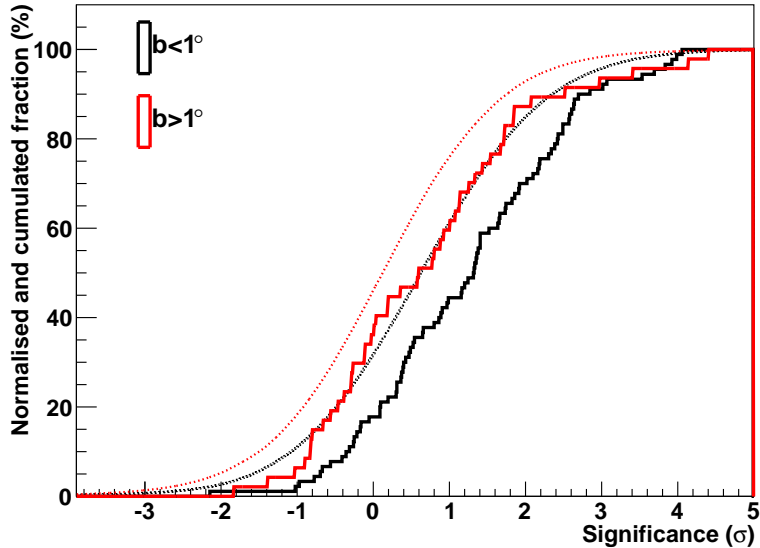
Figure 5.21.: Cumulated significance distributions of the real (solid) and the randomised samples (dashed). The sets were divided in sources that are within $1°$ of the galactic plane (black) and those that are farther away (red).

As one can see, there is a clear trend to higher significances closer to the galactic plane in the real as well as the simulated sample. The difference in median values between the two subsets of data is $\Delta q(0.5)=0.69\sigma$ for the real sample and $\Delta q(0.5) =0.47\sigma$ for the randomised sample.

This latitude-dependent shift in the significance distributions may be attributed to different factors such as

- (a) the lower exposure at higher galactic latitudes. However, this explains the difference in significance values only in the presence of a large scale and low-level emission.

- (b) an increased chance to randomly coincide with a region corresponding to any kind of unknown, galactic VHE source. In this case, the larger difference in median values for the real source sample might be explained by the fact that those positions are coincident with known radio SNRs that at least have the possibility for VHE emission.

- (c) a diffuse VHE emission component whose latitudinal scale is comparable or small compared to the dimension of the background extraction region. This factor is complementary to (a).

Again, by treating the significance distribution from the random sample as the null hypothesis in the statistical tests, also these latitude-dependent effects should be accounted for.

The origin of the shift in the significance distribution remains unclear and is currently still under investigation. Of course, this feature is not detected significantly and it is not possible to draw strong conclusions from it. However, an optimistic interpretation would account a faint VHE emission from the radio SNR for this effect. While not significant individually, these sources would cause a combined signal between the 3σ and 4σ confidence levels, depending on the source selection. The somewhat higher significance values for the *loose* selection would then be simply the result of a larger SNR number in this sample.

5.5.2. Flux Upper Limit Distribution

Resulting distributions of the integrated 99%CL flux upper limits above 500GeV (see Eq. 5.5), assuming power-law shaped spectra with indices of $\alpha = 2.1$, are shown in Fig.5.22.

The distributions are peaked around $8 \cdot 10^{-13} \mathrm{cm}^{-2}\mathrm{s}^{-1}$ which reflects the 1-2% Crab sensitivity of H.E.S.S. in the innermost galactic plane [Carrigan et al., 2013]. Those sources that are removed from the *conservative* sample do behave unremarkably and are populated around the peak of the distribution.

Model Comparison

In the bottom plot of Fig.5.22, the distribution is shown exclusively for radio-shells. Additionally, the simulated SNR flux distribution (again Model II, flux>500GeV) is shown. More precisely, three sets, corresponding to an increasingly stringent selection are shown. The lightest shaded distribution represents the whole SNR sample in the HGPS region while the medium shaded one corresponds to the subsample with radio surface brightness values larger than $\Sigma_{1GHz} > 10^{-21} \mathrm{Wm}^{-2}\mathrm{Hz}^{-1}\mathrm{sr}^{-1}$. This distribution is thus the theoretically expected counterpart to the Green-catalogue as a whole (compare to section 4.5.5). As one can see, only a small fraction of gamma-ray emitting SNRs is present in this sub-sample, so from this simulation it seems like radio-bright sources are only to a rather small fraction also gamma-bright. The dark-shaded distribution attempts to crudely emulate the source selection mechanism by removing sources which extend in radius below $0.5°$ in galactic latitude. Even though this is a rather strict cut, one can see that there is still a handful of sources expected to show fluxes above the peak of the UL-distribution, which should have been detected. As a matter of fact, there are at least two detections at such latitudes (HESS J1731-347 and Vela Jr.). Due to the very strict nature of this crude selection, the numbers would be expected to be higher overall if the real source selection algorithm instead of this crude cut was used. Therefore,
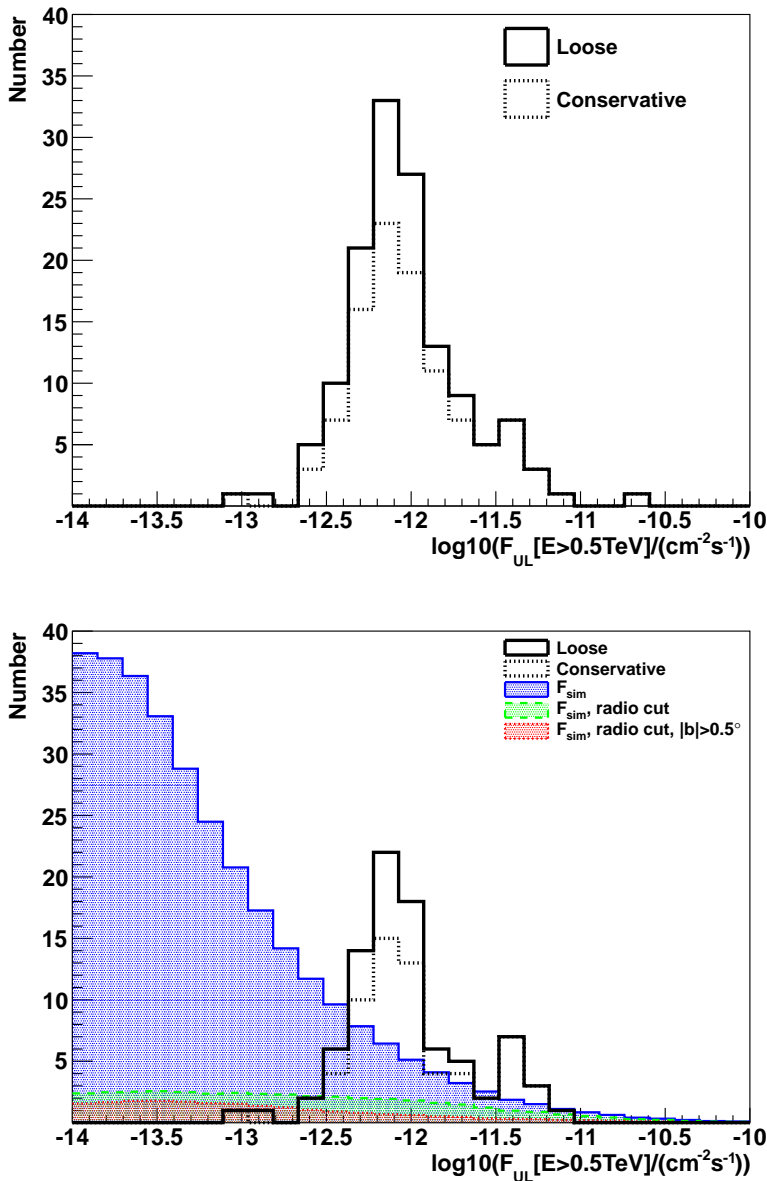
Figure 5.22.: Flux upper limit distributions. Top: All source types, bottom: Only shells. Here, also the simulated SNR flux distribution (Model II, E>0.5TeV) is shown.

one can conclude that the parameter set in Model II results in a too optimistic number of expected detections.

5.5.3. Acceleration Efficiency

One of the most important unresolved questions in the physics of SNRs is the efficiency θ at which the kinetic SN blast energy (E_{SN}) is converted into CR via DSA.

There are many theoretical models on the market that predict a relation of the gamma-ray flux to θ. One of the widely accepted ones has been forward by [Drury et al., 1994]. It allows to estimate the acceleration efficiency if the gamma-ray emission is of hadronic origin and the three parameters E_{SN}, n(ambient density) as well as d(distance to the source) are known. The model prediction on the gamma ray flux from this model is

$$F(> E) \approx 9 \times 10^{-11}\theta \left(\frac{E}{1\text{TeV}}\right)^{-1.1} \left(\frac{E_{SN}}{10^{51}\text{erg}}\right) \left(\frac{d}{1\text{kpc}}\right)^{-2} \left(\frac{n}{1\text{cm}^{-3}}\right) \text{cm}^{-2}\text{s}^{-1} \quad (5.12)$$

However, while information on d is limited, it is especially difficult to come by reliable values of n. This is a large problem in view of the vastly different CSM scenarios radio bright SNRs are expected to encounter. The simulation suggests that almost half of the radio-bright SNRs are of type SNIIP which are probably situated in a rarified stellar bubble with ambient densities of $n \leq 0.001 - 0.01\text{cm}^{-3}$, while roughly another half corresponds to SNIa. Those sources most probably see on average somewhat higher values of $n \sim 0.1\text{cm}^{-3}$, attributed with a large scatter. The situation might actually be more complex as observations of Tycho's and Kepler's SNRs (both of type SNIa) suggest a pre-modified CSM also in this scenario. To a smaller (but still huge) extent, E_{SN} is known only to a factor of a few.

In view of the large uncertainties, one can try to derive an upper limit on the product $H \equiv E_{SN}\theta n$ if a distance estimate is given. This has been previously done by [Bochow, 2011b]. The analogue distribution, reproduced with the results from the analysis described here, is shown in the top panel of Fig.5.23, together with the distribution of simulated H values. The latter is represented in analogue subsets as in Fig.5.22. As one can see, the distribution of the upper limits of H is, for shell-type radio SNRs, in the range of $\sim$0.04-2, the latter of which could be explained by an additional leptonic component. However, looking at the model prediction, it becomes apparent that the distribution is extremely smeared out which greatly limits the stringency of H with respect to physics interpretation and parameter space restriction.

To make matters worse, the simulation suggests that even in the ideal case of perfect knowledge of the parameters n, d and E_{SN}, there is still a considerable spread around the true value of θ (in Model II, the acceleration efficiency is fixed at a value of θ=0.3[5]), see the bottom panel of Fig.5.23. That is, there is an additional leptonic channel that can lead to overly large estimates of θ. On the

---

[5]The peak in bottom panel of Fig.5.23 is at a somewhat higher value of $\sim$35%. Differences are expected since the model assumes the parametrisation of [Kelner et al., 2006], while Drury et al. assumed the formalisms of [Stecker, 1971] and [Dermer, 1986]. Furthermore, the authors
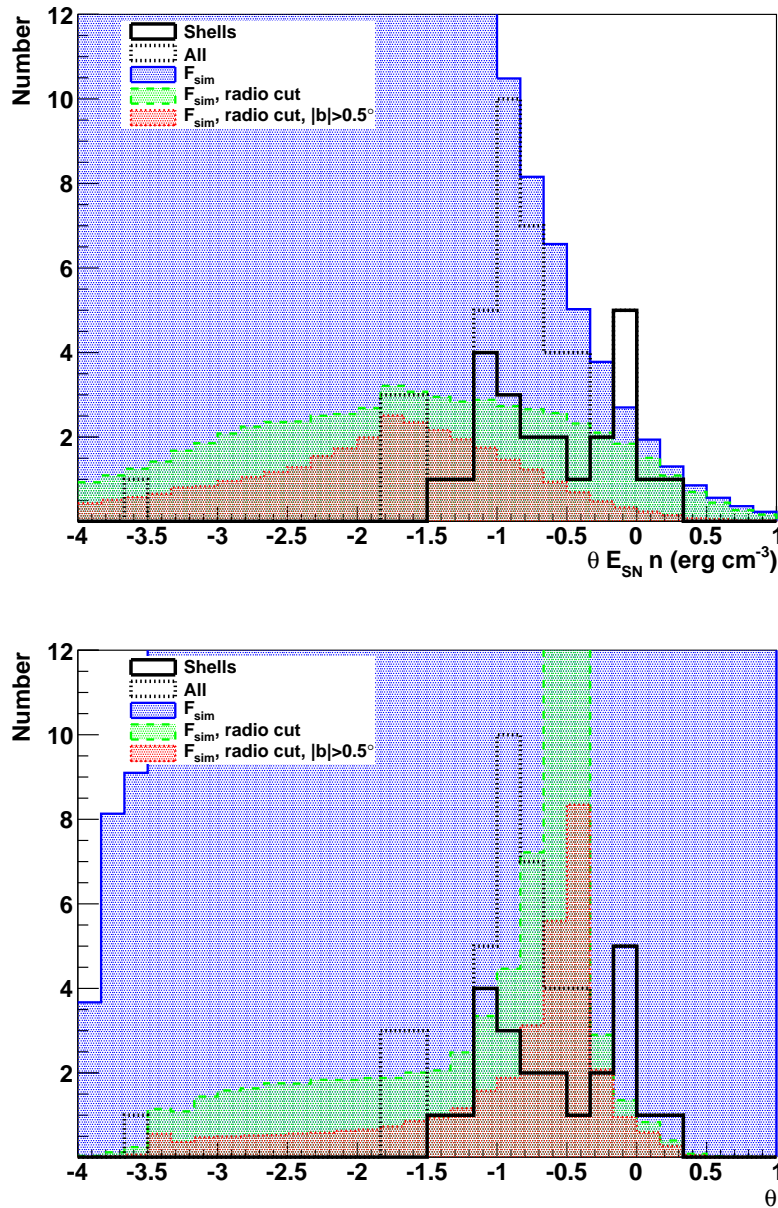
Figure 5.23.: Distribution of the upper limit on the product $E_{SN}\theta n$ (top) and θ itself (bottom, assuming $n = 1\text{cm}^{-3}$ and $E_{SN} = 10^{51}\text{erg}$). Additionally, the corresponding simulated distributions are shown.

other hand, medium-aged and old sources show particle- and gamma-ray spec-

_____

use a hadronic amplification factor of 1.5 whereas the simulation assumes a value of 1.8 (see section 3.5.2).

tra deviating from straight power-laws due to spectral energy cut-offs. This would result in underestimated values of θ because Eq.5.12 assumes a straight power-law spectrum. Note that a fixed value for θ is just a simplification; In reality some distribution would be expected and the peak should be much broader than what is shown here.

There might be the chance, however, that with the large expected sample of SNRs flux points a theoretically expected shape like in the bottom panel of Fig.5.23 could be constrained with CTA, but only if at this time there will be more reliable estimates on the remaining parameters. If not, CTA will only be able to probe the distribution in the upper panel from which it will be difficult to draw physical conclusions.

5.5.4. Source Radius Dependency of the Upper Limits

Fig.5.24 shows the flux upper limits as a function of the SNR radius as well as the eight detections of shell-type SNRs in VHE. Also, the predicted distribution from Model II is displayed together with the evolutionary tracks of the different SNR sub-types included in the simulation.

The first observation one can make is that, as expected, the UL follow the approximated sensitivity curve with source extension ($S = S_0\sqrt{PSF^2 + r^2}/PSF$ [Renaud, 2009] with PSF =0.1 and S_0 =1.5%Crab, white dotted line). Furthermore, all upper limit values are 0.5-1 order of magnitude above the bulk of the predicted SNR population. The distance is smallest in the range between $\sim$0.06° <R<0.1° where SNIa SNRs are predicted to cause a local maximum in the distribution. It is largest for extended source with radii R>0.3° where the distribution is dominated by cc-SNe which expand into thin media and are thus able to become very extended. Therefore, the simulation suggests that H.E.S.S. is most sensitive to the detection of thermonuclear SNRs.

Five out of the eight detections seem to roughly follow the ensemble of ULs and the simulated distribution. The remaining three (and brightest) sources HESS J1731-347, RX J1713-3946 and Vela Jr. are 2-3 orders of magnitude above the main part of the simulated distribution. Model II predicts 0.54$\pm$0.73 sources above 1CU (like Vela Jr), so these bright objects are covered by the model as outliers. However, at least in the case of RX J1713-3946 the interaction of streaming particles from the shock with the material of the progenitor wind shell might be observed [Fukui, 2013]. Thus, the energy in form of particle escape that is lost in the simulation might still be around and could be causing over-luminous shells (as compared to the model results).

5.5.5. Source Age Dependency of the Upper Limits

Fig.5.25 shows the upper limits as a function of age (if available). As in the previous plot, no limit enters into the bulk of the simulated population. Instead,
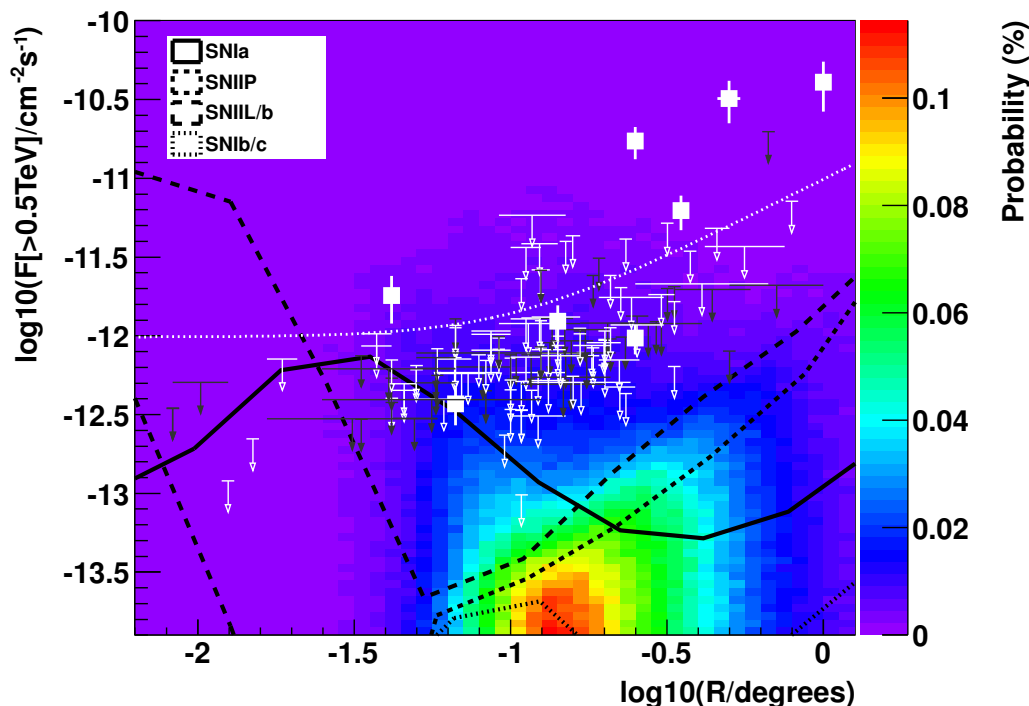
Figure 5.24.: Flux upper limits as a function of the source extension. White: Shell-type SNRs, grey: other. Also the eight shell-SNRs detected in VHE are shown as white points. Additionally, the simulated probability distribution of integrated flux above 500GeV and evolutionary tracks of the SN subtypes are shown. For the probability distribution each decade along the abscissa and ordinate is binned in 20 logarithmic bins. The white dotted line represents the approximated functional dependency of sensitivity with source extension (a nominal sensitivity of 1.5%Crab is assumed).

the UL follow the simulated curve remarkably well at a level that is again 0.5-1 orders of magnitude above the predicted population.

Again, the ULs are closes to the expected evolutionary track of SNIa SNRs, so that for these sources a future detection seems most probable.

Also the TeV-detected shell-type SNRs are in agreement with the predicted shape of the Flux-Age distribution. Cassiopeia A (the youngest of detections shown in Fig.5.25) is in the predicted track of SNIIb[6].

The upper limits in Figs.5.24 and 5.25 are 0.5-1 order of magnitudes from the

---

[6]it does not fit the track in source extension, see Fig.5.24. This might be attributed to the fact that in the simulation I assume somewhat higher values of the red giant wind mass luminosity than what is required to fit CasA(see section A.3), which leads to smaller sources.
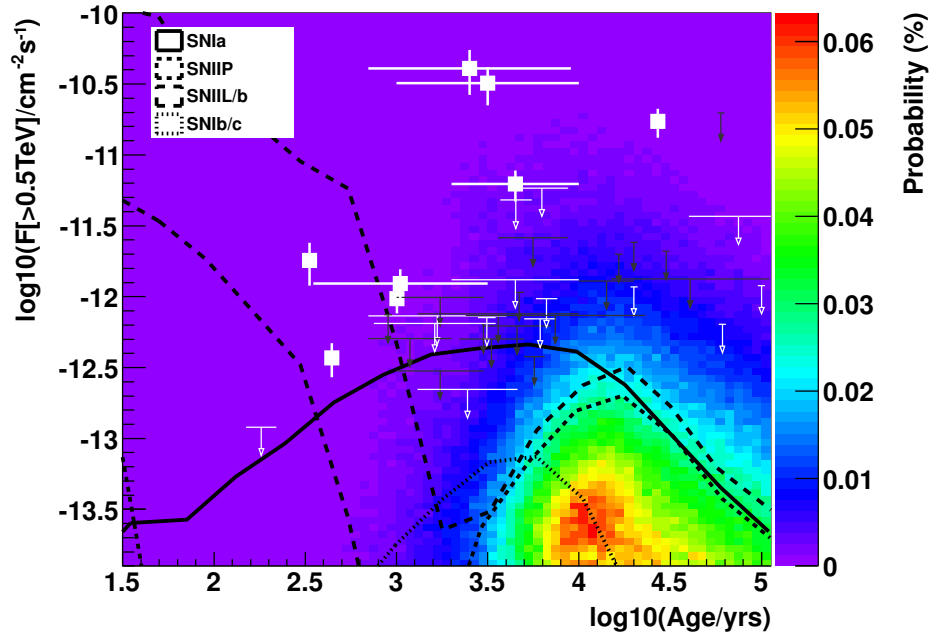
Figure 5.25.: Flux upper limits as a function of source age. White: Shell-type SNRs, grey: other. Also the eight shell-SNRs detected in VHE are shown as white points. Additionally, the simulated probability distribution (in percent) of integrated flux above 500GeV and evolutionary tracks of the SN subtypes are shown. For the probability distribution each decade along the abscissa and ordinate is binned in 20 logarithmic bins.

main body of simulated SNRs. In view of the large number of analysed sources, one might expect some detections. However, the situation is more complex as will be pointed out in the following.

5.5.6. TeV-Radio Flux Correlation

The analysed set of sources corresponds to radio-bright SNRs. Therefore it is interesting to study what to expect from these objects with respect to their VHE emission. Fig.5.26 shows the correlation between radio surface brightness at 1GHz to VHE flux above 500GeV.

No discernable feature can be seen in the correlation plot between the radio surface brightness and the VHE flux UL. The same holds for the simulated distribution.

From the simulations one can see that radio-bright sources do not necessarily have to be gamma-bright. This was already seen in Fig.5.22 and is not very surprising as SNRs emit in the radio through a leptonic channel and show
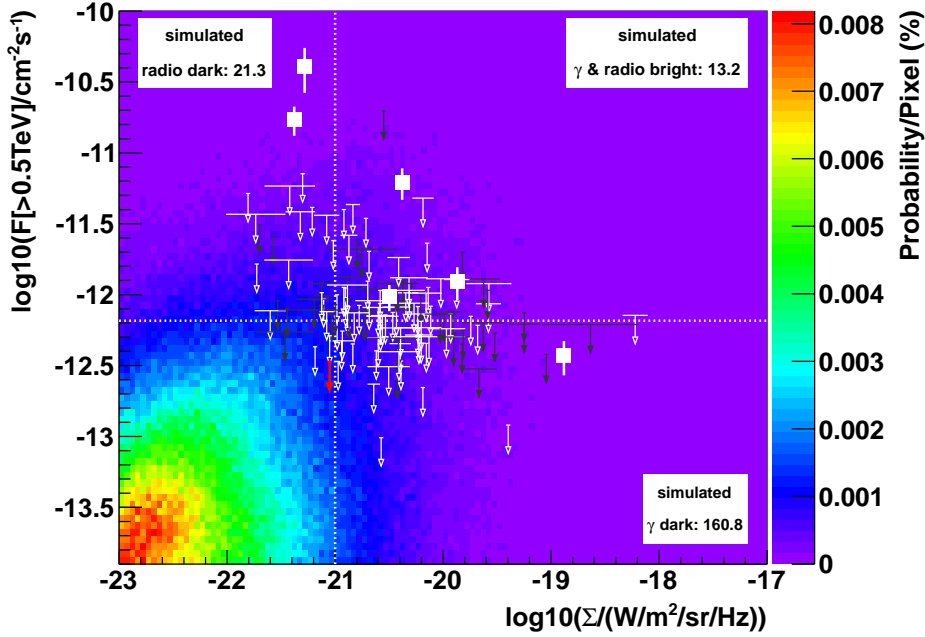
Figure 5.26.: Flux ULs above 500GeV against radio flux densities at 1GHz. White: Shell-type SNRs, red: G353.9-2.0, gray: other. Published VHE SNRs are indicated by white points. The dashed lines roughly represent the sensitivities of H.E.S.S. and the SNRcat. For the probability distribution each decade along the abscissa and ordinate is binned in 20 logarithmic bins.

the largest surface brightness when they so most efficiently in strong magnetic field and when they are compact, i.e. at young ages. In the VHE range, the majority of such young SNRs is expected to emit rather faintly via a hadronic mechanism. That is, electrons (as potential IC emitters) are cooled away by the strongly amplified fields and the population of accelerated protons requires several hundred years to build up. As a result, the model predicts that less than 90% of the radio-bright SNRs are also bright in gamma rays (above 1%Crab). If one imagines the x-axis in Fig.5.26 as a third dimension to Figs.5.24 and 5.25, extending out of the paper, it becomes clear that the upper limits in these figures are actually in front of the main SNR population and are almost not constrained by it at all.

The simulation also suggests a large number of expected sources like HESS J1731-347 that are radio-dark, but gamma-ray bright. With H.E.S.S., there might be a great potential for the discoveries of new SNRs.

Also, if the simulations are correct, with its estimated sensitivity of ~1mCrab and an improved angular resolution, CTA will be able to discover and resolve large amounts of new SNRs in the VHE regime and cut deeper into the SNR

distribution than the current generation of radio experiments. It may very well be that the roles will be reversed in the coming years and the IACT technique could become the pathfinder for radio and X-ray instruments in the observation of SNRs.

5.5.7. Observation Recommendation

Returning back to the present, Fig.5.26 can be used to suggest SNR follow-up observations. The simulation implies that sources at a low radio surface brightness have a higher chance to result in a VHE-detection. Also, compact sources appear most promising, as the distance of the UL to the simulated distribution is smallest for source radii between $\sim 0.06°- 0.1°$, see Fig.5.24. A literature study for those SNRs fulfilling these criteria was conducted and a promising candidate, G353.9-2.0, will be presented in following. The correlated ($0.1°$) excess map of the corresponding region is shown in Fig.5.27.
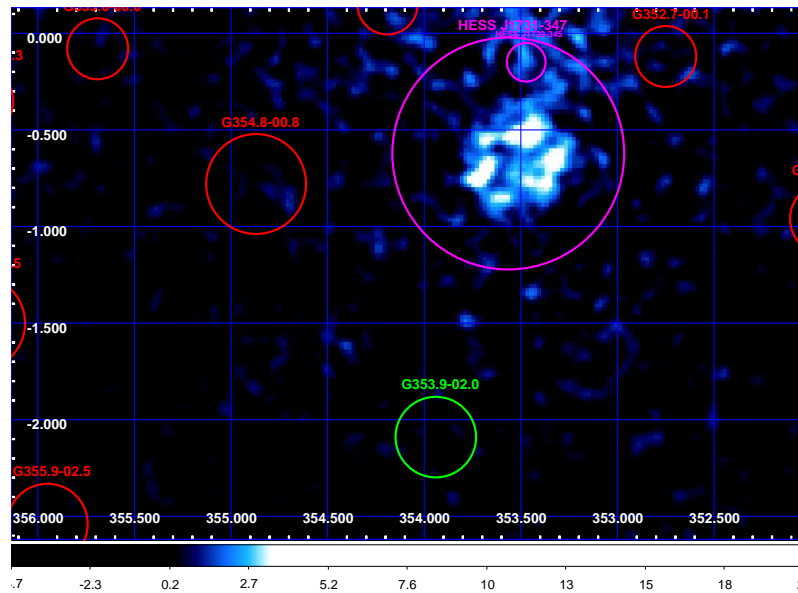
Figure 5.27.: Correlated ($0.1°$) excess map of the region around G353.9-2.0, which is marked in green colour.

G353.9-2.0 (green) is close to HESS J1731-347 and at a relatively low galactic latitude of b=-2°.

The SNR is of $0.11°$ in angular radius, its observed radio surface brightness amounts to $\Sigma_{1\text{GHz}} \approx 9 \cdot 10^{-22} \text{Wm}^{-2}\text{Hz}^{-1}\text{sr}^{-1}$ and the flux UL above 500GeV is measured as $F_{UL}(E > 0.5\text{TeV}) = 3.4 \cdot 10^{-13}\text{cm}^{-2}\text{s}^{-1}$. Since it is located only about 1.5° away from HESS J1731-347, one might keep the presence of G353.9-2 in mind when planning further observations of HESS 1731-347, as it might greatly benefit from an adapted observation strategy (as it already does benefit from being in the FoV of HESS 1731-347 with a live-time of almost 26h).

This SNR has been observed in radio as a faint shell with a bright central source [Green, 2001]. It was found, however, that the latter is probably an extragalactic coincidence. The radio contours of G353.9-2.0 are shown in Fig.5.28.
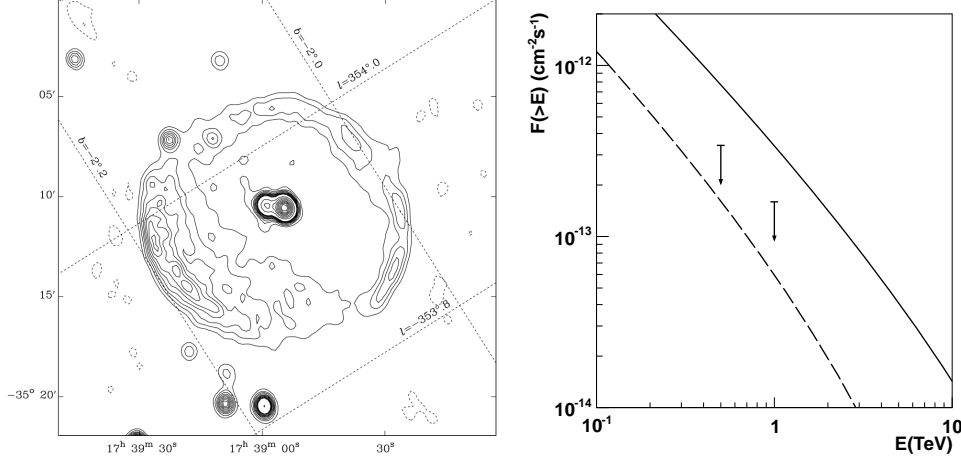
Figure 5.28.: Left panel: Radio contours of G353.9-2 (extracted from [Green, 2001]). Right panel: Model prediction on the integral flux in hypothetical scenarios where G353.9-2 is 1kyrs (solid) or 5kyrs old (dashed). Also, the UL at 500GeV and 1TeV ($\alpha = 2.1$) are shown.

The object has not been observed with X-ray or gamma-ray instruments, and information on the ambient medium is sparse. Also, there are no distance or age estimates.

However, in Fig.5.28 one can see that the shell is nearly circular, which suggests that the remnant may not be too old [Green, 2001]. If this is the case, then its extension implies that the source might be at a moderate distance. Assuming a SNIa event (which is most probable at large offsets from the plane), a typical ambient density of $n =0.1cm^{-3}$ and a moderate age of a $\sim$1-5kyrs, the source radius is roughly expected to be in the range of $\sim$7-15pc (see Fig.4.9). With an angular diameter of 13' this corresponds to a distance of $\sim$3.6-7.8kpc and would put the source at a distance of $\sim$125-270pc to the galactic plane. Applying the above mentioned scenarios to the SNR model (Model II, and also assuming the usual standard parameters for SNIa, see section A.3), I obtain VHE flux estimates that are comparable to the upper limit values, see right panel of Fig.5.28. Compared to the observed radio flux density of $\sim$1Jy, the old-source scenario ($S_{sim} =$1.7Jy at 5000yrs) is preferred to one assuming a relatively young SNR ($S_{sim} =$20Jy at 1000yrs). Of course, all this is highly hypothetical and not more than an educated guess. But as one can see, in this case the UL is already constraining a reasonable scenario for this source and

further observations might result in the detection of this SN1006-like object.

5.6. Conclusions and Outlook

An analysis of the H.E.S.S. HGPS data, coincident with position of known SNRs from lower (mostly radio) wavelengths, has been performed. This SNR sample is derived from the SNRcat, which combines SNR observations from 20 decades in energy. The 251 sources falling into the HGPS region show different types of morphology, the most prominent sub-group being that of shell-like SNRs.

However, not the whole sample has been investigated as the inner galactic region is densely populated by H.E.S.S. sources, and the physics interpretation of the VHE-emission from the radio SNR population as a whole requires a clean analysis sample in a sense that no emission from unrelated H.E.S.S detections contaminates their analysis regions.

Thus, the sample has to undergo a selection that excludes those sources where a contamination of the analysis regions by a signal of nearby H.E.S.S. detections is expected. The selection scheme is based on observational data as it makes use of the HGPS significance maps. After this selection 104-138 sources (depending on the stringency of the selection) remain as the analysis sample.

Two analysis pipelines were implemented to extract significance values and flux upper limits from the test regions, both using the same event reconstruction and selection method (hap-TMVA, *standard* selection cuts) but different background estimations (the Ring-Background and Reflected-Background methods). The resulting overall UL distributions are virtually identical, although for individual sources the results from the two methods scatter strongly within ~50% in relative difference. However, since the flux UL result from the analysis of background fluctuations, a large scatter is expected. The significance distributions are very similar as well, although the Ring-background method reconstructs a somewhat higher amount of sources at the low end of the distribution. No clear difference between the corresponding distributions for the different morphological sub-types is found. Also, no new significant detections were found.

However, in both cases an offset in the significance distribution towards positive values could be observed. The median of the significance distribution is at values between 0.74-1.03σ which might indicate emission from the ON-regions. In order to understand this offset, a study was performed where randomly generated test regions were analysed. To that end, the SNR positions, as provided by the SNRcat, were randomly shifted in galactic latitude, longitude and size so as to obtain randomised versions of the original catalogue. The so generated sample was then subjected to the usual selection and analysis schemes. In principle, the resulting significance distributions contain all effects that might cause the shift in the original distribution except for those linked to the specific

146

SNR positions. Using these distributions as a null-hypothesis, a Kolmogorov-Smirnoff test as well as a stacked analysis were performed and resulted in significances of the effect between 3-4σ. The situation remains unclear and is still under investigation. An optimistic interpretation would account a stacked low-level VHE emission from the radio SNRs for this effect.

The distribution of flux upper limits holds no surprises and reflects, as expected, the sensitivity of H.E.S.S. in the inner galactic plane. No obvious differences between the distributions for the morphological sub-classes could be found.

While the upper limits in itself are helpful, e.g. in the SED modelling of radio SNRs, it is difficult to use them in order to constrain VHE emission models of SNRs. One reason for that is connected to the very limited amount of information about important SNR parameters like age, distance, energy output of the SN, ambient density and so on. Thus, any limits on important parameters as e.g. the acceleration efficiency of CRs are attributed with immense errors and it is difficult to draw physical conclusions from the values. However, one can still compare the large sample of flux UL to the expectations from the population synthesis simulation presented in chapter 4. For this comparison, Model II was used which assumes a set of standard parameters and is able to approximately describe the radio SNR distributions in size, flux, surface brightness and galactic coordinates. It also reproduces a realistic number of expected shell-SNR detections at VHE (as compared to the amount of so far detected shell-type SNRs by H.E.S.S., MAGIC and VERITAS). The comparison to the upper limits shows that the H.E.S.S. sensitivity is roughly one order of magnitude above the VHE emission from the bulk of the simulated sources. The difference is smallest to the population of SNIa SNRs so that these sources might be easiest to detect in the future. Furthermore, the simulation suggests that less than 10% of radio-bright SNRs are also gamma-bright. If the model is correct, this explains the relatively low number of shell-type SNR detections in the VHE range as we are simply looking at predominantly gamma-dark sources. As a matter of fact, it is found that the chances for a VHE detection are elevated for radio faint sources, a prediction which allowed me to make an observation suggestion.

The concluding remark also of this chapter aims at the future experiment CTA. A galactic plane survey with this instrument will probably result in the discovery of a large amount of SNRs. Many of these objects will probably be radio-faint, and so the IACT technique might actually return the favour to the radio and IR colleagues by providing them with observation positions.

A. Appendix A

This appendix provides supplementary information on the SNR population synthesis simulation in chapter 4.

A.1. The 3D Model of the Ambient Gas Density

The ISM values on the gas number density in this model are derived from azimuth-averaged radio measurements. The measured values have been provided by the work of, amongst others, [Bronfman et al., 1988] [Clemens et al., 1988].

   [Ferrière, 2001] gives a good overview over the large scale distribution of interstellar matter in our galaxy. Many assumptions made here as well as the following short discussion is along the lines of the author's description.

   Interstellar galactic gas follows the spiral arm structure and is distributed close to the Galactic disk. It is roughly organised as follows: half of its total mass ($\sim$10-15% of the total mass of the Galactic disk) is found in more or less compact clouds while the rest is distributed between them. The clouds only fill a small fraction of interstellar space ($\sim$1-2%).

A.1.1. Molecular Hydrogen

Molecular hydrogen, which by itself has no permanent dipole and is thus difficult to detect. However, it is traced by carbon monoxide, which in turn is accessible to radio observations through the rotational transition J=1-0 in CO. Clemens et. all were able to image the most dominant features in the face-on galactic molecular gas distribution from the data collected in the Massachusetts-Stony Brook Galactic plane survey conducted by the 14m FCRAO radio telescope [Sanders et al., 1986]. Their derived map can be seen in Fig.A.1.

   As the main feature, a molecular ring at about $R = 5kpc$ from the galactic centre can be observed. It has been estimated by the authors to contain about 39% of the total molecular mass, while only 11% can be found beyond this ring. Also, the Sagittarius and Perseus arms are visible in the map. The authors estimate the inter-arm density to be lower by a factor of 3.6 than in the spiral arms.

   The same authors also derived azimuth-averaged mean values for the H_2 column density, which are shown by the bars in the top panel of FigA.2. Note that these values are taken from [Ferrière, 2001], who rescaled the values to
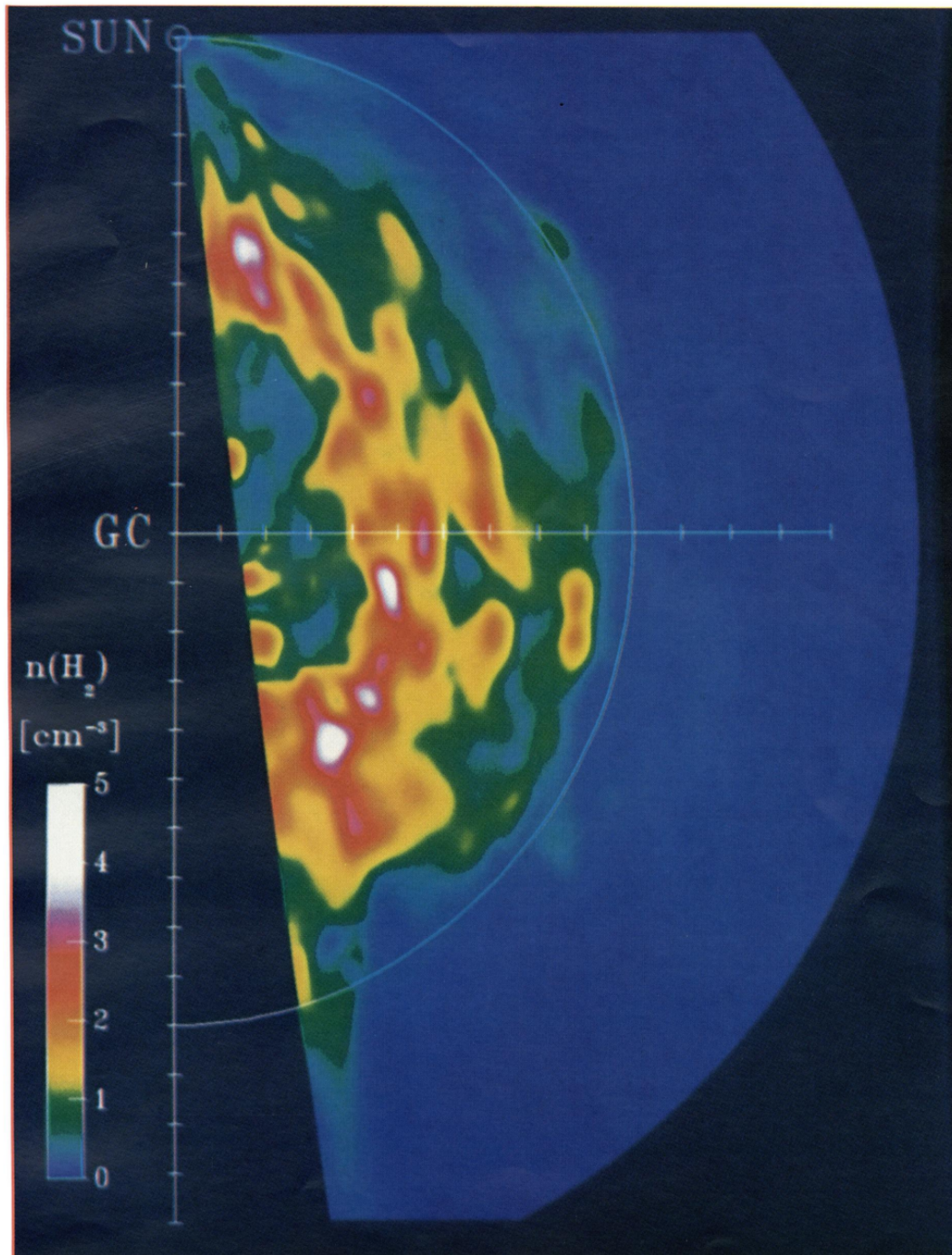
Figure A.1.: Map of H_2 peak number densities in the galaxy as derived by Clemens et al. Plot taken from [Clemens et al., 1988].

account for the updated value of 8.5kpc as Sun-GC distance (Clemens et al. assumed 10kpc).

The molecular gas is narrowly distributed perpendicular to the Galactic plane and the average density in that direction can be approximated by a Gaussian. Clemens et al. find for the azimuthally averaged[1] FWHM values of the H_2 layer a power-law dependency in R with an index of 0.58 with a value of 136pc at the solar circle. The function is displayed by the dashed line in the bottom panel of Fig.A.2. This translates into a Gaussian with a standard deviation of

$$\sigma_{H_2} = \left(\frac{R/1\mathbf{pc}}{7.81} \right)^{0.58}.$$ (A.1)

The increase of H_2 layer thickness can be understood from the decreasing surface density of matter and stars towards the outer galaxy. Consequently, at larger distances to the Galactic centre the gravitational pull towards the disk decreases which results in the observed behaviour of the H_2 layer thickness.

With the knowledge of the R-dependent shape of the z-distribution of the space-averaged number density of H-nuclei in molecular form, namely a Gaussian of known width, and the measured azimuth-averaged R-dependent column density of H_2, it is possible to derive estimations on the average H_2 densities anywhere in the galaxy. Here, the column density is empirically approximated by

$$CD_{H_2} = 1.54 \cdot 10^{19} \left(\frac{R}{1\mathbf{kpc}} \right)^8 \exp\left[-1.69 \left(\frac{R}{1\mathbf{kpc}} \right) \right] \mathbf{cm^{-2}},$$ (A.2)

shown by the dashed line in the top panel of Fig.A.2.

The resulting vertical profiles of proton number density in the form of H_2 for different values of Galactocentric radius are shown in the top panel of Fig.A.3. The step width is 200pc starting at a Galactocentric Radius of $R =$1.5kpc with the lightest color. The cyan line indicates the vertical density profile at the solar circle and is given by

$$n_{H_2} = 0.53 \exp\left[-\frac{1}{2} \left(\frac{z/1\mathbf{pc}}{57.7} \right)^2 \right] \mathbf{cm^{-3}}.$$ (A.3)

These values are close ($\leq$5%) to the ones provided by Ferrière. From the top panel in Fig.A.3 one can see that in the inner galaxy the average number densities of hydrogen nuclei in molecular form can reach values as high as 4cm^{-3}. In this region, they account for the largest contribution to the matter in the ISM. However, at Galactocentric radii $R \leq$ 9kpc, this contribution becomes negligible and most of the interstellar gas is found in the form of atomic hydrogen.

---

[1]The average was obtained over the first Galactic quadrant.
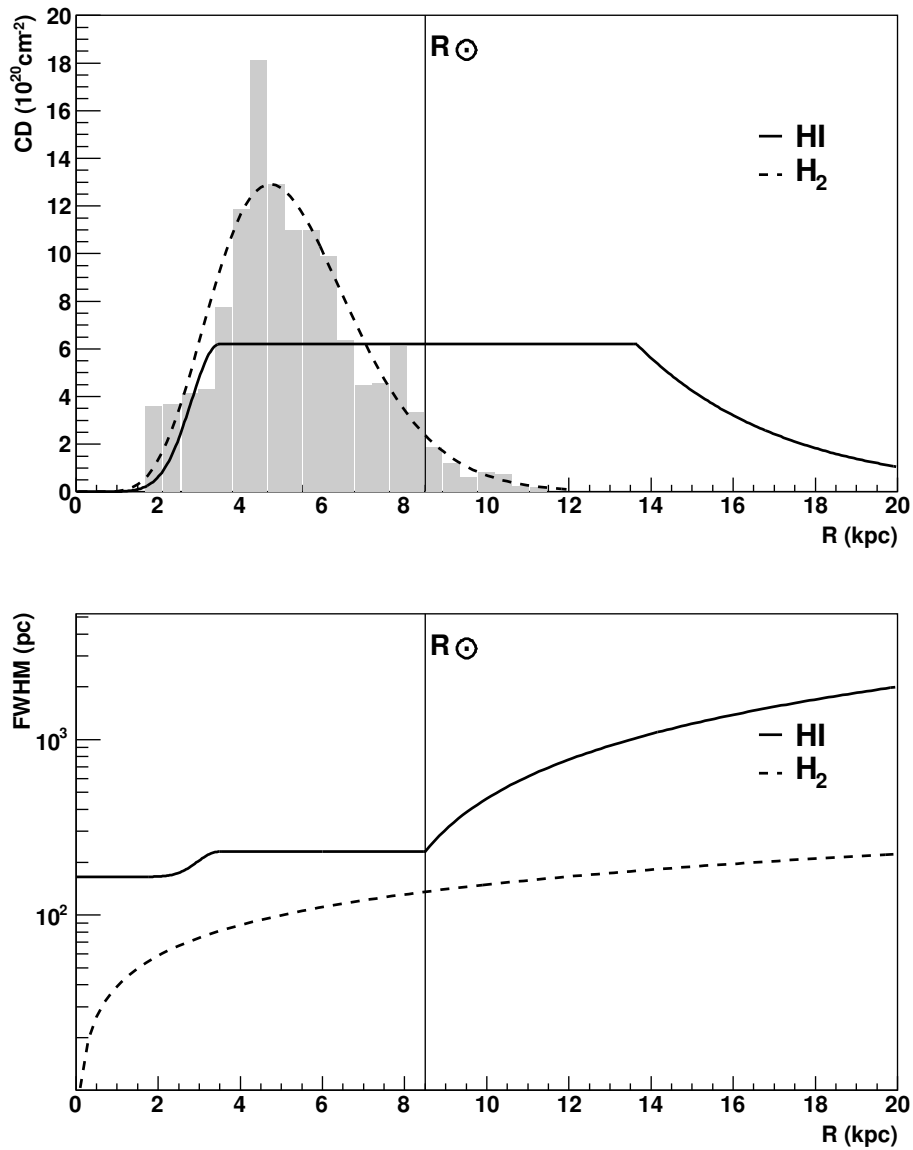
Figure A.2.: Top panel: Model assumption on the column number densities of HI (solid line) and H_2 gas (columns). The dashed line represents the empirical function that is used to sample the H_2 column density. Bottom panel: Assumed thickness of the HI (solid line) and the H_2 (dashed line) gas layers. The displayed data have been taken from Clemens et al (H_2, [Clemens et al., 1988]), [Ferrière, 2001] and [Dickey and Lockman, 1990].
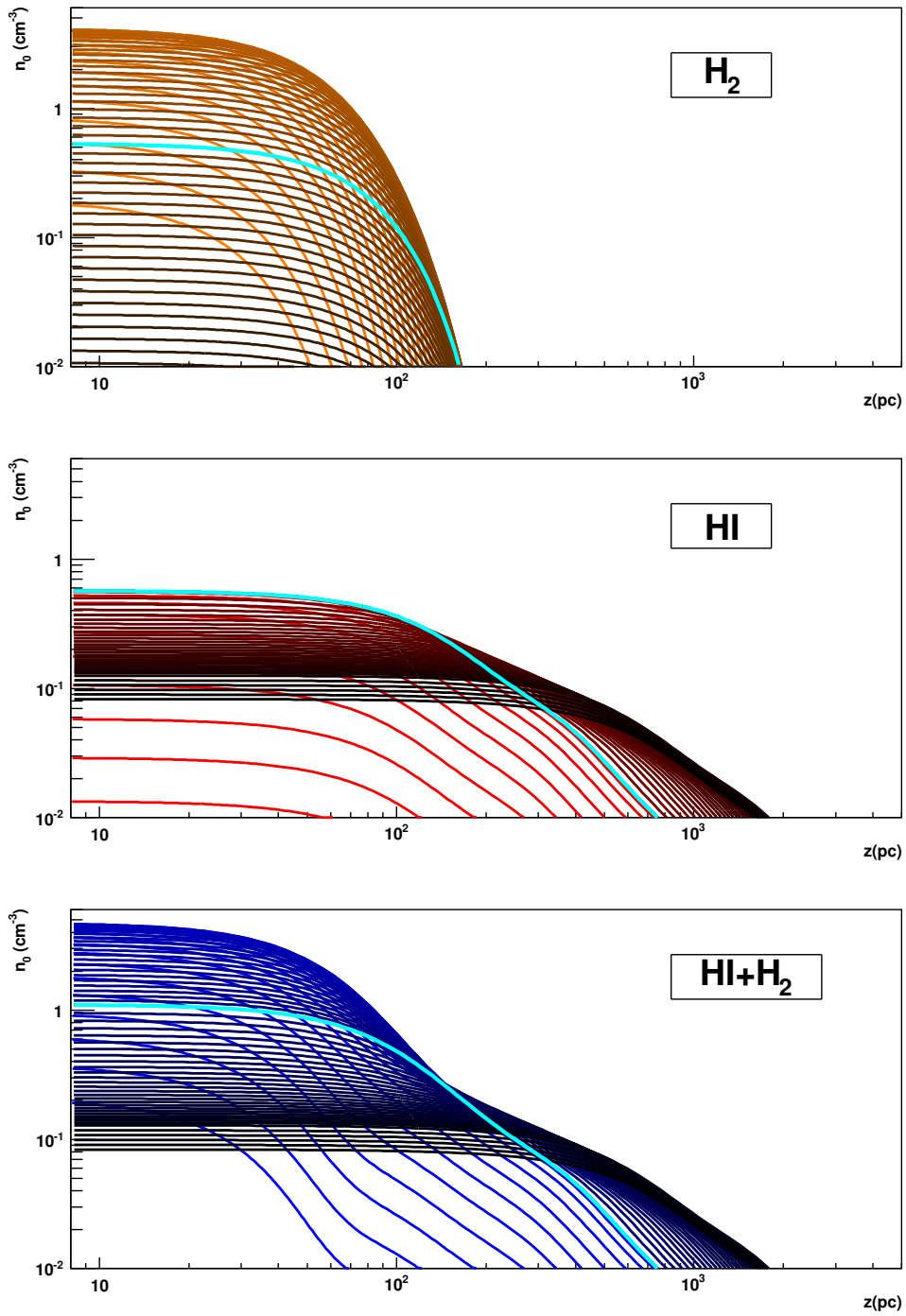
Figure A.3.: Profiles of average number densities of hydrogen nuclei in the form of molecular gas (top), atomic gas (middle) and the sum of both (bottom). The steps start at a Galactocentric radius of $R = 1.5$kpc with the lightest colour and have a width of 200pc.

A.1.2. Atomic Hydrogen

Atomic hydrogen can be observed in radio through its 21cm line emission. Since most of atoms are in the ground state [2], they are also accessible in the UV by observing the Lyman α-emission.

From these observations it is known, that the HI gas is following the spiral structures of the galaxy. While at Galactocentric radii R<$R_\odot$ the distribution is quite chaotic, the large scale structure is more clearly seen in the outer galaxy. There, three spiral arms become visible. Within these arms, the HI surface density is approximately constant and about a factor of four times larger than between them.

Ferrière summarises the radial, azimuth-averaged distribution of the HI column density , as found by [Dickey and Lockman, 1990], as follows: There is strong depletion in HI column density towards the galactic centre, starting at a radius of R =3.5kpc. At larger radii Dickey and Lockman find a constant regime that goes through the solar circle and out to R ~14kpc. Beyond this radius, the HI column density experiences a exponential drop. This radial column density profile is shown by the solid line in the top panel of Fig.A.2. In this simulation, it is realised by the following formalism:

$$CD_{\text{HI}}/(10^{20}\text{cm}^{\text{-2}}) = \begin{cases} 6.2 \cdot \exp\left[-\left(\frac{R/1\text{kpc}-3.5}{0.7}\right)^2\right] & \text{if } R < 3.5 \text{ kpc} \\ 6.2 & \text{else if } R < 13.65\text{kpc} \\ 6.2 \cdot \exp\left[-0.28 \cdot (R/1\text{kpc} - 13.65)\right] & \text{else} \end{cases}$$

(A.4)

The thickness of the HI layer strongly varies with the Galactocentric radius. Dickey and Lockman find a very thin layer in the region outside the galactic core but inside the galactic bulge with a FWHM value of ~165pc. In the range 3.5kpc≤ R <$R_\odot$ the gas layer shows an approximately constant thickness (although with large fluctuation) of FWHM=230pc. Beyond the solar circle, the layer flares strongly and increases in thickness roughly linearly, reaching a FWHM(it is actually the mean) value of ~2kpc at a Galactocentric distance distances R =20kpc [Henderson et al., 1982]. As the previous case of the H_2 layer, the thickening of the gas layer can be understood to result from a decreased gravitational pull towards the Galactic Disk connected to the decrease in surface densities of stars an matter in the outer galaxy. The combined function for the FWHM can be written as

$$\text{FWHM}_{\text{HI}}/1\text{pc} = \begin{cases} (230 - 165) \cdot \exp\left[-\left(\frac{R/1\text{pc}-3500}{708}\right)^2\right] & \text{if } R < 3.5 \text{ kpc} \\ 230 & \text{else if } R < 8.5\text{kpc} \\ 0.154 \cdot \exp\left[-0.28 \cdot (R/1\text{pc} - 8500)\right] + 230 & \text{else} \end{cases}$$

(A.5)

---

[2]Usually, particle collisions are rare under typical interstellar conditions.

Here, as vertical profile the structure provided by Ferrière is used [3]. It consists of the sum of two Gaussian and one exponential function. In this model, the scale h heights and standard deviations are rescaled as a function of the Galactocentric distance in a way that the FWHM values described earlier are obtained. The expression is given by

$$\langle n_{\mathrm{HI}}\rangle(R, z) = k(R) \left[0.7 \cdot \exp\left\{ -\left(\frac{z}{0.55 \cdot \mathbf{FWHM}(R)} \right)^2 \right\} \right.$$

$$+0.19 \cdot \exp\left\{ -\left(\frac{z}{1.38 \cdot \mathbf{FWHM}(R)} \right)^2 \right\} \tag{A.6}$$

$$+0.11 \cdot \exp\left\{ -\left(\frac{z}{1.75 \cdot \mathbf{FWHM}(R)} \right) \right\} \right] \mathrm{cm}^{-3}.$$

The FWHM values follow Eq.A.5 (solid line in bottom panel of Fig.A.2) and the normalisation $k(R)$ is fixed by the column density at R, as given in Eq.A.4 (solid line in top panel of Fig.A.2).

A set of density profiles along the z-direction, resulting from Eq.A.6, is shown in the middle panel of Fig.A.3. The steps are identical as in the top panel (where the corresponding profiles for molecular hydrogen are shown). They go from light to dark, start at $R =$1.5kpc and have a size of 200pc.

The profile at the solar circle, where Eqs.A.5 and A.4 yield FWHM=230pc and $k =$0.57cm^{-3}, is shown as the cyan line.

As one can see, the profiles are at the highest level and constant in the range between 3.5kpc and 8.5kpc. At smaller radii, the distribution is more narrow and shows a smaller normalisation. Towards the outer galaxy, the distributions grow broader. The exponential decline in column density gives rise to the equidistant lines in the logarithmic representation at $R >$13.65kpc.

Analogue steps for the combined H$_2$ and HI density are displayed in the bottom panel of Fig.A.3. Again, the cyan line depicts the distribution at $R_\odot$. It gives the familiar average proton density of $\sim$1cm^{-3} at our position. Profiles closer to the GC are more narrow and exceed the distribution at the solar circle in normalisation by a factor of up to almost five for radii $>$2kpc. Most of the hydrogen in this range is in molecular form, while at $R \leq$10kpc the atomic hydrogen component dominates.

These profiles correspond to *average* proton densities at a given Galactocentric radius and vertical distance to the disk. From this average the actual model value, n_0, is sampled by an exponential with a scale height of this average value.

This sampling function accounts to some degree to the fact that the matter is organised in compact structures embedded in a large-scale homogeneous medium of lower density.

---

[3]Dickey and Lockman suggested a simple Gaussian function for $R <$3.5kpc. However, here the profile given in A.6 is used to avoid a jump in the z-distribution at this radius.

Radio observations of the interstellar HI and H_2 gas show a modulation of the matter with the Galactic spiral arm structure. In the inter-arm regions the average density for both gas species is found to be decreased by a factor of ~ 4 [Ferrière, 2001].

Thus, in the presented model the density value n_0 is modulated in the following way:

$$n_0^{mod} = n_0 \cdot k \cdot (4 \exp(-d^2/w^2) + 1), \qquad \text{(A.7)}$$

where d is the distance to the nearest spiral arm and w is the parameter value for the arm width. The normalisation k is chosen in a way that the azimuth-averaged number densities are retained.

A.2. Calculating the Particle and Radiation Spectra

This section will shortly summarise how the particle and gamma-ray spectra are computed in this simulation.

A.2.1. The Particle Spectrum

The particle distribution is governed by Eq.4.5, for convenience repeated here:

$$N(E,t) = \frac{\theta(E - E_{max}(t))}{P(E)} \int_0^t dt_0 P(\varepsilon_{t_0}) Q(\varepsilon_{t_0}, t_0) \theta(\varepsilon_{t_0} - E_{max}(t_0)). \qquad \text{(A.8)}$$

The integral represents an integration over the spectral history of the particle distribution. The quantity ε_{t_0} describes the energy of a particle at a time t_0, assuming it has the energy E at time t. Both energies are connected via the trajectory of the particle in energy space:

$$t - x = \int_E^{\varepsilon_x(E,t)} \frac{dE}{P(E)}. \qquad \text{(A.9)}$$

Here, $x < t$, as one is interested in the past spectral evolution of the particles. Since the latter cool, they had higher energies at earlier times.

Expression Eq.A.8 is calculated numerically. For each energy bin, the time integration has to be performed. If $E < E_{max}(t)$, a zero value is returned instead. In the following, the most important components in the numerical calculation of Eq.A.8 will be discussed.

- *The Particle Injection Spectrum*
  In this work, simple power-law spectra are assumed: $Q(E) = N_0 E^{-\Gamma}$, although more realistically, a convex spectral shape is expected to result from particle acceleration in modified shocks, compare to section 3.4.1. Electrons are modelled to show an additional feature: A super-exponential

cut-off $\propto \exp(-E^2/E_{max,e}^2)$ (see [Zirakashvili and Aharonian, 2007]) is applied to the power law as the maximum particle energy in this case is also determined by the synchrotron loss rate, compare to section 4.5.2. Via the θ-function, the source spectra are sharply cut-off at $E = E_{max}(t)$, compare to section 4.5.2.

The normalisation is given by Eq.4.6.

In practical terms, Eq.A.9 implies that in the time integration in Eq.A.8 at each time step a specific spectral point in the source spectrum, $Q(\varepsilon_{t_0})$, has to be calculated. The lower integrational boundary in Eq.A.8 can be larger than zero and is energy dependent as it is given by Eq.A.9 and the condition $\varepsilon_x(E,t) < E_{max}(t)$.

- *The energy loss rate*
  As already mentioned Eq.A.8 is not strictly valid for the problem at hand as it is derived under the assumption of constant energy losses. Here, however, the losses are time-dependent. Thus, Eq.A.8 is approximated under the assumption of quasi-stationarity: The expression is divided into time intervals of a size where the total loss rate $P(E)$ can be assumed to be constant. The step size is adaptively chosen as $\Delta t \ll \dot{E}(t)/\ddot{E}(t) = k\dot{E}(t)/\ddot{E}(t)$, where k is a numerical constant and $\dot{E}(t)/\ddot{E}(t)$ is the characteristic time scale on which $P(E)$ changes. Technically, Eq.A.8 is then split up into a large number of steps (between $\sim$200 and $\sim$200000).

In order to check the validity of the approximation, the values resulting from differently assumed step sizes were calculated and compared. The results from the implemented scheme are consistent with those obtained for an extremely fine binning while still being reasonably fast. Checks with an independent, numerical solution to the underlying differential equation Eq.3.18 should be performed in the future in order to investigate this approach further. However, in view of the fine integrational binning assumed in this model, differences should be small. Also, as a sanity check the model was tested on real SNR data. The next section shows that the presented approximation yields realistic radiation spectra that agree with observations while at the same time reproducing the observed shock dynamics and magnetic field strengths. All four sources represent relatively young objects with an age of less than $\sim$1kyr where the time-dependency of the energy losses is most pronounced[4]. Since for these sources the results appear reasonable, one can conclude that the presented approximation should be even more viable for older sources, where the energy losses become more stable.

---

[4]as $P_{ad} = (v_s/R)E \propto 1/t$ and also P_{synch} changes most strongly in the beginning, see the time evolution of B in the bottom panels of Figs.4.12 and 4.14.

- *Lookups*

  The energy loss rate can be calculated at any time t with the knowledge of shock speed and radius as well as the ambient magnetic field strength, the radiation field and density profile. For a fast computation, the values of the ambient gas number density n, the shock speed v_s and radius R, the magnetic field strength B, the fraction of mechanical luminosity going into the acceleration process ΘL_{mech} and the maximum particle energy $E_{max}(t)$ are filled in lookup tables at the beginning of the calculation for each individual SNR. A fine binning of 10^5 linear time bins stores the evolution of the parameters from t=1yr[5] to t=Age. These quantities determine the magnetic field strength and therefore the synchrotron losses P_{synch}. They also allow it to calculate the adiabatic loss term $P_{ad} = (v_s/R)E$ and Bremsstrahlung loss rate, P_{Brems} as well as the maximum energy of electrons, $E_{max,e}(t)$ can be calculated on-the-fly using the stored dynamical parameters and the B-field values.

It should be noted that $N(E,t)$ has the dimension of a number density per energy. It is important to mention that since the spatial dimension was omitted in the derivation Eq.A.8 (see section 3.4.2), $N(E,t)$ has to be understood as an average particle density over the whole source.

Technically, spectral particle numbers[6] $H(E,t)$ for electrons and protons ($H_e(E,t)$ and $H_p(E,t)$) are calculated in an energy range between $E_{low} = m_{p/e}c^2$ and $E_{up} = 1.2 \cdot E_{max}(t)$ (the factor of 1.2 is a numerical safety margin). The values are then stored in lookups consisting of 200 and 100 logarithmic energy bins for electrons and protons, respectively.

A.2.2. The Radiation Spectrum

With the particle spectra at hand, it is possible to calculate the gamma-ray flux, both the leptonic and the hadronic component. To that end, the product of emissivity[7] and particle number is numerically integrated over the whole particle energy range for all contributions. The particle number at a given energy is obtained by a linear interpolation between the logarithmic energy bins of the corresponding lookup table.

Leptonic Gamma-Ray Flux

The leptonic emission channel in this work assumes three components: Synchrotron, Bremsstrahlung and inverse-Compton radiation. For a short summary of these mechanisms, see section 3.5. For the total photon emission from

---

[5]This is an arbitrary low boundary which probably corresponds to typical acceleration times of particles to TeV energies in strong shocks, see e.g. [Blasi et al., 2007].

[6]Related to the spectral particle density simply via $H(E,t) = N(E,t) \cdot (4\pi/3)R(t)^3$.

[7]With 'emissivity' the photon spectrum per particle is meant.

electrons one can write:

$$\frac{dN_\gamma^{lept}}{dEdAdt} = (1/4\pi d^2) \int\limits_{E_{low}}^{E_{up}} dE_e (dN_{Sy}/dEdt) H_e(E_e, t)$$

$$+ (1/4\pi d^2) \int\limits_{E_{low}}^{E_{up}} dE_e (dN_{Brems}/dEdt) H_e(E_e, t)$$

$$+ (1/4\pi d^2) \sum_i \int\limits_{E_{low}}^{E_{up}} dE_e (dN_{IC,i}/dEdt) H_e(E_e, t).$$

Here, d is the distance to the source and the emissivities for Synchrotron as well as inverse-Compton scattering, $(dN_{Sy}/dEdt)$ and $(dN_{IC}/dEdt)$, from section 3.5 are used. The index i in the case of the latter indicates the interaction with different photon fields. At the time of writing, only the cosmic microwave background is assumed, but future work should include also infra-rad to ultra-violet radiation fields.

The Bremsstrahlung component is in most cases negligible. Only in very dense media it becomes important. The emissivity is taken from [Blumenthal and Gould, 1970] (see Eq.3.26) and for simplicity the scattering from an un-shielded charge is assumed. In this case, the cross-section is given by [Blumenthal and Gould, 1970]:

$$(d\sigma/dk) = 4\alpha r_0^2 (kE_i^2)^{-1} \left[\ln(2E_i E_f/k) - \frac{1}{2} \right] (E_i^2 + E_f^2 - \frac{2}{3} E_i E_f). \qquad \text{(A.10)}$$

In this equation, E_i is the electron energy before and E_f after the scattering event. Furthermore, $k = E_i - E_f$, α is the fine structure constant and r_0 is the classical electron radius.

Hadronic Gamma-Ray Flux

The gamma-ray emission from the decay of products from inelastic p-p collisions is shortly described in section 3.5.2. Here, the flux is given by

$$\frac{dN_\gamma^{hadr}}{dEdAdt} = (1/4\pi d^2) cnq \int\limits_{E_{low}}^{E_{up}} \sigma_{inel}(E_p) H_p(E_p) F_\gamma(E, E_p) \frac{dE_p}{E_p}, \qquad \text{(A.11)}$$

where q=1.8 is the hadronic amplification factor that accounts for heavier nuclei in the accelerated particle distribution and target medium, see 3.5.2.

A.3. Modelling Prominent SNRs

In this section, SEDs of four of the most prominent SNRs are modelled by the approach discussed in section 4.5. Here, the modified shock solution is assumed. This solution is regarded as the default since it has the ability to explain the observed high magnetic field values in the shock region. Table A.1 lists literature (top row) as well as the input parameters (bottom row) for the respective SNRs: The source age T, the distance to the object d, the ambient density n, the ejecta mass M_{ej}, the blast energy E, the electron-to-proton fraction K_{ep}, the values for the ISM B-Field strength B_0, the spectral index of injected particles Γ and the acceleration efficiency θ.

The resulting model SEDs together with Radio, X-ray, HE- and VHE-γ ray data (if available) are shown in Figs.A.4-A.5.

In Tab.A.2 one can find literature values (top panel) as well as model results (bottom row) for the observables shock speed v, angular radius r and B-Field at the shock B.
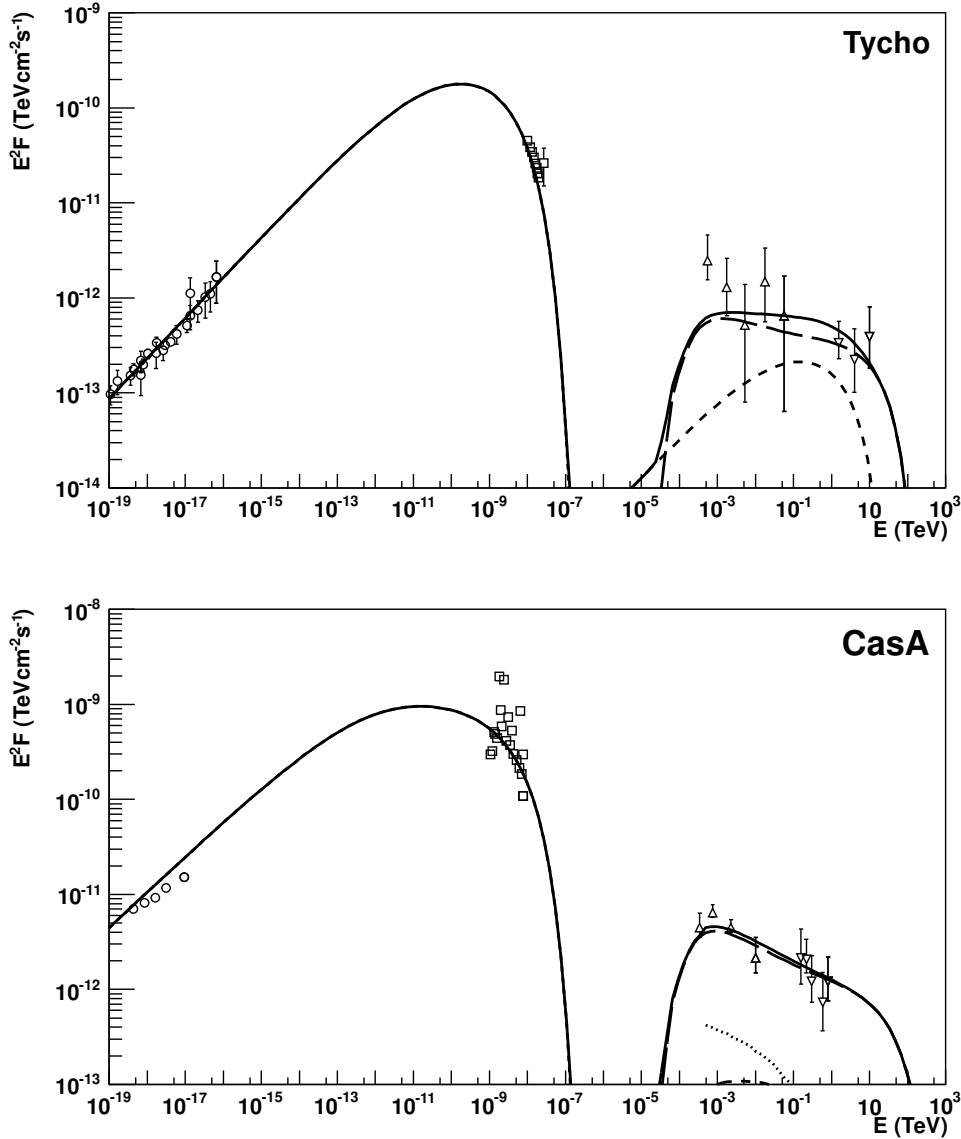
Figure A.4.: Top: SED model for Tycho Brahe's SNR. This SED represents a mixed hadronic-leptonic scenario. Radio points are taken from [Reynolds and Ellison, 1992], X-ray data are from [Völk et al., 2005], HE-γ ray points (Fermi-LAT) are taken from [Giordano et al., 2012] and VHE-γ ray data (VERITAS) are from [Acciari et al., 2011]. Bottom: Nineteen decades of emission from the SNR Cassiopeia A. The associated SN event has recently determined to be of type SNIIb [Krause et al., 2008a]. In the presented model, this means that the SNR blastwave is still inside the RGZ of the progenitor star. The SED is difficult to fit. Especially the radio slope is hard to reproduce, and also the low-energy Fermi points are challenging to describe. An additional emission zone seems necessary. However, the model is able to predict the extremely high magnetic field of more than 300μG in the acceleration region. Such strong fields have indeed been measured [Vink and Laming, 2003]. radio, HE and VHE data points are taken from [Acciari et al., 2011], X-ray data are from [Patnaude and Fesen, 2009].
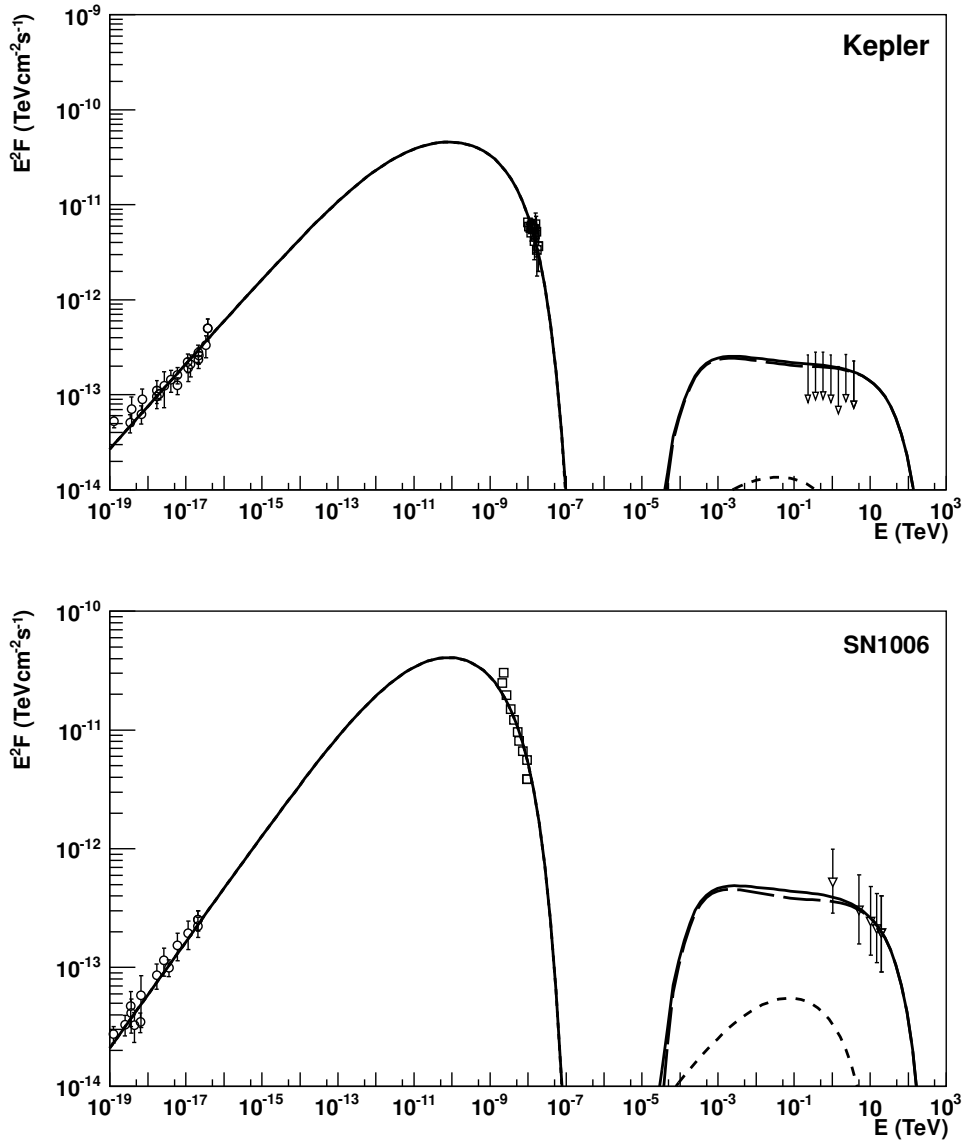
Figure A.5.: Top: The SED of Kepler's SNR. Modelling the synchrotron bump to fit Radio and X-ray data results in a high value of the B-Field of 185μG at the shock and lead to a hadronic VHE-emission scenario. Radio points are from [Reynolds and Ellison, 1992], X-ray data are taken from [Allen, 1999] and VHE-Flux ULs are from own analysis. Bottom: Broad-band spectrum of SN1006. The SED is modelled by a hadronic scenario at very high energies. The radio data shown here is from [Reynolds and Ellison, 1992], the X-ray points as well as the Fermi sensitivity curve are taken from [Acero et al., 2010].

	T/yrs	d/kpc	n/cm^{-3}	M$_{ej}$/M$_\odot$	E/E51	K$_{ep}$/10^{-3}	B$_0$/μG, Γ, θ
CasA SNIIb[l]	316-352[f]	3.3-3.7[f]	$(\sim 2,1)^{m,n*}$	2-4 [m,n]	2[m,n]		
	350	3.3	(3,1.1)	2	2	5	10, 2.25, 0.2
SN1006 SNIa[k]	historic	1.6-2.2[f]	0.05-0.25[j]	1.4[g]	$\sim$1[g]	0.1-7[i]	
	1006	1.7	0.06	1.4	1	0.25	2, 2.1, 0.2
Tycho SNIa[aa]	historic	1.7-5[f]	<0.6[a]	1.4[g]	$\sim$1[g]	1.1-4.[a,h]	
	441	3.1	0.3	1.4	1	3.	3, 2.15, 0.22
Kepler SNIa[z]	historic	3-7[f,u]	0.4-0.85[u,v]	1.4[g]	$\sim$1[g]		
	409	6.4	0.5	1.4	1	1.5	5, 2.1, 0.22

Table A.1.: Literature (top rows) and model input (bottom rows) values for four famous SNRs.*These are values for the suspected RGW, ($\dot{\mathrm{M}}_{RGW}$[10^{-5}M$_\odot$yr^{-1}],v$_{RGW}$[10^{6}cm s^{-1}]). The resulting ambient density of 0.98cm^{-3} is somewhat below literature estimates $\sim$(1-3)^{s,t}cm^{-3}.

name/type	v/1000kms^{-1}	r/arcmin	B/μG
CasA SNIIb[l]	4-5.2[o,c,p]	2.5[f]	80-485[q,r]
	5.4	2.53	304
SN1006 SNIa[k]	2.89-4.9[j]	15[f]	30[b]-150[e]
	3.9	14.6	86
Tycho SNIa	4.5[a,c]-6[d]	4[f]	(56-279)[a],(240-360)[b]
	4.5	4.	91
Kepler SNIa	1.66-6.7[w,x]	1.5-2[f,v]	(70-215)[y,q]
	4.3	1.7	186

Table A.2.: Literature (top rows) and model output (bottom rows) values for four famous SNRs.

[a] [Cassam-Chenaï et al., 2007]
[b] [Völk et al., 2008]
[c] [Vink, 2006]
[d] [Atoyan and Dermer, 2011]
[e] [Berezhko et al., 2009]
[f] [Ferrand and Safi-Harb, 2012]
[g] canonical value for SNIa
[h] [Völk et al., 2002]
[i] [Acero et al., 2010]
[j] [Acero et al., 2007]
[k] [González Hernández et al., 2012]
[l] [Krause et al., 2008a]
[m] [Chevalier and Oishi, 2003]
[n] [Young et al., 2006]

[o] [Willingale et al., 2002]
[p] [DeLaney and Rudnick, 2003]
[q] [Völk et al., 2005]
[r] [Vink and Laming, 2003]
[s] [Borkowski et al., 1996]
[t] [Lee et al., 2013]
[u] [Aharonian et al., 2008]
[v] [Patnaude et al., 2012]
[w] [Vink, 2008]
[x] [Katsuda et al., 2008]
[y] [Matsui et al., 1984]
[z] [Reynolds et al., 2007]
[aa] [Krause et al., 2008b]

B. Appendix B

B.1. Importance of the Source Ellipticity

The analysis presented in chapter 5 uses circular ON-regions. However, many SNRs show an elliptic shape. If both a major and minor axis are provided in the SNRcat (see section 5.1), the geometric mean of these two radii is assumed in the analysis. The effect of this simplification on the analysis results has been investigated and is shown in Fig.B.1. Here, the SNR sample is divided into two sub-sets according to their values of $q = $ (minor axis/major axis): One sub-set encompasses only sources where $q > 0.9$ (this includes circular SNRs) and only such where $q < 0.9$. For the analysis the ON-region definition presented in section 5.1.4 is used. As one can see from Fig.B.1, there is no obvious impact on the significance distribution. Similarly, no obvious trend can be seen in the flux distribution, see right panel, and therefore the ellipticity seems to have no influence on the conclusions from the analysis.
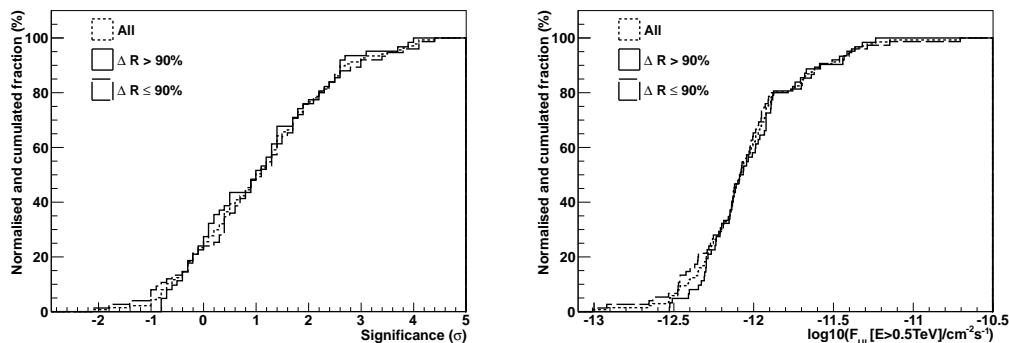
Figure B.1.: cumulative significance distributions (Ring-BG method) for sources where $q = $ (minor axis/major axis) as a measure of ellipticity is $q > 0.9$ (this includes circular SNRs) and $q < 0.9$.

B.2. Cross-Check

In the following, some cross-check plots for the two analysis pipelines of MethodI (Ring-BG Maker, from the survey maps) and MethodII (Reflected-BG maker, individual analyses) will be shown.
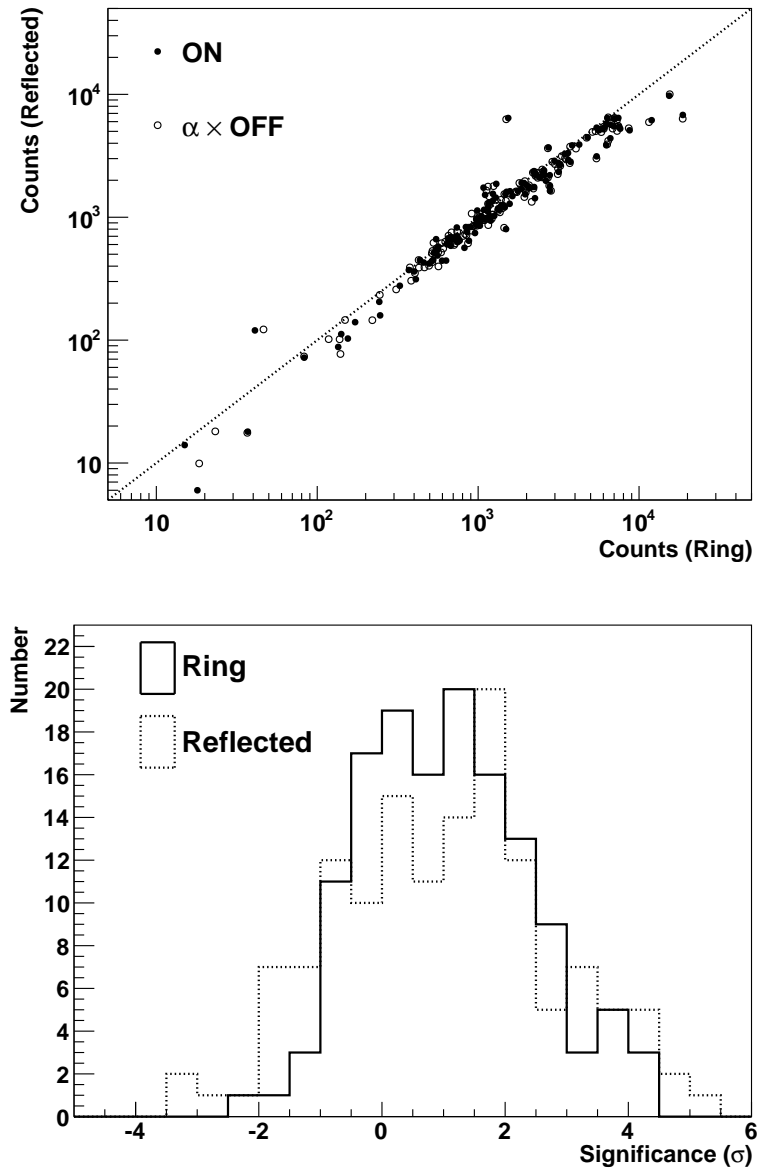
Figure B.2.: Top: Correlation between ON-region and OFF-region counts (rescaled by the α-value). Bottom: Significance distributions from the two analysis pipelines.

In the bottom panel of Fig.B.2 one can see the significance distributions for the *loose* sample obtained with both the Ring and the Reflected background method. The distributions are quite similar in that they are both shifted to positive values and that there are no significant detections. However, the Reflected-BG method results in a broader distribution, especially towards the low end.

The flux upper limit distribution for both background methods can be observed in the top panel of Fig.B.3. As one can see, they are virtually identical.
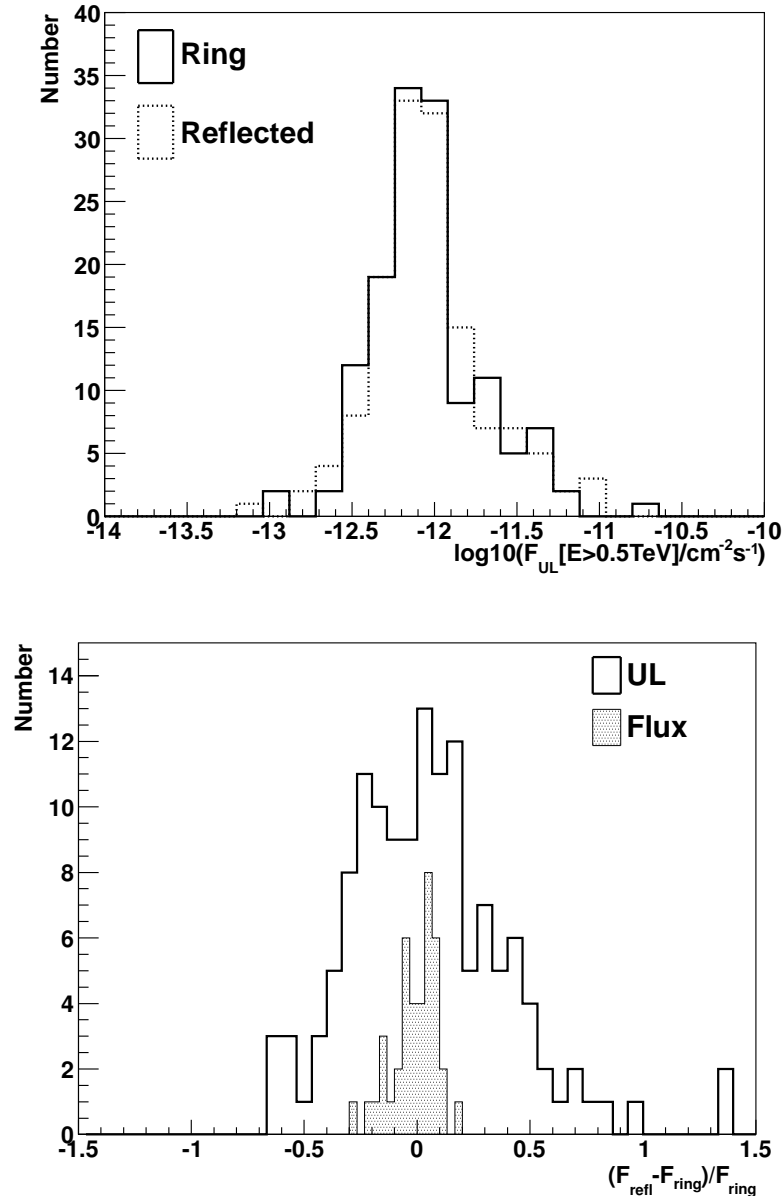
Figure B.3.: Top: Upper limit distributions for the two methods. Bottom: Relative difference between ULs for the individual sources. Here, also the relative difference in integrated flux (assuming the same energy range as for the UL calculation) for 40 significant sources is shown.

However, the relative difference in the flux UL values for individual sources scatters strongly within ~50% around zero, see bottom panel of Fig.B.3. A Gaussian results in a width of 31%. In the same panel, one can find the relative difference in integrated flux (assuming the same energy range as for the UL calculation) for 40 SNRcat sources that yield a significance of $\sigma > 10$ in the Ring background method. The flux was derived with the identical method and spectral hypothesis that is also applied in the UL extraction. However in these cases the confidence level is set to 1%, which in the case of significant sources yields flux points. The resulting relative differences in estimated flux are for the majority of sources within 10-15%, while a handful of sources scatters to somewhat larger values. This scatter in flux values between the two background methods is acceptable, so the analysis method itself appears reliable. Therefore, it can be concluded that the large scatter in the relative difference of flux UL values is the manifestation of background fluctuations and reflects systematic differences in the background reconstruction between the two techniques.

Since the UL values from the two different analysis methods scatter around zero, they do not change the overall shape of the UL distribution and so the physics interpretation is not impacted. As an example, the scatter plot of flux ULs versus source extension is shown in Fig.B.4.
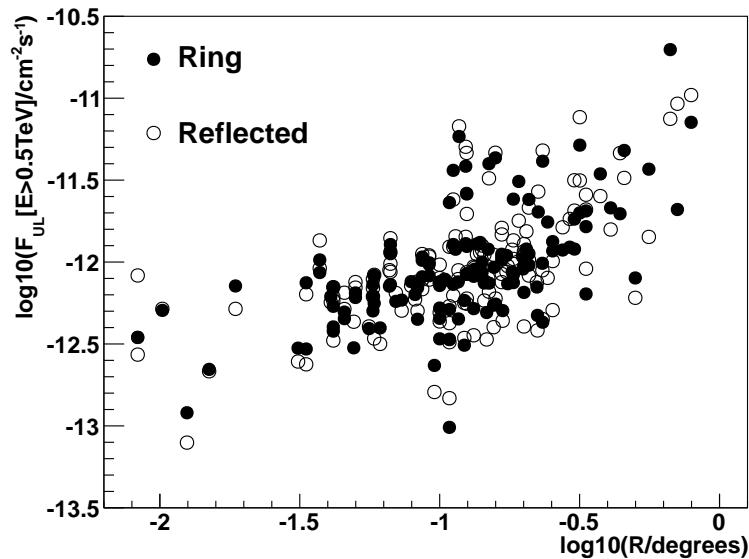
Figure B.4.: Flux ULs from the two methods vs. source extension.

Here, the overall shape of the scatter plot is quite similar for the two analysis methods. The distribution seems a little broader along the ordinate for the Reflected background method. However, the difference is small and has no impact on the interpretation of the result.

Name	Type	GL	GB	Ext	R(ON)	livetime	$\log_{10}(UL)_{ri}$	$\log_{10}(UL)_{re}$	σ_{ri}	σ_{re}	ON_{ri}	OFF_{ri}	$(OFF\cdot\alpha)_{ri}$	ON_{re}	OFF_{re}	$(OFF\cdot\alpha)_{re}$
G001.9+00.3	S	1.87	0.33	0.013	0.118	93.6	-12.92	-12.89	-0.4	-0.2	2055	3882330	2073.3	2060	3674700	2071.4
G004.2-03.5	S	4.21	-3.51	0.233	0.333	2.5	-11.38	-11.38	1.7	1.7	246	1141260	220.0	246	1141260	220.0
G005.2-02.6	S	5.2	-2.6	0.15	0.25	1.7	-11.4	-11.4	2.1	2.1	141	566010	117.8	141	566010	117.8
G005.4-01.2	C?	5.35	-1.13	0.292	0.392	22.1	-11.91	-11.9	0.6	0.7	6089	10019000	6042.0	6089	10331700	6033.9
G005.9+03.1	S	5.9	3.13	0.167	0.267	6.6	-11.95	-11.96	-0.3	-0.3	371	1754400	376.5	381	1801480	386.5
G006.1+00.5	S	6.1	0.53	0.122	0.222	35.0	-12.51	-12.47	-0.8	-0.6	2796	4967780	2836.8	2809	5540230	2841.7
G006.1+01.2	F?	6.1	1.21	0.233	0.333	29.6	-12.01	-12.02	0.9	0.8	4787	12773500	4725.8	4839	14976300	4783.8
G007.0-00.1	S	7.05	-0.08	0.125	0.225	34.4	-12.08	-12.08	2.4	2.4	3453	5607080	3312.6	3453	5741260	3312.6
G007.2+00.2	S	7.2	0.2	0.1	0.2	32.6	-12.14	-12.15	2.1	2.1	2580	4280660	2474.6	2580	4338210	2475.8
G007.5-01.7	C?	7.54	-1.9	0.303	0.403	10.6	-11.92	-11.93	-0.3	-0.3	3222	12085800	3238.8	3222	12371500	3241.3
G007.7-03.7	S	7.75	-3.77	0.183	0.283	3.1	-12.13	-12.13	-1.4	-1.4	400	2067570	428.3	400	2067570	428.3
G009.8+00.6	S	9.75	0.57	0.1	0.2	66.3	-12.47	-12.43	0.7	0.9	3750	4565430	3710.2	3785	4838890	3727.6
G009.9-00.8	S	9.96	-0.81	0.1	0.2	69.8	-12.37	-12.37	1.9	1.6	3843	5173240	3728.8	3859	5793270	3761.7
G011.1-01.0	S	11.17	-1.04	0.122	0.222	51.2	-12.23	-12.23	1.8	1.9	3627	5703650	3517.1	3630	5901350	3515.6
G012.2+00.3	S	12.26	0.3	0.046	0.146	32.0	-12.35	-12.34	1.3	1.3	1259	1976280	1215.1	1259	1928020	1214.4
G013.3-01.3	S?	13.32	-1.3	0.441	0.541	10.4	-11.71	-11.69	0.2	0.3	5448	16300200	5434.2	5448	15833800	5427.7
G013.5+00.2	S	13.45	0.15	0.037	0.137	14.9	-12.06	-12.06	2.7	2.7	632	1508540	566.6	632	1492930	565.5
G014.1-00.1	S	14.19	0.11	0.046	0.146	11.0	-12.31	-12.32	-0.2	-0.2	515	1549360	518.8	515	1640660	520.2
G014.3+00.1	S	14.3	0.14	0.037	0.137	10.7	-11.99	-11.99	2.6	2.6	459	1236030	404.9	459	1293080	406.3
G015.1-01.6	S	15.11	-1.61	0.224	0.324	38.8	-12.33	-12.29	-0.5	-0.3	6643	17527600	6680.4	6643	18025200	6666.6
G015.9+00.2	S?	15.88	0.2	0.049	0.149	47.4	-12.52	-12.53	0.4	0.3	1578	2494840	1563.4	1578	2825040	1565.5
G016.2-02.7	S	16.12	-2.61	0.142	0.242	61.0	-12.0	-12.0	4.4	4.4	5451	9196440	5131.7	5451	9854650	5130.4
G017.4-02.3	S	17.39	-2.3	0.2	0.3	86.8	-12.02	-12.02	4.1	4.2	11976	12557200	11528.3	11976	13499600	11520.9
G017.8-02.6	S	17.79	-2.61	0.2	0.3	54.8	-12.16	-12.16	1.1	1.4	7526	9394320	7427.5	7526	10891000	7408.5
G018.88+00.3	S	18.8	0.35	0.114	0.214	16.7	-11.92	-11.91	2.6	2.7	1328	2428050	1236.5	1328	2494330	1231.2
G018.9-01.1	C?	18.95	-1.18	0.275	0.375	38.3	-11.96	-11.89	1.7	2.1	7433	9807820	7285.0	7433	10579100	7251.7
G019.1+00.2	S	19.15	0.27	0.225	0.325	8.5	-11.69	-11.69	2.2	2.2	2255	6399870	2152.6	2255	6517670	2153.0
G020.0-00.2	F	19.98	-0.17	0.083	0.183	18.0	-12.35	-12.37	-0.3	-0.4	973	3237340	982.6	973	3532720	985.3
G020.4+00.1	S	20.47	0.16	0.067	0.167	20.5	-11.96	-11.96	4.1	3.9	1055	2726750	928.6	1055	2685240	932.1
G021.0-00.4	S	21.04	-0.47	0.066	0.166	32.3	-12.16	-12.16	2.6	2.5	1464	2641320	1365.0	1466	2815300	1372.6
G021.5-00.1	S	21.56	-0.1	0.042	0.142	37.4	-12.4	-12.43	1.2	0.9	1196	2011620	1156.0	1203	2092840	1171.9
G021.8-00.6	C	21.8	-0.51	0.167	0.267	38.4	-11.97	-12.0	3.0	2.6	4247	6967980	4053.0	4276	7083620	4108.6
G025.1-02.3	S	25.1	-2.25	0.408	0.508	6.6	-11.67	-11.65	-0.0	0.1	2636	8843640	2637.2	2636	8412710	2630.8
G030.7-02.0	?	30.69	-1.98	0.133	0.233	12.9	-12.04	-12.05	0.6	0.5	1044	4202920	1025.3	1044	4036600	1027.4
G030.7+01.0	S?	30.72	0.95	0.173	0.273	30.1	-11.96	-11.96	2.6	2.6	3148	5887810	3003.8	3148	5955820	3002.1
G031.5-00.6	S?	31.55	-0.63	0.15	0.25	36.6	-12.13	-12.16	1.6	1.3	2979	4745600	2890.2	2979	4591080	2907.6
G032.1-00.9	C?	32.12	-0.9	0.333	0.433	33.0	-11.69	-11.71	3.8	3.5	7635	12806900	7304.6	7635	12921300	7332.7
G036.6-00.7	S?	36.59	-0.69	0.208	0.308	19.3	-12.02	-12.04	0.5	0.4	2794	6224460	2765.1	2794	6423380	2772.5
G036.6+02.6	S	36.58	2.6	0.124	0.224	0.4	-11.42	-11.42	0.0	0.0	37	177198	36.8	37	177198	36.8
G039.2-00.3	C	39.24	-0.32	0.058	0.158	34.2	-12.21	-12.22	2.2	2.1	1089	3279900	1018.4	1100	3301700	1032.1
G039.7-02.0	?	39.69	-2.39	0.707	0.807	22.7	-11.68	-11.67	0.2	0.3	18705	73300000	18678.3	18960	76120200	18922.2
G042.8+00.6	S	42.82	0.64	0.2	0.3	54.1	-12.03	-12.03	2.5	2.5	6631	22343300	6430.1	6680	23187000	6475.4
G043.9+01.6	S?	43.91	1.61	0.5	0.6	31.2	-12.1	-12.07	-0.9	-0.8	15404	52941000	15516.0	15555	53481400	15651.3
G045.7-00.4	S	45.69	-0.3	0.183	0.283	45.6	-12.08	-12.09	1.8	1.6	5961	19246700	5826.9	5961	19576600	5836.3
G046.8-00.3	S	46.77	-0.3	0.124	0.224	21.9	-11.89	-11.88	3.1	3.1	2115	8618720	1976.6	2115	9312540	1973.5
G047.4-03.9	F	47.38	-3.88	0.008	0.118	1.5	-12.46	-12.46	-1.8	-1.8	15	117436	23.2	15	117436	23.2
G053.6-02.2	C	53.63	-2.26	0.253	0.353	5.3	-11.88	-12.0	-0.8	-1.2	822	3535540	845.6	845	3682600	880.7
G054.4-00.3	S	54.47	-0.29	0.333	0.433	26.7	-12.19	-12.19	-1.0	-0.9	6257	26364300	6333.8	6258	25698300	6332.6
G055.0+00.3	S	55.11	0.42	0.144	0.244	24.5	-12.11	-12.11	0.5	0.5	1961	7593130	1937.7	1961	7664270	1937.3
G057.2+00.8	S?	57.3	0.83	0.1	0.2	15.7	-12.12	-12.12	0.4	0.4	876	4016130	864.9	876	4016130	864.9
G059.5+00.1	S	59.58	0.12	0.125	0.225	14.3	-11.9	-11.9	1.3	1.3	1025	4630410	983.3	1025	4630420	983.3
G059.8+01.2	?	59.81	1.2	0.149	0.249	6.3	-11.92	-11.92	-0.3	-0.3	558	2686460	564.3	558	2686460	564.3
G063.7+01.1	F	63.79	1.17	0.067	0.167	10.0	-11.89	-11.89	1.3	1.3	410	1815790	383.6	410	1815790	383.6
G064.5+00.9	S	64.52	0.95	0.067	0.167	13.1	-11.93	-11.93	1.4	1.4	526	2287150	495.4	526	2287150	495.4

Name	Type	l														
G065.1+00.6	S	65.27	0.3	0.559	0.659	14.6	-11.43	-11.43	1.2	1.2	8736	42075100	8628.0	8736	42075100	8628.0
G065.7+01.2	F?	65.72	1.21	0.183	0.283	8.8	-11.62	-11.62	1.5	1.5	956	4485100	909.1	956	4485100	909.1
G067.7+01.8	S	67.74	1.82	0.112	0.212	2.5	-11.44	-11.44	1.4	1.4	155	598658	137.8	155	598658	137.8
G068.6-01.2	C?	68.6	-1.2	0.192	0.292	2.5	-11.51	-11.51	-0.1	-0.1	243	1184670	244.7	243	1184670	244.7
G069.0+02.7	S	68.84	2.78	0.667	0.767	0.7	-10.7	-10.7	0.4	0.4	597	2438190	588.3	597	2438190	588.3
G069.7+01.0	S	69.69	1.0	0.125	0.225	2.4	-11.58	-11.58	-0.4	-0.4	135	634856	139.4	135	634856	139.4
G260.4+03.4	C	260.4	-3.44	0.456	0.556	3.7	-11.32	-11.32	1.1	1.1	1538	7623620	1493.8	1538	7623620	1493.8
G272.2+03.2	S	272.22	-3.18	0.125	0.225	0.7	-11.58	-11.58	-0.8	-0.8	41	200820	46.3	41	200820	46.3
G279.0+01.1	S?	278.63	1.22	0.792	0.892	3.0	-11.15	-11.15	0.8	0.8	3168	14528100	3124.7	3168	14528100	3124.7
G286.5+01.2	F	286.57	-1.21	0.104	0.204	30.2	-12.11	-12.11	1.2	1.3	1505	6538570	1458.0	1503	6389800	1454.8
G287.4+00.6	S	287.43	0.57	0.008	0.118	31.7	-12.46	-12.46	0.6	0.7	531	2553870	516.6	531	2421150	516.0
G289.7+00.3	C	289.69	-0.29	0.132	0.232	16.4	-12.09	-12.09	0.3	0.3	1102	4996500	1092.9	1103	4981710	1064.9
G290.1-00.8	C	290.15	-0.78	0.136	0.236	17.3	-11.91	-11.89	1.7	1.8	1123	5087060	1068.4	1125	4541750	2004.6
G291.0-00.1	S	291.02	-0.08	0.116	0.216	35.3	-12.13	-12.12	1.3	1.4	2069	7870930	2009.1	2068	7527410	1118.1
G292.0+01.8	C	292.03	1.75	0.082	0.182	29.1	-12.2	-12.2	1.0	1.0	1152	5416800	1117.7	1152	5417550	6850.9
G294.1-00.0	C	294.12	-0.06	0.333	0.433	27.5	-11.77	-11.78	1.5	1.5	6961	30218100	6836.6	6961	33054000	2226.4
G296.1-00.5	S	296.05	-0.5	0.253	0.353	15.2	-11.93	-11.93	-0.2	-0.2	2219	10413600	2226.4	2219	10413600	624.5
G296.7+00.9	S	296.66	-0.92	0.092	0.192	15.0	-12.01	-12.01	1.0	1.0	649	2674860	624.5	649	2674860	1168.9
G296.8-00.3	S	296.88	-0.34	0.139	0.239	18.9	-11.88	-11.88	1.9	1.9	1235	5241420	1168.9	1235	5241420	527.9
G298.5-00.3	?	298.53	-0.33	0.042	0.142	23.3	-12.27	-12.27	0.9	0.9	548	2520860	527.9	548	2520860	911.6
G298.6-00.0	S	298.61	-0.06	0.087	0.187	20.8	-11.99	-11.99	2.5	2.5	988	4531350	911.6	988	4531350	18.5
G299.2-02.9	S	299.18	-2.89	0.117	0.217	0.2	-11.23	-11.23	-0.1	-0.1	18	72864	18.5	18	72864	1171.1
G299.6-00.5	S	299.59	-0.47	0.108	0.208	24.1	-12.29	-12.29	-0.2	-0.2	1164	5466410	1171.1	1164	5466410	2500.7
G301.4+01.0	S	301.44	-0.98	0.243	0.343	10.7	-11.76	-11.76	1.3	1.3	2568	10936300	2500.5	2568	10103400	1288.0
G302.3-00.7	S	302.29	0.73	0.142	0.242	10.4	-12.0	-12.06	0.4	-0.1	1286	2958970	1273.3	1286	2559110	748.0
G306.3-00.9	S	306.31	-0.89	0.015	0.118	38.8	-12.67	-12.65	-0.3	-0.3	749	1901580	757.4	741	1839140	1218.6
G308.1-00.7	S	308.13	-0.66	0.108	0.208	23.9	-12.47	-12.47	-1.0	-1.0	1183	5922850	1218.5	1183	5922850	829.9
G308.4+01.4	C?	308.81	-1.38	0.083	0.183	21.3	-12.16	-12.16	0.8	0.8	853	3783930	830.2	853	3816780	2714.4
G308.8-00.1	S	309.16	-0.1	0.204	0.304	25.2	-11.92	-11.92	1.4	1.4	2786	13053200	2714.4	2786	13053200	1403.9
G309.2-00.6	S	309.79	-0.7	0.112	0.212	27.5	-12.13	-12.14	0.9	0.9	1438	6449660	1402.5	1438	6570410	2205.7
G309.8+00.0	C	310.6	-0.0	0.182	0.282	23.8	-12.06	-12.06	0.5	0.5	2228	10596900	2205.7	2228	10596900	309.5
G310.6+01.6	S	310.62	-1.6	0.01	0.118	19.1	-12.29	-12.3	1.0	0.9	326	1067800	308.7	326	1094160	718.5
G310.8-00.4	S	310.81	-0.28	0.067	0.167	20.8	-12.14	-12.14	1.4	0.9	756	3028100	718.9	756	2957300	983.7
G311.5-00.3	S	311.53	-0.46	0.1	0.2	19.9	-12.28	-12.28	-0.3	1.4	976	3972540	986.0	976	3848100	463.9
G312.5-03.0	?	312.49	-0.34	0.042	0.142	16.5	-12.15	-12.15	1.5	-0.2	497	1343140	464.0	497	1305880	82.9
G315.4+00.3	C	315.41	-3.0	0.158	0.258	0.9	-11.36	-11.36	0.0	1.5	83	338838	82.9	83	338838	2537.9
G315.9-00.0	S	315.86	-0.29	0.147	0.247	30.2	-12.31	-12.24	-0.2	0.0	2520	8860320	2529.2	2520	7901890	1951.6
G316.3-00.0	S	316.29	-0.03	0.156	0.256	23.5	-12.26	-12.31	-0.4	-0.4	1927	7624960	1946.7	1927	6020010	2327.2
G317.3-00.2	S	317.31	-0.01	0.168	0.268	25.5	-12.3	-12.26	-0.7	-0.6	2294	8235820	2330.1	2294	6647600	1739.8
G319.9-00.7	F?	319.97	-0.24	0.092	0.192	36.2	-12.08	-12.3	2.6	-0.7	1860	3799150	1751.2	1860	2969960	1722.6
G321.9-01.1	S	321.89	-0.62	0.031	0.131	57.6	-12.53	-12.11	-1.0	2.8	1764	2757770	1710.1	1764	2856540	6436.3
G321.9-00.3	F?	321.9	-1.07	0.233	0.333	32.1	-12.37	-12.49	0.2	1.0	6354	21204000	6433.4	6354	20458300	5618.4
G322.5-00.1	S	322.46	-0.3	0.223	0.323	30.3	-12.15	-12.36	1.4	-1.0	5626	20462000	5612.8	5626	20077400	1803.9
G323.5+00.1	C	323.49	-0.11	0.125	0.225	20.1	-12.07	-12.14	-2.7	0.1	1864	9079410	1806.0	1864	8839300	1151.8
G326.3-01.8	C	326.3	0.11	0.108	0.208	22.1	-13.01	-12.08	2.5	1.4	1200	5594280	1295.1	1080	4800770	3468.4
G327.2-00.1	C	327.24	-1.76	0.317	0.417	26.5	-11.7	-14.54	-0.2	-2.1	3878	15886100	3725.9	3618	14694800	551.3
G327.4+00.4	C	327.25	-0.13	0.033	0.133	34.9	-12.53	-11.72	0.2	2.5	562	2376880	566.7	556	1903600	2024.0
G327.4+01.0	S	327.37	0.49	0.175	0.275	27.5	-12.13	-12.6	-0.8	0.2	2071	9708130	2063.3	2042	7894340	1096.4
G328.4+00.2	F?	328.41	1.01	0.117	0.217	22.4	-12.35	-12.17	0.4	0.4	1090	5264690	1117.0	1078	4244660	551.7
G329.7+00.4	S?	329.72	0.23	0.042	0.142	28.0	-12.42	-12.41	1.6	-0.6	568	2683830	559.2	559	2530890	3134.5
G330.2+01.0	S	330.17	0.41	0.303	0.403	17.5	-11.74	-12.42	1.7	0.3	3228	15231800	3135.4	3228	15124200	606.6
G337.2-00.7	S	337.19	0.98	0.092	0.192	15.0	-12.0	-11.74	2.5	1.7	648	2999040	606.6	648	2997900	962.5
G337.3+01.0	S	337.33	-0.74	0.05	0.15	33.4	-12.19	-12.0	3.5	1.7	1056	1399610	977.1	1039	1315350	1488.3
G340.4+00.4	S	340.4	0.96	0.112	0.212	25.0	-11.91	-12.19	1.7	2.4	1650	2841420	1510.4	1633	2773960	1339.9
G340.6-00.3	S	340.6	0.45	0.07	0.17	40.4	-12.25	-11.89	2.5	3.7	1412	2403160	1349.7	1404	2397170	991.4

G341.2+00.9	C	341.19	0.86	0.156	0.256	16.5	-12.03	-12.02	0.5	0.6	1350	2828990	1332.1	1350	2797160	1328.4
G341.9+00.3	S	341.86	-0.32	0.058	0.158	17.9	-12.08	-12.08	1.9	2.0	565	1834100	520.4	565	1889290	519.0
G342.0+00.2	S	341.94	-0.21	0.087	0.187	13.9	-11.97	-11.96	2.2	2.2	768	2735520	709.5	768	2792180	708.0
G342.1+00.9	S	342.1	0.89	0.079	0.179	10.7	-12.12	-12.11	0.4	0.4	435	1595750	426.8	435	1552870	426.0
G343.1-00.7	S	343.08	-0.59	0.198	0.298	17.9	-12.4	-12.04	0.1	0.1	2279	7190840	2274.8	2279	6728720	2275.1
G349.2-00.1	S	349.13	-0.07	0.061	0.161	60.7	-12.4	-12.45	1.2	0.8	2409	4192420	2350.3	2424	4410390	2383.8
G349.7+00.2	S	349.73	0.18	0.019	0.119	28.7	-12.15	-12.16	3.9	3.7	690	1273970	592.0	696	1293410	603.0
G350.0-02.0	S	349.92	-2.05	0.375	0.475	3.3	-11.46	-11.46	1.1	1.1	1491	6496700	1449.9	1492	6370900	1450.9
G350.1-00.3	S?	349.72	0.25	0.033	0.133	28.6	-12.13	-12.15	3.5	3.3	839	1595670	740.7	846	1622640	754.0
G351.2+00.1	C?	351.27	0.16	0.058	0.158	18.5	-12.25	-12.27	0.8	0.7	675	2876460	654.4	675	2956340	657.1
G351.7+00.8	S	351.7	0.82	0.132	0.232	15.7	-12.28	-12.29	-0.7	-0.7	1153	5253430	1175.6	1153	5295140	1175.8
G351.9-00.9	S	351.92	-0.96	0.087	0.187	24.1	-12.09	-12.09	2.3	2.4	1231	4493820	1151.8	1231	4427500	1150.2
G352.7-00.1	C	352.75	-0.12	0.058	0.158	45.4	-12.3	-12.3	2.4	2.3	1477	3011180	1387.1	1477	3118120	1389.2
G353.9-02.0	S	353.94	-2.09	0.108	0.208	25.9	-12.47	-12.47	-0.7	-0.6	1105	3966490	1126.9	1105	3937460	1125.9
G354.1+00.1	C?	354.19	0.15	0.056	0.156	44.8	-12.41	-12.41	1.4	1.4	1296	2726030	1245.9	1296	2665110	1247.4
G354.8+00.8	S	354.87	-0.78	0.158	0.258	34.7	-12.26	-12.27	0.4	0.3	2735	8619920	2712.5	2735	9375840	2718.2
G355.4+00.7	S	355.4	0.73	0.208	0.308	16.9	-11.95	-11.95	0.9	0.9	2230	10096200	2188.3	2230	10227900	2188.2
G355.6-00.0	C	355.69	-0.08	0.058	0.158	19.2	-12.14	-12.14	2.0	2.0	737	3290160	683.5	737	3291500	683.5
G355.9-02.5	S	355.95	-2.54	0.108	0.208	3.1	-11.64	-11.64	1.9	1.9	172	729263	148.8	172	729263	148.8
G356.2+04.5	S	356.22	4.46	0.208	0.308	6.9	-11.62	-11.62	1.7	1.7	739	3172290	694.4	739	3172290	694.4
G356.3-01.5	S	356.31	-1.5	0.144	0.244	6.2	-12.13	-12.13	-0.8	-0.8	639	3248190	660.1	639	3248190	660.1
G356.3-00.3	S	356.3	-0.35	0.073	0.173	12.3	-12.23	-12.23	0.1	0.1	676	3283020	673.7	676	3283020	673.7
G357.7-00.1	C?	357.69	-0.12	0.041	0.141	52.3	-12.21	-12.19	4.0	4.3	1569	2568960	1416.0	1569	2823060	1405.7
G357.7+00.3	S	357.67	0.35	0.2	0.3	48.5	-11.97	-11.98	2.6	2.5	6267	13516300	6064.4	6267	14700100	6073.3
G358.0+03.8	S	357.96	3.8	0.317	0.417	4.7	-11.29	-11.29	3.0	3.0	893	3854740	806.9	893	3854740	806.9
G358.1+00.1	S	358.12	1.04	0.167	0.267	53.4	-11.99	-12.01	3.4	3.1	5622	10586100	5370.2	5622	13860000	5391.2
G359.1+00.9	S	359.1	0.99	0.096	0.196	107.8	-12.63	-12.64	0.3	0.3	7069	13468300	7043.1	7069	12481400	7047.2

Table B.1.: The SNR sample after the selection procedure described in section 5.2. Sources that are in the *loose* but not in the *conservative* sample are marked in bold letters. Coordinates and ON-region radii are in degrees, live-times in hours, flux ULs in units of cm^{-2}s^{-1}.

171

Name	GL	GB
HESS J0534+220	184.56	-5.78
HESS J0536-691	279.55	-31.75
HESS J0632+057	205.66	-1.44
HESS J0835-455	263.86	-3.09
HESS J0852-463	266.29	-1.24
HESS J1018-589	284.24	-1.74
HESS J1023-575	284.22	-0.4
HESS J1026-582	284.8	-0.52
HESS J1119-614	292.12	-0.56
HESS J1302-638	304.19	-0.99
HESS J1303-631	304.24	-0.36
HESS J1345-639	308.9	-1.78
HESS J1356-645	309.81	-2.49
HESS J1406-613	311.81	0.22
HESS J1414-619	312.49	-0.57
HESS J1418-609	313.25	0.15
HESS J1420-607	313.56	0.27
HESS J1427-608	314.42	-0.14
HESS J1442-624	315.41	-2.3
HESS J1457-593	318.32	-0.4
HESS J1459-608	317.87	-1.73
HESS J1502-421	327.37	14.5
HESS J1503-582	319.62	0.29
HESS J1504-418	327.84	14.57
HESS J1507-622	317.95	-3.49
HESS J1514-591	320.33	-1.19
HESS J1534-571	323.68	-0.9
HESS J1554-550	327.1	-1.11
HESS J1614-518	331.52	-0.58
HESS J1616-508	332.39	-0.14
HESS J1626-490	334.77	0.05
HESS J1632-478	336.38	0.19
HESS J1634-472	337.11	0.22
HESS J1640-465	338.32	-0.02
HESS J1641-462	338.49	0.07
HESS J1646-458	339.55	-0.35
HESS J1654-396	344.63	2.37
HESS J1702-420	344.3	-0.18
HESS J1708-410	345.66	-0.44
HESS J1708-443	343.04	-2.38
HESS J1713-381	348.64	0.38
HESS J1713-397	347.34	-0.47
HESS J1714-385	348.39	0.11
HESS J1718-385	348.83	-0.49
HESS J1729-345	353.44	-0.13
HESS J1731-347	353.56	-0.62
HESS J1741-302	358.28	0.12
HESS J1745-290	359.94	-0.04

HESS J1745-303	358.71	-0.64
HESS J1747-248	3.78	1.72
HESS J1747-281	0.87	0.08
HESS J1754-257	3.74	0.04
HESS J1757-249	4.6	-0.22
HESS J1800-240A	6.14	-0.63
HESS J1800-240B	5.9	-0.36
HESS J1800-240C	5.71	-0.06
HESS J1801-233	6.66	-0.27
HESS J1804-216	8.4	-0.03
HESS J1808-204	9.99	-0.25
HESS J1809-193	11.18	-0.09
HESS J1813-127	17.31	2.45
HESS J1813-178	12.81	-0.03
HESS J1818-155	15.42	0.18
HESS J1825-137	17.71	-0.7
HESS J1826-148	16.88	-1.29
HESS J1831-098	21.85	-0.11
HESS J1832-084	23.29	0.3
HESS J1833-105	21.51	-0.88
HESS J1834-087	23.24	-0.32
HESS J1837-069	25.18	-0.11
HESS J1841-055	26.8	-0.2
HESS J1843-033	29.08	0.27
HESS J1844-031	29.42	0.11
HESS J1846-023	30.25	-0.13
HESS J1846-029	29.7	-0.24
HESS J1848-018	30.98	-0.16
HESS J1849-000	32.64	0.53
HESS J1852-000	32.8	-0.08
HESS J1854+011	33.99	0.12
HESS J1857+026	35.96	-0.06
HESS J1858+020	35.58	-0.58
HESS J1908+063	40.39	-0.79
HESS J1910+091	43.17	0.0
HESS J1911+090	43.26	-0.19
HESS J1912+101	44.39	-0.07
HESS J1923+141	49.1	-0.39
HESS J1930+186	54.06	0.27
HESS J1943+213	57.76	-1.29

Table B.2.: Galactic H.E.S.S. sources that are used in the deselection region generation.

174

Bibliography

[Acciari et al., 2011] Acciari, V. A., Aliu, E., Arlen, T., Aune, T., Beilicke, M.,
Benbow, W., Bradbury, S. M., Buckley, J. H., Bugaev, V., Byrum, K., Can-
non, A., Cesarini, A., Ciupik, L., Collins-Hughes, E., Cui, W., Dickherber, R.,
Duke, C., Errando, M., Finley, J. P., Finnegan, G., Fortson, L., Furniss, A.,
Galante, N., Gall, D., Gillanders, G. H., Godambe, S., Griffin, S., Grube, J.,
Guenette, R., Gyuk, G., Hanna, D., Holder, J., Hughes, J. P., Hui, C. M., Hu-
mensky, T. B., Kaaret, P., Karlsson, N., Kertzman, M., Kieda, D., Krawczyn-
ski, H., Krennrich, F., Lang, M. J., LeBohec, S., Madhavan, A. S., Maier, G.,
Majumdar, P., McArthur, S., McCann, A., Moriarty, P., Mukherjee, R., Ong,
R. A., Orr, M., Otte, A. N., Pandel, D., Park, N. H., Perkins, J. S., Pohl, M.,
Quinn, J., Ragan, K., Reyes, L. C., Reynolds, P. T., Roache, E., Rose, H. J.,
Saxon, D. B., Schroedter, M., Sembroski, G. H., Senturk, G. D., Slane, P.,
Smith, A. W., Tešić, G., Theiling, M., Thibadeau, S., Tsurusaki, K., Varlotta,
A., Vassiliev, V. V., Vincent, S., Vivier, M., Wakely, S. P., Ward, J. E., Weekes,
T. C., Weinstein, A., Weisgarber, T., Williams, D. A., Wood, M., and Zitzer,
B. (2011). Discovery of TeV Gamma-ray Emission from Tycho's Supernova
Remnant. ApJ, 730:L20.

[Acero et al., 2010] Acero, F., Aharonian, F., Akhperjanian, A. G., Anton, G.,
Barres de Almeida, U., Bazer-Bachi, A. R., Becherini, Y., Behera, B., Beilicke,
M., Bernlöhr, K., Bochow, A., Boisson, C., Bolmont, J., Borrel, V., Brucker, J.,
Brun, F., Brun, P., Bühler, R., Bulik, T., Büsching, I., Boutelier, T., Chad-
wick, P. M., Charbonnier, A., Chaves, R. C. G., Cheesebrough, A., Conrad,
J., Chounet, L.-M., Clapson, A. C., Coignet, G., Dalton, M., Daniel, M. K.,
Davids, I. D., Degrange, B., Deil, C., Dickinson, H. J., Djannati-Ataï, A.,
Domainko, W., O'C. Drury, L., Dubois, F., Dubus, G., Dyks, J., Dyrda, M.,
Egberts, K., Eger, P., Espigat, P., Fallon, L., Farnier, C., Fegan, S., Feinstein,
F., Fiasson, A., Förster, A., Fontaine, G., Füßling, M., Gabici, S., Gallant,
Y. A., Gérard, L., Gerbig, D., Giebels, B., Glicenstein, J. F., Glück, B., Goret,
P., Göring, D., Hauser, D., Hauser, M., Heinz, S., Heinzelmann, G., Henri,
G., Hermann, G., Hinton, J. A., Hoffmann, A., Hofmann, W., Hofverberg,
P., Holleran, M., Hoppe, S., Horns, D., Jacholkowska, A., de Jager, O. C.,
Jahn, C., Jung, I., Katarzyński, K., Katz, U., Kaufmann, S., Kerschhaggl,
M., Khangulyan, D., Khélifi, B., Keogh, D., Klochkov, D., Kluźniak, W.,
Kneiske, T., Komin, N., Kosack, K., Kossakowski, R., Lamanna, G., Lemoine-
Goumard, M., Lenain, J.-P., Lohse, T., Marandon, V., Marcowith, A., Masbou,
J., Maurin, D., McComb, T. J. L., Medina, M. C., Méhault, J., Moderski, R.,

Moulin, E., Naumann-Godo, M., de Naurois, M., Nedbal, D., Nekrassov, D., Nicholas, B., Niemiec, J., Nolan, S. J., Ohm, S., Olive, J.-F., de Oña Wilhelmi, E., Orford, K. J., Ostrowski, M., Panter, M., Paz Arribas, M., Pedaletti, G., Pelletier, G., Petrucci, P.-O., Pita, S., Pühlhofer, G., Punch, M., Quirrenbach, A., Raubenheimer, B. C., Raue, M., Rayner, S. M., Reimer, O., Renaud, M., de Los Reyes, R., Rieger, F., Ripken, J., Rob, L., Rosier-Lees, S., Rowell, G., Rudak, B., Rulten, C. B., Ruppel, J., Ryde, F., Sahakian, V., Santangelo, A., Schlickeiser, R., Schöck, F. M., Schönwald, A., Schwanke, U., Schwarzburg, S., Schwemmer, S., Shalchi, A., Sushch, I., Sikora, M., Skilton, J. L., Sol, H., Stawarz, Ł., Steenkamp, R., Stegmann, C., Stinzing, F., Superina, G., Szostek, A., Tam, P. H., Tavernet, J.-P., Terrier, R., Tibolla, O., Tluczykont, M., van Eldik, C., Vasileiadis, G., Venter, C., Venter, L., Vialle, J. P., Vincent, P., Vink, J., Vivier, M., Völk, H. J., Volpe, F., Vorobiov, S., Wagner, S. J., Ward, M., Zdziarski, A. A., Zech, A., and H.E.S.S. Collaboration (2010). First detection of VHE γ-rays from SN 1006 by HESS. A&A, 516:A62.

[Acero et al., 2007] Acero, F., Ballet, J., and Decourchelle, A. (2007). The gas density around SN 1006. A&A, 475:883–890.

[Ackermann et al., 2013] Ackermann, M., Ajello, M., Allafort, A., Baldini, L., Ballet, J., Barbiellini, G., Baring, M. G., Bastieri, D., Bechtol, K., Bellazzini, R., Blandford, R. D., Bloom, E. D., Bonamente, E., Borgland, A. W., Bottacini, E., Brandt, T. J., Bregeon, J., Brigida, M., Bruel, P., Buehler, R., Busetto, G., Buson, S., Caliandro, G. A., Cameron, R. A., Caraveo, P. A., Casandjian, J. M., Cecchi, C., Çelik, Ö., Charles, E., Chaty, S., Chaves, R. C. G., Chekhtman, A., Cheung, C. C., Chiang, J., Chiaro, G., Cillis, A. N., Ciprini, S., Claus, R., Cohen-Tanugi, J., Cominsky, L. R., Conrad, J., Corbel, S., Cutini, S., D'Ammando, F., de Angelis, A., de Palma, F., Dermer, C. D., do Couto e Silva, E., Drell, P. S., Drlica-Wagner, A., Falletti, L., Favuzzi, C., Ferrara, E. C., Franckowiak, A., Fukazawa, Y., Funk, S., Fusco, P., Gargano, F., Germani, S., Giglietto, N., Giommi, P., Giordano, F., Giroletti, M., Glanzman, T., Godfrey, G., Grenier, I. A., Grondin, M.-H., Grove, J. E., Guiriec, S., Hadasch, D., Hanabata, Y., Harding, A. K., Hayashida, M., Hayashi, K., Hays, E., Hewitt, J. W., Hill, A. B., Hughes, R. E., Jackson, M. S., Jogler, T., Jóhannesson, G., Johnson, A. S., Kamae, T., Kataoka, J., Katsuta, J., Knödlseder, J., Kuss, M., Lande, J., Larsson, S., Latronico, L., Lemoine-Goumard, M., Longo, F., Loparco, F., Lovellette, M. N., Lubrano, P., Madejski, G. M., Massaro, F., Mayer, M., Mazziotta, M. N., McEnery, J. E., Mehault, J., Michelson, P. F., Mignani, R. P., Mitthumsiri, W., Mizuno, T., Moiseev, A. A., Monzani, M. E., Morselli, A., Moskalenko, I. V., Murgia, S., Nakamori, T., Nemmen, R., Nuss, E., Ohno, M., Ohsugi, T., Omodei, N., Orienti, M., Orlando, E., Ormes, J. F., Paneque, D., Perkins, J. S., Pesce-Rollins, M., Piron, F., Pivato, G., Rainò, S., Rando, R., Razzano, M., Razzaque, S., Reimer, A., Reimer, O., Ritz, S., Romoli, C., Sánchez-Conde, M., Schulz, A., Sgrò, C., Simeon, P. E., Siskind,

E. J., Smith, D. A., Spandre, G., Spinelli, P., Stecker, F. W., Strong, A. W., Suson, D. J., Tajima, H., Takahashi, H., Takahashi, T., Tanaka, T., Thayer, J. G., Thayer, J. B., Thompson, D. J., Thorsett, S. E., Tibaldo, L., Tibolla, O., Tinivella, M., Troja, E., Uchiyama, Y., Usher, T. L., Vandenbroucke, J., Vasileiou, V., Vianello, G., Vitale, V., Waite, A. P., Werner, M., Winer, B. L., Wood, K. S., Wood, M., Yamazaki, R., Yang, Z., and Zimmer, S. (2013). Detection of the Characteristic Pion-Decay Signature in Supernova Remnants. *Science*, 339:807–811.

[Actis et al., 2011] Actis, M., Agnetta, G., Aharonian, F., Akhperjanian, A., Aleksić, J., Aliu, E., Allan, D., Allekotte, I., Antico, F., Antonelli, L. A., and et al. (2011). Design concepts for the Cherenkov Telescope Array CTA: an advanced facility for ground-based high-energy gamma-ray astronomy. *Experimental Astronomy*, 32:193–316.

[Aharonian et al., 2008] Aharonian, F., Akhperjanian, A. G., Barres de Almeida, U., Bazer-Bachi, A. R., Behera, B., Beilicke, M., Benbow, W., Berge, D., Bernlöhr, K., Boisson, C., Bolz, O., Borrel, V., Braun, I., Brion, E., Brucker, J., Bühler, R., Bulik, T., Büsching, I., Boutelier, T., Carrigan, S., Chadwick, P. M., Chounet, L.-M., Clapson, A. C., Coignet, G., Cornils, R., Costamante, L., Dalton, M., Degrange, B., Dickinson, H. J., Djannati-Ataï, A., Domainko, W., O'C. Drury, L., Dubois, F., Dubus, G., Dyks, J., Egberts, K., Emmanoulopoulos, D., Espigat, P., Farnier, C., Feinstein, F., Fiasson, A., Förster, A., Fontaine, G., Füßling, M., Gallant, Y. A., Giebels, B., Glicenstein, J. F., Glück, B., Goret, P., Hadjichristidis, C., Hauser, D., Hauser, M., Heinzelmann, G., Henri, G., Hermann, G., Hinton, J. A., Hoffmann, A., Hofmann, W., Holleran, M., Hoppe, S., Horns, D., Jacholkowska, A., de Jager, O. C., Jung, I., Katarzyński, K., Kendziorra, E., Kerschhaggl, M., Khélifi, B., Keogh, D., Komin, N., Kosack, K., Lamanna, G., Latham, I. J., Lemoine-Goumard, M., Lenain, J.-P., Lohse, T., Martin, J. M., Martineau-Huynh, O., Marcowith, A., Masterson, C., Maurin, D., McComb, T. J. L., Moderski, R., Moulin, E., Naumann-Godo, M., de Naurois, M., Nedbal, D., Nekrassov, D., Nolan, S. J., Ohm, S., Olive, J.-P., de Oña Wilhelmi, E., Orford, K. J., Osborne, J. L., Ostrowski, M., Panter, M., Pedaletti, G., Pelletier, G., Petrucci, P.-O., Pita, S., Pühlhofer, G., Punch, M., Quirrenbach, A., Raubenheimer, B. C., Raue, M., Rayner, S. M., Renaud, M., Ripken, J., Rob, L., Rosier-Lees, S., Rowell, G., Rudak, B., Ruppel, J., Sahakian, V., Santangelo, A., Schlickeiser, R., Schöck, F. M., Schröder, R., Schwanke, U., Schwarzburg, S., Schwemmer, S., Shalchi, A., Sol, H., Spangler, D., Stawarz, Ł., Steenkamp, R., Stegmann, C., Superina, G., Tam, P. H., Tavernet, J.-P., Terrier, R., van Eldik, C., Vasileiadis, G., Venter, C., Vialle, J. P., Vincent, P., Vivier, M., Völk, H. J., Volpe, F., Wagner, S. J., Ward, M., Zdziarski, A. A., and Zech, A. (2008). HESS upper limits for Kepler's supernova remnant. A&A, 488:219–223.

Bibliography

[Aharonian et al., 2006a] Aharonian, F., Akhperjanian, A. G., Bazer-Bachi, A. R., Beilicke, M., Benbow, W., Berge, D., Bernlöhr, K., Boisson, C., Bolz, O., Borrel, V., Braun, I., Breitling, F., Brown, A. M., Bühler, R., Büsching, I., Carrigan, S., Chadwick, P. M., Chounet, L.-M., Cornils, R., Costamante, L., Degrange, B., Dickinson, H. J., Djannati-Ataï, A., O'C. Drury, L., Dubus, G., Egberts, K., Emmanoulopoulos, D., Espigat, P., Feinstein, F., Ferrero, E., Fiasson, A., Fontaine, G., Funk, S., Funk, S., Gallant, Y. A., Giebels, B., Glicenstein, J. F., Goret, P., Hadjichristidis, C., Hauser, D., Hauser, M., Heinzelmann, G., Henri, G., Hermann, G., Hinton, J. A., Hofmann, W., Holleran, M., Horns, D., Jacholkowska, A., de Jager, O. C., Khélifi, B., Komin, N., Konopelko, A., Kosack, K., Latham, I. J., Le Gallou, R., Lemière, A., Lemoine-Goumard, M., Lohse, T., Martin, J. M., Martineau-Huynh, O., Marcowith, A., Masterson, C., McComb, T. J. L., de Naurois, M., Nedbal, D., Nolan, S. J., Noutsos, A., Orford, K. J., Osborne, J. L., Ouchrif, M., Panter, M., Pelletier, G., Pita, S., Pühlhofer, G., Punch, M., Raubenheimer, B. C., Raue, M., Rayner, S. M., Reimer, A., Reimer, O., Ripken, J., Rob, L., Rolland, L., Rowell, G., Sahakian, V., Saugé, L., Schlenker, S., Schlickeiser, R., Schwanke, U., Sol, H., Spangler, D., Spanier, F., Steenkamp, R., Stegmann, C., Superina, G., Tavernet, J.-P., Terrier, R., Théoret, C. G., Tluczykont, M., van Eldik, C., Vasileiadis, G., Venter, C., Vincent, P., Völk, H. J., Wagner, S. J., and Ward, M. (2006a). Observations of the Crab nebula with HESS. A&A, 457:899–915.

[Aharonian et al., 2006b] Aharonian, F., Akhperjanian, A. G., Bazer-Bachi, A. R., Beilicke, M., Benbow, W., Berge, D., Bernlöhr, K., Boisson, C., Bolz, O., Borrel, V., Braun, I., Breitling, F., Brown, A. M., Chadwick, P. M., Chounet, L.-M., Cornils, R., Costamante, L., Degrange, B., Dickinson, H. J., Djannati-Ataï, A., O'C. Drury, L., Dubus, G., Emmanoulopoulos, D., Espigat, P., Feinstein, F., Fontaine, G., Fuchs, Y., Funk, S., Gallant, Y. A., Giebels, B., Glicenstein, J. F., Goret, P., Hadjichristidis, C., Hauser, D., Hauser, M., Heinzelmann, G., Henri, G., Hermann, G., Hinton, J. A., Hofmann, W., Holleran, M., Horns, D., Jacholkowska, A., de Jager, O. C., Khélifi, B., Klages, S., Komin, N., Konopelko, A., Latham, I. J., Le Gallou, R., Lemière, A., Lemoine-Goumard, M., Lohse, T., Martin, J. M., Martineau-Huynh, O., Marcowith, A., Masterson, C., McComb, T. J. L., de Naurois, M., Nedbal, D., Nolan, S. J., Noutsos, A., Orford, K. J., Osborne, J. L., Ouchrif, M., Panter, M., Pelletier, G., Pita, S., Pühlhofer, G., Punch, M., Raubenheimer, B. C., Raue, M., Rayner, S. M., Reimer, A., Reimer, O., Ripken, J., Rob, L., Rolland, L., Rowell, G., Sahakian, V., Saugé, L., Schlenker, S., Schlickeiser, R., Schuster, C., Schwanke, U., Siewert, M., Sol, H., Spangler, D., Steenkamp, R., Stegmann, C., Superina, G., Tavernet, J.-P., Terrier, R., Théoret, C. G., Tluczykont, M., van Eldik, C., Vasileiadis, G., Venter, C., Vincent, P., Völk, H. J., and Wagner, S. J. (2006b). A detailed spectral and morphological study of the gamma-ray supernova remnant <ASTROBJ>RX J1713.7-3946</ASTROBJ> with HESS.

A&A, 449:223–242.

[Aharonian et al., 2004] Aharonian, F. et al. (2004). Calibration of cameras of the H.E.S.S. detector. *Astropart.Phys.*, 22:109–125.

[Aharonian, 2004] Aharonian, F. A. (2004). *Very high energy cosmic gamma radiation : a crucial window on the extreme Universe*.

[Allen, 1999] Allen, G. (1999). Evidence of 10-100 TeV Electrons in Supernova Remnants. In *International Cosmic Ray Conference*, volume 3 of *International Cosmic Ray Conference*, page 480.

[Arola et al., 2007] Arola, A., Lindfors, A., Natunen, A., and Lehtinen, K. E. J. (2007). A case study on biomass burning aerosols: effects on aerosol optical properties and surface radiation levels. *Atmospheric Chemistry & Physics*, 7:4257–4266.

[Atoyan and Dermer, 2011] Atoyan, A. and Dermer, C. (2011). Gamma Rays from the Tycho Supernova Remnant: Leptonic or Hadronic? *ArXiv e-prints*.

[Atoyan and Aharonian, 1999] Atoyan, A. M. and Aharonian, F. A. (1999). Modelling of the non-thermal flares in the Galactic microquasar GRS 1915+105. MNRAS, 302:253–276.

[Axford et al., 1977] Axford, W. I., Leer, E., and Skadron, G. (1977). The acceleration of cosmic rays by shock waves. In *International Cosmic Ray Conference*, volume 11 of *International Cosmic Ray Conference*, pages 132–137.

[Baade and Zwicky, 1934a] Baade, W. and Zwicky, F. (1934a). Cosmic Rays from Super-novae. *Proceedings of the National Academy of Science*, 20:259–263.

[Baade and Zwicky, 1934b] Baade, W. and Zwicky, F. (1934b). On Super-novae. *Proceedings of the National Academy of Science*, 20:254–259.

[Bell, 1978] Bell, A. R. (1978). The acceleration of cosmic rays in shock fronts. I. MNRAS, 182:147–156.

[Bell, 2011] Bell, T. (2011). Diffusive Shock Acceleration and magnetic fields in SNR. *http://www3.mpifr-bonn.mpg.de/div/meetings/2ndRU1254/pdf-files/programme/Bell_T.ppt*.

[Berezhko et al., 2009] Berezhko, E. G., Ksenofontov, L. T., and Völk, H. J. (2009). Cosmic ray acceleration parameters from multi-wavelength observations. The case of SN 1006. A&A, 505:169–176.

[Berezhko and Völk, 2010] Berezhko, E. G. and Völk, H. J. (2010). Nonthermal and thermal emission from the supernova remnant RX J1713.7-3946. A&A, 511:A34.

Bibliography

[Berge et al., 2007] Berge, D., Funk, S., and Hinton, J. (2007). Background modelling in very-high-energy γ-ray astronomy. A&A, 466:1219–1229.

[Bernlöhr, 2000] Bernlöhr, K. (2000). Impact of atmospheric parameters on the atmospheric Cherenkov technique*. *Astroparticle Physics*, 12:255–268.

[Blandford and Ostriker, 1978] Blandford, R. D. and Ostriker, J. P. (1978). Particle acceleration by astrophysical shocks. ApJ, 221:L29–L32.

[Blasi et al., 2007] Blasi, P., Amato, E., and Caprioli, D. (2007). The maximum momentum of particles accelerated at cosmic ray modified shocks. MNRAS, 375:1471–1478.

[Blumenthal and Gould, 1970] Blumenthal, G. R. and Gould, R. J. (1970). Bremsstrahlung, Synchrotron Radiation, and Compton Scattering of High-Energy Electrons Traversing Dilute Gases. *Reviews of Modern Physics*, 42:237–271.

[Bochow, 2011a] Bochow, A. (2011a). *A Systemtatic Study of Supernova Remnants as seen with H.E.S.S.* PhD thesis, PhD Thesis, Ruperto-Carola University of Heidelberg, 2011.

[Bochow, 2011b] Bochow, A. (2011b). Very-high-energy gamma-radiation from supernova remnants as seen with H.E.S.S. In *International Cosmic Ray Conference*, volume 7 of *International Cosmic Ray Conference*, page 110.

[Bolmont et al., 2013] Bolmont, J., Corona, P., Gauron, P., Ghislain, P., Goffin, C., Guevara Riveros, L., Huppert, J.-F., Martineau-Huynh, O., Nayman, P., Parraud, J.-M., Tavernet, J.-P., Toussenel, F., Vincent, D., Vincent, P., Bertoli, W., Espigat, P., Punch, M., Besin, D., Delagnes, E., Glicenstein, J.-F., Moudden, Y., Venault, P., Zaghia, H., Brunetti, L., Dubois, J., Fiasson, A., Geffroy, N., Gomes Monteiro, I., Journet, L., Krayzel, F., Lamanna, G., Le Flour, T., Lees, S., Lieunard, B., Maurin, G., Mugnier, P., Panazol, J., Prast, J., Chounet, L.-M., Edy, E., Fontaine, G., Giebels, B., Hormigos, S., Khélifi, B., Manigot, P., Maritaz, P., de Naurois, M., Compin, M., Feinstein, F., Fernandez, D., Mehault, J., Rivoire, S., Royer, S., Sanguillon, M., and Vasileiadis, G. (2013). The camera of the fifth H.E.S.S. telescope. Part I: System description. *ArXiv e-prints*.

[Bolz, 2004] Bolz, O. (2004). PhD thesis.

[Borkowski et al., 1996] Borkowski, K., Szymkowiak, A. E., Blondin, J. M., and Sarazin, C. L. (1996). A Circumstellar Shell Model for the Cassiopeia A Supernova Remnant. ApJ, 466:866.

[Brand and Blitz, 1993] Brand, J. and Blitz, L. (1993). The Velocity Field of the Outer Galaxy. A&A, 275:67.

[Bronfman et al., 1988] Bronfman, L., Cohen, R. S., Alvarez, H., May, J., and Thaddeus, P. (1988). A CO survey of the southern Milky Way - The mean radial distribution of molecular clouds within the solar circle. ApJ, 324:248–266.

[Caprioli, 2011] Caprioli, D. (2011). Understanding hadronic gamma-ray emission from supernova remnants. J. Cosmology Astropart. Phys., 5:26.

[Carrigan et al., 2013] Carrigan, S., Brun, F., Chaves, R. C. G., Deil, C., Donath, A., Gast, H., Marandon, V., Renaud, M., and for the H. E. S. S. collaboration (2013). The H.E.S.S. Galactic Plane Survey - maps, source catalog and source population. *ArXiv e-prints*.

[Casanova and Dingus, 2008] Casanova, S. and Dingus, B. L. (2008). Constraints on the TeV source population and its contribution to the galactic diffuse TeV emission. *Astroparticle Physics*, 29:63–69.

[Case and Bhattacharya, 1998] Case, G. L. and Bhattacharya, D. (1998). A New Sigma -D Relation and Its Application to the Galactic Supernova Remnant Distribution. ApJ, 504:761.

[Cassam-Chenaï et al., 2007] Cassam-Chenaï, G., Hughes, J. P., Ballet, J., and Decourchelle, A. (2007). The Blast Wave of Tycho's Supernova Remnant. ApJ, 665:315–340.

[Castor et al., 1975] Castor, J., McCray, R., and Weaver, R. (1975). Interstellar bubbles. ApJ, 200:L107–L110.

[Chen et al., 2013] Chen, Y., Zhou, P., and Chu, Y.-H. (2013). Linear relation for wind-blown bubble sizes of main-sequence ob stars in a molecular environment and implication for supernova progenitors. *The Astrophysical Journal Letters*, 769(1):L16.

[Chevalier, 1981] Chevalier, R. A. (1981). Exploding white dwarf models for Type I supernovae. ApJ, 246:267–277.

[Chevalier, 1982a] Chevalier, R. A. (1982a). Self-similar solutions for the interaction of stellar ejecta with an external medium. ApJ, 258:790–797.

[Chevalier, 1982b] Chevalier, R. A. (1982b). The radio and X-ray emission from type II supernovae. ApJ, 259:302–310.

[Chevalier, 2005] Chevalier, R. A. (2005). Young Core-Collapse Supernova Remnants and Their Supernovae. ApJ, 619:839–855.

[Chevalier and Oishi, 2003] Chevalier, R. A. and Oishi, J. (2003). Cassiopeia A and Its Clumpy Presupernova Wind. ApJ, 593:L23–L26.

Bibliography

[Clark and Caswell, 1976] Clark, D. H. and Caswell, J. L. (1976). A study of galactic supernova remnants, based on Molonglo-Parkes observational data. MNRAS, 174:267–305.

[Clemens et al., 1988] Clemens, D. P., Sanders, D. B., and Scoville, N. Z. (1988). The large-scale distribution of molecular gas in the first Galactic quadrant. ApJ, 327:139–155.

[Colgate and McKee, 1969] Colgate, S. A. and McKee, C. (1969). Early Supernova Luminosity. ApJ, 157:623.

[Cordes and Lazio, 2002] Cordes, J. M. and Lazio, T. J. W. (2002). NE2001.I. A New Model for the Galactic Distribution of Free Electrons and its Fluctuations. *ArXiv Astrophysics e-prints*.

[Cristofari et al., 2013] Cristofari, P., Gabici, S., Casanova, S., Terrier, R., and Parizot, E. (2013). Acceleration of cosmic rays and gamma-ray emission from supernova remnants in the Galaxy. MNRAS, 434:2748–2760.

[Daniel et al., 2012] Daniel, M. K., Vasileiadis, G., and H. E. S. S. Collaboration (2012). Determining atmospheric aerosol content with an infra-red radiometer. In Aharonian, F. A., Hofmann, W., and Rieger, F. M., editors, *American Institute of Physics Conference Series*, volume 1505 of *American Institute of Physics Conference Series*, pages 717–720.

[DeLaney and Rudnick, 2003] DeLaney, T. and Rudnick, L. (2003). The First Measurement of Cassiopeia A's Forward Shock Expansion Rate. ApJ, 589:818–826.

[Dermer, 1986] Dermer, C. D. (1986). Secondary production of neutral pi-mesons and the diffuse galactic gamma radiation. A&A, 157:223–229.

[Dickey and Lockman, 1990] Dickey, J. M. and Lockman, F. J. (1990). H I in the Galaxy. ARA&A, 28:215–261.

[Diner et al., 2002] Diner, D. J., Beckert, J. C., Bothwell, G. W., and Rodriguez, J. I. (2002). Performance of the MISR instrument during its first 20 months in Earth orbit. *IEEE Transactions on Geoscience and Remote Sensing*, 40:1449–1466.

[Dorner et al., 2009] Dorner, D., Nilsson, K., and Bretz, T. (2009). A method to correct IACT data for atmospheric absorption due to the Saharan Air Layer. A&A, 493:721–725.

[Drury et al., 1994] Drury, L. O., Aharonian, F. A., and Voelk, H. J. (1994). The gamma-ray visibility of supernova remnants. A test of cosmic ray origin. A&A, 287:959–971.

[Drury et al., 2001] Drury, L. O., Ellison, D. E., Aharonian, F. A., Berezhko, E., Bykov, A., Decourchelle, A., Diehl, R., Meynet, G., Parizot, E., Raymond, J., Reynolds, S., and Spangler, S. (2001). Test of galactic cosmic-ray source models - Working Group Report. Space Sci. Rev., 99:329–352.

[Dwarkadas, 2005] Dwarkadas, V. V. (2005). The Environments of the Most Massive Stars. In Humphreys, R. and Stanek, K., editors, *The Fate of the Most Massive Stars*, volume 332 of *Astronomical Society of the Pacific Conference Series*, page 320.

[Faucher-Giguère and Kaspi, 2006] Faucher-Giguère, C.-A. and Kaspi, V. M. (2006). Birth and Evolution of Isolated Radio Pulsars. ApJ, 643:332–355.

[Ferrand and Safi-Harb, 2012] Ferrand, G. and Safi-Harb, S. (2012). A census of high-energy observations of Galactic supernova remnants. *Advances in Space Research*, 49:1313–1319.

[Ferrière, 2001] Ferrière, K. M. (2001). The interstellar environment of our galaxy. *Reviews of Modern Physics*, 73:1031–1066.

[Freudenreich, 1998] Freudenreich, H. T. (1998). A COBE Model of the Galactic Bar and Disk. ApJ, 492:495.

[Fukui, 2013] Fukui, Y. (2013). Molecular and Atomic Gas in the Young TeV γ-Ray SNRs RX J1713.7-3946 and RX J0852.0-4622; Evidence for the Hadronic Production of γ-Rays. In Torres, D. F. and Reimer, O., editors, *Cosmic Rays in Star-Forming Environments*, volume 34 of *Advances in Solid State Physics*, page 249.

[Funk et al., 2005] Funk, S., Hinton, J., Hermann, G., Berge, D., Bernlöhr, K., Hofmann, W., Nayman, P., Toussenel, F., and Vincent, P. (2005). The Central Trigger System of the H.E.S.S. Telescope Array. In Aharonian, F. A., Völk, H. J., and Horns, D., editors, *High Energy Gamma-Ray Astronomy*, volume 745 of *American Institute of Physics Conference Series*, pages 753–757.

[Ghisellini et al., 1988] Ghisellini, G., Guilbert, P. W., and Svensson, R. (1988). The synchrotron boiler. ApJ, 334:L5–L8.

[Ginzburg and Syrovatskii, 1964] Ginzburg, V. L. and Syrovatskii, S. I. (1964). *The Origin of Cosmic Rays*.

[Giordano et al., 2012] Giordano, F., Naumann-Godo, M., Ballet, J., Bechtol, K., Funk, S., Lande, J., Mazziotta, M. N., Rainò, S., Tanaka, T., Tibolla, O., and Uchiyama, Y. (2012). Fermi Large Area Telescope Detection of the Young Supernova Remnant Tycho. ApJ, 744:L2.

[Gonzales and Woods, 2008] Gonzales, R. C. and Woods, R. W. (2008). *Digital Image Processing*.

Bibliography

[González Hernández et al., 2012] González Hernández, J. I., Ruiz-Lapuente, P., Tabernero, H. M., Montes, D., Canal, R., Méndez, J., and Bedin, L. R. (2012). No surviving evolved companions of the progenitor of SN1006. Nature, 489:533–536.

[Green, 2001] Green, D. A. (2001). G353.9-2.0, a new Galactic supernova remnant identified from the NRAO Very Large Array Sky Survey. MNRAS, 326:283–286.

[Green, 2009] Green, D. A. (2009). A revised Galactic supernova remnant catalogue. *Bulletin of the Astronomical Society of India*, 37:45–61.

[Green, 2012] Green, D. A. (2012). The distribution of SNRs with galactocentric radius. In Aharonian, F. A., Hofmann, W., and Rieger, F. M., editors, *American Institute of Physics Conference Series*, volume 1505 of *American Institute of Physics Conference Series*, pages 5–12.

[Hahn et al., 2013a] Hahn, J., de los Reyes, R., Bernlöhr, K., Krüger, P., Lo, Y., Chadwick, P., Daniel, M., Deil, C., Gast, H., Kosack, K., and Marandon, V. (2013a). Impact of aerosols and adverse atmospheric conditions on the data quality for spectral analysis of the H. E. S. S. telescopes. *Astroparticle Physics (In Press)*.

[Hahn et al., 2013b] Hahn, J., Gast, H., de los Reyes, R., Deil, C., Bernlöhr, K., Kosack, K., and Marandon, V. (2013b). Heidelberg Data Quality Selection. *H. E. S. S. Internal Note*.

[Han and Qiao, 1994] Han, J. L. and Qiao, G. J. (1994). The magnetic field in the disk of our Galaxy. A&A, 288:759–772.

[Heger et al., 2003] Heger, A., Fryer, C. L., Woosley, S. E., Langer, N., and Hartmann, D. H. (2003). How Massive Single Stars End Their Life. ApJ, 591:288–300.

[Heiles, 1996] Heiles, C. (1996). The Local Direction and Curvature of the Galactic Magnetic Field Derived from Starlight Polarization. ApJ, 462:316.

[Henderson et al., 1982] Henderson, A. P., Jackson, P. D., and Kerr, F. J. (1982). The distribution of neutral atomic hydrogen in our galaxy beyond the solar circle. ApJ, 263:116–122.

[Hillas, 1985] Hillas, A. M. (1985). Cerenkov light images of EAS produced by primary gamma. In Jones, F. C., editor, *International Cosmic Ray Conference*, volume 3 of *International Cosmic Ray Conference*, pages 445–448.

[Hofverberg et al., 2013] Hofverberg, P., Kankanyan, R., Panter, M., Hermann, G., Hofmann, W., Deil, C., Benkhali, F. A., and for the H. E. S. S. Collaboration (2013). Commissioning and initial performance of the H.E.S.S. II drive system. *ArXiv e-prints*.

[Hugoniot, 1889] Hugoniot, M. (1889). . *J. Ec. Polyt. Paris*.

[Jaffe et al., 2010] Jaffe, T. R., Leahy, J. P., Banday, A. J., Leach, S. M., Lowe, S. R., and Wilkinson, A. (2010). Modelling the Galactic magnetic field on the plane in two dimensions. MNRAS, 401:1013–1028.

[Kalashnikova et al., 2007] Kalashnikova, O. V., Mills, F. P., Eldering, A., and Anderson, D. (2007). Application of satellite and ground-based data to investigate the uv radiative effects of australian aerosols. *Remote Sensing of Environment*, 107:65 – 80.

[Kaspi et al., 2001] Kaspi, V. M., Roberts, M. E., Vasisht, G., Gotthelf, E. V., Pivovaroff, M., and Kawai, N. (2001). Chandra X-Ray Observations of G11.2-0.3: Implications for Pulsar Ages. ApJ, 560:371–377.

[Katsuda et al., 2008] Katsuda, S., Tsunemi, H., Uchida, H., and Kimura, M. (2008). Forward Shock Proper Motions of Kepler's Supernova Remnant. ApJ, 689:225–230.

[Kelner et al., 2006] Kelner, S. R., Aharonian, F. A., and Bugayov, V. V. (2006). Energy spectra of gamma rays, electrons, and neutrinos produced at proton-proton interactions in the very high energy regime. Phys. Rev. D, 74(3):034018.

[Keohane et al., 2007] Keohane, J. W., Reach, W. T., Rho, J., and Jarrett, T. H. (2007). A Near-Infrared and X-Ray Study of W49 B: A Wind Cavity Explosion. ApJ, 654:938–944.

[Kippenhahn and Weigert, 1990] Kippenhahn, R. and Weigert, A. (1990). *Stellar Structure and Evolution*.

[Kolpak et al., 2003] Kolpak, M. A., Jackson, J. M., Bania, T. M., Clemens, D. P., and Dickey, J. M. (2003). Resolving the Kinematic Distance Ambiguity toward Galactic H II Regions. ApJ, 582:756–769.

[Krause et al., 2008a] Krause, O., Birkmann, S. M., Usuda, T., Hattori, T., Goto, M., Rieke, G. H., and Misselt, K. A. (2008a). The Cassiopeia A Supernova Was of Type IIb. *Science*, 320:1195–.

[Krause et al., 2008b] Krause, O., Tanaka, M., Usuda, T., Hattori, T., Goto, M., Birkmann, S., and Nomoto, K. (2008b). Tycho Brahe's 1572 supernova as a standard typeIa as revealed by its light-echo spectrum. Nature, 456:617–619.

[Krymskii, 1977] Krymskii, G. F. (1977). A regular mechanism for the acceleration of charged particles on the front of a shock wave. *Akademiia Nauk SSSR Doklady*, 234:1306–1308.

Bibliography

[Lebohec and Holder, 2003] Lebohec, S. and Holder, J. (2003). The cosmic ray background as a tool for relative calibration of atmospheric Cherenkov telescopes. *Astroparticle Physics*, 19:221–233.

[Lee et al., 2013] Lee, J.-J., Park, S., Hughes, J. P., and Slane, P. O. (2013). X-ray observation of the shocked red supergiant wind of Cassiopeia A. *ArXiv e-prints*.

[Li and Ma, 1983] Li, T.-P. and Ma, Y.-Q. (1983). Analysis methods for results in gamma-ray astronomy. ApJ, 272:317–324.

[Li et al., 2011] Li, W., Chornock, R., Leaman, J., Filippenko, A. V., Poznanski, D., Wang, X., Ganeshalingam, M., and Mannucci, F. (2011). Nearby supernova rates from the Lick Observatory Supernova Search - III. The rate-size relation, and the rates as a function of galaxy Hubble type and colour. MNRAS, 412:1473–1507.

[Lorimer, 2013] Lorimer, D. R. (2013). The Galactic Millisecond Pulsar Population. In *IAU Symposium*, volume 291 of *IAU Symposium*, pages 237–242.

[Matsui et al., 1984] Matsui, Y., Long, K. S., Dickel, J. R., and Greisen, E. W. (1984). A detailed X-ray and radio comparison of Kepler's supernova remnant. ApJ, 287:295–306.

[Mori, 2009] Mori, M. (2009). Nuclear enhancement factor in calculation of Galactic diffuse gamma-rays: A new estimate with DPMJET-3. *Astroparticle Physics*, 31:341–343.

[Nadezhin, 1985] Nadezhin, D. K. (1985). On the initial phase of interaction between expanding stellar envelopes and surrounding medium. Ap&SS, 112:225–249.

[Nolan et al., 2010] Nolan, S. J., Pühlhofer, G., and Rulten, C. B. (2010). Detailed studies of atmospheric calibration in imaging Cherenkov astronomy. *Astroparticle Physics*, 34:304–313.

[Ohm et al., 2009] Ohm, S., van Eldik, C., and Egberts, K. (2009). γ/hadron separation in very-high-energy γ-ray astronomy using a multivariate analysis method. *Astroparticle Physics*, 31:383–391.

[Ostriker and McKee, 1988] Ostriker, J. P. and McKee, C. F. (1988). Astrophysical blastwaves. *Reviews of Modern Physics*, 60:1–68.

[Patnaude et al., 2012] Patnaude, D. J., Badenes, C., Park, S., and Laming, J. M. (2012). The Origin of Kepler's Supernova Remnant. ApJ, 756:6.

[Patnaude and Fesen, 2009] Patnaude, D. J. and Fesen, R. A. (2009). Proper Motions and Brightness Variations of Nonthermal X-ray Filaments in the Cassiopeia A Supernova Remnant. ApJ, 697:535–543.

[Perlmutter et al., 1997] Perlmutter, S., Aldering, G., Deustua, S., Fabbro, S., Goldhaber, G., Groom, D. E., Kim, A. G., Kim, M. Y., Knop, R. A., Nugent, P., Pennypacker, C. R., della Valle, M., Ellis, R. S., McMahon, R. G., Walton, N., Fruchter, A., Panagia, N., Goobar, A., Hook, I. M., Lidman, C., Pain, R., Ruiz-Lapuente, P., Schaefer, B., and Supernova Cosmology Project (1997). Cosmology From Type IA Supernovae: Measurements, Calibration Techniques, and Implications. In *American Astronomical Society Meeting Abstracts*, volume 29 of *Bulletin of the American Astronomical Society*, page 1351.

[Pooley et al., 2002] Pooley, D., Lewin, W. H. G., Fox, D. W., Miller, J. M., Lacey, C. K., Van Dyk, S. D., Weiler, K. W., Sramek, R. A., Filippenko, A. V., Leonard, D. C., Immler, S., Chevalier, R. A., Fabian, A. C., Fransson, C., and Nomoto, K. (2002). X-Ray, Optical, and Radio Observations of the Type II Supernovae 1999em and 1998S. ApJ, 572:932–943.

[Ptuskin et al., 2010] Ptuskin, V., Zirakashvili, V., and Seo, E.-S. (2010). Spectrum of Galactic Cosmic Rays Accelerated in Supernova Remnants. ApJ, 718:31–36.

[Ptuskin and Zirakashvili, 2003] Ptuskin, V. S. and Zirakashvili, V. N. (2003). Limits on diffusive shock acceleration in supernova remnants in the presence of cosmic-ray streaming instability and wave dissipation. A&A, 403:1–10.

[Ptuskin and Zirakashvili, 2005] Ptuskin, V. S. and Zirakashvili, V. N. (2005). On the spectrum of high-energy cosmic rays produced by supernova remnants in the presence of strong cosmic-ray streaming instability and wave dissipation. A&A, 429:755–765.

[Pühlhofer et al., 2003] Pühlhofer, G., Bolz, O., Götting, N., Heusler, A., Horns, D., Kohnle, A., Lampeitl, H., Panter, M., Tluczykont, M., Aharonian, F., Akhperjanian, A., Beilicke, M., Bernlöhr, K., Börst, H., Bojahr, H., Coarasa, T., Contreras, J. L., Cortina, J., Denninghoff, S., Fonseca, M. V., Girma, M., Heinzelmann, G., Hermann, G., Hofmann, W., Jung, I., Kankanyan, R., Kestel, M., Konopelko, A., Kornmeyer, H., Kranich, D., Lopez, M., Lorenz, E., Lucarelli, F., Mang, O., Meyer, H., Mirzoyan, R., Moralejo, A., Ona-Wilhelmi, E., Plyasheshnikov, A., de Los Reyes, R., Rhode, W., Ripken, J., Rowell, G., Sahakian, V., Samorski, M., Schilling, M., Siems, M., Sobzynska, D., Stamm, W., Vitale, V., Völk, H. J., Wiedner, C. A., Wittek, W., and HEGRA Collaboration (2003). The technical performance of the HEGRA system of imaging air Cherenkov telescopes. *Astroparticle Physics*, 20:267–291.

[Rankine, 1870] Rankine, W. (1870). . *Phil. Trans. R. Soc.*, 160:277.

[Renaud, 2009] Renaud, M. (2009). Latest results on Galactic sources as seen in VHE gamma-rays. *ArXiv e-prints*.

Bibliography

[Reynolds, 2008] Reynolds, S. P. (2008). Supernova Remnants at High Energy. ARA&A, 46:89–126.

[Reynolds et al., 2007] Reynolds, S. P., Borkowski, K. J., Hwang, U., Hughes, J. P., Badenes, C., Laming, J. M., and Blondin, J. M. (2007). A Deep Chandra Observation of Kepler's Supernova Remnant: A Type Ia Event with Circumstellar Interaction. ApJ, 668:L135–L138.

[Reynolds and Ellison, 1992] Reynolds, S. P. and Ellison, D. C. (1992). Electron acceleration in Tycho's and Kepler's supernova remnants - Spectral evidence of Fermi shock acceleration. ApJ, 399:L75–L78.

[Riess et al., 2001] Riess, A. G., Nugent, P. E., Gilliland, R. L., Schmidt, B. P., Tonry, J., Dickinson, M., Thompson, R. I., Budavári, T., Casertano, S., Evans, A. S., Filippenko, A. V., Livio, M., Sanders, D. B., Shapley, A. E., Spinrad, H., Steidel, C. C., Stern, D., Surace, J., and Veilleux, S. (2001). The Farthest Known Supernova: Support for an Accelerating Universe and a Glimpse of the Epoch of Deceleration. ApJ, 560:49–71.

[Roepke, 2008] Roepke, F. K. (2008). Thermonuclear Supernovae. *ArXiv e-prints*.

[Rolke et al., 2005] Rolke, W. A., López, A. M., and Conrad, J. (2005). Limits and confidence intervals in the presence of nuisance parameters. *Nuclear Instruments and Methods in Physics Research A*, 551:493–503.

[Salpeter, 1955] Salpeter, E. E. (1955). The Luminosity Function and Stellar Evolution. ApJ, 121:161.

[Sanders et al., 1986] Sanders, D. B., Clemens, D. P., Scoville, N. Z., and Solomon, P. M. (1986). Massachusetts-Stony Brook Galactic plane CO survey. I - (b,V) maps of the first Galactic quadrant. ApJS, 60:1–296.

[Sanuki et al., 2000] Sanuki, T., Motoki, M., Matsumoto, H., Seo, E. S., Wang, J. Z., Abe, K., Anraku, K., Asaoka, Y., Fujikawa, M., Imori, M., Maeno, T., Makida, Y., Matsui, N., Matsunaga, H., Mitchell, J., Mitsui, T., Moiseev, A., Nishimura, J., Nozaki, M., Orito, S., Ormes, J., Saeki, T., Sasaki, M., Shikaze, Y., Sonoda, T., Streitmatter, R., Suzuki, J., Tanaka, K., Ueda, I., Yajima, N., Yamagami, T., Yamamoto, A., Yoshida, T., and Yoshimura, K. (2000). Precise Measurement of Cosmic-Ray Proton and Helium Spectra with the BESS Spectrometer. ApJ, 545:1135–1142.

[Schaller et al., 1992] Schaller, G., Schaerer, D., Meynet, G., and Maeder, A. (1992). New grids of stellar models from 0.8 to 120 solar masses at Z = 0.020 and Z = 0.001. A&AS, 96:269–331.

[Sedov, 1946] Sedov, L. I. (1946). Propagation of strong shock waves. *Journal of Applied Mathematics and Mechanics*, 10:241–250.

[Shklovsky, 1957] Shklovsky, I. S. (1957). Optical emission from the Crab nebula in the continuous spectrum. In van de Hulst, H. C., editor, *Radio astronomy*, volume 4 of *IAU Symposium*, page 201.

[Smartt et al., 2009] Smartt, S. J., Eldridge, J. J., Crockett, R. M., and Maund, J. R. (2009). The death of massive stars - I. Observational constraints on the progenitors of Type II-P supernovae. MNRAS, 395:1409–1437.

[Stecker, 1971] Stecker, F. W. (1971). Cosmic gamma rays. *NASA Special Publication*, 249.

[Taylor, 1950] Taylor, G. (1950). The Formation of a Blast Wave by a Very Intense Explosion. I. Theoretical Discussion. *Royal Society of London Proceedings Series A*, 201:159–174.

[Taylor and Cordes, 1993] Taylor, J. H. and Cordes, J. M. (1993). Pulsar distances and the galactic distribution of free electrons. ApJ, 411:674–684.

[Taylor and Manchester, 1977] Taylor, J. H. and Manchester, R. N. (1977). Galactic distribution and evolution of pulsars. ApJ, 215:885–896.

[Tesfaye et al., 2011] Tesfaye, M., Sivakumar, V., Botai, J., and Mengistu Tsidu, G. (2011). Aerosol climatology over South Africa based on 10 years of Multiangle Imaging Spectroradiometer (MISR) data. *Journal of Geophysical Research (Atmospheres)*, 116:20216.

[Tian and Leahy, 2008] Tian, W. W. and Leahy, D. A. (2008). The distances of supernova remnants Kes 69 and G21.5-0.9 from HI and ^{13}CO spectra. MNRAS, 391:L54–L58.

[Torii et al., 2008] Torii, S., Yamagami, T., Tamura, T., Yoshida, K., Kitamura, H., Anraku, K., Chang, J., Ejiri, M., Iijima, I., Kadokura, A., Kasahara, K., Katayose, Y., Kobayashi, T., Komori, Y., Matsuzaka, Y., Mizutani, K., Murakami, H., Namiki, M., Nishimura, J., Ohta, S., Saito, Y., Shibata, M., Tateyama, N., Yamagishi, H., Yamashita, T., and Yuda, T. (2008). High-energy electron observations by PPB-BETS flight in Antarctica. *ArXiv e-prints*.

[Truelove and McKee, 1999] Truelove, J. K. and McKee, C. F. (1999). Evolution of Nonradiative Supernova Remnants. ApJS, 120:299–326.

[Turatto, 2003] Turatto, M. (2003). Classification of Supernovae. In Weiler, K., editor, *Supernovae and Gamma-Ray Bursters*, volume 598 of *Lecture Notes in Physics, Berlin Springer Verlag*, pages 21–36.

[Vallée, 2005] Vallée, J. P. (2005). The Spiral Arms and Interarm Separation of the Milky Way: An Updated Statistical Study. AJ, 130:569–575.

Bibliography

[Vink, 2006] Vink, J. (2006). X-ray High Resolution and Imaging Spectroscopy of Supernova Remnants. In Wilson, A., editor, *The X-ray Universe 2005*, volume 604 of *ESA Special Publication*, page 319.

[Vink, 2008] Vink, J. (2008). The Kinematics of Kepler's Supernova Remnant as Revealed by Chandra. ApJ, 689:231–241.

[Vink and Laming, 2003] Vink, J. and Laming, J. M. (2003). On the Magnetic Fields and Particle Acceleration in Cassiopeia A. ApJ, 584:758–769.

[Völk et al., 2005] Völk, H. J., Berezhko, E. G., and Ksenofontov, L. T. (2005). Magnetic field amplification in Tycho and other shell-type supernova remnants. A&A, 433:229–240.

[Völk et al., 2008] Völk, H. J., Berezhko, E. G., and Ksenofontov, L. T. (2008). Internal dynamics and particle acceleration in Tycho's SNR. A&A, 483:529–535.

[Völk et al., 2002] Völk, H. J., Berezhko, E. G., Ksenofontov, L. T., and Rowell, G. P. (2002). The high energy gamma-ray emission expected from Tycho's supernova remnant. A&A, 396:649–656.

[Völk and Bernlöhr, 2009] Völk, H. J. and Bernlöhr, K. (2009). Imaging very high energy gamma-ray telescopes. *Experimental Astronomy*, 25:173–191.

[von Neumann, 1947] von Neumann, J. (1947). *Los Alamos Scientific Laboratory Technical Series 7*.

[Williams et al., 2011] Williams, B. J., Blair, W. P., Blondin, J. M., Borkowski, K. J., Ghavamian, P., Long, K. S., Raymond, J. C., Reynolds, S. P., Rho, J., and Winkler, P. F. (2011). RCW 86: A Type Ia Supernova in a Wind-blown Bubble. ApJ, 741:96.

[Willingale et al., 2002] Willingale, R., Bleeker, J. A. M., van der Heyden, K. J., Kaastra, J. S., and Vink, J. (2002). X-ray spectral imaging and Doppler mapping of Cassiopeia A. A&A, 381:1039–1048.

[Woltjer, 1972] Woltjer, L. (1972). Supernova Remnants. ARA&A, 10:129.

[Woosley and Janka, 2005] Woosley, S. and Janka, T. (2005). The physics of core-collapse supernovae. *Nature Physics*, 1:147–154.

[Woosley et al., 1993] Woosley, S. E., Langer, N., and Weaver, T. A. (1993). The evolution of massive stars including mass loss - Presupernova models and explosion. ApJ, 411:823–839.

[Young et al., 2006] Young, P. A., Fryer, C. L., Hungerford, A., Arnett, D., Rockefeller, G., Timmes, F. X., Voit, B., Meakin, C., and Eriksen, K. A. (2006). Constraints on the Progenitor of Cassiopeia A. ApJ, 640:891–900.

[Yusifov and Küçük, 2004] Yusifov, I. and Küçük, I. (2004). Revisiting the radial distribution of pulsars in the Galaxy. A&A, 422:545–553.

[Zirakashvili and Aharonian, 2007] Zirakashvili, V. N. and Aharonian, F. (2007). Analytical solutions for energy spectra of electrons accelerated by nonrelativistic shock-waves in shell type supernova remnants. A&A, 465:695–702.

[Zirakashvili and Ptuskin, 2008a] Zirakashvili, V. N. and Ptuskin, V. S. (2008a). Diffusive Shock Acceleration with Magnetic Amplification by Nonresonant Streaming Instability in Supernova Remnants. ApJ, 678:939–949.

[Zirakashvili and Ptuskin, 2008b] Zirakashvili, V. N. and Ptuskin, V. S. (2008b). The influence of the Alfvénic drift on the shape of cosmic ray spectra in SNRs. In Aharonian, F. A., Hofmann, W., and Rieger, F., editors, *American Institute of Physics Conference Series*, volume 1085 of *American Institute of Physics Conference Series*, pages 336–339.

Danksagung

An dieser Stelle möchte ich mich bei all den Menschen bedanken, die mir beim Schreiben dieser Arbeit beigestanden haben und ohne die ich heute ganz sicher nicht diese Danksagung schreiben würde.

Zuallererst möchte ich mich bei meinem Doktorvater Werner Hofmann bedanken, der es mir ermöglicht hat, bei H.E.S.S. - und auch CTA - mitzumachen. Ihre Ratschläge treffen immer genau ins Schwarze, und ich habe dadurch viel bei Ihnen gelernt. Vielen Dank für alles!

Ich danke Stefan Wagner sehr herzlich für die Zweitkorrektur meiner Arbeit.

Des weiteren gilt mein Dank German Hermann, der mich am Anfang der Promotion betreut hat und dafür viel Geduld mitbringen musste.

Ferner möchte ich mich bei Vincent 'Vince' Marandon bedanken, der mir bei den SNRs mit Rat und Tat zur Seite stand und das ganze auch noch mit einem sympathischen französisch-Akzent!

Danke sage ich Raquel de los Reyes für die transparente Zusammenarbeit in stets guter Atmosphäre! (Und natürlich auch für das Sangria-Rezept)

Ein dickes Dankeschön geht an Konrad Bernlöhr den ich so oft mit dummen Fragen gelöchert habe, dass er mich inzwischen sicher für einen Neandertaler hält... Naja, bin in Heidelberg geboren, das passt ja schon mal!

Vielen Dank, Willi Domainko, dass du ein wandelndes Astronomie-Lexikon bist! Du hast immer ein offenes Ohr, guten Rat und super Anregungen. Und ein Wohnzimmer in der Unteren Straße, was natürlich auch cool ist!

Weiterhin möchte ich Henning 'Eging' Gast für Rat und Unterstützung danken, der ja jetzt als Professor in Aachen residiert und sich inzwischen doch hoffentlich nicht zu fein ist, in eine rote Uniform zu schlüpfen und mit uns auf die Star-Trek Convention zu gehen!

Ich möchte auch Andreas Hilbert, mit dem ich mich durch's Physik-Studium gehangelt habe, für die Unterstützung, die vielen Grillparties und die Ingwerbonbons bedanken.

Sabrina, vielen Dank für deinen wertvollen Input zu den theoretischen Fragen in der Astrophysik. Du bist immer freundlich, und das obwohl du in Fortran

programmierst!

Danke, liebe Heidelberger H.E.S.S.-Gruppe, für die tolle Stimmung am Institut und das hohe Level an Expertise, das sich dort tummelt. Zu jeder Frage, die man hat, gibt es garantiert jemanden, der einem helfen kann.

Heidelberg ist bekanntermaßen ein gefährliches Pflaster, und ich habe es meiner Bürokollegin Chia Chun zu verdanken, das ich aus so manch brenzliger Situation heil herausgekommen bin. Danke für die Unterweisung in Shaolin-Kung-Fu, du hast mir das Leben gerettet!

Ich möchte ferner Anne Bochow danken, die mit ihren Anekdoten aus der DDR eigentlich immer in der Lage war, die typischen Probleme eines Doktoranden zu relativieren und mich so aufzubauen. Selbiges gilt auch für Stefan Ohm und in ähnlicher Weise Daniil Nekrassov (der mich aber nicht versucht hat aufzubauen).

Vielen Dank an Dan Parsons, Tanya Edwards und Svenja 'Schwani' Carrigan für's Korrekturlesen. Dan und Peter Eger, ich danke Euch auch für die Diskussionen rund um Gadgets, Science-Fiction und anderen Nerdkram und Schwani, dass Du mich dann jedesmal mit Frauenklatsch wieder in die Realität zurückgeholt hast!

Petter Hofverberg, du wirst der lebende Beweis sein, dass es die Wikinger sogar bis auf die Inseln des Indischen Ozeans geschaft haben. Ich weiss zwar nicht warum, aber dafür danke ich dir. Ich hoffe, dein Jagdbeil wird dir bei der Bekämpfung von Riesenspinnen und Hundertfüßlern behilflich sein.

Danke, Ruth, dass Du dem verplantesten Menschen auf dieser Welt mehrfach den Kragen gerettet hast! Wahrscheinlich hätte ich es ohne dich vergessen, etliche Stipendienformulare zu unterschreiben und müsste heute unter der Brücke leben.

Ich möchte François 'Mitterand' Brun, Christoph 'Criss-Cross' Deil, Quirin 'Q' Weitzel und Andreas Förster für die anregenden Gespräche und ihre coolen Spitznamen danken (OK, Andreas, für dich müssen wir uns noch mal was überlegen). Selbiges gilt für Ramin Marx, dessen Spitznamen ich hier nicht nennen will und der besser mal damit aufhören sollte, Saltos aus dem Stand zu machen.

An all die Anderen möchte ich sagen: Danke für die tolle Zusammenarbeit und Arbeitsatmosphäre! Ich kann mir keine bessere Arbeitsgruppe vorstellen!

Am wichtigsten jedoch ist es mir an dieser Stelle, meiner großartigen Familie und jenen, die ich dazu zähle, zu danken. Ihr habt mich gestützt in den

schwierigen Phasen der letzten Jahre, und ohne euch hätte ich es ganz gewiss nicht geschafft.

Das dickste Dankeschön gilt dabei meinen Eltern Maria Feid und Reinhard Hahn. Ohne euren weisen Rat, eure Unterstützung und eure Liebe wäre ich heute nicht dort, wo ich es bin! Dafür bin ich euch unendlich dankbar.